Advanced Electrodes from 2D Layered Materials for Li- and Na- Storage

BY

MANAS RANJAN PANDA

DEPARTMENT OF ENERGY SCIENCE AND ENGINEERING

INDIAN INSTITUTE OF TECHNOLOGY BOMBAY, INDIA

DEPARTMENT OF MATERIALS SCIENCE AND ENGINEERING

MONASH UNIVERSITY, AUSTRALIA

DEPARTMENT OF MECHANICAL AND AEROSPACE ENGINEERING

MONASH UNIVERSITY, AUSTRALIA

2021

Advanced Electrodes from 2D Layered Materials for Li- and Na- Storage

Submitted in partial fulfillment of the requirements

of the degree of
Doctor of Philosophy
of the
Indian Institute of Technology Bombay, India
and
Monash University, Australia

by

Manas Ranjan Panda

Supervisors:

Prof. Sagar Mitra (IIT Bombay)

Prof. Mainak Majumder (Monash University)

Prof. Qiaoliang Bao (Monash University)

The course of study for this award was developed jointly by
Monash University, Australia and the Indian Institute of Technology Bombay, India
and was given academic recognition by each of them.
The programme was administrated by the IITB-Monash Research Academy

(2021)

Dedicated to my parents

Declaration

I declare that this written submission represents my ideas in my own words, and where ideas or words by others have been included, I have adequately cited and referenced the original sources.

I additionally declare that I have adhered to all principles of academic honesty and integrity and have not misrepresented, fabricated, or falsified any idea/data/fact/source in my submission. I understand that any violation of the above will be cause for disciplinary action by the Institute, and additional penal action can be taken by sources that have not been appropriately cited or by those from whom appropriate permission has not been obtained where required.

Notice 1

Notice 2

I certify that I have made all reasonable efforts to secure copyright permissions for third-party content included in this thesis and have not knowingly added copyright content to my work without the owner's permission.

Student Name: Manas Ranjan Panda

IITB ID:

Monash ID:

Abstract

Two-dimensional (2D) materials with large surface areas, high charge-carrier mobility, and unique chemical and electronic properties are finding applications in various fields including energy-storage applications. These materials are promising candidates in rechargeable batteries to fulfill the demands for superior rate performance, long cycle life, and higher power and energy density requirements. As a part of this objective, we have studied a new class of bulk semiconducting transition metal dichalcogenides (TMDs), specifically, the 2D layered structure molybdenum ditelluride ($MoTe_2$). It is composed of stacked layers of Mo and Te (Te–Mo–Te) that are held together by weak van der Waals interactions. The relatively high interlayer spacing of $MoTe_2$ about 0.70 nm (graphite (0.335 nm) and MoS_2 (0.615 nm)) and the higher electronic conductivity of $MoTe_2$ make it an efficient anode material for both lithium and sodium-ion batteries (SIBs); the risk of substantial volume change is also absent in $MoTe_2$. We studied both 2H and 1T' phases of molybdenum ditelluride ($MoTe_2$), which was synthesized through a facile solid-state reaction route synthesis process. We have further investigated the lithium and sodium storage mechanism in both 2H and 1T' phases of $MoTe_2$ during the Li^+/Na^+ insertion and desertion process by using different Synchrotron-based in situ/ex situ experimental techniques alongside theoretical studies. The electrochemistry of the discharge/charge reaction that occurs in the first discharge/charge in the remaining cycles, and the observed high theoretical capacity including the polarization loss are investigated throughout our studies.

To understand the electrochemical storage properties of the new class of bulk semiconducting 2H phases of $MoTe_2$, we first studied its charge-storage capability against lithium. It has been found that the as-prepared $MoTe_2$ electrodes exhibit an initial lithium-storage specific capacity of 432 mAh g^{-1} at a current density of 1.0 A g^{-1}. Further, it retains the property of a reversible specific capacity of 291 mAh g^{-1} after 250 cycles. An investigation by in situ X-ray absorption near-edge structure (XANES) and a comparison with density functional theory (DFT) calculations reveals that this anode material exhibits a unique lithium reaction pathway and storage mechanism. Conventional electrochemical techniques are employed to estimate the Li^+ diffusion coefficient and transport kinetics. A full-cell electrochemical performance measurement between the $MoTe_2$ anode and a lithium cobalt oxide (LCO) cathode showed a high energy density of 454 Wh kg^{-1} (at a current density of 0.5 A g^{-1}, based on the mass of the anode).

Further, the semimetallic 1T' phase of $MoTe_2$ was investigated against lithium metal. The as-prepared 1T' phase of $MoTe_2$ has shown a specific capacity of 501mAh g^{-1} at 1.0 A g^{-1}. The half cell showed capacity retention of 91.5 % (with reference to the 2nd cycle) and 99 % of Coulombic efficiency over 200 cycles. The experimental observation shows that during the Li^+ insertion at the initial concentration, the mechanism follows the intercalation process. As the Li^+ insertion concentration increases, the reaction pathway changes to the conversion process at the end of the 1st discharge process. At the end of the discharge process, the followed conversion reaction results in Mo-nanoparticles with lithium telluride (Li_2Te). The ex situ XANES observation shows that the lithiation/delithiation process is reversible. The theory study shows that the reaction is reversible for a specific concentration of Li ($x \leq 2$). The 1T'-$MoTe_2$//LCO full battery displays a reversible capacity of 388.4 mAh g^{-1} at 100 mA g^{-1} for 100 cycles, which able to retain 74 % of its initial capacity (with reference to 2nd cycle) with a Coulombic efficiency of ≈96 % at a current density of 0.1 A g^{-1}, based on the mass of the anode.

In this work, after the successful investigation of $MoTe_2$ against lithium, we extended our study to the layered structured 2H phase of $MoTe_2$ as an anode material for an alternative cation, that is, sodium, in SIBs applications. Since sodium is abundant in nature, SIBs are considered next-generation rechargeable batteries for grid-scale energy-storage applications; SIBs display electrochemical behavior that is similar to LIBs. Several high-performance sodium-rich cathode materials have been developed, which show excellent electrochemical performance. Nevertheless, the large-scale application of the ultimate metal-free SIB that has a full-cell configuration is hampered due to the unavailability of reliable anode materials. In a half-cell configuration (with respect to the sodium metal), the $MoTe_2$ electrode exhibits an initial specific capacity of 320 mAh g^{-1} at a current density of 1.0 A g^{-1}, and it retains a high capacity of 270 mAh g^{-1} after 200 cycles. The SXRD and XANES observation shows that the sodiation/desodiation process is reversible. Further, a sodium-ion full cell is constructed by coupling the $MoTe_2$ as the anode and sodium vanadium phosphate $Na_3V_2(PO_4)_3$ (NVP) as the cathode. The sodium-ion full cell retains 88 % of its initial capacity after 150 cycles at a current density of 0.5 A g^{-1}. Operating at an average potential of ~2 V, the full cell delivers a high energy density of 414 Wh kg^{-1}.

Further, the effect of crystallite size, crystallinity, and the impact of electrolyte additives on 2H phase of $MoTe_2$ in SIB applications have been investigated in detail. It has been observed that the increase in the heating rate results in a decrease of crystallite size. The electrochemical

sodium storage performance improved for the sample that was prepared at a higher heating rate with a smaller crystallite size. With the higher heating rate variation, the densification differs, which affects the thermal and electrical conductivity properties. The higher heating rate causes higher thermal gradients, resulting in the sintering of the exterior portion before the interior, which further enhances the porosity and the defects that are responsible for the higher electrochemical performances of $MoTe_2$ in SIB applications. The 2 ^oC/ min heating rate of the $MoTe_2$ anode//NVP full cell shows an energy density of 440 Wh Kg^{-1} with a Coulombic efficiency of 98 % after 100 cycles and an overall capacity retention of 78 % (with reference to the second cycle) over 100 cycles. This thesis presents a novel approach to implement a new class of 2D layered TMD material for energy-storage applications, which opens up possibilities of new anode materials for rechargeable LIBs/SIBs.

Keywords: 2D Materials; Molybdenum Ditelluride; Anode material; Lithium-ion Battery, Sodium-ion Battery

Table of contents

List of figures

List of tables

List of abbreviations

1.	CMC	Carboxymethyl cellulose
2.	CV	Cyclic Voltammetry
3.	DC	Direct Current
4.	DEC	Diethyl carbonate
5.	DFT	Density Functional Theory
6.	DI- water	Deionized water
7.	DMC	Dimethyl carbonate
8.	EC	Ethylene carbonate
9.	EDXS	Energy-dispersive X-ray Spectroscopy
10.	EIS	Electrochemical Impedance Spectroscopy
11.	EV	Electric Vehicle
12.	EXAFS	X-ray Absorption Near Edge Structure
13.	FEC	Fluoroethylene carbonate
14.	FEG-SEM	Field Emission Gun Scanning Electron Microscopy
15.	FEG-TEM	Field Emission Gun Transmission Electron Microscopy
16.	FWHM	Full width at half maximum
17.	GO	Graphene oxide
18.	rGO	Reduced graphene oxide
19.	HRTEM	High Resolution Transmission Electron Microscopy
20.	IPA	Isopropyl alcohol
21.	JCPDS	Joint Committee of Powder Diffraction Standards
22.	LIB	Lithium-ion battery
23.	LIBs	Lithium-ion batteries
24.	$LiClO_4$	Lithium perchlorate
25.	$LiCoO_2$	Lithium cobalt oxide
26.	$LiFePO_4$	Lithium iron phosphate
27.	LSV	Linear Sweep Voltammetry
28.	NMP	N-Methyl-2-pyrrolidone
29.	OCV	Open Circuit Potential
30.	PA	Propyl acetate
31.	PC	Propylene carbonate

32.	PP	Polypropylene
33.	PVDF	Polyvinylidene difluoride
34.	SAED	Selected area electron diffraction
35.	SEI	Solid Electrolyte Interphase
36.	SEM	Scanning Electron Microscopy
37.	SIB	Sodium-ion battery
38.	TEM	Transmission electron microscopy
39.	STEM	Scanning transmission electron microscopy
40.	SXRD	Synchrotron X-Ray Diffraction
41.	VASP	Vienna ab-initio simulation package
42.	VC	Vinylene carbonate
43.	XANES	X-ray absorption near edge structure
44.	XPS	X-ray photoelectron spectroscopy
45.	XRD	X-ray diffraction

CHAPTER 1

Introduction

"This chapter describes a general introduction, background of different 2D materials used in energy-storage applications, motivations, and the aims of the thesis."

1.1 General background

Electrical storage in batteries is a common, conventional, and convenient way to store electricity, and it is widely used in various applications. The battery technology is classified into two categories: the primary battery (not reversible) and the secondary battery (reversible, such as lead-acid battery, nickel-cadmium battery, lithium-ion battery, manganese battery, and the like).[1–4]

A rechargeable battery comprises three major components. The anode, which is known as the negative electrode that releases electrons to the external circuit, gets oxidized during the electrochemical cycle. An anode should be a good reducing agent that is stable under electrochemical cycle, has low cost and is easy to fabricate, and has better electronic conductivity. The cathode, which is termed the positive electrode, receives the electrons from the external circuit. The cathode should have a higher working voltage and electrolyte compatibility, and be a better oxidizing agent that is low cost and easy to fabricate. Electrolytes should have higher ionic conductivity; they should also be electronic insulators and cost-effective. These three components should be selected in such that they possess a higher cell voltage and the overall cell is lightweight to enable higher energy density.[1–8]

Recently developed lithium-ion batteries (LIBs) that are dependent on graphite anodes have certain restrictions. The contemporary challenges to electrode materials in LIBs are their low electronic and ionic conductivities. The low electronic and ionic conductivities affect the material's ability to store Li^+ effectively. This phenomenon further reduces the cycle life of the battery, which results in less power density.[1–5] The primary challenge is to restrict the severe volume expansion or contraction of the electrode materials, which results in eventual electrode pulverization and performance decay during the charging/discharging process. There is a requirement of additive carbonaceous material or doping of heteroatoms to overcome these difficulties, which are not straightforward and are also not cost-effective.[1–10] However, LIBs have been extensively used as a potential candidate in portable electronic devices and electric vehicles because they possess higher output voltages, higher energy densities, and long cycle lives. For large-scale energy-storage systems, the limited lithium and cobalt sources, which are the two of the most critical LIB elements; and the unavailability of economical recycling methods are significant concerns. Since all functionalities of sodium-ion Batteries (SIBs) are similar to LIBs, they are garnering interest. Sodium is the sixth most abundant element in the earth, and it is geographically not as limited as lithium, which is an advantage that SIBs have

over LIBs. The cost of Li_2Co_3 is USD 6600/Mt, whereas the cost of Na_2CO_3 is USD 60/Mt. In addition to the great cost difference between these two carbonates, SIBs provide better safety than LIBs. In SIBs, aluminum can be used as both an anode and cathode current collector because Al does not form an alloy with sodium at a lower voltage (below 0.1 V), whereas it forms alloys with Li/Li^+ below 0.1 V. So, by using Al as a current collector in SIB, safe transportation of battery can be achieved at 0V.[3,10–12] Researchers are primarily interested in developing electrode materials to improvise the performance of batteries without incurring any extra cost. The SIB has added to expectations about its growth in the market with an inspiring annual rate of ~ 24 % for 2018–2022. This is because sodium is abundant in nature, and SIBs display electrochemical behavior similar to LIBs. Developing a low-cost electrode material for both LIBs and SIBs with a good rate capability, high specific capacity, and high Coulombic efficiency will be immensely beneficial for renewable energy storage.[10–17]

1.2 Motivation

The primary motivation of this work is to identify a different class of TMDC layered material as suitable lithium/sodium-ion storage materials.[15–20] Since LIBs have higher output voltages, higher energy density, and long cycle life, they are potential candidates in portable electronic devices and electric vehicles. However, in large-scale energy-storage systems, where cost and availability are critical factors, the limited lithium and cobalt sources and the lack of suitable recycling methods are significant concerns.[9,12,15] Layered structure 2D materials provide multiple advantages as electrode materials for rechargeable LIBs/SIBs. The 2D morphology provides a higher surface area, which results in the reduction of the ion diffusion distance, allowing easy electrolyte access to active materials by enhancing the ion diffusion kinetics. Among these groups of materials, transition metal chalcogenides that have an MX_2-type of structure (where M=Mo and X=S, Se, Te) are now of research interest as electrode materials in the field of lithium and SIBs.[15–25] Among these materials, Te-based TMDs are gaining attention due to higher electronic conductivity, higher interlayer spacing, and bandgap tunability. Two polymorphic structures are exhibited by $MoTe_2$: the 2H-$MoTe_2$ phase, which has a semiconducting bandgap; and its complement, the 1T' phase of the semi metallic bandgap. The implementation of this new class of materials within LIB and SIB device applications is still a matter of significant concern due to several reasons such as electrochemical reactions that are still not understood with certainty, which would affect safety and industrial scale-up.

The synthesis process of these materials must include scalable, low-cost, and environment-friendly methods with associated energy savings that need to be more advantageous than currently used techniques. Besides, to overcome most of the challenges, special attention has been given to the design and engineering of the cell structure, including in aspects of fabricating the electrode, choosing a suitable binder and the conducting agent, and designing of appropriate anode active materials. In situ/operando experiments have been emphasized to understand the electrochemical mechanisms in LIB/SIB applications for these potential new anode materials, which were also supported by DFT calculations. Recent studies have been undertaken to identify the underlying electrochemical mechanism of these materials. Further, the obtained results have allowed us to work on material chemistry engineering to improve the electrochemical performance, which would enable the developing of potential electrodes for lithium/SIBs.[20–30]

1.3Aim of the thesis

The aim of this research work is to identify a different electrode material for high-performance lithium/SIBs. The main objective is to study anode materials, their working principles, and technical challenges along with the possibility of fabricating the half cell and full cell prototypes. Initially, we briefly discuss 2D layered TMDCs materials as an anode for LIBs and SIBs. We also discuss the relevant physical and electrochemical characterization techniques, technical challenges, and the like.

The developments in LIBs have been well implemented in the field of portable electronics. The reason is the greater energy density of LIBs in comparison to other rechargeable systems of portable electronics. However, its application as a large energy-storage device has some disadvantages due to the high cost and low abundance of lithium and related electrode composition elements. Due to the abundance, sodium could be an ideal candidate to compete with lithium. The current SIB technology is based on the insertion-compound anode and cathode materials, which limit their charge-storage capacity and energy density. Due to the large size, the insertion of Na^+ ions into the anode is the major challenge. The 2D layered structure of the electrode materials could play a vital role in developing both LIB and SIB technology to overcome the fundamental challenges that motivate the researchers to work on this topic. Since the use of 2D materials for LIBs and SIBs applications is new technology (although it was introduced a few years ago), only certain problems have been solved. Therefore, researchers have a broad scope to develop new materials to improve LIBs and SIBs.

In this research work, we have tried to overcome certain problems (such as long-term cycling instability, the lithiation/sodiation mechanism, improvement of the cell capacity, and the like) and introduce possible solutions for the studied anode materials. In particular, along with the full-cell prototype study, we also discuss the 2D layered $MoTe_2$ material and its electrochemical performance as an anode material in LIB and SIB applications. Although only some literature is available on $MoTe_2$ for LIB and SIB applications, the study is limited to the understanding of the lithium and sodium reaction mechanisms. We have thoroughly examined the electrochemical reaction mechanism through various experimental measurements as well as DFT studies of the discharge/charge reaction, which occurs in the first discharge/charge to the remaining cycles and the storage mechanism in both 2H and 1T' phases of $MoTe_2$ during the Li^+/Na^+ insertion and desertion process. This thesis presents a novel approach to implement a new class of 2D layered TMD materials for energy-storage applications; the work also introduces avenues to identify anode materials for rechargeable LIBs/SIBs.[15–25,26,28]

1.4 Thesis outline

We have discussed the role and advantages of applying a layered 2D material in LIB and SIB applications throughout our thesis. **Chapter 1** presents a general introduction, background of different 2D materials used in energy-storage applications, motivations, and the aims of the thesis. **Chapter 2** deals with the literature reviews of TMDCs, and applications of other classes of TMDCs in LIBs and SIBs. The literature on the new class of transition metal tellurides, specifically, $MoTe_2$ and its applications in various fields such as energy-storage applications has been reviewed. **Chapter 3** discusses the methodology and the different chemicals that have been used; it also presents synthesis procedures and characterization techniques that have been used in our current studies. **Chapter 4** introduces the semiconducting 2H-phase of $MoTe_2$ that is synthesized by a solid-state route as an anode material in LIBs. In situ X-ray absorption near-edge structures (XANES) have been used to reveal the unique lithium reaction pathway and storage mechanism, which is further complemented by DFT calculations and the corresponding full-cell prototype study. **Chapter 5** investigates the 1T'-phase of $MoTe_2$ that is synthesized by a solid-state route as a fast anode for LIBs. Ex situ XANES are used to reveal the unique lithium reaction pathway and storage mechanism, which is further complemented by DFT calculations along with the full-cell prototype study. **Chapter 6** presents information about the use of as-synthesized $MoTe_2$ as an active material for SIBs without any further surface modification or conductive coating. Synchrotron X-ray diffraction (SXRD) and XANES are used to detect the

phase changes during the sodiation/desodiation process to explore the sodium storage mechanism. Finally, a full-cell SIB has been demonstrated using the $MoTe_2$ anode and sodium vanadium phosphate (NVP) as the cathode to investigate numerous practical energy-storage applications. **Chapter 7** deals with the effect of crystallite size, crystallinity, additives on the electrochemical performance of SIBs, and cause of higher specific capacity. Ex situ/in situ EXAFS provides the corresponding sodium storage mechanism. **Chapter 8** discusses a summary of our work, the scope of the studied materials, and the enhancement of their charge-storage mechanism in future applications of LIBs and SIBs.

1.5 References

(1) Slater, M. D.; Kim, D.; Lee, E.; Johnson, C. S. Sodium-Ion Batteries. *Adv. Funct. Mater.* **2013**, 23, 947–958.

(2) Yabuuchi, N.; Kubota, K.; Dahbi, M.; Komaba, S. Research Development on Sodium-Ion Batteries. *Chem. Rev.* **2014**, 114, 11636–11682.

(3) Besenhard, J. O.; Winter, M. Advances in Battery Technology: Rechargeable Magnesium Batteries and Novel Negative Electrode Materials for Lithium Ion Batteries. *ChemPhysChem* **2002**, 3, 155–159.

(4) Bellis, M. History and Timeline of the Battery. **2018**.

(5) Tarascon, J. M. The Li-Ion Battery: 25 Years of Exciting and Enriching Experiences. *Interface Mag.* **2016**, 25, 79–83.

(6) Dell, R. M.; Rand, D. A. J. Understanding Batteries. *R. Soc. Chem.* **2001**.

(7) Scrosati, B. History of Lithium Batteries. *J. Solid State Electrochem.* **2011**, 15, 1623–1630.

(8) Linden, D.; Reddy, T. B. Hand Book of Batteries. **2002**.

(9) Bruce, P. G.; Freunberger, S. A.; Hardwick, L. J.; Tarascon, J. M. Li–O_2 and Li–S Batteries with High Energy Storage. *Nat. Mater.* **2012**, 11, 19–29.

(10) Kumar, P.; Wu, F. Y.; Hu, L. H.; Abbas, S. A.; Ming, J.; Lin, C, N.; Fang, J.; Chu, C. W.; Li, L. J. High-Performance Graphene/Sulphur Electrodes for Flexible Li-Ion Batteries using the Low-Temperature Spraying Method. *Nanoscale* **2015**, 7, 8093–8100.

(11) Ming, J.; Li, M.; Kumar, P.; Li, L. J. Multilayer Approach for Advanced Hybrid Lithium Battery. *Acs Nano* **2016**, 10, 6037–6044.

(12) Armand, M.; Tarascon, J. M. Building Better Batteries. *Nature* **2008**, 451, 652–657.

(13) Gao, W.; Singh, N.; Song, L.; Liu, Z.; Reddy, A. L. M.; Ci, L.; Vajtai, R.; Zhang, Q.; Wei, B.; Ajayan, P. M. Direct Laser Writing of Micro-Supercapacitors on Hydrated Graphite Oxide Films. *Nat Nanotechnol.* **2011**, 6, 496–500.

(14) Chen, Z.; Ren, W.; Gao, L.; Liu, B.; Pei, S.; Cheng, H. M. Three-Dimensional Flexible and Conductive Interconnected Graphene Networks Grown by Chemical Vapour Deposition. *Nat. Mater*. **2011**, 10, 424–428.

(15) Olivetti, E. A.; Ceder, G.; Gaustad, G. G.; Fu, X.; Lithium-Ion Battery Supply Chain Considerations: Analysis of Potential Bottlenecks in Critical Metals. *Joule* **2017**, 1, 229–243.

(16) Hou, G.; Cheng, B.; Cao, Y.; Yao, M.; Li, B.; Zhang, C.; Weng, Q.; Wang, X.; Bando, Y.; Golberg, D.; Yuan, F. Scalable Production of 3D Plum-Pudding-Like Si/C Spheres: Towards Practical Application in Li-Ion Batteries. *Nano Energy* **2016**, 24, 111–120.

(17) Dong, J.; Xue, Y.; Zhang, C.; Weng, Q.; Dai, P.; Yang, Y.; Zhou, M.; Li, C.; Cui, Q.; Kang, X. Improved Li^+ Storage Through Homogeneous N-Doping within Highly Branched Tubular Graphitic Foam. *Adv. Mater.* **2017**, 29, 1603692.

(18) Li, H. N.; Shi, Y. M.; Chiu, M. H.; Li, L. J. Emerging Energy Applications of Two-Dimensional Layered Transition Metal Dichalcogenides. *Nano Energy* **2015**, 18, 293–305.

(19) Chhowalla, M.; Shin, H. S.; Eda, G.; Li, L. J.; Loh, K. P.; Zhang, H. The Chemistry of Two-Dimensional Layered Transition Metal Dichalcogenide Nanosheets. *Nat. Chem.* **2013**, 5, 263–275.

(20) Butler, S. Z.; Hollen, S. M.; Linyou, C.; Cui, Y.; Gupta, A. J.; Gutiérrez, H. R.; Heinz, T. F.; Hong, S. S.; Huang, J.; Ismach, A. F.; Johnston-Halperin, E.; Kuno, M.; Plashnitsa, V. V.; Robinson, R. D.; Ruoff, R. S.; Salahuddin, S.; Shan, J.; Shi, L.; Spencer, M. G.; Terrones, M.; Windl,W.; Goldberger, J. E. Progress, Challenges, and Opportunities in Two-Dimensional Materials Beyond Graphene. *ACS Nano* **2013**, 7, 4, 2898–2926.

(21) Duan, X.; Wang, C.; Pan, A.; Yu, R.; Duan, X. Two-Dimensional Transition Metal Dichalcogenides as Atomically Thin Semiconductors: Opportunities and Challenges. *Chem. Soc. Rev.* **2015**, 44, 8859–8876.

(22) Jariwala, D.; Sangwan, V. K.; Lauhon, L. J.; Marks, T. J.; Hersam, M. C. Emerging Device Applications for Semiconducting Two-Dimensional Transition Metal Dichalcogenides *ACS Nano* **2014**, 8, 2, 1102–1120.

(23) Mahatha, S. K.; Patel, K. D.; Menon, K. S. R. Electronic Structure Investigation of MoS_2 and $MoSe_2$ Using Angle-Resolved Photoemission Spectroscopy and ab initio Band Structure Studies. *J. Phys.: Condens. Matter* **2012**, 24, 475504.

(24) Hwang, W. S.; Remskar, M.; Yan, R.; Protasenko, V.; Tahy, K.; Chae, S. D.; Zhao, P.; Konar, A.; Xing, H.; Seabaugh, A.; Jena, D. Transistors with Chemically Synthesized Layered Semiconductor WS_2 Exhibiting 10^5 Room Temperature Modulation and Ambipolar Behavior. *Appl. Phys. Lett.* **2012**, 101, 013107.

(25) Vogt, P.; Padova, P. D.; Quaresima, C.; Avila, J.; Frantzeskakis, E.; Asensio, M. C.; Resta, A.; Ealet, B.; Lay, G. L. Silicene: Compelling Experimental Evidence for Graphenelike Two-Dimensional Silicon. *Phys. Rev. Lett.* **2012**, 108, 155501.

(26) Pakdela, A.; Zhia, C.; Bandoa, Y.; Golberg, D. Low-Dimensional Boron Nitride Nanomaterials *Mater. Today* **2012** 15, 256–265.

(27) Ni, Z.; Liu, Q.; Tang, K.; Zheng, J.; Zhou, J.; Qin, R.; Gao, Z.; Yu, D.; Lu, J. Tunable Bandgap in Silicene and Germanene. *Nano Lett.* **2012**, 12, 113–118.

(28) Song, L.; Balicas, L.; Mowbray, D. J.; Capaz, R. B.; Storr, K.; Ci, L.; Jariwala, D.; Kurth, S.; Louie, S. G.; Rubio, A.; Ajayan, P. M. Anomalous Insulator-Metal Transition in Boron Nitride-Graphene Hybrid Atomic Layers. *Phys. Rev. B* **2012**, 86, 075429.

(29) Ci, L.; Song, L.; Jin, C.; Jariwala, D.; Wu, D.; Li, Y.; Srivastava, A.; Wang, Z. F.; Storr, K.; Balicas, L.; Liu, F.; Ajayan, P. M. Atomic Layers of hybridized Boron Nitride and Graphene Domains. *Nat Mater* **2010**, 9(5), 430–5.

(30) Liu, Z.; Song, L.; Zhao, S.; Huang, J.; Ma, L.; Zhang, J.; Lou, J.; Ajayan, P. M. Direct Growth of Graphene/Hexagonal Boron Nitride Stacked Layers. *Nano Lett.* **2011**, 11, 5, 2032–2037.

CHAPTER 2

Literature review

"This chapter deals with the literature reviews of TMDCs, applications of TMDCs in LIBs and SIBs. The literature on $MoTe_2$ and its applications in various fields including energy-storage applications."

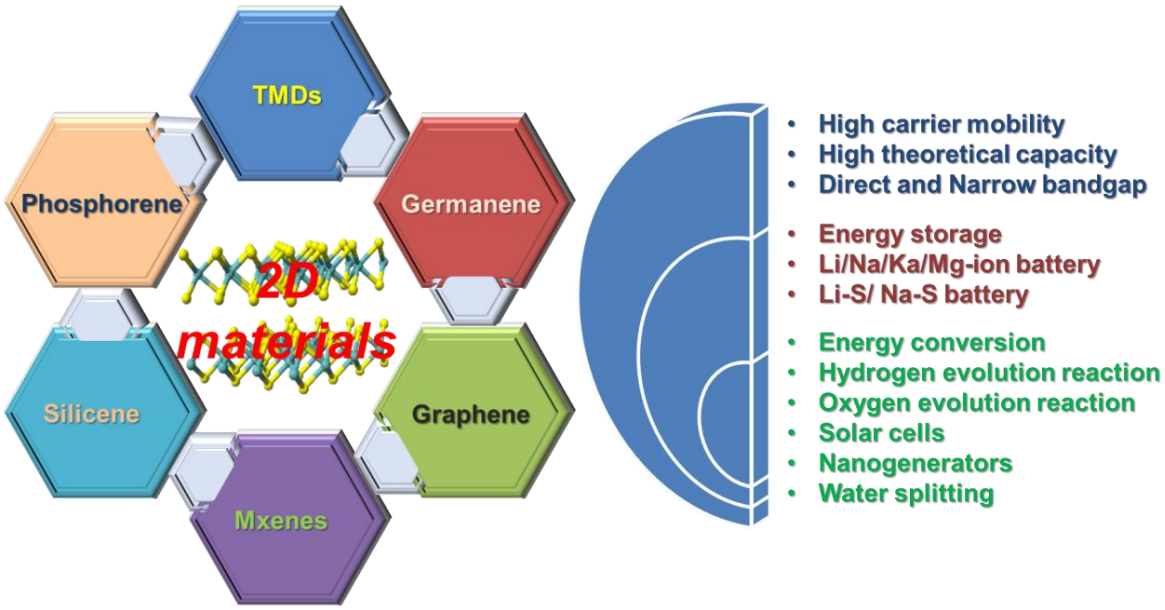

2.1 Classification of 2D materials

The future requirement for energy-storage materials will demand higher energy density, powder density, and better electrochemical performance. New materials need to be introduced to achieve higher capacity, rate capability, and better cycle life to fulfill these requirements.[1–3] The existing 2D materials are classified into different subclasses such as TMDs, Germanene, Graphene, Mxenes, Silicene, Phosphorine (**Figure 2.1**).[3–7] These materials that have high carrier mobility, high theoretical capacity, and a tunable bandgap have been shown to be promising candidates for energy storage, energy conversion, hydrogen evolution reaction, oxygen evolution reaction, solar cells, nanogenerators, and water splitting applications.[3–14]

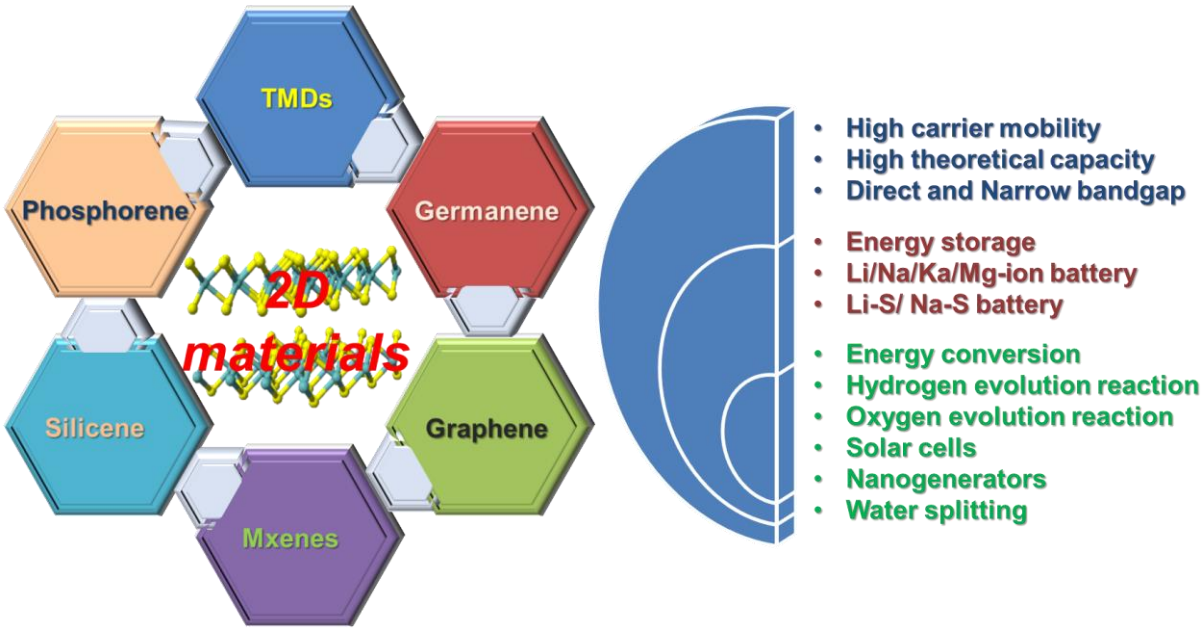

Figure 2.1 Schematic presentation of the classification of 2D layered materials and the relevant properties and applications.

Among these classes of materials, the classes of 2D materials, such as transition metal dichalcogenides (TMDCs) and transition metal carbide/nitrite (MXene) have generated considerable attention in recent years in energy-storage applications due to their high surface-area-to-volume ratio and van der Waals interaction-dominated interlayer bonding. Intensive research interest has been generated by TMDCs due to their potential for broad applications.[15–18] A family of layered materials, MX_2 (where M=transition metal and X=chalcogen), namely, TMDCs, exhibit three structural polytypes: 1T, 2H, and 3R. All three polytypes have layered structures that show a six-fold trigonal prismatic coordination of the transition metal atoms by the chalcogens within the layers. The terms 1T, 2H, and 3R represent one (1), two (2), and

three (3) layers in the tetragonal (T), hexagonal (H), and rhombohedral (R) unit cells, respectively.[18,19] Remarkably, various types of electronic structures such as insulating (HfS_2), semiconducting (MoS_2, WS_2), semi metallic (VS_2, TiS_2), and superconducting ($TaSe_2$, $NbSe_2$) are possessed by TMDCs.[2, 10–18]

Depending upon their stability in ambient conditions, a possible library of numerous 2D materials is shown in **Figure 2.2**. The materials in yellow are stable at room temperature in air and the ones in gray are stable in air, while blue corresponds to the unstable compounds in air; however, these may be stable in an inert atmosphere. Violet represents the successfully exfoliated 3D compounds, which results in the monolayers.[20,21]

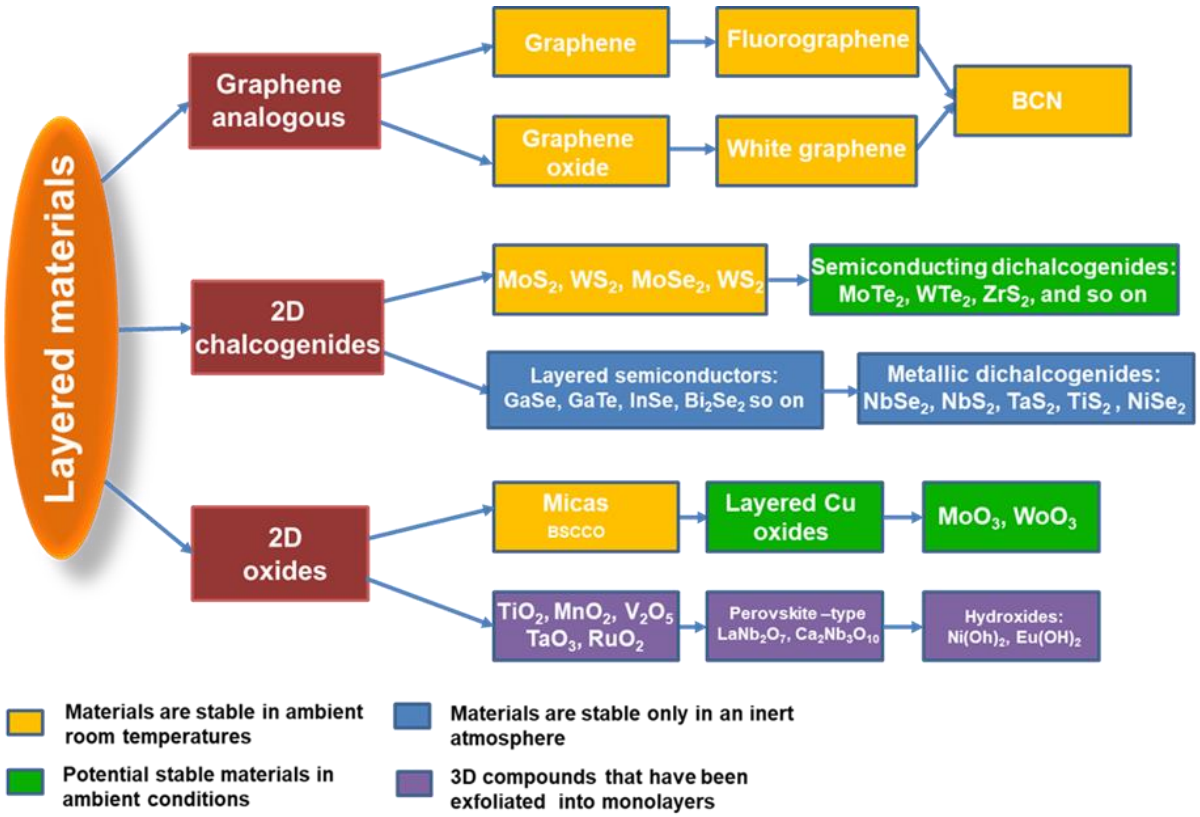

Figure 2.2 Possible layered electrode materials for Lithium/Sodium-ion batteries. *BCN = 2D nanocomposite bearing B, C, and N, Micas BSCCO = bismuth strontium calcium copper oxide.[20]

Due to the wide range of potential applications, 2D TMDs are currently being investigated. They are promising due to their electrochemical, catalytic, electronic, and optoelectronic properties, which give these unique layered structures high specific capacity and remarkable stable electrochemical performances.[3,15,22–25] B. T. Kolomiets and S. Ovshinsky first emphasized the use of semiconducting TMDs in the view of the bandgap in disordered

chalcogenides.[26] TMDs were recognized as a 2D graphene analog. The outcome of the direct gap along with the substantial exciton energies and the strong spin-orbital coupling in monolayer TMDs, what offer many new application opportunities. Chalcogenides and their structures are extensively studied among layered materials; MoS_2, due to its layered structure, was the first material studied in 1923.[27] Similar to graphite, graphitic MoS_2 has been used in numerous electronic applications, for example, as an anode in LIBs and SIBs. Another advantage of TMDCs is the tunability of their band structures, that is, from semiconductors to metals, which extends their applications to a broader range. Nonbonding d bands and the extent of their filling give rise to these different electronic properties. Among ~60 numbers of TMDs, a large percentage of these (66 %) have a layered structure. The exfoliation of bulk TMDCs to single or few-layer TMDCs with different intercalated ions such as sodium, lithium, or potassium is remarkably easy due to the weak van der Waals force between the layers of the TMDCs. They are widely used as electrodes in capacitors and rechargeable batteries such as Li-ion, Na-ion, and K-ion batteries due to the large surface area, which enables utilization of a greater number of sites and facilitates highly reversible and fast redox reaction. However, the additional challenges are low stability during cycling and high irreversibility at a high current rate. Various strategies such as the developing of hybrid electrodes that have conductive additives such as graphene, graphene oxide, and doping are being exercised to overcome these challenges. MXenes are additionally used as electrodes in rechargeable batteries and supercapacitors, but much work is needed for their use in practical application.

A wide range of electronic properties are shown by TMDCs, which can be classified into semiconducting, superconducting, semi metallic or metallic; all these properties depend upon the crystal phase.[28,29] The TMDCS that are based on elements from Group V and VI are widely studied, because they form stable compounds with tunable electronic properties.[7,28–31] Recently, 2D TMDCs have gained interest in biological and chemical sensing, and catalysis and energy-storage applications.[7,30–33] The electronic structure of 2D materials, which depends upon the number of layers, can be easily tuned by varying those layer numbers that show the strong quantum confinement.[32–36] Group VI TMDCs in the 2H phase in which the tunability of the bandgap is possible between the indirect bandgap to direct bandgap by changing bulk to monolayer.[30,37] The other possible switching of the semiconducting 2H and the metallic 1T phase of the TMDCs is by Li^+ intercalation; recovery may be possible with thermal annealing. Apart from the thickness-dependent bandgap tunability of 2D materials, and the transitions between metallic, insulating, and semiconducting properties, the defects substrate effect and

surface treatments make the 2D materials versatile for application in various electronic devices.[7,29,30,31,36,37] The use of such materials in Li and future non-Li metal ions such as Na, Mg, Zn, Cd, and Pb metal batteries (**Table 2.1**) can add significantly to the knowledge base of the field.

Table 2.1 Comparisons of different battery metals as the anode.

Metal	Charge	Atomic weight ($g\ mol^{-1}$)	Electrode Potential (*vs.* RHE) (V)	Theoretical Specific Energy density ($Ah\ kg^{-1}$)	Terrestrial Abundance (%)
Li	+1	6.94	-3.05	3862	0.006
Na	+1	22.99	-2.71	1166	2.64
Mg	+2	24.31	-2.38	2205	1.94
Zn	+2	65.38	-0.76	820	0.012
Cd	+2	112.41	-0.40	477	0.00003
Pb	+2	207.20	-0.13	259	0.0018

2.2 LIB applications using TMDCs

In modern electronics, LIBs are ubiquitous, and they function as the principal power source of electronic and electric vehicles;[1,3,7,39–42] this is especially true wherever high specific energy-storage capacity is a determining factor. However, given the variety in the demands for energy-storage devices in varying applications, recent LIBs are not suitable to all changing scenarios of energy density, efficiency, long cycle life, and cost. In LIB applications, graphite has been the anode material of choice since the past two decades. However, due to increasing market demands, graphite with its low rate capability will not be able to meet the demand, which provokes the search for more efficient intercalation based-anode materials with good rate capability, high specific capacity, and high Coulombic efficiency.[40,41,43,44] The challenges that are faced by candidate electrode materials in LIBs include their low electronic and ionic conductivities. These affect the ability to store Li^+ effectively, resulting in stresses during cycling.[41,42,45] To ensure the reliability of future energy-storage devices that require a higher rate capacity and longer cycle life, significant efforts have been expended into developing new anode materials to fulfill these requirements.

The compounds of group 6 TMDs that have an MX_2 structure, where M stands for (Mo and W) and X stands for chalcogens (S, Se, Te) such as MoS_2,[46] $MoSe_2$,[47] WS_2,[39,48] WSe_2,[44] and WTe_2[49] and so on, have been studied as anodes in LIBs due to similarity in their properties;

such as graphite and improved chemical stability. Layered TMDCs are preferable to bulk TMDCs. In the case of bulk TMDCs, the high-volume change observed during the insertion/extraction of Li-ion leads to poor performance. On the other hand, the layered structure with more electrochemically active sites in Li-ion insertion leads to improved performance. More facile movement of the Li-ion is enabled by WS_2 with an interlayer distance of 0.63 nm, which is approximately double that of the graphite. Liu et al. prepared the mesoporous WS_2 by the vacuum-assisted impregnation method; they forced the inner pores that had residual gas atoms to come outward, which led to a high surface area. Mesoporous WS_2, when used as an anode, delivers a discharge capacity of 805 mAh g^{-1} at 0.1 A g^{-1}after 100 cycles.[39] Bhandavat et al. exfoliated bulk WS_2 using chlorosulfonic acid into few-layer 2D WS_2. The acid-exfoliated WS_2 anode delivers a high reversible capacity of 469 mAh g^{-1} at current density of 25 mA g^{-1}.[40] In another study, Zhou et al. converted the impurities in WO_3 to WS_2 by sulfuration, which improves the electrical property and the capacity from 381.7 to 566.8 mA g^{-1} at a current density of 800 mA g^{-1}.[41] Yang et al. prepared highly crystalline WSe_2 nanoplates by physically mixing W and Se in a metal form in an atomic ratio of 1:2. The as-prepared anode shows capacity fading on the first cycle but stable capacity after 100 cycles.[44] Another promising TMDC anode is TiS_2, which was first reported by Chi et al. in 1997.[42] They used template synthesis followed by chemical vapor deposition to form a thin film of TiS_2. The enhancement in the surface area leads to a high discharge capacity of 256 mAh g^{-1}.[42] The layered TM diselenides are an excellent choice for the anode. Xue et al. prepared $NiSe_2$ for the first time in 2006.[43] They used the pulsed laser deposition technique to prepare a thin layer of $NiSe_2$, which shows a discharge capacity of 351.4 mAh g^{-1} at 5 μA g^{-1}.[43] Zhang et al. prepared red $MoSe_2$ nanosheets by oxidizing them with a Mo-O bond, which was found to have a lower bandgap than black $MoSe_2$. Red $MoSe_2$ delivers an excellent performance as an anode, showing a discharge capacity of 1125.5 mAh g^{-1} for up to 500 cycles.[43] Following the study, Im et al. prepared $GeSe_x$ and $SnSe_x$ by a photolysis reaction, which shows a capacity of 400–800 mAh g^{-1} after 70 cycles.[50] A similar class of selenide materials such as Mo_6Se_6, $NbSe_2$, Ta_2Se, $TiSe_2$, VSe, and $ZrSe_2$ have been studied for LIB applications.[51–57]

2.3 SIB applications using TMDCs

As a reliable alternative to LIBs, SIBs are gaining attention because sodium possesses electrochemical properties that are similar to lithium, and it is present in abundance in the earth's crust.[58] However, the practical application of SIBs is being hindered primarily by their

inability to achieve high practical cell energy density and long cycle life. Due to the large size of Na^+, it is imperative to develop layered electrode materials with a higher sodium storage capacity. Fortunately, it has been observed that the SIB cathode materials possess a layered structure with appropriate interlayer spacing to store Na^+ ions.[59] The development of an anode for SIB is still a challenge. Graphite, a well-known anode for LIB, is not suitable for SIB due to the differences in size, limited cycle number, and electrolyte stability. A few research efforts have been devoted to identifying similar layered structured anode materials with enough interlayer spacing to store Na^+ ions. For example, Stevens et al. investigated pyrolytic carbon as an anode material, and they found that it shows more than 200 mAh g^{-1} of capacity in sodium batteries.[60] Inspired by this work, further research has been carried out on carbon and layered transition metal oxides as sodium storage materials.[61–63] However, these anode materials do not meet the practical applications of SIBs mainly because of their unstable layered structure that has smaller interlayer spacing than the size of the Na^+ ion, which causes larger stress on the material lattice. As a result, the host material structure collapses during cycling, which may result in poor cycle stability. On the other hand, larger-sized Na^+ ions diffuse slowly in the lattice, causing low specific capacity and poor energy density. Therefore, due to the unavailability of suitable sodium storage anode materials, the commercialization of SIBs is still in its infancy. Recently, 2D materials such as transition metal dichalcogenides have attracted intensive research interest due to their potential in broad applications.[15–18,64] Different TMDCs such as semiconducting MoS_2[65], WS_2[66], semimetallic VS_2[67], TiS_2[68], WSe_2[44] and superconducting $MoTe_2$[19], $NbSe_2$[69] and the like have been used as potential anode materials in SIBs because they are structurally similar to graphene.[70,71] Among these materials, Mo-based dichalcogenides have recently been applied to LIBs because of their unique sandwich structure. Theoretical studies show stable binding between Na and MoS_2; hence, MoS_2 can be a favorable choice as anode.[72] Nanocrystals of FeS_2 were prepared and used as an anode by Walter et al. in 2015. It delivers a specific capacity of more than 500 mAh g^{-1} at a current density of 1A g^{-1} at the 400th cycles.[73] Following the above study, Hu et al. studied the electrochemical behavior of the Na/FeS_2 cell by varying the electrolyte and the voltage window. In the voltage window of 0.1–3 V, the specific capacity declines from 780 to 100 mAh g^{-1} in 50 cycles; however, highly reversible capacity was obtained in the voltage range of 0.8–3V.[74] Another promising anode, VS_2, was first reported in 1977[75] but was used in Na-ion batteries in 2015 by Yuan et al.[76] Following this, Zhou et al. prepared nanosheet assemblies of VS_2, which comprised aligned ultrathin nanosheets by the facile solvothermal process. The as-prepared VS_2, when

used as an anode, delivers a specific capacity of 700 mAh g^{-1} at a current density of 100 mA g^{-1} and excellent rate capacity of 400 mAh g^{-1} at a current density of 2 A g^{-1}.[77] In addition, Wang et al. reported the 3D hierarchical VS_2 structure. The 3D morphology compensates for the volume changes during the insertion and extraction of the Na-ion and improves electrolyte diffusion. It shows a reversible capacity of 720 mAh g^{-1} after 100 cycles with a Coulombic efficiency of 96 % and excellent rate capability.[78] Hu et al. reported the synthesis of ultrathin TiS_2 nanosheets. They used mechanical exfoliation, which drastically improved the capacity from 220 mAh g^{-1} to 386 mAh g^{-1} at a current density of 200 mA g^{-1} on the 200th cycle. The performance improvement was due to the synergic effect of the physical property of TiS_2 and the suitable intercalation mechanism.[79] Selenium-based TMDCs additionally drew attention as anodes for SIB. Ko et al., for the first time, reported the yolk-shell type $MoSe_2$ microsphere by a facile selenization process. The yolk-shell structure represents a flower-type structure, which facilitates the migration of the Na ion and accommodates the volume changes. It shows an initial capacity of 448 mAh g^{-1} at a current density of 200 mA g^{-1}, and it has a Coulombic efficiency of 85 %.[80] When WSe_2 was used as an electrode by Share et al., it showed a reversible capacity of 200 mAh g^{-1} at a current density of 20 mA g^{-1}.[81]

2.4 Preparations and various applications of $MoTe_2$

Molybdenum ditelluride ($MoTe_2$), another member of the Mo-based dichalcogenide family, shows a rich variety of tunable properties with potential industrial applications such as in microelectronic, power, microwave devices, and telecommunications.[82–87] The use of the $MoTe_2$ material as potential electrodes in electrochemical capacitors and rechargeable Li-ion/Na-ion batteries is an application with great demand.[5,32,88–91].$MoTe_2$ is a fascinating TMD because it is a polymorphic material that can exist both in a hexagonal semiconducting (2H) phase and a monoclinic semi metallic (1T') phase.[90,91]Although the energy difference between 2H- and 1T'-$MoTe_2$ is ≈35 m eV, 2H-$MoTe_2$ with a bandgap of ≈1.0 eV is the thermodynamically more stable phase, which is much easier to prepare than the 1T' phase.[91–94] The various preparation techniques and the related applications of $MoTe_2$ are discussed below.

Keum et al. prepared the single-crystal $MoTe_2$ by the flux method, which shows a reversible 2H-to-1T' phase transition and an electronic phase transition between semi metallic and semiconducting monoclinic single-crystal $MoTe_2$. The prepared 1T' $MoTe_2$ phase has shown an excellent property of carrier mobility of 4000 cm^2 $V^{-1}S^{-1}$ and giant magnetoresistance of 16000 % at 14T magnetic field and 1.8 K.[91] Si et al. investigated the laser-induced 2H-to-1T'

structural transition in $MoTe_2$. The phase transition occurs in two steps; 1) vacancy ordering that is achieved by vacancy diffusion, and 2) local 2H-to-1T' structural transition.[95] Qi et al. tuned the electronic property of $MoTe_2$ by functionalizing the surface via in situ deposition of Al adatoms. Since Al has strongly n-doped $MoTe_2$, it improves the electron mobility of $MoTe_2$ by one order to 12.8 $cm^2\ V^{-1}S^{-1}$and can be used as an inverter device.[96] Wu et al. coupled the oppositely polarized P(VDF-TrFE) with $MoTe_2$, which results in the accumulation of electrons and holes in the corresponding region of the ambipolar $MoTe_2$, and the formation of the p-n homojunction. This $MoTe_2$ p-n junction has shown excellent properties and can be used in diverse electronic and optoelectronic applications such as current-rectifying diodes, photovoltage devices, and a short-wavelength infrared photodetector.[97] Xu et al. gated the $MoTe_2$ field-effect transistor with Poly(ethylene oxide)-$CsClO_4$ by the electrostatic gating method. The electrolyte helps the Field-Effect Transistor (FET) to effectively reconfigure between the n and the p channel with an on-and-off ratio of approximately 5 orders of magnitude and subthreshold swings of 90 mv/decade. The sheet carrier density is additionally improved to 1.6 $x10^{13}$ cm^{-2} due to the large electric double layer capacitance (4 µF cm^{-2}).[98] McGlynn et al. improved the catalytic behavior of 1T' $MoTe_2$ by placing the electrode at cathode bias. The improvement in performance is due to the adsorption of H onto the Te site on the 1T'- $MoTe_2$ surface. The overpotential required to maintain a current density of 10 mA cm^{-2} reduces from 320 mv to 178 mv.[99] Kim et al. studied carrier multiplication (CM), a way to relax free energy radical by generating additional electron energy pairs) in transition metal dichalcogenide films of 2H $MoTe_2$ and 2H-WSe_2. They achieved a small CM threshold energy and high CM conversion efficiency of around 93 %, which is promising for the solar system or cells.[100] Park et al. proposed a new reversible method to prepare centimeter-scale 2H-$MoTe_2$film through tellurization of Mo thin films via Te sublimation. Initially, 1T'-$MoTe_2$ was kept in an excessive Te atmosphere to obtain the 2H-$MoTe_2$ phase. The 1T'-$MoTe_2$ was further annealed under a lower partial pressure of Te at the same temperature, followed by quenching to achieve the 1T'-$MoTe_2$ phase[101] Lin et al. prepared vertically aligned $MoTe_2$ on reusable Mo foil through the chemical vapor deposition (CVD) technique; they demonstrated the mass production of $MoTe_2$ nanosheets. They are able to produce a length of 0.66 to 7.5 µm on Mo foil, and they observed that the dominant phase (2H to 1T') can additionally be tuned by increasing the CVD temperature from 630 to 780 ºC. The internal strain generation causes the vertical growth of $MoTe_2$ during tellurization of the Mo foil. The as-grown $MoTe_2$ shows good solubility in the solvent and forms high-quality nanosheets.[102] Yang et al. used photoluminescence of negatively charged (X^-), neutral (X), and positively charged (X^+)

excitation of the monolayer $MoTe_2$. They obtained 24 and 27 meV binding energies for X^+ and X^-, respectively, and the excitation binding energy of the monolayer $MoTe_2$ was 0.58 ± 0.08 eV, which was obtained through photoluminescence excitation (PLE) spectroscopy.[103] Mc Manus et al. successfully prepared a thin film of 1T' $MoTe_2$ from a predeposited molybdenum and an electrodeposition tellurium layer at a temperature of 450 ºC. The prepared 1T' $MoTe_2$ was used as a catalyst in the HER process, and it showed a Tafel plot of 70 mV dec^{-1}, which indicates a strong electrocatalyst when compared to other $MoTe_2$ catalysts that have been reported.[104] Shang et al. systematically examined the manner in which an ALD reaction can enable the tuned synthesis of 2D transistors such as MoS_2 and $MoTe_2$ during growth by in situ operando studies. They found that the field-effect mobility improves significantly during the first five cycles of ALD growth, with $Mo(NMe_2)_4$ and H_2O as the metal-organic precursor and the oxidant, respectively. This shows that dielectric-induced mobility and carrier concentration changes occur before a continuous, stoichiometric, and air-stable dielectric is formed.[105] Li et al. used rapid thermal annealing (RTA) or electron-beam (EB) treatment without any chemical dopant in dry air to modulate the carrier type manipulation of the α-$MoTe_2$ FETs.[106] This approach has several advantages such as low cost due to chemical free-electron dominance of $MoTe_2$, excellent stability of the processed $MoTe_2$, and an adjustable range of back-gate voltage.[107] Duong et al. developed a vertical vdW heterostructure by using a bilayer (2L) MoS_2 and thickness-modulated $MoTe_2$. It shows high-performance p-n forward diodes, Zener diodes, backward diodes transistors, and multi-valued logic due to the thickness-dependent Fermi level and different band structures.[108] Pan et al. reported an experimental study on the spatiotemporal dynamics of photo carriers in monolayer and bulk $MoTe_2$. For the above study on the monolayer, they obtained an exciton diffusion coefficient of 20 ± 10 cm^2 s^{-1}, a mean free time of 200 fs, a mean free path of 20 nm, and a diffusion length of 350 nm. The corresponding values of the bulk sample are 40 ± 10 cm^2 s^{-1}, 400 fs, 40 nm, and 570 nm.[109] Zhu et al. improved the mechanical strength and thermoelectric properties of PbTe by incorporating $MoTe_2$ through in the situ mode. An improved compressive strength, binding strength, and fraction toughness of 67 % is shown by PbTe/$MoTe_2$ when compared to the pristine $MoTe_2$; the electric transport property is also boosted.[110] Liu et al. introduced a dopant-free method to rationally control the $MoTe_2$ transistor's polarity from p to n-type. In this study, they coated the top of the $MoTe_2$ with a thin layer of boron nitride (h-BN), which prevented direct contact between Te and the surface of the device. Interestingly, simple thermal annealing of around 100–350 ºC transfers it to the n-type with excellent enhancement in performance.[111] Liu et al. studied the defective $MoTe_2$ with Te vacancies, which was used in FET devices. A DFT study reveals the reduced

bandgap at the Te vacancies, which results in localized charge pebbles over the defective $MoTe_2$. All the charged localization can be removed from $MoTe_2$ by filling all the Te vacancies with reactive oxygen.[112]

2.5 Application of $MoTe_2$ in supercapacitors, LIBs, and SIBs

The $MoTe_2$ is currently considered a potential electrode for electrochemical capacitors and rechargeable LIBs and SIBS.[88,89] The crystal structure of the $MoTe_2$ allows facile insertion/extraction of Na^+ and Li^+ ions into/from the host.[19] Molybdenum ditelluride is composed of alternately stacked layers of Mo and Te (Te–Mo–Te), which are held together by weak van der Waals interactions. The interlayer spacing of the $MoTe_2$ is about 0.70 nm, which is considerably larger than that of graphite (0.335 nm); the layer gaps are expected to allow the efficient diffusion of Li^+ and Na^+ without any significant disturbance to the crystal structure. Moreover, tellurium has a comprehensively higher electronic conductivity ($2\times10^2\ Sm^{-1}$), which enables the higher utilization of active materials than does sulfur ($5\times10^{-13}\ Sm^{-1}$) and selenium ($1\times10^{-3}Sm^{-1}$). Additionally, in SIBs, due to the small interlayer distance between the layers in the MoS_2 and the $MoSe_2$, both suffer from massive lattice distortion during the insertion or extraction of the Na^+ ion, which leads to structural instability during cycling.[71,80,113] Hence, the $MoTe_2$ can be considered an intercalation host and a promising electrode material for LIBs and SIBs. Recently studied literature are listed below. In these, $MoTe_2$ is used as a potential candidate in supercapacitors, LIB, and SIBs.

Pawar et al. used metal-organic chemical vapor deposition (MOCVD) on Si/SiO_2 to grow 1T'-Mo_6Te_6 nanoplates on top of the 2H-$MoTe_2$ thin-film polymorphic structure. After the preparation, they successfully transferred it to a nickel foam current collector by the single chemical etching protocol for high-performance supercapacitors. The as-prepared supercapacitor showed a threefold enhancement of areal capacitance (1542 $mFcm^{-2}$ at 10 mVs^{-1}) when compared to the single-layer transferred electron; it also showed electrochemical stability of 96 % and a high energy density of 140.36 $mWcm^{-2}$ at 4 mA.[114] Liu et al. used a colloidal chemical strategy to prepare metastable ultrathin 1T'-$MoTe_2$ nanosheets from $Mo(CO)_6$ and the Te-tri-octylphosphine (Te-ToP) precursor. The as-prepared 1T'-$MoTe_2$ nanosheet has an interlayer distance of 0.723 nm and is rich in defect, whereas the interlayer distance and the defect can be varied by changing the concentration of CO. The optimized few-layer 1T'-$MoTe_2$ nanosheet was used as a supercapacitor, and it exhibited a maximum specific capacitance of 1393 Fg^{-1} and 714 Fg^{-1} at a current density of $1Ag^{-1}$ and 100 Ag^{-1}, respectively.

The asymmetric 1T'-$MoTe_2$//activated carbon supercapacitor showed a specific capacity of 158.9 Fg^{-1} with an energy density of 56.4 Wh Kg^{-1}.[88]

Cho et al. prepared a composite microsphere of carbon and $MoTe_2$ for the first time by a two-stage process. The initial precursor (C-MoO_x), which was prepared through spray pyrolysis was tellurized to convert it into C-$MoTe_2$ composite (C/$MoTe_2$) and a core-shell structured C-$MoTe_2$ composite (C@$MoTe_2$) by tellurization at 450 and 600 ºC, respectively. They tested the electrochemical performances of C/$MoTe_2$, C@$MoTe_2$, and bare $MoTe_2$ against sodium metal, which showed an initial discharge capacity of 328, 388, and 341 mAh g^{-1}, respectively, at 1 Ag^{-1}. They concluded that the well-developed 2D layer of the $MoTe_2$ of the C@$MoTe_2$ showed excellent performance with respect to the C/$MoTe_2$ microsphere and the bare $MoTe_2$.[19] Ma et al. prepared $MoTe_2$ nanosheets with Te vacancies encapsulated in a few layers of graphene ($MoTe_2$/FLG) by mechanical milling. They then used it as an anode for LiBs. They observed that the nano-sized $MoTe_2$ improved Li-ion diffusion and lowered the structural stress/strain. Graphene improves the electronic conductivity, minimizes the volume change, and avoids $MoTe_2$ from aggregation. The as-prepared anode showed excellent properties with a reversible capacity of 596.5 mAh g^{-1} at 100 mAg^{-1}, and a capacity retention of 99.5 % over 400 cycles at 0.5 Ag^{-1}. Further, they fabricated the full-cell $MoTe_2$/FEG//$0.35Li_2MnO_3 \cdot 0.65LiMn_{0.5}Ni_{0.5}O_2$, which delivered a reversible capacity of 499 mAh g^{-1} at 100 mAg^{-1}, and a capacity retention of 78 % over 50 cycles.[89] Kim et al. manipulated the deposition potential to electro-deposit thin films of $MoTe_2$ from the aqueous electrolyte in the presence of argon. They observed that the deposition at -0.8 V versus Ag/AgCl for 10 min led to the formation of a film of 1D $MoTe_2$ nanorods. In contrast, at -0.9 V versus Ag/AgCl, a nanoplate-like structure was formed. They used the nanorod films as an anode in LIBs, which delivered a discharge capacity of 770 mAh g^{-1} at 50 mA g^{-1} and good electrochemical reversibility.[115]

2.6 References

(1) Bruce, P. G.; Freunberger, S. A.; Hardwick, L. J.; Tarascon, J. M. Li–O_2 and Li–S Batteries with High Energy Storage. *Nature Mater* **2012**, 11**,** 19–29.

(2) Kumar, P.; Wu, F. Y.; Hu, L. H.; Abbas, S. A.; Ming, J.; Lin, C. N.; Fang, J.; Chu, C. W.; Li, L. J. High-Performance Graphene/Sulphur Electrodes for Flexible Li-Ion Batteries Using the Low-Temperature Spraying Method. *Nanoscale* **2015**, 7, 8093–8100.

(3) Yang, Y.; Liu, X.; Zhu, Z.; Zhong, Y.; Bando, Y.; Golberg, D.; Yao, J.; Wang, X. The Role of Geometric Sites in 2D Materials for Energy Storage. *Joule* **2018**, 2, 1075–1094.

(4) Ci, L.; Song, L.; Jin, C.; Jariwala, D.; Wu, D.; Li, Y.; Srivastava, A.; Wang, Z. F.; Storr, K.; Balicas, L.; Liu, F.; Ajayan, P. M. Atomic Layers of Hybridized Boron Nitride and Graphene Domains *Nat. Mater.* **2010**, 9, 430–435.

(5) Butler, S. Z.; Hollen, S. M.; Cao, L.; Cui, Y.; Gupta, J. A.; Gutie´rrez, H. A.; Heinz, T. F.; Hong, S. S.; Huang, J.; Ismach, A. F.; Johnston-Halperin, E.; Kuno, M.; Plashnitsa, V. V.; Robinson, R. D.; Ruoff, R. S.; Salahuddin, S.; Shan, J.; Shi, L.; Spencer, M. G.; Terrones, M. T.; Windl, W.; Goldberger, J. E. Progress, Challenges, and Opportunities in Two-Dimensional Materials Beyond Graphene. *ACS Nano* **2013**, 7, 4, 2898–2926.

(6) Duan, X.; Wang, C.; Pan, A.; Yu, R.; Duan, X. Two-Dimensional Transition Metal Dichalcogenides as Atomically Thin Semiconductors: Opportunities and Challenges. *Chem. Soc. Rev.* **2015**, 44, 8859–8876.

(7) Jariwala, D.; Sangwan, V. K.; Lauhon, L. J.; Marks, T. J.; Hersam, M. C. Emerging Device Applications for Semiconducting Two-Dimensional Transition Metal Dichalcogenides. *ACS Nano* **2014**, 8, 2, 1102–1120.

(8) Mahatha S. K.; Patel K. D.; Menon, K. S. R. Electronic Structure Investigation of MoS_2 and $MoSe_2$ Using Angle-Resolved Photoemission Spectroscopy and Ab Initio Band Structure Studies. *J. Phys.: Condens. Matter* **2012**, 24, 475504.

(9) Hwang, W. S.; Remskar, M.; Yan, R.; Protasenko, V.; Tahy, K.; Chae, S. D.; Zhao, P.; Konar, A.; Xing, H.; Seabaugh, A.; Jena, D. Transistors with Chemically Synthesized Layered Semiconductor WS_2 Exhibiting 10^5 Room Temperature Modulation and Ambipolar Behavior. *Appl. Phys. Lett.* **2012**, 101, 013107.

(10) Vogt, P.; Padova, P. D.; Quaresima, C.; Avila, J.; Frantzeskakis, E.; Asensio, M. C.; Resta, A.; Ealet, B.; Lay, G. L. Silicene: Compelling Experimental Evidence for Graphenelike Two-Dimensional Silicon. *Phys. Rev. Lett.* **2012**, 108, 155501.

(11) Pakdela, A.; Zhia, C.; Bandoa, Y.; Golberg, D. Low-Dimensional Boron Nitride Nanomaterials. *Mater. Today* **2012,** 15(6), 256–265.

(12) Ni, Z.; Liu, Q.; Tang, K.; Zheng, J.; Zhou, J.; Qin, R.; Gao, Z.; Yu, D.; Lu, J. Tunable Bandgap in Silicene and Germanene. *Nano Lett.* **2012**, 12, 113–118.

(13) Song, L.; Balicas, L.; Mowbray, D. J.; Capaz, R. B.; Storr, K.; Ci, L.; Jariwala, D.; Kurth, S.; Louie, S. G.; Rubio, A.; Ajayan, P. M. Anomalous Insulator-Metal Transition in Boron Nitride-Graphene Hybrid Atomic Layers. *Phys. Rev. B* **2012**, 86, 075429.

(14) Liu, Z.; Song, L.; Zhao, S.; Huang, J.; Ma, L.; Zhang, J.; Lou, J.; Ajayan, P. M. Direct Growth of Graphene/Hexagonal Boron Nitride Stacked Layers. *Nano Lett.* **2011**, 11, 5, 2032–2037.

(15) Lee, C. H.; Lee, G. H.; Van Der Zande, A. M.; Chen, W.; Li, Y.; Han, M.; Cui, X.; Arefe, G.; Nuckolls, C.; Heinz, T. F.; Guo, J. Atomically Thin p–n junctions with van der Waals Heterointerfaces. *Nat. Nanotechnol.* **2014**, 9, 676–681.

(16) Gong, C.; Zhang, Y.; Chen, W.; Chu, J.; Lei, T.; Pu, J.; Dai, L.; Wu, C.; Cheng, Y.; Zhai, T.; Li, L. Electronic and Optoelectronic Applications Based on 2D Novel Anisotropic Transition Metal Dichalcogenides. *Adv. Sci.* **2017**, 4, 1700231.

(17) Zheng, C.; Zhang, Q.; Weber, B.; Ilatikhameneh, H.; Chen, F.; Sahasrabudhe, H.; Rahman, R.; Li, S.; Chen, Z.; Hellerstedt, J.; Zhang, Y. Direct Observation of 2D Electrostatics and Ohmic Contacts in Template-Grown Graphene/WS_2 Heterostructures. *ACS nano* **2017**, 11, 2785–2793.

(18) Zhou, T.; Pang, W. K.; Zhang, C.; Yang, J.; Chen, Z.; Liu, H. K.; Guo, Z. Enhanced Sodium-Ion Battery Performance by Structural Phase Transition from Two-Dimensional Hexagonal-SnS_2 to Orthorhombic-SnS. *Acs Nano* **2014**, 8, 8323–8333.

(19) Cho, J. S.; Ju, H. S.; Lee, J. K.; Kang, Y. C. Carbon/Two-Dimensional $MoTe_2$ Core/Shell-Structured Microspheres as an Anode Material for Na-Ion Batteries. *Nanoscale* **2017**, 9, 1942–1950.

(20) Zhu, C.; Du, D.; Lin, Y. Graphene and Graphene-Like 2D Materials for Optical Biosensing and Bioimaging: A Review. *2D Mater.* **2015**, 2, 032004.

(21) Khan, K.; Tareen, A. K.; Aslam, M.; Wang, R.; Zhang, Y.; Mahmood, A.; Ouyang, Z.; Zhang, H.; Guo, Z. Recent Developments in Emerging Two-Dimensional Materials and their Applications. *J. Mater. Chem .C* **2020**, 8, 387–440.

(22) Chhowalla M.; Shin, H. S.; Eda, G.; Li, L.; Loh, K. P.; Zhang, H. The Chemistry of Two-Dimensional Layered Transition Metal Dichalcogenide Nanosheets. *Nat Chem.* **2013**, 5, 263–75.

(23) Mahmood, N.; Zhang, C.; Yin, H.; Hou, Y. Graphene-Based Nanocomposites for Energy Storage and Conversion in Lithium Batteries, Supercapacitors and Fuel Cells. *J. Mater. Chem. A* **2014**, 2, 15–32.

(24) Tang, X.; Guo, X.; Wu, W.; Wang, G. 2D Metal Carbides and Nitrides (MXenes) as High Performance Electrode Materials for Lithium-Based Batteries. *Adv. Energy Mater.* **2018**, 8, 1801897.

(25) Zheng, F.; Cai, C.; Ge, S.; Zhang, X.; Liu, X.; Lu, H.; Zhang, Y.; Qiu, J.; Taniguchi, T.; Watanabe, K.; Jia, S.; Qi, J.; Chen, J. H.; Sun, D.; Feng, J. On the Quantum Spin Hall Gap of Monolayer 1T′-WTe_2. *Adv. Mater*. **2016**, 28, 4845–4851.

(26) Kolomiets, B. T.; Averyanov, V. L. Electrical and Photoelectric Properties of Modified Chalcogenide Vitreous Semiconductors. *Physics of Disordered Materials*. Institute for Amorphous Studies Series. **1985** Springer, Boston, MA.

(27) Dickinson, R. G.; Pauling, L. The Crystal Structure of Molybdenite, *J. Am. Chem. Soc.* **1923**, 45, 6, 1466–1471.

(28) Wilson, J. A.; Di Salvo, F. J.; Mahajan, S. Charge-Density Waves and Superlattices in the Metallic Layered Transition Metal Dichalcogenides. *Advances in Physics* **1975**, 24, 117–201.

(29) Kappera, R.; Voiry, D.; Yalcin, S. E.; Branch, B.; Gupta, G.; Mohite, A. D.; Chhowalla, M. Phase-Engineered Low-Resistance Contacts for Ultrathin MoS_2 Transistors. *Nat Mater* **2014**, 13, 1128–1134.

(30) Wang, Q. H.; Kalantar-Zadeh, K.; Kis, A.; Coleman, J. N.; Strano, M. S. Electronics and Optoelectronics of Two-Dimensional Transition Metal Dichalcogenides. *Nat. Nanotechnol.* **2012**, 7, 699–712.

(31) Fiori, G.; Bonaccorso, F.; Iannaccone, G.; Palacios, T.; Neumaier, D.; Seabaugh, A.; Banerjee, S. K.; Colombo, L. Electronics Based on Two-Dimensional Materials. *Nat. Nanotechnol.* **2014**, 9, 768–779.

(32) Ryder, C. R.; Wood, J. D.; Wells, S. A.; Hersam, M. C. Chemically Tailoring Semiconducting Two-Dimensional Transition Metal Dichalcogenides and Black Phosphorus. *ACS Nano* **2016**, 10, 3900–3917.

(33) Bhimanapati, G. R.; Lin, Z.; Meunier, V.; Jung, Y.; Cha, J.; Das, S.; Xiao, D.; Son, Y.; Strano, M. S.; Cooper, V. R.; Liang, L.; Louie, S. G.; Ringe, E.; Zhou, W.; Kim, S. S.; Naik, R. R.; Sumpter, B. G.; Terrones, H.; Xia, F.; Wang, Y.; Zhu, J.; Akinwande, D.; Alem, N.; Schuller, J. A.; Schaak, R. E.; Terrones, M.; Robinson, J. A. Recent Advances in Two-Dimensional Materials beyond Graphene. *ACS Nano* **2015**, 9, 11509–11539.

(34) Mak, K. F.; Lee, C.; Hone, J.; Shan, J.; Heinz, T. F. Atomically Thin MoS_2: A New Direct-Gap Semiconductor. *Phys Rev Lett.* **2010**, 105, 136805.

(35) Bandurin, D. A.; Tyurnina, A. V.; Yu, G. L.; Mishchenko, A.; Zólyomi, V.; Morozov, S. V.; Kumar, R. K.; Gorbachev, R. V.; Kudrynskyi, Z. R.; Pezzini, S.; Kovalyuk, Z. D.; Zeitler, U.; Novoselov, K. S.; Patanè, A.; Eaves, L.; Grigorieva, I. V.; Fal'ko, V. I.;

Geim, A. K.; Cao, Y. High Electron Mobility, Quantum Hall Effect and Anomalous Optical Response in Atomically Thin InSe. *Nat Nanotechnol.* **2017**, 12, 223–227.

(36) Kuc, A.; Zibouche, N.; Heine, T. Influence of Quantum Confinement on the Electronic Structure of the Transition Metal Sulfide TS_2. *Physical Review B* **2011**, 83, 245213.

(37) Gong, C.; Zhang, H.; Wang, W.; Colombo, L.; Wallace, R. M.; Cho, K. Band Alignment of Two-Dimensional Transition Metal Dichalcogenides: Application in Tunnel Field Effect Transistors. *Appl. Phys. Lett.* **2013**, 103, 053513.

(38) Besenhard, J. O.; Winter, M. Advances in Battery Technology: Rechargeable Magnesium Batteries and Novel Negative- Electrode Materials for Lithium Ion Batteries. *ChemPhysChem* **2002**, 3, 155–159.

(39) Liu, H.; Su, D.; Wang, G.; Qiao, S. Z. An Ordered Mesoporous WS_2 Anode Material with Superior Electrochemical Performance for Lithium Ion Batteries. *J. Mater. Chem* **2012,** 22, 17437–17440.

(40) Bhandavat, R.; David, L.; Singh, G. Synthesis of Surface-Functionalized WS_2 Nanosheets and Performance as Li-Ion Battery Anodes. *J. Phys. Chem. Lett.* **2012**, 3, 1523–1530.

(41) Zhou, L.; Yan, S.; Pan, L.; Wang, X.; Wang, Y.; Shi, Y. A Scalable Sulfuration of WS_2 to Improve Cyclability and Capability of Lithium-ion Batteries. *Nano Res.* **2016**, 857–865.

(42) Che, G.; Jirage, K. B.; Fisher, E. R.; Martin, C. R.; Yoneyama, H. Chemical-Vapor Deposition-Based Template Synthesis of Microtubular TiS_2 Battery Electrodes. *J. Electrochem. Soc.* **1997**, 144, 4296.

(43) Xue, M. Z.; Fu, Z. W. Lithium Electrochemistry of $NiSe_2$: A New Kind of Storage Energy Material. *Electrochem. commun.* **2006**, 8, 1855–1862.

(44) Yang, W.; Wang, J.; Si, C.; Peng, Z.; Zhang, Z. Tungsten Diselenide Nanoplates as Advanced Lithium/Sodium Ion Electrode Materials with Different Storage Mechanisms. *Nano Res.* **2017**, 10, 2584–2598.

(45) Zhang, S.; Wang, G.; Jin, J.; Zhang, L.; Wen, Z.; Yang, J. Robust and Conductive Red $MoSe_2$ for Stable and Fast Lithium Storage. *ACS nano* **2018**, 12, 4010–4018.

(46) Sen, U. K.; Johari, P.; Basu, S.; Nayak, C.; Mitra, S. An Experimental and Computational Study to Understand the Lithium Storage Mechanism in Molybdenum Disulfide. *Nanoscale* **2014**, 6, 10243–10254.

(47) Luo, Z.; Zhou, J.; Wang, L.; Fang, G.; Pan, A.; Liang, S. Two-Dimensional Hybrid Nanosheets of Few Layered $MoSe_2$ on Reduced Graphene Oxide as Anodes for Long-Cycle-Life Lithium-Ion Batteries. *J. Mater. Chem. A* **2016**, 4, 15302–15308.

(48) Zhou, L.; Yan, S.; Pan, L.; Wang, X.; Wang, Y.; Shi, Y. A Scalable Sulfuration of WS_2 to Improve Cyclability and Capability of Lithium-Ion Batteries. *Nano Res.* **2016**, 9, 857–865.

(49) Srinivaas, M.; Wu, C. Y.; Duh, J. G.; Hu, Y. C.; Wu, J. M. Multi-Walled Carbon-Nanotube-Decorated Tungsten Ditelluride Nanostars as Anode Material for Lithium-Ion Batteries. *Nanotechnology* **2019**, 31, 035406.

(50) Im, H. S.; Lim, Y. R.; Cho, Y. J.; Park, J.; Cha, E. H.; Kang, H. S. Germanium and Tin Selenide Nanocrystals for High-Capacity Lithium Ion Batteries: Comparative Phase Conversion of Germanium and Tin. *J. Phys. Chem.* **2014**, 118, 21884–21888.

(51) Tarascon, J. M. Mo_6Se_6: A New Solid-State Electrode for Secondary Lithium Batteries. *J. Electrochem. Soc.* **1985**, 132, 2089.

(52) Dahn, J. R.; McKinnon, W. R. Understanding the Behaviour of Rechargeable Lithium Batteries. *J. Power Sources* **1989**, 26, 77–80.

(53) Abraham, K. M. Status of Rechargeable Positive Electrodes for Ambient Temperature Lithium Batteries. *J. Power Sources* **1981**, 7, 1–43.

(54) Lavela, P.; Conrad, M.; Mrotzek, A.; Harbrecht, B.; Tirado, J. L. Electrochemical Lithium and Sodium Intercalation into the Tantalum-Rich Layered Chalcogenides Ta_2Se and Ta_2Te_3. *J. Alloys Compd.* **1999**, 282, 93–100.

(55) Whittingham, M. S. Chemistry of Intercalation Compounds: Metal Guests in Chalcogenide hosts. *Prog. Solid. State Ch.* **1978**, 12, 41–99.

(56) Whittingham, M. S. Electrical Energy Storage and Intercalation Chemistry. *Science* **1976**, 192, 1126–1127.

(57) Murphy, D. W.; Trumbore, F. A.; Carides, J. N. Closure to Discussion of a New Niobium Selenide Cathode for Nonaqueous Lithium Batteries. *J. Electrochem. Soc.* **1977**, 124, 325–329.

(58) Narins, T. P. The Battery Business: Lithium Availability and the Growth of the Global Electric Car Industry. *Extr Ind Soc.* **2017**, 4, 321–328.

(59) Xiao, Y.; Wang, P. F.; Yin, Y. X.; Zhu, Y. F.; Yang, X.; Zhang, X. D.; Wang, Y.; Guo, X. D.; Zhong, B. H.; Guo, Y. G. A Layered–Tunnel Intergrowth Structure for High-Performance Sodium-Ion Oxide Cathode. *Adv. Energy Mater.* **2018**, 8, 1800492.

(60) Stevens, D. A.; Dahn, J. R. High Capacity Anode Materials for Rechargeable Sodium-Ion Batteries. *J. Electrochem. Soc.* **2000**, 147, 1271–1273.

(61) Panda, M. R.; Dutta, D. P.; Mitra, S. Bio-Derived Mesoporous Disordered Carbon: An Excellent Anode in Sodium-Ion Battery and Full-Cell lab Prototype. *Carbon* **2019**, 143, 402–412.

(62) Su, H.; Jaffer, S.; Yu, H. Transition Metal Oxides for Sodium-Ion Batteries. *Energy Storage Mater.* **2016**, 5, 116–131.

(63) Lu, Y.; Yanilmaz, M.; Chen, C.; Ge, Y.; Dirican, M.; Zhu, J.; Li, Y.; Zhang, X. Lithium-Substituted Sodium Layered Transition Metal Oxide Fibers as Cathodes for Sodium-Ion Batteries. *Energy Storage Mater.* **2015**, 1, 74–81.

(64) Zhang, H.; Wang, J.; Hasan, T.; Bao, Q. Photonics of 2D Materials. *Opt. Commun.* **2018**, 406, 1–2.

(65) Sahu, T. S.; Mitra, S. Exfoliated MoS_2 Sheets and Reduced Graphene Oxide-An Excellent and Fast Anode for Sodium-Ion Battery. *Sci. Rep.* **2015**, 5, 12571.

(66) Su, D.; Dou, S.; Wang, G. WS_2@Graphene Nanocomposites as Anode Materials for Na-Ion Batteries with Enhanced Electrochemical Performances. *ChemComm* **2014**, 50, 4192–4195.

(67) Yu, D.; Pang, Q.; Gao, Y.; Wei, Y.; Wang, C.; Chen, G.; Du, F. Hierarchical Flower-Like VS_2 Nanosheets–A High Rate-Capacity and Stable Anode Material for Sodium-Ion Battery. *Energy Storage Mater.* **2018**, 11, 1–7.

(68) Liu, Y.; Wang, H.; Cheng, L.; Han, N.; Zhao, F.; Li, P.; Jin, C.; Li, Y. TiS_2 Nanoplates: A High-Rate and Stable Electrode Material for Sodium Ion Batteries. *Nano Energy* **2016**, 20, 168–175.

(69) Lv, X.; Wei, W.; Sun, Q.; Huang, B.; Dai, Y. A First-Principles Study of $NbSe_2$ Monolayer as Anode Materials for Rechargeable Lithium-Ion and Sodium-Ion Batteries. *J. Phys. D: Appl. Phys.* **2017**, 50, 235501.

(70) Guo, Y. G.; Hu, J. S.; Wan, L. J. Nanostructured Materials for Electrochemical Energy Conversion and Storage Devices. *Adv. Mater.* **2008**, 20, 2878–2887.

(71) Yang, E.; Ji, H.; Jung, Y. Two-Dimensional Transition Metal Dichalcogenide Monolayers as Promising Sodium Ion Battery Anodes. *J. Phys. Chem. C* **2015**, 119, 26374–26380.

(72) Kumar, P.; Abuhimd, H.; Wahyudi, W.; Li, M.; Ming, J.; Li, L. J. Review Two-Dimensional Layered Materials for Energy Storage Applications. *ECS J. Solid State Sci. Technol.* **2016**, 5, 3021–3025.

(73) Walter, M.; Zünd, T.; Kovalenko, M. V. Pyrite (FeS_2) Nanocrystals as Inexpensive High-Performance Lithium-Ion Cathode and Sodium-Ion Anode Materials. *Nanoscale* **2015**, 7, 9158–9163.

(74) Hu, Z.; Zhu, Z.; Cheng, F.; Zhang, K.; Wang, J.; Chen, C.; Chen, J. Pyrite FeS_2 for High-Rate and Long-Life Rechargeable Sodium Batteries. *Energy Environ. Sci.* **2015**, 8, 1309–1316.

(75) Murphy, D. W.; Cros, C.; Di Salvo, F. J.; Waszczak, J. V. Preparation and Properties of Li_xVS_2 (0. ltoreq. x. ltoreq. 1). *Inorg. Chem.* **1977**, 16, 3027–3031.

(76) Yuan, J.; Wu, J.; Hardy, W. J.; Loya, P.; Lou, M.; Yang, Y.; Najmaei, S.; Jiang, M., Qin, F.; Keyshar, K.; Ji, H. Facile Synthesis of Single Crystal Vanadium Disulfide Nanosheets by Chemical Vapor Deposition for Efficient Hydrogen Evolution Reaction. *Adv. Mater.* **2015**, 27, 5605–5609.

(77) Zhou, J.; Wang, L.; Yang, M.; Wu, J.; Chen, F.; Huang, W.; Han, N.; Ye, H.; Zhao, F.; Li, Y. Hierarchical VS_2 Nanosheet Assemblies: A Universal Host Material for the Reversible Storage of Alkali Metal Ions. *Adv. Mater.* **2017**, 29, 1702061.

(78) Wang, J.; Luo, N.; Wu, J.; Huang, S.; Yu, L.; Wei, M. Hierarchical Spheres Constructed by Ultrathin VS_2 Nanosheets for Sodium-Ion Batteries. *J. Mater. Chem. A* **2019**, 7, 3691–3696.

(79) Hu, Z.; Tai, Z.; Liu, Q.; Wang, S. W.; Jin, H.; Wang, S.; Lai, W.; Chen, M.; Li, L.; Chen, L.; Tao, Z. Ultrathin 2D TiS_2 Nanosheets for High Capacity and Long-Life Sodium Ion Batteries. *Adv. Energy Mater.* **2019**, 9(8), 1803210.

(80) Ko, Y. N.; Choi, S. H.; Park, S. B.; Kang, Y. C. Hierarchical $MoSe_2$ Yolk–Shell Microspheres with Superior Na-Ion Storage Properties. *Nanoscale* **2014**, 6, 10511–10515.

(81) Share, K.; Lewis, J.; Oakes, L.; Carter, R. E.; Cohn, A. P.; Pint, C. L. Tungsten Diselenide (WSe_2) as a High Capacity, Low Overpotential Conversion Electrode for Sodium Ion Batteries. *RSC Adv.* **2015**, 5, 101262–101267.

(82) Pradhan, N. R.; Rhodes, D.; Feng, S.; Xin, Y.; Memaran, S.; Moon, B. H.; Terrones, H.; Terrones, M.; Balicas, L. Field-Effect Transistors Based on Few-Layered α-$MoTe_2$. *ACS nano* **2014**, 8, 5911–5920.

(83) Yamamoto, M.; Wang, S. T.; Ni, M.; Lin, Y. F.; Li, S. L.; Aikawa, S.; Jian, W. B.; Ueno, K.; Wakabayashi, K.; Tsukagoshi, K. Strong Enhancement of Raman Scattering from a Bulk-Inactive Vibrational Mode in Few-Layer $MoTe_2$. *Acs Nano* **2014**, 8, 3895–3903.

(84) Lin, Y. F.; Xu, Y.; Wang, S. T.; Li, S. L.; Yamamoto, M.; Aparecido-Ferreira, A.; Li, W.; Sun, H.; Nakaharai, S.; Jian, W. B.; Ueno, K. Ambipolar $MoTe_2$ Transistors and their Applications in Logic Circuits. *Adv. Mater.* **2014**, 26, 3263–3269.

(85) Roy, A.; Movva, H. C.; Satpati, B.; Kim, K.; Dey, R.; Rai, A.; Pramanik, T.; Guchhait, S.; Tutuc, E.; Banerjee, S.K. Structural and Electrical Properties of $MoTe_2$ and $MoSe_2$ Grown by Molecular Beam Epitaxy. *ACS Appl. Mater. Interfaces* **2016**, 8, 7396–7402.

(86) Choi, K.; Lee, Y. T.; Kim, J. S.; Min, S. W.; Cho, Y.; Pezeshki, A.; Hwang, D. K.; Im, S. Non-Lithographic Fabrication of All-2D α-$MoTe_2$ Dual Gate Transistors. *Adv. Funct. Mater.* **2016**, 26, 3146–3153.

(87) Deng, K.; Wan, G.; Deng, P.; Zhang, K.; Ding, S.; Wang, E.; Yan, M.; Huang, H.; Zhang, H.; Xu, Z.; Denlinger, J. Experimental Observation of Topological Fermi Arcs in Type-II Weyl Semimetal $MoTe_2$. *Nat. Phys.* **2016**, 12, 1105–1110.

(88) Liu, M.; Wang, Z.; Liu, J.; Wei, G.; Du, J.; Li, Y.; An, C.; Zhang, J. Synthesis of Few-Layer 1T′-$MoTe_2$ Ultrathin Nanosheets for High-Performance Pseudocapacitors. *J. Mater. Chem. A* **2017**, 5, 1035–1042.

(89) Ma, N.; Jiang, X. Y.; Zhang, L.; Wang, X. S.; Cao, Y. L.; Zhang, X. Z. Novel 2D Layered Molybdenum Ditelluride Encapsulated in Few-Layer Graphene as High-Performance Anode for Lithium-Ion Batteries. *Small* **2018**, 14, 1703680.

(90) Qi, Y.; Naumov, P. G.; Ali, M. N.; Rajamathi, C. R.; Schnelle, W.; Barkalov, O.; Hanfland, M.; Wu, S. C.; Shekhar, C.; Sun, Y.; Süß, V. Superconductivity in Weyl Semimetal Candidate $MoTe_2$. *Nat. Commun.* **2016**, 7, 1–7.

(91) Keum, D. H.; Cho, S.; Kim, J. H.; Choe, D. H.; Sung, H. J.; Kan, M.; Kang, H.; Hwang, J. Y.; Kim, S. W.; Yang, H.; Chang, K.J.; Bandgap Opening in Few-Layered Monoclinic $MoTe_2$. *Nat. Phys.* **2015**, 11, 482–486.

(92) Panda, M. R.; Bao, Q.; Mitra, S. $MoTe_2$, A Novel Anode Material for Sodium Ion Battery. *AIP Conf. Proc.* **2018**, 1942, 140078.

(93) Panda, M. R.; Ghosh, A.; Kumar, A.; Muthuraj, D.; Sau, S.; Yu, W.; Zhang, Y.; Sinha, A. K.; Weyland, M.; Bao, Q.; Mitra, S. Blocks of Molybdenum Ditelluride: A High Rate Anode for Sodium-Ion Battery and Full Cell Prototype Study. *Nano Energy* **2019**, 64, 103951.

(94) Li, W.; Li, J. Ferroelasticity and Domain Physics in Two-Dimensional Transition Metal Dichalcogenide Monolayers. *Nat. Commun.* **2016**, 7, 1–8.

(95) Si, C.; Choe, D.; Xie, W.; Wang, H.; Sun, Z.; Bang, J.; Zhang, S. Photoinduced Vacancy Ordering and Phase Transition in $MoTe_2$. *Nano Lett.* **2019**, 19, 3612–3617.

(96) Qi, D.; Han, C.; Rong, X.; Zhang, X. W.; Chhowalla, M.; Wee, A. T.; Zhang, W. Continuously Tuning Electronic Properties of Few-Layer Molybdenum Ditelluride with in Situ Aluminum Modification toward Ultrahigh Gain Complementary Inverters. *ACS nano* **2019**, 13, 9464–9472.

(97) Wu, G.; Wang, X.; Chen, Y.; Wu, S.; Wu, B.; Jiang, Y.; Shen, H.; Lin, T.; Liu, Q.; Wang, X.; Zhou, P. $MoTe_2$ p–n Homojunctions Defined by Ferroelectric Polarization. *Adv. Mater.* **2020**, 32, 1907937.

(98) Xu, H.; Fathipour, S.; Kinder, E. W.; Seabaugh, A. C.; Fullerton-Shirey, S. K. Reconfigurable Ion Gating of 2H-$MoTe_2$ Field-Effect Transistors Using Poly (Ethylene Oxide)-$CsClO_4$ Solid Polymer Electrolyte. *ACS nano* **2015**, 9, 4900–4910.

(99) McGlynn, J. C.; Dankwort, T.; Kienle, L.; Bandeira, N. A.; Fraser, J. P.; Gibson, E. K.; Cascallana-Matías, I.; Kamarás, K.; Symes, M. D.; Miras, H. N.; Ganin, A. Y. The Rapid Electrochemical Activation of $MoTe_2$ for the Hydrogen Evolution Reaction. *Nat. Commun.* **2019**, 10, 1–9.

(100) Kim, J. H.; Bergren, M. R.; Park, J. C.; Adhikari, S.; Lorke, M.; Frauenheim, T.; Choe, D.H.; Kim, B.; Choi, H.; Gregorkiewicz, T.; Lee, Y. H. Carrier Multiplication in Van Der Waals Layered Transition Metal Dichalcogenides. *Nat. Commun.* **2019**, 10, 1–9.

(101) Park, J. C.; Yun, S. J.; Kim, H.; Park, J. H.; Chae, S. H.; An, S. J.; Kim, J.G.; Kim, S. M.; Kim, K. K.; Lee, Y. H. Phase-Engineered Synthesis of Centimeter-Scale 1T′-and 2H-Molybdenum Ditelluride Thin Films. *ACS nano* **2015**, 9, 6548–6554.

(102) Lin, J.; Wang, H.; Tay, R. Y.; Li, H.; Shakerzadeh, M.; Tsang, S. H.; Liu, Z.; Teo, E. H. T. Versatile and Scalable Chemical Vapor Deposition of Vertically Aligned $MoTe_2$ on Reusable Mo Foils. *Nano Res.* **2020**, 13, 2371–2377.

(103) Yang, J.; Lu, T.; Myint, Y. W.; Pei, J.; Macdonald, D.; Zheng, J. C.; Lu, Y. Robust Excitons and Trions in Monolayer $MoTe_2$. *ACS nano* **2015**, 9, 6603–6609.

(104) Mc Manus, J. B.; Cunningham, G.; McEvoy, N.; Cullen, C. P.; Gity, F.; Schmidt, M.; McAteer, D.; Mullarkey, D.; Shvets, I. V.; Hurley, P.K.; Hallam, T. Growth of 1T′ $MoTe_2$ by Thermally Assisted Conversion of Electrodeposited Tellurium Films. *ACS Appl. Energy Mater.* **2018**, 2, 521–530.

(105) Shang, J. Y.; Moody, M. J.; Chen, J.; Krylyuk, S.; Davydov, A. V.; Marks, T. J.; Lauhon, L. J. In Situ Transport Measurements Reveal Source of Mobility Enhancement of MoS_2 and $MoTe_2$ During Dielectric Deposition. *ACS Appl. Electron. Mater.* **2020**, 2, 1273–1279.

(106) Liu, J.; Wang, Y.; Xiao, X.; Zhang, K.; Guo, N.; Jia, Y.; Zhou, S.; Wu, Y.; Li, Q.; Xiao, L. Conversion of Multi-layered $MoTe_2$ Transistor Between P-Type and N-Type and Their Use in Inverter. *Nanoscale Res. Lett.* **2018**, 13, 1–9.

(107) Li, M.; Lin, C. Y.; Chang, Y. M.; Yang, S. H.; Lee, M. P.; Chen, C. F.; Lee, K. C.; Yang, F. S.; Chou, Y.; Lin, Y. C.; Ueno, K. Facile and Reversible Carrier-Type Manipulation of Layered $MoTe_2$ Toward Long-Term Stable Electronics. *ACS Appl. Mater. Interfaces* **2020**, 12, 42918–42924.

(108) Duong, N. T.; Lee, J.; Bang, S.; Park, C.; Lim, S. C.; Jeong, M. S. Modulating the Functions of MoS_2/$MoTe_2$ Van Der Waals Heterostructure via Thickness Variation. *ACS nano* **2019**, 13, 4478–4485.

(109) Pan, S.; Kong, W.; Liu, J.; Ge, X.; Zereshki, P.; Hao, S.; He, D.; Wang, Y.; Zhao, H. Understanding Spatiotemporal Photocarrier Dynamics in Monolayer and Bulk $MoTe_2$ for Optimized Optoelectronic Devices. *ACS Appl. Nano Mater.* **2018**, 2, 459–464.

(110) Zhu, T.; Xie, H.; Zhang, C.; Cheng, X.; Zhang, J.; Poudeu, P. F. P.; Tan, G.; Yan, Y.; Liu, W.; Su, X.; Tang, X. Enhanced Mechanical Properties of Na0.02Pb0.98Te/$MoTe_2$ Thermoelectric Composites Through in-Situ-Formed $MoTe_2$. *ACS Appl. Mater. Interfaces* **2019**, 11, 41472–41481.

(111) Liu, X.; Islam, A.; Guo, J.; Feng, P. X. L. Controlling Polarity of $MoTe_2$ Transistors for Monolithic Complementary Logic via Schottky Contact Engineering. *ACS nano* **2020**, 14, 1457–1467.

(112) Liu, X.; Qu, D.; Wang, L.; Huang, M.; Yuan, Y.; Chen, P.; Qu, Y.; Sun, J.; Yoo, W. J. Charge Density Depinning in Defective $MoTe_2$ Transistor by Oxygen Intercalation. *Adv. Funct. Mater.* **2020**, 2004880.

(113) David, L.; Bhandavat, R.; Singh, G. MoS_2/Graphene Composite Paper for Sodium-Ion Battery Electrodes. *ACS nano* **2014**, 8, 1759–1770.

(114) Pawar, S. A.; Kim, D.; Lee, R.; Kang, S. W.; Patil, D. S.; Kim, T. W.; Shin, J. C. Efficient Supercapacitor Based on Polymorphic Structure of 1T′-Mo_6Te_6 Nanoplates and Few-Atomic-Layered 2H-$MoTe_2$: A Layer by Layer Study on Nickel Foam. *Chem. Eng. J.* **2019**, 371, 182–192.

(115) Kim, E. K.; Yoon, S. J.; Bui, H. T.; Patil, S. A.; Bathula, C.; Shrestha, N. K.; Im, H.; Han, S. H. Epitaxial Electrodeposition of Single Crystal $MoTe_2$ Nanorods and Li^+ Storage Feasibility. *J. Electroanal. Chem.* **2020**, 878, 114672.

CHAPTER 3

Materials and experimental methods

"This chapter deliberates the synthesis of the molybdenum ditelluride ($MoTe_2$) anode and the sodium vanadium phosphate $Na_3V_2(PO_4)_3$ (NVP) cathode in different conditions. The detailed experimental techniques used for the characterization of synthesized electrode materials. The preparation of electrodes and the cell fabrication process along with the various electrochemical techniques."

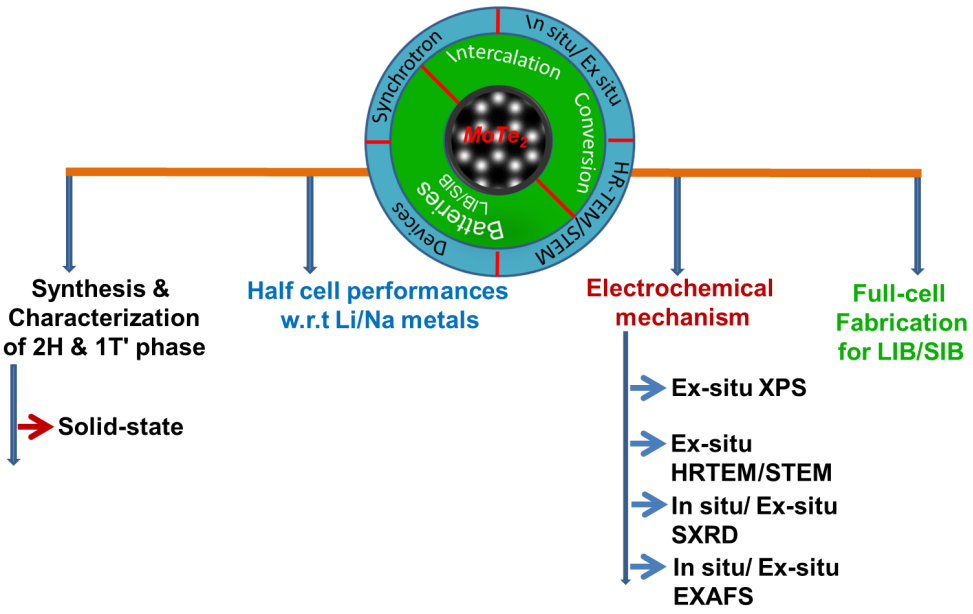

3.1 Chemicals

3.1.1 Chemicals for synthesis

The chemicals that were used for the synthesis of anode and cathode materials were Molybdenum powder (99.999 %, Sigma–Aldrich, USA), Tellurium powder (99.999%, Sigma–Aldrich, USA), Ammonium metavanadate (NH_4VO_3,99 %, Sigma–Aldrich, USA), Sodium phosphate monobasic monohydrate ($NaH_2PO_4.2H_2O$, 99 %, Sigma–Aldrich, USA), Sucrose (Sigma–Aldrich, USA), Ethyl alcohol(CH_3CH_2OH, Sigma–Aldrich, USA), Hydrochloric acid (HCl, 37 %, Merck, India), Oxalic acid (99.5 %, Fisher Scientific, India), Sodium chloride (NaCl, 99 %, Merck, India), Sodium hydroxide (NaOH, 97 %, Fisher Scientific, India).

3.1.2 Chemicals for electrode (anode and cathode) fabrication

The chemicals that were used for electrode (anode and cathode) fabrication were Lithium cobalt oxide ((LCO), Xiamen Tob New Energy Technology Co., Ltd.), Polyvinylidene fluoride ((PVDF), (CH_2CF_2)n Sigma–Aldrich, USA), Carbon black (Super C-65, Timcal, Switzerland), Sodium salt of Carboxymethyl cellulose ((CMC), high viscous 1100–1900 cp, LobaChemie, India), Aluminum foil (15 μm, MIT Corporation, USA), Copper foil (9 μm, MIT Corporation, USA).

3.1.3 Chemicals for electrolyte preparation and cell fabrication

The chemicals that were used for electrolyte preparation and cell fabrication were 1 M $LiPF_6$ in EC/DMC (1:1 vol./vol.) (LP-30, Merck, Germany), Sodium perchlorate ($NaClO_4$, 98 %, Sigma–Aldrich, USA), Ethylene carbonate ((EC), $C_4H_4O_3$ anhydrous, 99 %, Sigma–Aldrich, India), Propylene carbonate ((PC), $C_4H_6O_3$, 99.7 % Sigma–Aldrich, USA), Fluoroethylene carbonate (FEC, $C_4H_3FO_3$, > 99 %, acid less than 200 ppm, anhydrous, Sigma–Aldrich, USA), Sodium metal foil (Na, 99.95 %, Alfa Aesar, India), Borosilicate glass microfiber filter (GF/D, Whatman, UK), CR2032 coin-cell casing.

3.2 Material synthesis

3.2.1 Synthesis of molybdenum ditelluride (2H-$MoTe_2$)

A 2H-$MoTe_2$ polycrystalline powder was prepared by mixing a stoichiometric amount of molybdenum (Sigma–Aldrich, 99.999 %) and tellurium (Sigma–Aldrich, 99.999 %) powders. The Mo powder was pre-sintered at 600 °C in an argon atmosphere for 8 h. Subsequently, the

powder was uniformly mixed with tellurium powder by hand-grinding in an argon atmosphere to obtain a precursor for $MoTe_2$ synthesis (**Figure 3.1**). The mixed powder was then sealed in a 150-mm-long quartz ampoule (15 mm inner diameter) under vacuum at 10^{-5} torr of pressure. The ampoule was vibrated for ten minutes and purged under an argon atmosphere five times while evacuating it to eliminate more oxygen. After sealing the precursor powder, it was spread along the horizontal ampoule length and introduced into a furnace. The temperature was increased slowly from room temperature to 800 °C. The temperature was maintained at 800 °C for 20 h to complete the alloying reaction.[1] Slow heating avoids a possible explosion due to the strongly exothermic reaction between the elements. The heating and cooling rate during the annealing process was maintained at a ramping rate of 1 °C/min. After cooling to room temperature, a black powder of $MoTe_2$ was obtained, which was ground in an inert atmosphere before further characterization.[1,2]

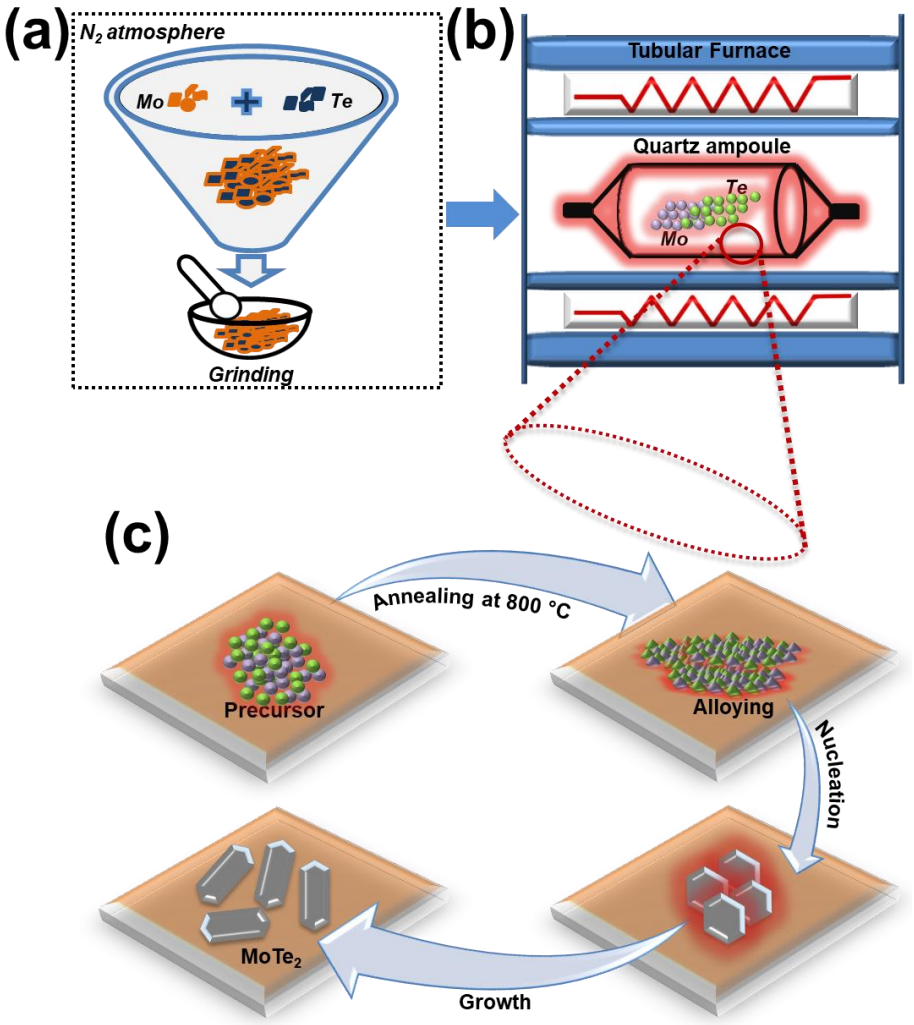

Figure 3.1 Schematic representation of $MoTe_2$ preparation and the growth process.

3.2.2 Synthesis of molybdenum ditellurides (2H-$MoTe_2$) of different crystallite sizes

A stoichiometric amount of molybdenum (Sigma–Aldrich, 99.999 %) and tellurium (Sigma–Aldrich, 99.999 %) powders have been mixed, and a mixture has been prepared for the synthesis of $MoTe_2$. The mixture was uniformly mixed by hand-grinding in an argon atmosphere to obtain a precursor for $MoTe_2$ synthesis. The mixed powder was then sealed in three different 150-mm-long quartz ampoules under vacuum at 10^{-5} torr of pressure.[1,2] The temperature was increased slowly at three different heating rates (0.5 °C/min, 2 °C/min, and 10 °C/min) from room temperature to 810 °C, 820 °C, and 825 °C, respectively. We chose the higher heating rate of 10 °C/min to avoid an exothermic reaction. The higher sintering temperature was limited to 825 °C to retain the phase purity of the 2H-$MoTe_2$ phase. The respective holding temperatures were maintained for 20 h to complete the alloying reaction.[1] After cooling to room temperature, three black powders of $MoTe_2$ were obtained, which was ground in an inert atmosphere before further characterization.[2]

3.2.3 Synthesis of the molybdenum ditelluride (1T'-$MoTe_2$)

A 1T'-$MoTe_2$ polycrystalline powder was prepared by mixing a stoichiometric amount of molybdenum (Sigma–Aldrich, 99.999 %) and tellurium (Sigma–Aldrich, 99.999 %) powders. The Mo powder was pre-sintered at 600 °C in an argon atmosphere for 8 h. Subsequently, the powder was uniformly mixed with tellurium powder by hand-grinding in an argon atmosphere to obtain a precursor for $MoTe_2$ synthesis.

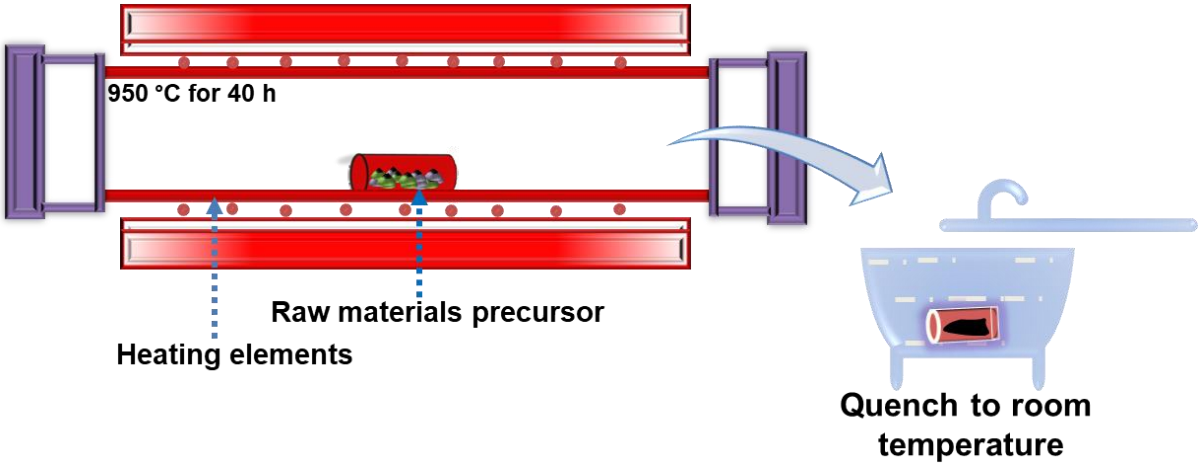

Figure 3.2 Schematic representation of the preparation of 1T' $MoTe_2$.

The mixed powder was then sealed in a 150-mm-long quartz ampoule (15 mm inner diameter) under vacuum at 10^{-5} torr of pressure. The ampoule was vibrated for ten minutes and purged

under an argon atmosphere five times while evacuating it to eliminate more oxygen. After sealing the precursor powder, it was spread along the horizontal ampoule length and introduced into a furnace. The temperature was increased slowly from room temperature to 950 °C. The temperature was maintained at 950 °C for 40 h to complete the alloying reaction.[1,2] The temperature was quenched to room temperature through an ice bath to capture the1T' phase **(Figure 3.2)**. After cooling to room temperature, a black powder of 1T'-$MoTe_2$ was obtained, which was ground in an inert atmosphere before further characterization.

3.2.4 Preparation of sodium vanadium phosphate$Na_3V_2(PO_4)_3$ (NVP)

A simple two-step process that comprised a solid-state reaction followed by carbothermal reduction was followed to obtain a nearly phase-pure $Na_3V_2(PO_4)_3$. In the first step, a stoichiometric amount of NH_4VO_3 (Sigma–Aldrich, ≥ 99 %) and $NaH_2PO_4.2H_2O$ (Sigma–Aldrich, ≥ 99 %) were mixed with 20 % of sucrose in 20 ml of ethanol medium. This mixture was subjected to a ball mill for 24 h at 300 rpm. After ball milling, the obtained mixture was dried at 100 °C in air; it was then crushed to a powder. In the second step, two-step heating of the precursor was carried out to obtain a calcined powder. During the two-step heating process, the powder was initially kept at 350 °C for 3 h and followed by final calcinations at 800 °C in an N_2/H_2 (95:5) atmosphere for 8 h, with a ramp rate of 5 °C/min to obtain the desired pure-phase $Na_3V_2(PO_4)_3$ material.[2,3]

3.3 Material characterizations techniques

The as-prepared materials and the cycled electrode characterizations were investigated by using sophisticated equipment such as the lab source Cu Kα radiation (λ = 0.15418 nm) X-ray diffraction (XRD) technique and the SXRD technique. For imaging, the field-emission gun scanning electron microscope (FEGSEM), field-emission gun transmission electron microscope (FEGTEM), and aberration-corrected STEM (and correlative bright-field TEM and SAED) in the STEM mode were used. For the analysis of chemical compositions, X-ray photoelectron spectroscopy (XPS), Raman spectroscopy, Brunauer–Emmett–Teller (BET), in situ and ex situ modes of synchrotron-based XANES, Extended X-ray absorption fine structure (EXAFS) characterization techniques, and the like were used. Each characterization technique is briefly described in the following sections.

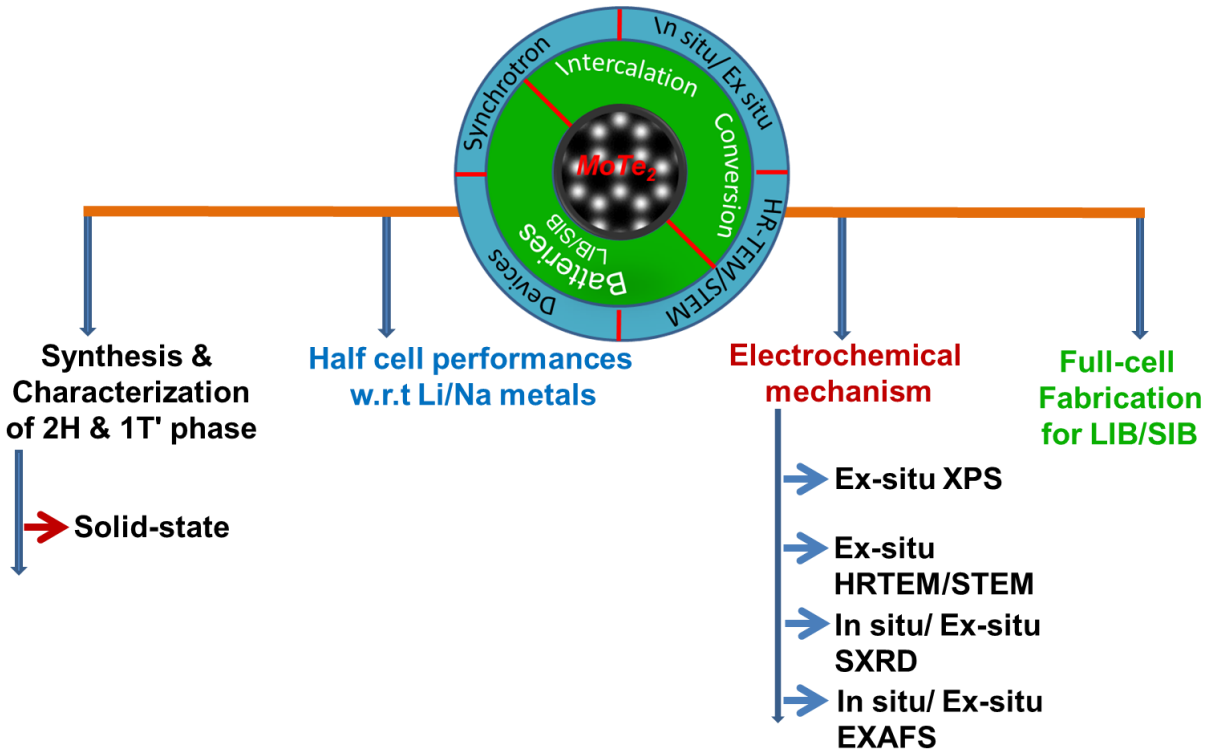

Figure 3.3 Schematic of the work plan.

3.3.1 Lab source X-ray powder Diffraction

To obtain the phase confirmation and crystallographic information of as-prepared materials and the phase change information of the cycled electrode materials, lab source XRD spectra of the samples were recorded at room temperature using a Rigaku Smartlab X-ray diffractometer with Cu Kα radiation (λ = 1.5418 Å) at 40 kV and 40 mA between the 2θ range of 5º to 90º. For as-prepared materials, the powder samples were ground well and homogenized to obtain better XRD data.

3.3.2 Synchrotron X-ray powder Diffraction

Synchrotron XRD and XANES were performed on an angle-dispersive XRD (ADXRD) beamline (BL-12) at INDUS-2 Synchrotron Source (2.5 GeV), Raja Ramanna Centre for Advanced Technology (RRCAT), Indore, India. The beamline consisted of an Si (111)-based double crystal monochromator and two experimental stations, namely, a six-circle diffractometer (Huber 5020) with a scintillation point detector and an image plate (Mar 345) area detector. This experimental setup was used for the present SXRD measurements, and the obtained image plate data was processed by the Fit2D program.[2,4,5] To calibrate the distance between the photon energy and the sample detector, the LaB_6 NIST standard was used as the

reference. An X-ray of a wavelength of 0.71184 Å was used for the SXRD measurement. Ex situ SXRD measurements were carried out using the transmission mode after removing the active material from the electrodes. **Figure 3.4** shows the setup used to record the in situ XRD spectra at PDXRD beamline Australian synchrotron source, Clayton, Australia.

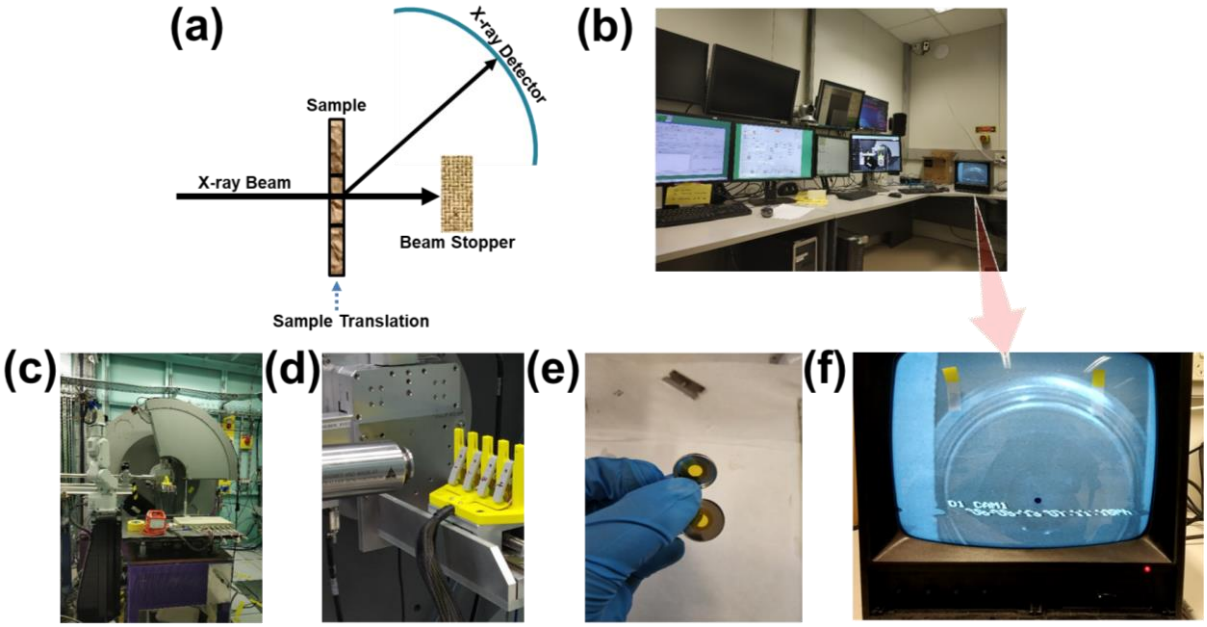

Figure 3.4 The setup while recording in situ XRD spectra at PDXRD beamline Australian synchrotron source, Clayton, Australia.

3.3.3 X-ray Photoelectron Spectroscopy

X-ray photoelectron spectroscopy measurements were carried out under the instrument model (Kratos Analytical (SHIMADZU group), AXIS Supra) and the UK analysis chamber at Pr< 2.0×10^{-7} Pa and a take-off angle of 90°. For high-resolution scans, the pass energy is 20 eV, and the resolution is ~ 0.5 eV. For the survey, the scans pass energy is 160 eV, and the resolution ~2 eV. Chemical information about a sample for up to 10 nm from the surface is provided by XPS, which is a surface analytical technique. It enables the investigation of various oxidation states and chemical bonding information of the as-prepared and cycled electrode materials' surface elements

3.3.4 X-ray absorption near-edge structure in the ex situ mode

Measurements using XANES were made for the as-prepared $MoTe_2$ powder and cycled electrodes in the ex situ mode. The samples were in the form of a thin film of around 50 microns on a Cu foil of 9 microns. The XANES measurements were carried out in the fluorescence

mode at room temperature. A sample absorption around the Mo K-edge was measured by monitoring fluorescence using an energy-dispersive detector (Vortex-EX). The incident intensity was measured with the help of an ionization chamber, which was placed before the sample. Photon energies below and above the Mo K-edge were resolved using an Si (111) double crystal monochromator. The energy resolution (ΔE/E) was estimated to be 1.5×10^{-4} around the Mo K-edge. The spectra were recorded in steps of 1 eV.

3.3.5 Extended X-ray absorption fine structure (EXAFS) and X-ray absorption near-edge structure (XANES) in the in situ mode

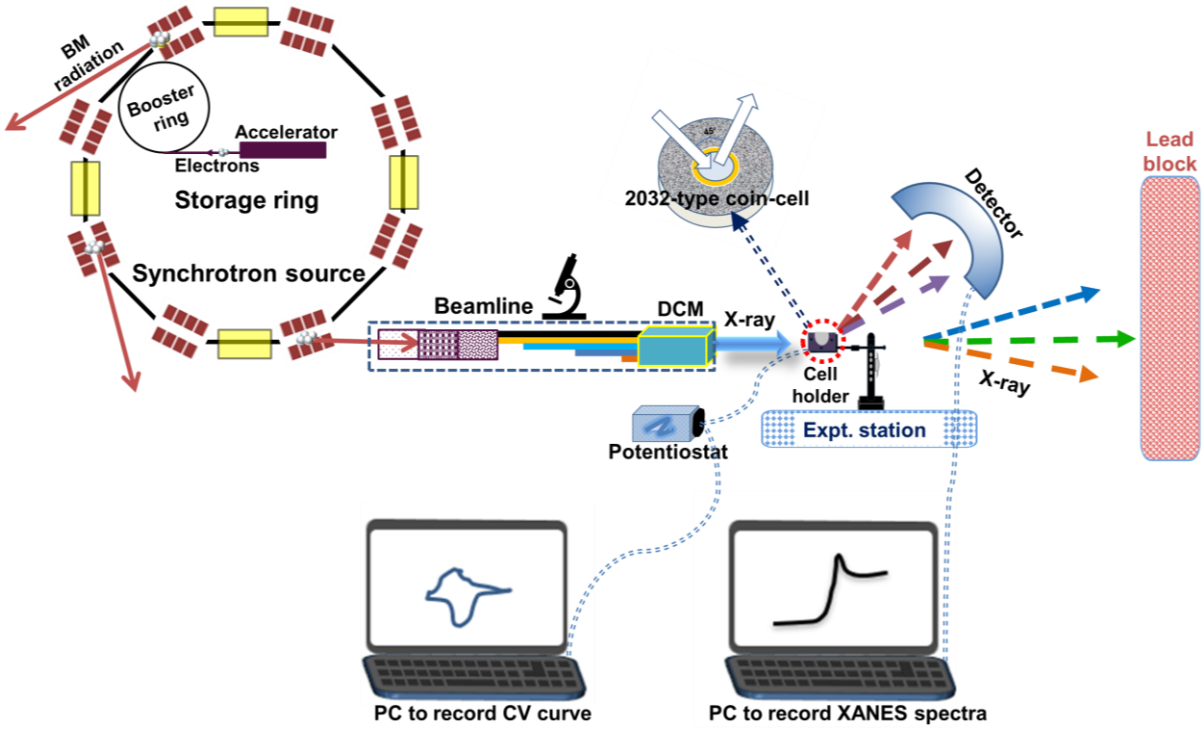

Figure 3.5 Schematic of the in situ XAS cell-holder setup used in the in situ XANES experiments at the synchrotron radiation (SR) source. Monochromatic X-rays are focused on the CR2032-type coin cell. The coin cell is positioned with a stage that is capable of rotation and three-axis translation in the beam path; a series of in situ XANES spectra are recorded over the investigated energy range.

The X-ray absorption fine structure (XAFS), which comprises both the near-edge (XANES) and extended (EXAFS) structure spectroscopy measurements for as-prepared and cycled electrode samples were carried out at the Energy scanning EXAFS beamline (BL-9). The beamline operated in the photon energy range of 4–25 KeV. Beamline optics consists of a Rh/Pt-coated collimating meridional cylindrical mirror for beam collimation and higher harmonic rejection to some extent. The collimated beam was monochromatized by an Si (111)

(2d = 6.2709)-based double crystal monochromator (DCM). The second crystal of the DCM was a sagittal cylindrical crystal, which was used to horizontally focus the beam. At the same time, another Rh/Pt-coated bendable post mirror that faced downward was used to vertically focus the beam at the sample position. **Figure 3.5** shows the schematic of the in situ XAS cell-holder setup used in the in situ XANES experiments at the synchrotron radiation (SR) source. Monochromatic X-rays are focused on the CR2032-type coin cell (the different parts of the in situ coin cell shown in **Figure 3.6**).

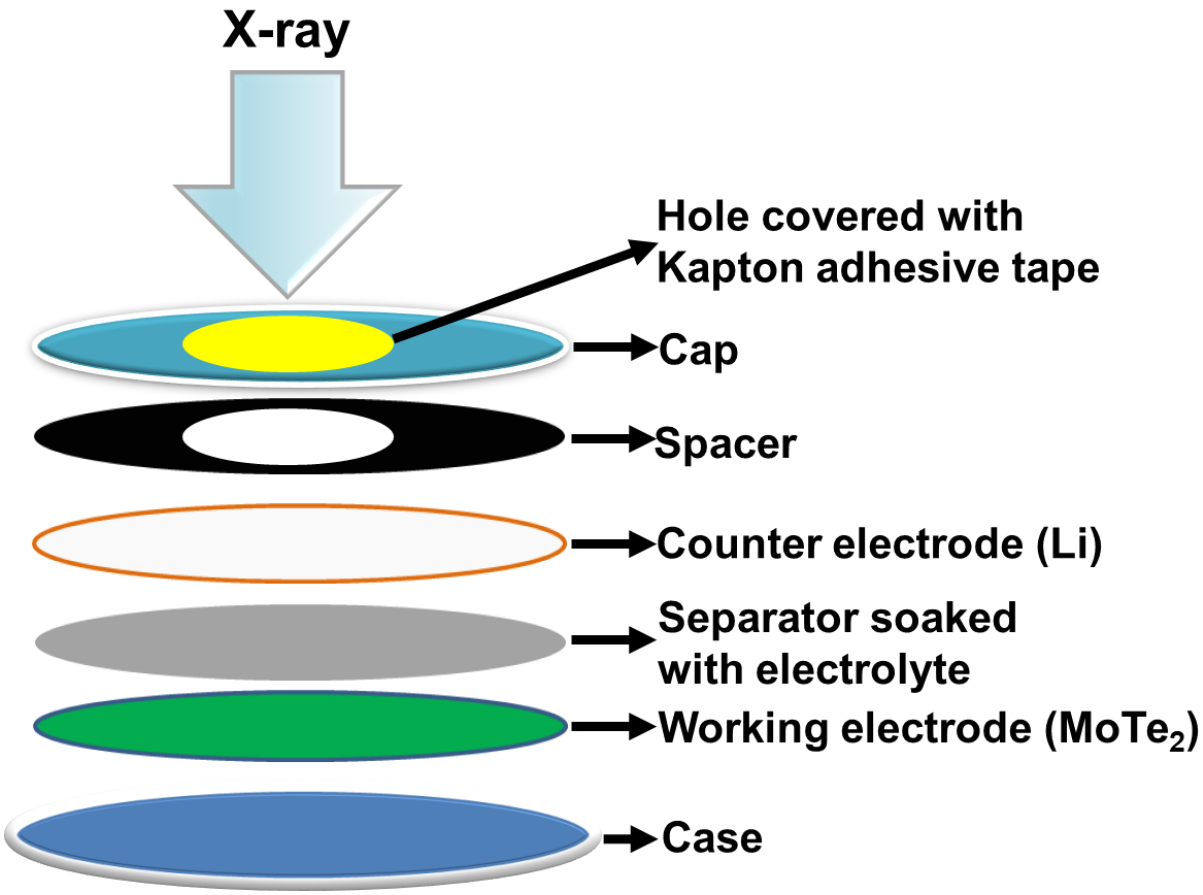

Figure 3.6 Different parts of the in situ coin cell.

The coin cell is positioned with a stage that is capable of rotation and three-axis translation in the beam path; a series of in situ XANES spectra are recorded over the investigated energy range. **Figure 3.7** shows the setup while recording in situ XANES spectra at ADXRD beamline Indian synchrotron source, RRCAT, Indore, India.

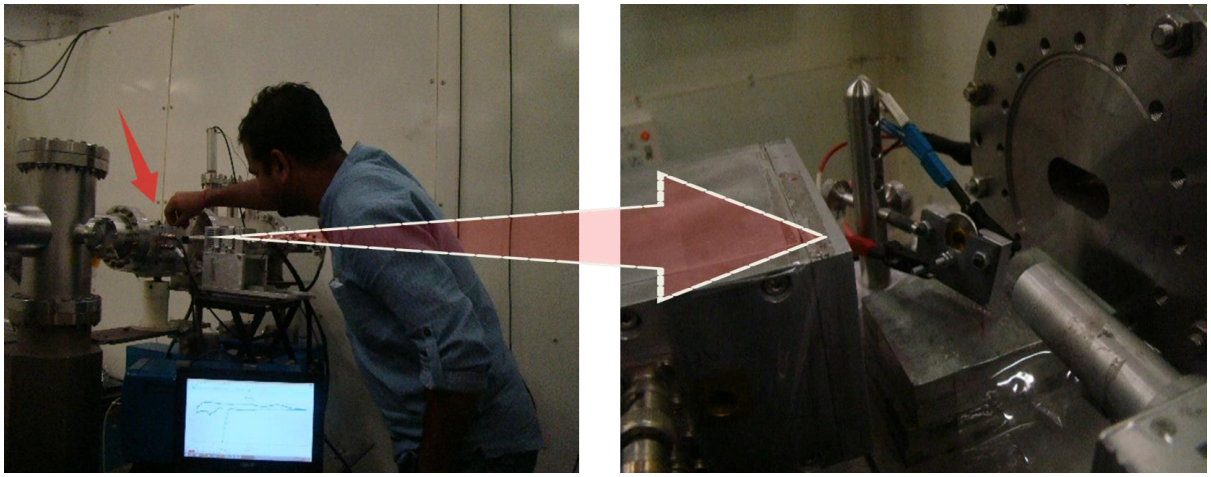

Figure 3.7 The setup while recording in situ XANES spectra at ADXRD beamline Indian synchrotron source, RRCAT, Indore, India.

3.3.6 Field-Emission Gun Scanning Electron Microscopy

The as-prepared and cycled electrode sample's surface morphology was examined using secondary electron imaging in a JEOL-7600F FEGSEM. Elemental mapping of the surfaces of the cathode and the anode was performed by the Energy-dispersive X-ray analysis (EDX) that was attached to the FEGSEM instruments to depict the chemical compositional information about the distribution of different elements.

3.3.7 Field-Emission Gun Transmission Electron Microscopy and Scanning transmission electron microscope (STEM)

Another powerful electron microscope technique, FEGTEM, is used for morphological characterization at the atomic level. To identify areas that are suitable for HR-STEM imaging, a whole TEM sample was grid-mapped using MAPS software (Thermo Fischer Scientific) on an FEI Magellan FEGSEM prior to inserting the sample specimen into the aberration-corrected TEM. This enabled the location of thin delaminated sections of $MoTe_2$ (for c-axis imaging) and the edge on the crystals (for perpendicular-to-c-axis imaging). Aberration-corrected STEM (and correlative bright-field TEM and SAD) was carried out on a dual Cs-corrected FEI Titan^3 FEGTEM that was operated at 305kV. A probe-forming aperture of 15 mrad was used, high-angle annular dark field (HAADF) images were collected from 57 to 220 mrad, annular bright-field (ABF) images were collected from 7.3 to 15 mrad, and incoherent bright-field images were collected with a 35 mrad outer angle. Position-averaged convergent beam electron diffraction (PACBED)[2,6] was carried out on sample areas after imaging to determine the

thickness for simulation. Simulations of PACBED patterns over a range of thicknesses were calculated by JEMS[7], and they were matched by eye to the nearest 1 nm. Simulations of HAADF and ABF images, based on the measured thickness of PACBED were carried out using Multislice formulation using an absorptive model.[8]

Conventional TEM, HRTEM and selected area diffraction (SAD) characterization of the ex situ HRTEM and SAD characterization of the cycled electrode samples were carried out using a JEOL-2100F FEGTEM to detect the crystallographic arrangement.

3.3.8 SEM and TEM sample Preparation

Samples for TEM were prepared by suspending a solution of $MoTe_2$ powder in ultraclean ethanol, which was further sonicated to create a suspension; 5µl of the suspension was disposed on a holey carbon film on a 3 mm Cu grid, and the alcohol was then wicked off with filter paper to ensure good dispersion.

3.3.9 Preparation of electrodes for ex situ SXRD, HRTEM, XPS, and XANES analyses

For ex situ SXRD, HRTEM, XPS, and XANES analyses of cycled (discharge/charge) electrodes, the cells were first disassembled inside an Ar-filled glove box. The electrodes were then washed with dimethyl carbonate (DMC) to remove salt (if any) and kept inside the glove box for 12 h. After the electrodes dried completely, they were sealed in separate airtight sample boxes and taken out from the glove box for their respective SXRD, HRTEM, XANES, and XPS analyses.

3.4. Electrode preparation and cell fabrications

3.4.1 Preparation of the $MoTe_2$ anode against the lithium metal half cell

The anode was prepared by mixing the active material ($MoTe_2$), conductive carbon (super C65, Timcal, Switzerland), and polyvinylidene fluoride (PVDF) as the binder in N-Methyl-2-Pyrrolidone (NMP) at a wt. ratio of 7:2:1, respectively. The slurry was cast on Cu foil and dried at 80 ºC for 10 h in a vacuum oven. After complete drying, circular electrode disks of 12 mm were cut and placed against the lithium metal anode into CR2032-type coin cells. The CR2032-type coin cells were assembled in an argon-filled glove box (Unilab, Mbraun, $H_2O \leq 0.5$ ppm, $O_2 \leq 0.5$ ppm), which had a cell configuration of Li/Electrolyte/$MoTe_2$. The cell design was maintained in such a way that the cast disk acted as working electrodes against the Li foil (Alfa Aesar) anode, which was considered both the counter and the reference electrode. Borosilicate

glass fiber (GF/D, Whatman) was used as the separator, and 1 M $LiPF_6$ in EC/DMC (1:1 vol./vol.) (LP-30, Merck, Germany) was used as the electrolyte with 3 wt % of Fluoroethylene carbonate (FEC) added as an additive.

3.4.2 Construction and electrochemical measurements of lithium full cells

To fabricate lithium-ion full cells, commercially available LCO (Xiamen Tob New Energy Technology Co., Ltd.) was used as a cathode against the as-synthesized $MoTe_2$ anode. To prepare the cathode, a slurry was made by mixing the active material (LCO) and conductive carbon (super C65) in the PVDF solution that was made of an NMP solvent in the weight ratio 80:10:10. The slurry was then cast onto aluminum foil of a thickness of 16 µm using the doctor blade technique; the slurry was then dried in an oven overnight to remove the solvent molecules. The electrodes were pressed to achieve 30–40 % porosity. The active material loading in the electrode was estimated to be 2.0–2.2 mg cm^{-2}. The coin-type (CR2032) full cell was constructed using the $MoTe_2$ sample anode and the LCO cathode. The charge balance in the electrode was carried out by adjusting the mass ratio to 3:1. A full-cell configuration of the $MoTe_2$ electrode (Anode) | borosilicate glass separator soaked in electrolyte | LCO (cathode) was assembled in an Ar-filled glove box with an oxygen-and-water level of < 0.5 ppm. LP-30; an additive of fluoroethylene carbonate (FEC) (3 wt %) was used as the electrolyte. CV measurements were performed at a scan rate of 0.05 mV s^{-1} in the range of 2.5 to 4.5 V. Galvanostatic measurements were carried out in the range of 1.8 to 3.8 V at a current density of 0.5 A g^{-1}. The specific capacities were evaluated based on the mass loading of the $MoTe_2$ anode. All the electrochemical performances were measured at a temperature of 20 ± 2 ºC with a controlled atmosphere.[2]

3.4.3 Preparation of the $MoTe_2$ anode against the sodium metal half-cell

The $MoTe_2$ electrode was prepared by mixing the active material ($MoTe_2$), conductive carbon (super C65, Timcal, Switzerland), and sodium carboxymethylcellulose (CMC) as the binder in deionized water in the wt. ratio of 7:2:1, respectively. The slurry was cast on Cu foil and dried overnight in a vacuum oven at 80 °C. After the slurry dried completely, circular disks (12 mm) of the electrodes were cut and placed against the sodium metal anode into a 2032-type coin cell. The cell design was maintained such that the cast disks acted as working electrodes against the Na-foil (Alfa Aesar) anode, which acted as both the counter and the reference electrode. Borosilicate glass fiber (GF/D, Whatman) was used as the separator; and 1 M of $NaClO_4$ in a

mixture of EC and propylene carbonate (respectively, 1:1 v/v), and 3 wt % Fluoroethylene carbonate (FEC) was used as an electrolyte.[2]

3.4.4 Preparation of NVP cathode against sodium

In order to fabricate the full cell, NVP was synthesized. Additionally, an electrode was prepared by mixing the active material (NVP) and the conductive carbon (super C65) in a PVDF solution that comprised NMP in the weight ratio, 80:10:10, for about 7 h at 600 rpm. Subsequently, the slurry was cast onto the aluminum foil that had a thickness of 16 µm by using the doctor blade technique. The slurry was then dried in an air oven overnight to remove the solvent molecules. The electrodes were pressed to achieve 30–40 % porosity. A circular disk of 12 mm was used to evaluate the performance of NVP against that of the sodium metal cell. The average active material loading in the electrode was estimated at 2.0–2.2 mg cm^{-2}. All the electrochemical performances were measured at 20 ± 2 °C in a controlled atmosphere.[2]

3.4.5 Fabrication and electrochemical measurements of $MoTe_2$// NVP sodium-ion full cells

The coin-type (CR2032) full cell was constructed using the $MoTe_2$ anode and the NVP cathode. The charge balance in the electrode was carried out by adjusting the mass ratio to 3:1 (NVP: $MoTe_2$). The full-cell configuration of the $MoTe_2$ (Anode), the borosilicate glass separator that was soaked in an electrolyte, and the NVP (cathode) were assembled in an argon-filled glove box (Mbraun, Germany), with oxygen and water levels at < 0.5 ppm. A mixture of EC, PC (1:1 v/v), and fluoroethylene carbonate (FEC) (3 wt %) along with 1 M of $NaClO_4$ was used as the electrolyte. Galvanostatic measurements were made in the voltage range of 1.0 to 3.5 V at a current density of 0.5 A g^{-1}. The specific capacities were evaluated based on the mass loading of $MoTe_2$.

3.4.6 Electrochemical characterizations

3.4.6.1 Cyclic Voltammetry

Cyclic voltammetry (CV) measurements were performed on the BioLogic VMP-3 model (France) at a scan rate of 0.05 mV s^{-1} in the voltage range of 0.01 to 3.0 V. The scan rate varies between 0.05 and 5 mV s^{-1} at several voltage (it differs for the anode, cathode, and full cell) ranges at 20 ± 2 °C. For electrochemical quantitative kinetics analysis CV at different scan rates were studied within the potential limit of 0.01 to 3.00 V (in comparison to Na/Na^+ and Li/Li^+). The CV is a potentiodynamic electrochemical technique, by which the scanning is possible in both positive and negative directions. The output signal is in the form of current.

The obtained current is plotted as a function of the applied potential to obtain the corresponding CV data.

3.4.6.2 Galvanostatic charge-discharge

The galvanostatic charge-discharge tests were carried out at various current rates within the voltage window of 0.10–2.50 V (versus Li/Li^+) by Arbin Instrument (BT2000, USA) under different current densities. All electrochemical experiments were performed at 20 ºC within 2 ºC of accuracy. The specific capacities were evaluated based on active material loading in the electrode. For anode materials, the potential windows were between 0.01 and 2.5 V; and for the cathode materials, between 1.0 and 4.5 V. The applied current rate was decided based on the active material loading (mA g^{-1}). The galvanostatic charge-discharge test is an essential electrochemical performed in the galvanostatic mode. It provides information about the battery's health, whereas the average cell voltage is known from the charge-discharge profile. A constant current at a particular potential window is applied during the charge-discharge process.

3.4.6.3 Electrochemical Impedance Spectroscopy and Transport kinetics mechanism

In situ Electrochemical Impedance Spectroscopy (EIS) was performed with a BioLogic VMP-3 model (France) at 20 ± 2 °C in the frequency range of 1 MHz to 10 mHz. The EIS data were fitted with a suitable circuit model using EC-Lab software by BioLogic. The EIS data were recorded at OCV and with different discharge and charge voltages during the second cycle; this was followed by repeated discharge-charge cycles of the $MoTe_2$ electrode samples versus Li/Li^+ and Na/Na^+. At each state, EIS was recorded with a voltage amplitude of ΔV=5 mV within a frequency range of 10 mHz to 1 MHz. To understand the electrochemical behavior at both electrode and electrolyte interfaces, EIS, which is a unique technique is used. It is generally used to identify the diffusion and charge transfer process and to analyze the improved electrochemical performance of the $MoTe_2$ anode during cycling. For transport kinetics studies, CV of different scan rates were studied, and the related calculations were performed to determine the capacitive-controlled and diffusion-controlled insertion process, respectively.

3.5 Computational details

3.5.1 Computational details in 2H–$MoTe_2$

To understand the evolution of the structure of the $MoTe_2$ anode that results from the

intercalation of lithium atoms (lithiation process) of various concentrations between the two layers of $MoTe_2$, we performed DFT-based spin-polarized electronic structure calculations. For this purpose, we employed the Vienna ab initio Simulation Package (VASP).[9,10] In all the calculations, we used the projector augmented-wave (PAW)[11] method and the generalized gradient approximation (GGA), as given by Perdew, Burke, and Ernzerhof (PBE)[12] to account for the exchange-correlation functionals. We augmented the PBE functionals with the DFT-D3 method of Grimme et al.[13] to include the effect of the van der Waals (vdW) interaction. The conjugate gradient technique was employed to perform the optimization of the geometry of various structures with different concentrations of lithium atoms.

We first constructed a unit cell of the bulk $MoTe_2$ structure with a 2H symmetry (2H-$MoTe_2$), which had two layers of $MoTe_2$ arranged in an AB-type of stacking[14] that interacted via a weak vdW interaction. It is well known that the unit cell of the 2H-$MoTe_2$ has one Mo and two Te atoms per layer, in which the Mo atom is located between two Te atoms, and these atoms are covalently bonded with each other.[14] We carried out full geometry optimization calculations for the unit cell of 2H-$MoTe_2$. The lattice constants that were obtained after geometry optimization are as follows: a = b = 3.52 Å, c = 13.93 Å; the unit cell has a $P6_3/mmc$ symmetry. In the optimized structure, the bond length between Mo and Te atoms (d_{Mo-Te}) and the interlayer distance were found to be 2.73 Å and 7.2 Å, respectively. These values are in good agreement with the previously reported theoretical results.[14] By using the optimized unit cell, we constructed a 2 x 2 x 1 supercell to determine the structures of the lithiated $MoTe_2$ material (Li_xMoTe_2). We varied the concentration x of Li atoms in Li_xMoTe_2 over a range of $0 < x \leq 3.0$, with a step of x = 0.25. For example, x = 3 corresponds to 24 Li atoms, since a 2 x 2 x 1 supercell of $MoTe_2$ comprises 8 Mo and 16 Te atoms. Each value of the concentration of Li atoms can give rise to different possible configurations, and in this work, we have considered these configurations to study the lithiation process. The full ab initio geometry optimization of each of these configurations is computationally expensive. Therefore, to identify the lowest energy structure for each concentration, we performed geometry optimization of the possible polymorphs in two steps. In the first step, all the configurations for each value of the concentration, x, were optimized by using the coarse-DFT approach. In these calculations, we used an energy cutoff of 400 eV for the plane-wave basis set along with a 9 x 9 x 1 k-mesh, which was centered at the Γ point, using the Monkhorst-Pack scheme for the k-points. In the second step, with the aim of more accurate results, three of the lowest energy configurations for each value of x, which were obtained through the coarse-DFT calculations, were considered

for another set of optimization calculations with refined parameters (fine-DFT). To this end, convergence tests were performed for the plane-wave cutoff and k-mesh. The converged parameters were an energy cutoff of 500 eV and a k-mesh of 11 x 11 x 3. The energy convergence criterion for the total energy was set to be 10^{-6} eV. Structure optimization was carried out by allowing the volume and the cell shape to change and the atoms to relax until the Hellmann–Feynman force on each atom was less than 0.01 eV/Å.

3.5.2 Computational details in 1T'–$MoTe_2$

In this work, we investigate the process of intercalation of the lithium (Li) atoms between two layers of bulk $MoTe_2$ in the 1T' phase. Various concentrations of Li atoms have been probed in the process of lithiation to understand the evolution of the structure of $MoTe_2$, which acts as an anode material. We wish to mention here that a unit cell of the bulk $MoTe_2$ structure (with two Mo and four Te atoms per layer) with 1T' symmetry (1T'-$MoTe_2$) is a monoclinic lattice that can be considered a distorted 1T phase (octahedral coordination of the transition metal, Mo) in which the formation of in-plane Mo-Mo bonds results in a pseudo-hexagonal layer with zigzag metal chains.[15] In order to simulate the lithiation process, we performed spin-polarized density functional theory (DFT)-based electronic structure calculations, as implemented in the Vienna ab initio Simulation Package (VASP).[9,10,16,17] The Projector augmented-wave (PAW)[11] method with GGA, which was given by Perdew, Burke, and Ernzerhof (PBE)[12] as exchange-correlation functionals, was used. The DFT-D3 method by Grimme et al.[13,18] was used to incorporate the effect of the van der Waals (vdW) interaction. We employed the conjugate gradient algorithm for the full geometry optimization of the structures, with variable concentrations of Li atoms.

Convergence tests were performed for plane-wave cutoff and k-mesh, and an energy cutoff of 500 eV with 11 x 11 x 3 Γ-centered Monkhorst-Pack grid of k-points were used in the DFT calculations. The total energy convergence criterion in the self-consistent field cycle was 10^{-6} eV. Full geometry optimization, including the relaxation of atomic coordinates along with volume and cell shape variation was performed. The atomic positions were allowed to relax until the Hellmann–Feynmann force on each atom was less than 0.01 eV/Å. We note that, for the optimized structure of the $MoTe_2$ in the 1T' phase, the bond length between Mo and Te atoms d_{Mo-Te} lies in the range of 2.71 to 2.82 Å, and the interlayer distance is found to be around 6.85 Å. These geometric values show excellent matching with the previously reported theoretical results.[15]

3.6 References

(1) Keum, D. H.; Cho, S.; Kim, J. H.; Choe, D. H.; Sung, H. J.; Kan, M.; Kang, H.; Hwang, J. Y.; Kim, S. W.; Yang, H.; Chang, K. J. Bandgap Opening in Few-Layered Monoclinic $MoTe_2$. *Nat. Phys.* **2015**, 11, 482–486.

(2) Panda, M. R.; Ghosh, A.; Kumar, A.; Muthuraj, D.; Sau, S.; Yu, W.; Zhang, Y.; Sinha, A. K.; Weyland, M.; Bao, Q.; Mitra, S. Blocks of Molybdenum Ditelluride: A High Rate Anode for Sodium-Ion Battery and Full Cell Prototype Study. *Nano Energy* **2019**, 64, 103951.

(3) Manohar, C. V.; Kar, M.; Forsyth, M.; MacFarlane, D. R.; Mitra, S. Stability Enhancing Ionic Liquid Hybrid Electrolyte for NVP@C Cathode Based Sodium Batteries. *Sustain. Energy Fuels* **2018**, 2, 566–576.

(4) Panda, M. R.; Bhowmik, R. N.; Singh, H.; Singh, M. N.; Sinha, A. K. Air Annealing Effects on Lattice Structure, Charge State Distribution of Cations, and Room Temperature Ferrimagnetism in the Ferrite Composition $Co_{2.25}Fe_{0.75}O_4$. *Mater. Res. Express* **2015**, 2, 036101.

(5) Bhowmik, R. N.; Panda, M. R.; Yusuf, S. M.; Mukadam, M. D.; Sinha, A. K. Structural Phase Change in $Co_{2.25}Fe_{0.75}O_4$ Spinel Oxide by Vacuum Annealing and Role of Coexisting CoO Phase on Magnetic Properties. *J. Alloys Compd.* **2015**, 646, 161–169.

(6) Findlay, S. D.; Shibata, N.; Sawada, H.; Okunishi, E.; Kondo, Y.; Ikuhara, Y. Dynamics of Annular Bright Field Imaging in Scanning Transmission Electron Microscopy. *Ultramicroscopy* **2010**, 110, 903–923.

(7) Stadelmann, P. A. EMS-A Software Package for Electron Diffraction Analysis and HREM Image Simulation in Materials Science. *Ultramicroscopy* **1987**, 21, 131–145.

(8) Kirkland, E. J. Advanced Computing in Electron Microscopy (Second Edition), Springer, New York, **2010**.

(9) Kresse, G.; Hafner, J. Ab Initio Molecular-Dynamics Simulation of the Liquid-Metal–Amorphous-Semiconductor Transition in Germanium. *Phys. Rev. B* **1994**, 49, 14251–14271.

(10) Kresse, G.; Furthmuller, J. Efficient Iterative Schemes for ab Initio Total-Energy Calculations Using a Plane-Wave Basis Set. *Phys. Rev. B* **1996**, 54, 11169–11186.

(11) Bloechl, P. E. Projector Augmented-Wave Method. *Phys. Rev. B* **1994**, 50, 17953–17979.

(12) Perdew, J. P.; Ernzerhof, M.; Rationale for Mixing Exact Exchange with Density Functional Approximations. *Chem. Phys.* **1996**, 105, 9982.

(13) Grimme, S.; Ehrlich, S.; Goerigk, L. Effect of the Damping Function in Dispersion Corrected Density Functional Theory. *J. Comput. Chem.* **2011**, 32, 1456–1465.

(14) Dawson, W. G.; Bullett, D. W. Electronic structure and crystallography of $MoTe_2$ and WTe_2. *J. Phys. C.* **1987**, 20, 6159.

(15) Qi, Y.; Naumov, P. G.; Ali, M. G.; Rajamathi, C. R.; Schnelle, W.; Barkalov, O.; Hanfland, M.; Wu, S.; Shekhar, C.; Sun, Y.; Su, V.; Schmidt, M.; Schwarz, U.; Pippel, E.; Werner, P.; Hillebrand, R.; Forster, T.; Kampert, E.; Parkin, S.; Cava, R. J.; Felser, C.; Yan, B.; Medvedev, S. A. Superconductivity in Weyl semimetal candidate $MoTe_2$. *Nat Commun.* **2016**, 7, 11038.

(16) Kresse, G.; Hafner, J. Ab Initio Molecular Dynamics for Liquid Metals. *J. Phys. Rev. B* **1993**, 47, 558–561.

(17) Kresse, G.; Furthmmuller, J. Efficiency of Ab-initio Total Energy Calculations for Metals and Semiconductors using a Plane-Wave Basis Set. *Comput. Mater. Sci.* **1996**, 6, 15–50.

(18) Grimme, S.; Antony, J.; Ehrlich, S.; Krieg, H. A Consistent and Accurate Ab-initio Parametrization of Density Functional Dispersion Correction (DFT-D) for the 94 Elements H-Pu. *J. Chem. Phys.* **2010**, 132, 154104.

CHAPTER 4

High-performance lithium-ion batteries using layered 2H-$MoTe_2$ as the anode

"This chapter introduces the semiconducting 2H-phase of the $MoTe_2$ that is synthesized by a solid-state route as the anode material in LIBs. In situ X-ray absorption near-edge structures (XANES) was performed to reveal the unique lithium reaction pathway and storage mechanism, which were further complemented by density functional theory calculations and the corresponding full-cell prototype study."

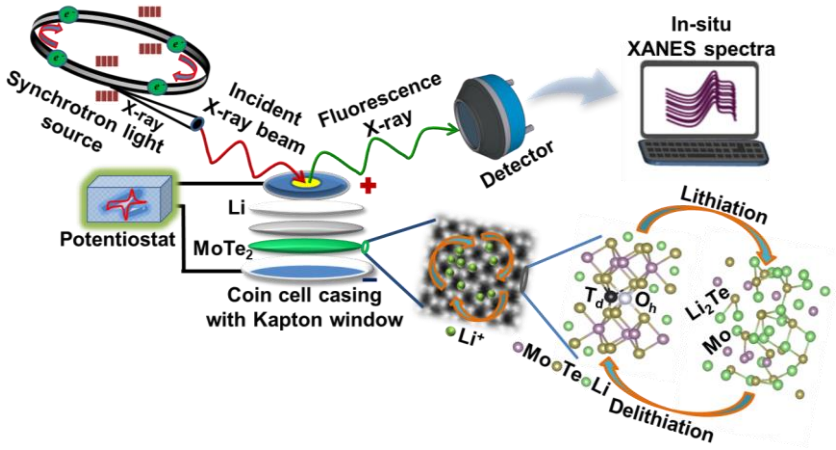

*An excerpt from this chapter has been published in ***Small***, 2020, 16, 2002669.

4.1 Introduction

Molybdenum-based $MoTe_2$ is a fascinating TMD, because it is a polymorphic material that can exist both in a hexagonal semiconducting (2H) phase and a monoclinic semi-metallic (1T') phase.[1,2] Due to its unique structure and tunable properties, it has been examined as a candidate in microelectronics, microwave sensors, telecom and supercapacitor applications.[3–5] Although the energy difference between the 2H- and the 1T'-$MoTe_2$ phases is ≈35 m eV, 2H-$MoTe_2$ with a bandgap of ≈1.0 eV is the thermodynamically more stable phase, and it is much easier to prepare than the 1T' phase.[2,6–8] The structure variance between the 2H and the 1T' phases arises from the spatial arrangement of Te atoms and native tellurium defects, which results in an efficient conversion reaction and faster Li^+ diffusion.[9] In addition, it has been seen that the 2H-$MoTe_2$ has weak interlayer interaction, which leads to a comparatively larger interlayer spacing. This may result in higher electronic conductivity and faster Li^+ insertion and deinsertion than any other TMDCs structures, when used as a LIB anode.[7,10–12] Several recent reports describe the use of the 2H-$MoTe_2$ as an anode in sodium-ion battery applications.[6,7,12] In addition, in LIB applications, Ma et al. reported the use of an anode that has a few layers of graphene along with the 1T'-$MoTe_2$.[9] Hence, we believe that 2H-$MoTe_2$, which is studied in this work, has a few advantages over the 1T'-$MoTe_2$ structure, and it can be used as an efficient anode in LIB applications.

In this work, we report a 2D layered 2H-$MoTe_2$ that is prepared by a simple solid-state synthesis process as an efficient reversible lithium-storage anode material for LIBs. The as-prepared bulk $MoTe_2$ is characterized by scanning transmission electron microscopy (STEM), which confirms the hexagonal structure and an almost perfect regular stacking of the layers. The as-prepared bulk $MoTe_2$ anode shows stable electrochemical lithium-storage in a half-cell configuration; it also exhibits an initial specific capacity of 432 mAh g^{-1}. The results of the in situ X-ray absorption near-edge structure (XANES) test confirm the reversibility and structural stability of the $MoTe_2$ during the lithiation/delithiation process. We use the density functional theory (DFT) to investigate the metastable intermediate phases (which are hard to observe at the small-time scale of the experimental measurements), the variation in charge distribution, and the crystal structure during the lithiation/delithiation process. This report provides combined experimental and theoretical results of the lithiation/delithiation process of the $MoTe_2$ layers. Further, we demonstrate a full-cell prototype by using our studied $MoTe_2$ anode along with the lithium cobalt oxide (LCO) cathode, which work at a nominal voltage of ≈2.1

V. The full cell has a reversible capacity retention of up to 100 cycles along with a high energy density of ≈454 Wh kg^{-1} (based on the $MoTe_2$ mass) at a current rate of 0.5 A g^{-1}. This study suggests that these 2D materials may have a great potential in energy-storage applications.

4.2 Synthesis of $MoTe_2$

The material was synthesized by mixing stoichiometric amounts of pure molybdenum (Sigma–Aldrich, 99.999 %) and tellurium (Sigma–Aldrich, 99.999 %) in a powder form in an inert atmosphere (inside the glove box, in an Ar atmosphere). After uniform grinding, the mixed powder was sealed in a quartz ampoule of a length of 80 mm (8 mm inner diameter) under vacuum, which was maintained at a pressure of 10^{-5} torr. After sealing, the precursor powder was introduced into a tubular furnace and sintered at a slow heating rate from room temperature to 800 ºC and held for 22 h at 800 ºC to complete the alloying reaction.[2,6,7]

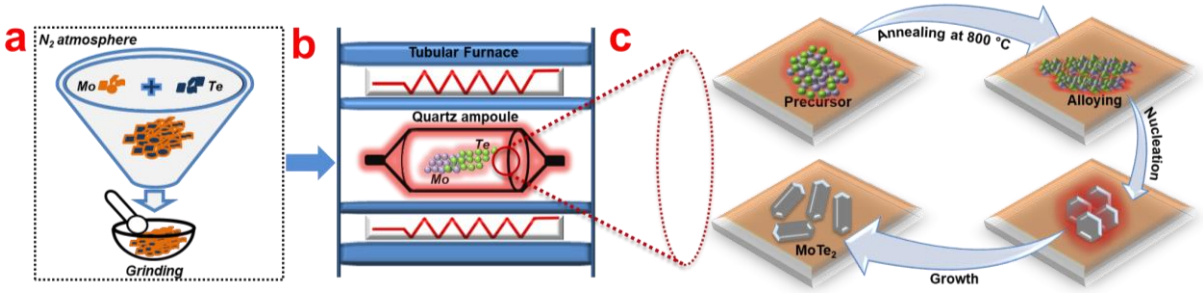

Figure 4.1 Preparation of $MoTe_2$ powders. (a–c) Schematic representation of $MoTe_2$ preparation and the growth process.

These procedures are schematically shown in **Figure 4.1a-c**. The as-formed black powder was uniformly ground before the characterizations and preparation of the slurry for electrode fabrications.

4.3 Results and discussion

Techniques such as X-ray diffraction (XRD), X-ray photoelectron spectroscopy (XPS), and electron microscopy have been performed for phase confirmation and morphologies of as-prepared samples. The surface chemical compositions as well as the reaction mechanisms of the cycled electrode samples were characterized by XPS in the ex situ mode. The in situ/operando synchrotron-based XANES characterization technique, the in situ cell configurations, and practical operating tips for cell design and experimental set-ups are discussed to provide valuable information about the lithiation/delithiation mechanism. Electrochemical measurements have been performed to inspect the performance of the system

and to explore the storage mechanism of Li^+ through kinetic studies. DFT calculations have been used to investigate the structural evolution of the lithiated and delithiated phases and charge distributions. This guides the atomic understanding of the reaction mechanism to match the experimental results.

4.3.1 Crystal structure and microstructural analysis of as-prepared $MoTe_2$

Figure 4.2 shows the powder XRD pattern fitted with the Rietveld refinement program.

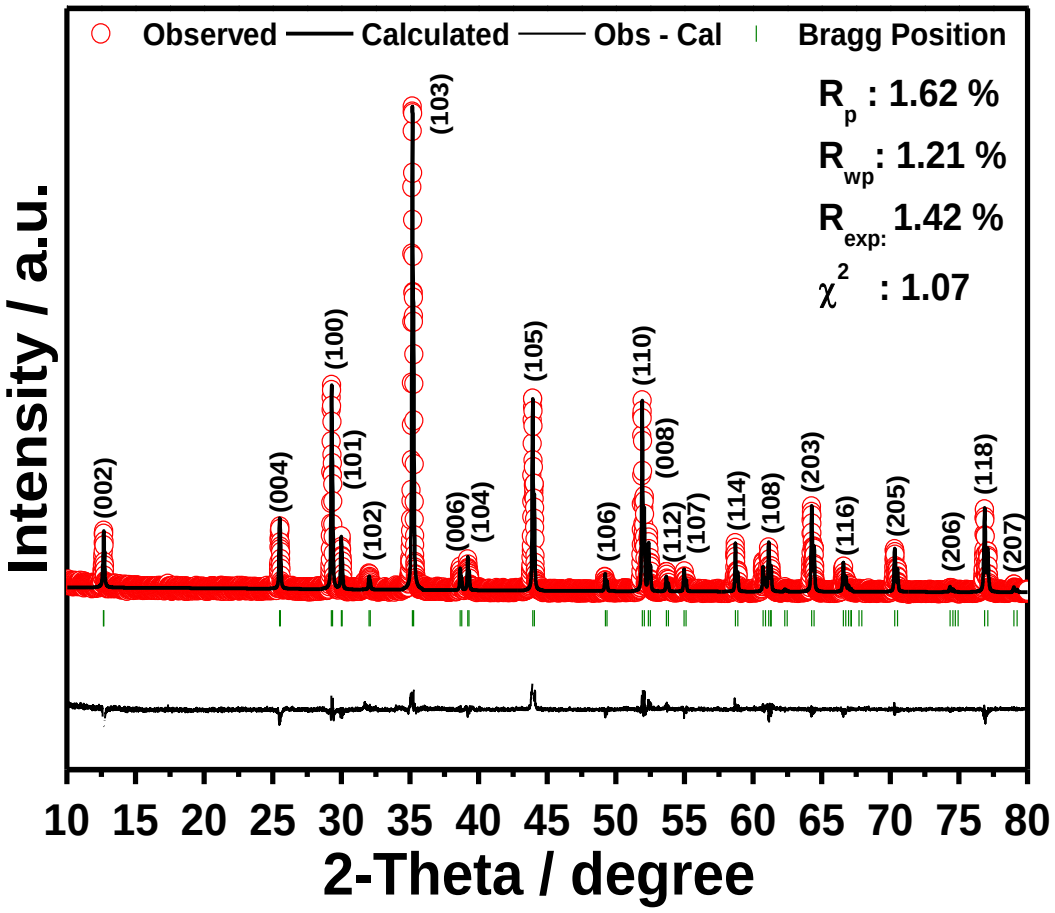

Figure 4.2 Powder XRD pattern and Rietveld refinement plot of as-synthesized $MoTe_2$ powders; the inset shows the fitted parameters.

The XRD pattern is fitted with the hexagonal structure and the $P6_3/mmc$ space group. The values of R factors and the goodness of fit (R_p: 1.62 %, R_{wp}: 1.21 %, R_{exp}: 1.42 % and χ^2: 1.07), which were found from the Rietveld refinement program, confirm the accuracy of the phase. The refined lattice constants (a = 3.518 Å, b = 3.518 Å, and c = 13.962 Å) are additionally shown to be in good agreement with the previous literature of the 2H-$MoTe_2$ phase.[7,12] Further,

we calculated the grain size by using the conventional Debye–Scherer formula.[7] The obtained grain size of ≈144 nm agreed well with the literature.[7]

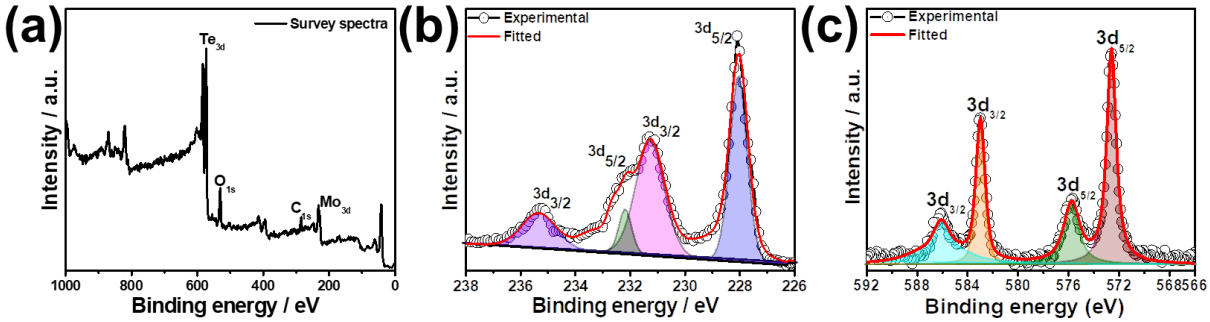

Figure 4.3 Structural characterization of as-synthesized $MoTe_2$ powders. (a) Survey spectra of the $MoTe_2$ powder sample. (b–c) Mo and Te HRXPS spectra of as-synthesized $MoTe_2$ powders.

Figure 4.3b, c shows the Mo and Te HRXPS spectra of the as-prepared $MoTe_2$ powder. The survey XPS spectrum is given in **Figure 4.3a**. The survey spectra confirm the presence of Mo, Te, and O in the sample. The Mo 3d HRXPS spectra, as shown in **Figure 4.3b**, show the major peaks at corresponding binding energies of 228.05 eV (Mo $3d_{5/2}$) and 231.26 eV (Mo $3d_{3/2}$). These energies are a confirmation of the 2H-$MoTe_2$ phase, according to the existing literature.[7,12–14] There are two additional XPS peaks at 232.16 (Mo $3d_{5/2}$) eV and 235.33 eV (Mo $3d_{3/2}$), which are due to the molybdenum oxide (MoO_3) phase that results from the formation of an oxide on the surface of the sample that is under air exposure, and the same feature is observed in the earlier literature.[12,14] **Figure 4.3c** shows that the Te 3d HRXPS spectra at 572.87 (Te $3d_{5/2}$) and 583.26 eV (Te $3d_{3/2}$) are the characteristic peaks of the 2H-$MoTe_2$.[7,12–14] The two additional peaks at 576.04 (Te $3d_{5/2}$) and 586.48 eV (Te $3d_{3/2}$) are due to the TeO_2 phase that results from air exposure.[12,14] The XRD and XPS results above confirm the phase purity of the 2H-$MoTe_2$ structure.

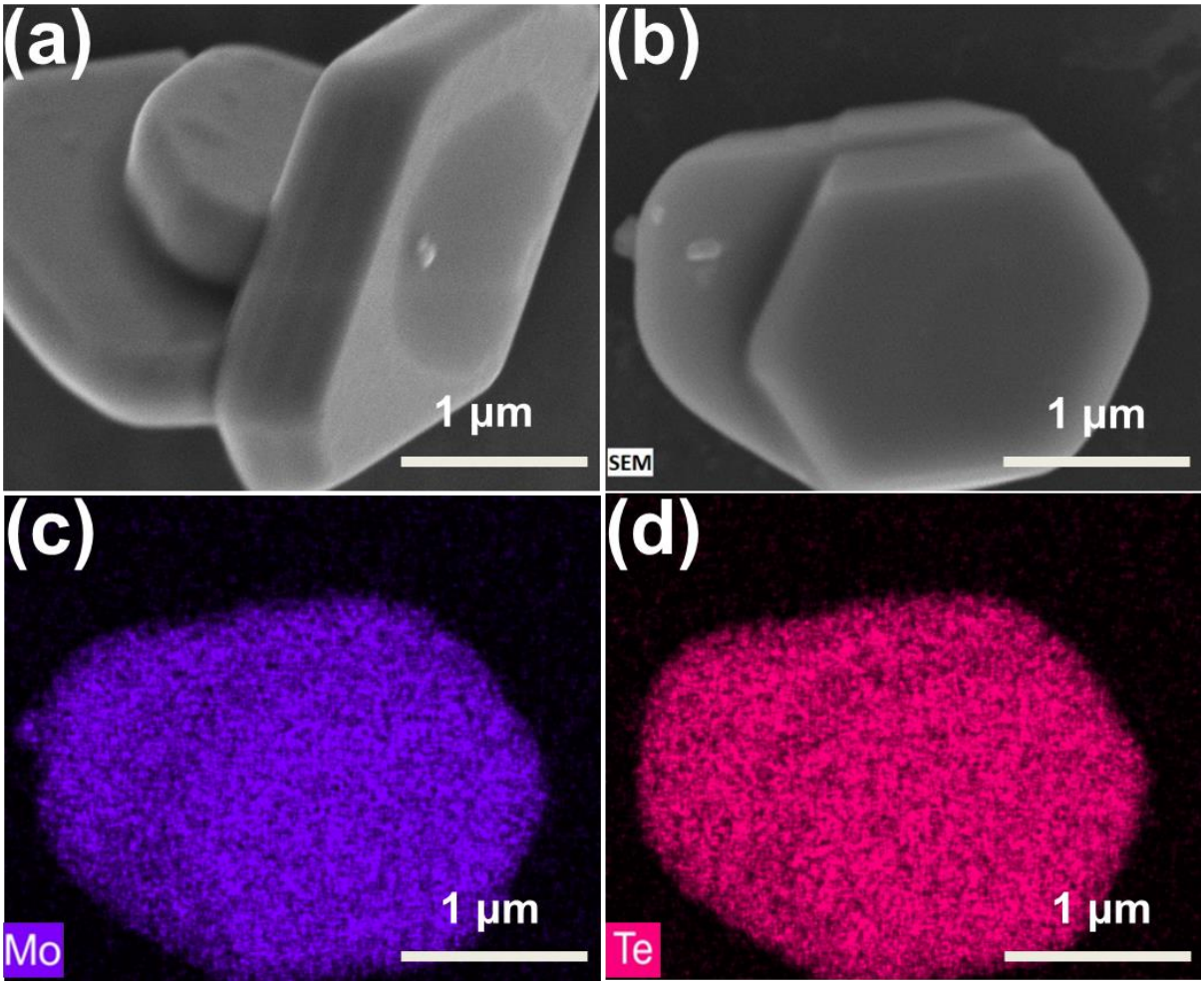

Figure 4.4 Electron microscopy studies of as-synthesized $MoTe_2$ powders. (a–b) Field-emission scanning electron microscopy image of the as-prepared $MoTe_2$ sample. (c–d) Energy dispersive X-ray mapping of the $MoTe_2$ powder sample.

Field-emission scanning electron microscopy (FESEM) images indicate a solid-hexagonal block type of morphology, as shown in **Figure 4.4a,b**. Elemental mapping by energy dispersive X-ray (EDX) confirms the composition of the as-prepared $MoTe_2$ powder, which is shown in **Figure 4.4c,d**. The atomic structure of the specimen is confirmed by aberration-corrected STEM. Bright-field (BF) and high angle annular dark-field (HAADF) STEM of the as-prepared $MoTe_2$ powder sample found that the majority of the crystals were multilayered within regions and that they had the distinctive hexagonal structure, as shown in **Figure 4.5a,b**. A combination of this with the selected area electron diffraction (SAED) pattern along the [0001] direction, as shown in **Figure 4.5d** of the indicated area (**Figure 4.5c**) and is consistent; this further confirms the 2H stacking of the $MoTe_2$ samples. Shown in **Figure 4.5e** is an edge-on view of the plate along the $[1\bar{1}00]$ direction. This shows that the layers have a spacing of

0.71 nm, which corresponds with the (0002) plane and is consistent with XRD results; this is additional direct evidence for the higher interlayer spacing.

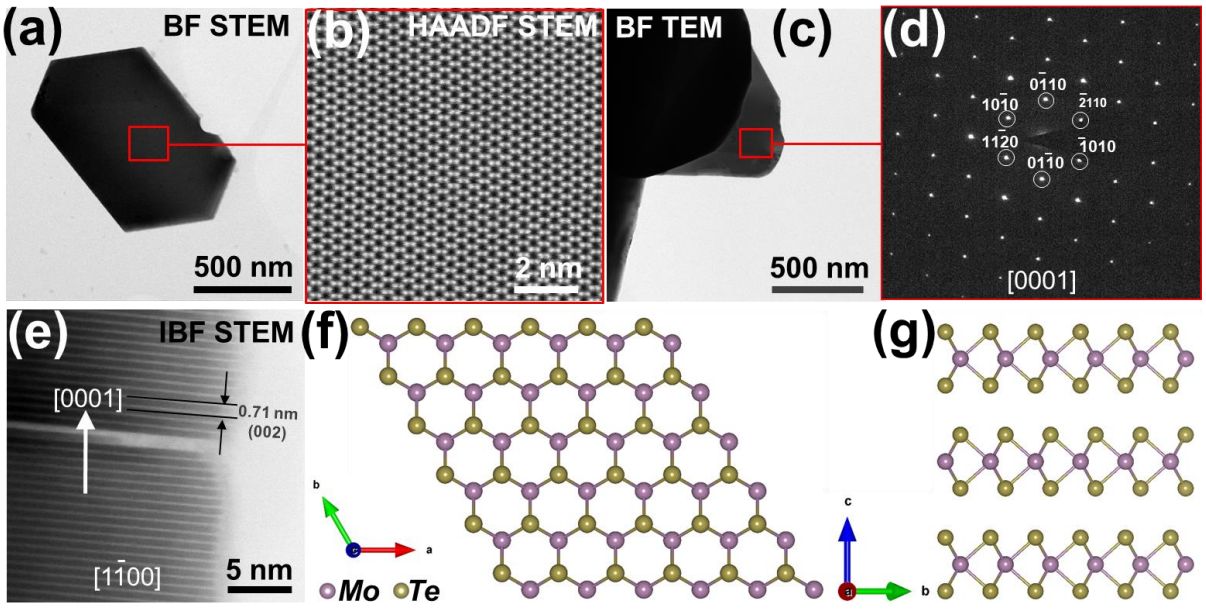

Figure 4.5 Electron microscopy studies of as-synthesized $MoTe_2$ powders. (a) BF-STEM image of a flat crystal showing the hexagonal structure. (b) atomic resolution HAADF images in the [0001] direction. (c) BF-TEM image and (d) SAD pattern from the indicated area in g). (e) IBF STEM images, along the [1$\bar{1}$00] direction, showing interlayer spacing in the order of 0.71 nm and error in layer stacking. (f–g) Model structure of $MoTe_2$ in the [1$\bar{1}$00] and [0001] directions, respectively.

Additionally, the novel feature of the $MoTe_2$ electrode in the lithiation/delithiation process further confirmed that the easiest path followed by the lithium the [0002] direction during the intercalation and deintercalation processes. Further, we have observed occasional missing layers, as shown in **Figure 4.5e**. This defect may be related to the Te vacancy of native tellurium defects, which are related to the efficient diffusion of Li^+ during the redox conversion reaction.[9] **Figure 4.5f,g** represents the model structures of $MoTe_2$ in the [1$\bar{1}$00] and [0001] directions, respectively.

4.3.2 Half-cell electrochemical measurements

Electrochemical measurements were performed to understand the suitability of $MoTe_2$ in LIB applications. The lithiation and delithiation mechanisms and performance studies of the 2H-$MoTe_2$ have not been determined or carried out by previous studies. The electrochemical

reaction of the $MoTe_2$ for Li^+ storage was adapted from the recent report against Na^+ [7,12] and 1T'-$MoTe_2$ by Ma et al. for LIBs as the reference.[9]Additionally, we have considered as references the mechanism that was followed by other chalcogenides, namely, MoS_2,[10,15] $MoSe_2$,[11,16] WS_2,[17] WSe_2,[18,19] and WTe_2,[20,21] because their crystal structures are similar to that of the $MoTe_2$. Additional emphasis is placed on the delithiation mechanism, which we have explored in this work through the in situ XANES analysis that is supplemented by DFT.

A CV study of the $MoTe_2$ electrode against lithium metal in the voltage window of 0.01V–3.00 V at a scan rate of 0.05 mV s^{-1} was carried out to understand the redox activity of the $MoTe_2$, as shown in **Figure 4.6a**. In the first cathodic scan, two broad peaks were seen between 1.5 and 0.9 V (in the magnified region in **Figure 4.6b**), which conforms to the intercalation of Li^+ into the $MoTe_2$ lattice to form the Li_xMoTe_2 structure.

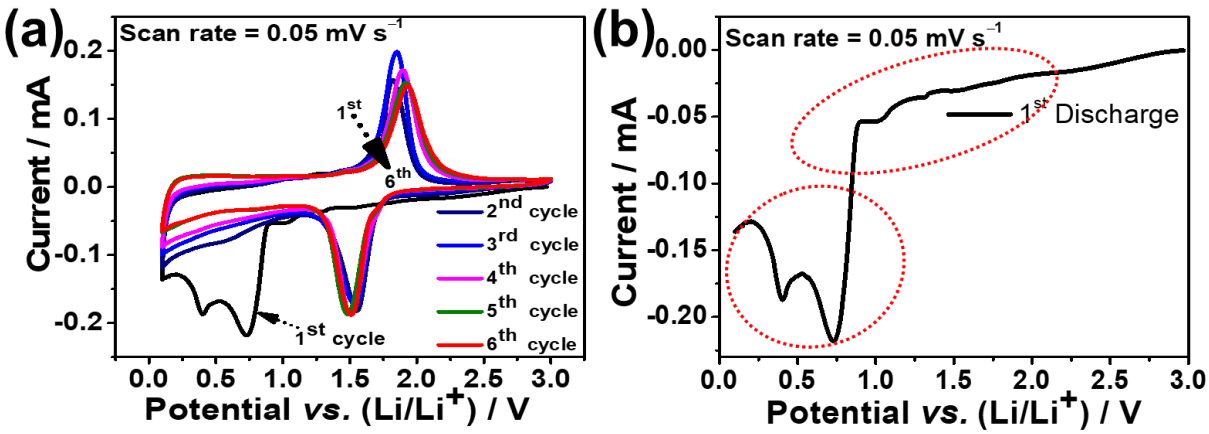

Figure 4.6 The electrochemical performance of the $MoTe_2$ anode in a half-cell configuration (against lithium metal). (a) CV of the $MoTe_2$ electrode at 0.05 mV s^{-1} in the voltage range of 0.01 to 3.00 V. (b). Magnified CV of the $MoTe_2$ electrode at 0.05 mV s^{-1} during the first discharge.

A sharp peak is observed at 0.72 V, which is followed by a small peak at 0.4 V. The sharp peak is due to the conversion of $MoTe_2$ to Mo and Li_2Te, and the solid-electrolyte interphase (SEI) formation with the lithium metal during the first discharge process.[7,9,12] In the higher cycle, the cathodic peaks are shifted to ≈1.5 V due to the decrease in electronic polarization that results from the distortion of the $MoTe_2$ lattice.[9] The sharp anodic peak at ≈1.82 V corresponds to the reconstitution of Mo and Li_2Te to form the $MoTe_2$ structure, which is confirmed by the succeeding cycles; and is highly reversible. The consistent nature of the CV curve from the second cycle onward confirms the high structural stability of the $MoTe_2$ anode during the lithiation/delithiation process.

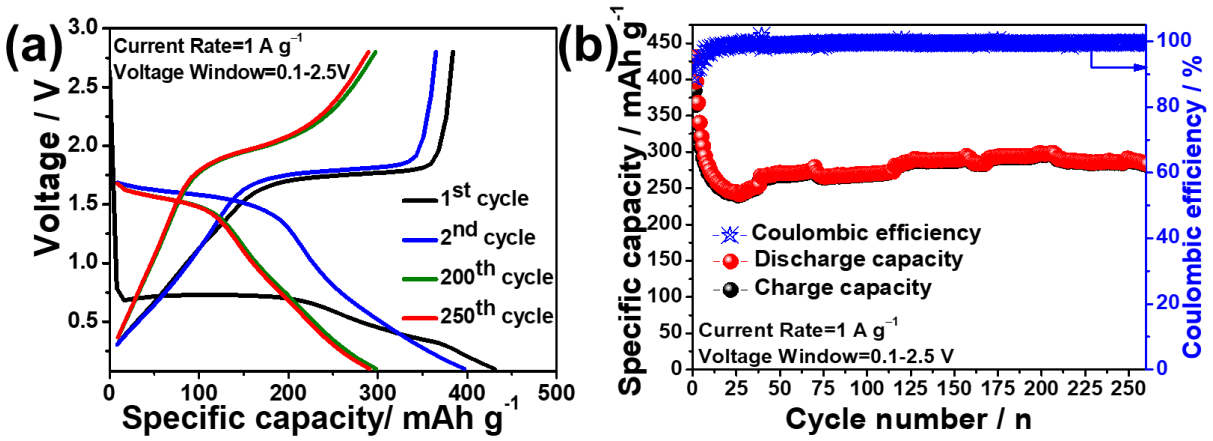

Figure 4.7 The electrochemical performance of the $MoTe_2$ anode in a half-cell configuration (against lithium metal). (a) Galvanostatic charge/discharge curves versus specific capacity of $MoTe_2$ electrodes at 1 A g^{-1} in the voltage range of 0.01 to 2.8 V. (b) The cycling performance of the $MoTe_2$ electrode at a current rate of 1 A g^{-1} over 250 cycles.

To determine the charge-storage capacity of the $MoTe_2$, galvanostatic discharge/charge tests were performed at a current rate of 1 A g^{-1}, as shown in **Figure 4.7b**. The observed plateaus corresponded to the discharge/charge profiles, which resembled those of the CV curve, as shown in **Figure 4.6a**. The initial discharge capacity of 432 mAh g^{-1}, which corresponded to a charge capacity of 385 mAh g^{-1}, was achieved at a current rate of 1 A g^{-1} with a Coulombic efficiency of 89 %. In the second cycle, a discharge capacity of 396 mAh g^{-1} and a charge capacity of 364 mAh g^{-1} was achieved (**Figure 4.7a**); there was also an increase of 92 % in the Coulombic efficiency with reference to the first cycle (89 %). The increase in the electrochemical performance may be attributed to the high specific surface area, which provided more active sites to $MoTe_2$, and enhanced the rate of electrochemical reactions. A fast capacity fading during the initial cycles was observed, which occurred because the layered $MoTe_2$ underwent a conversion reaction ($MoTe_2 + 4Li^+ + 4e^- \rightarrow Mo + 2Li_2Te$). The Mo nanoparticles that were formed during the discharge process were prone to aggregation. The volume change induced the re-exposure of the fresh electrode surface to the electrolyte and to the reconstruction of the SEI layer, which resulted in further decomposition of the electrolyte. The organic solvent in $LiPF_6$-based electrolytes were spontaneously reduced into the organic Li interphase at the expense of intercalated Li-ions in the near-surface region.[9,15,22] The $MoTe_2$/electrolyte reduction reaction resulted in a gel-like polymeric layer from electrochemically driven electrolyte degradation, which, leads to the formation of a thick SEI film. The large initial capacity loss of the $MoTe_2$ anode can be assigned to the consumption of

Li^+ for the formation of the SEI layer upon first discharge, which results in fast capacity fading and low Coulombic efficiency.[22]

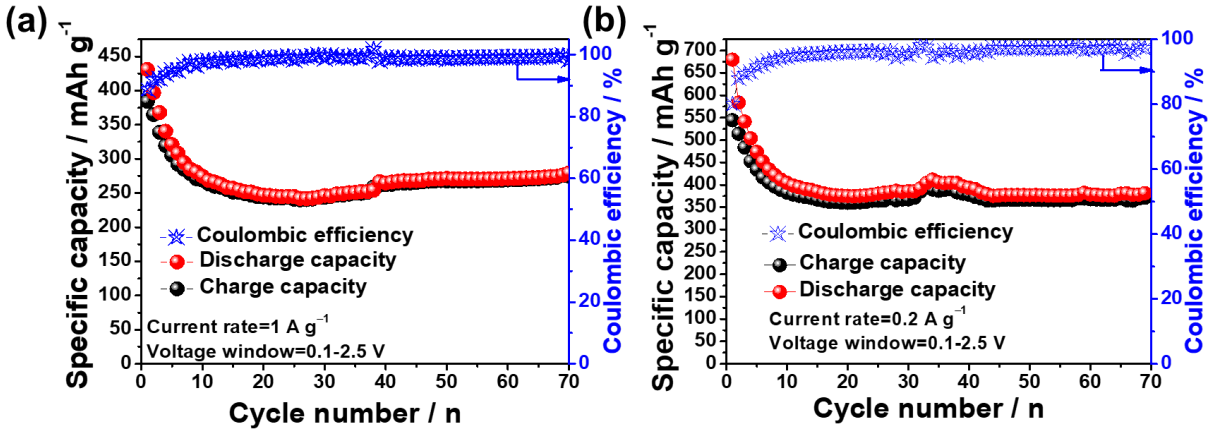

Figure 4.8 The cycling performance of the $MoTe_2$anode in a half-cell configuration at (a) a current rate of 1 A g^{-1} and at (b) a current rate of 0.2 A g^{-1} for the initial 70 cycles at 20 ± 2 ºC.

The electrode that was cycled at a low current (200 mA g^{-1}) rate also exhibited a similar type of capacity fading (as shown in **Figure 4.8a,b**), which confirmed the inherent property of the pristine $MoTe_2$, as observed in other Mo-based chalcogenides.[22–24]

Table 4.1 Percentage of capacity retention and decay rate for the initial 25 cycles of the $MoTe_2$ anode against lithium.

	Capacity retention (%)		**Decay rate**	
	Current rate 1 A g^{-1}	**Current rate 0.2 A g^{-1}**	**Current rate 1 A g^{-1}**	**Current rate 0.2 A g^{-1}**
3rd cycle	92.93	92.64	2.36	2.45
5th cycle	81.06	80.99	3.79	3.80
8th cycle	71.97	72.26	3.50	3.47
11th cycle	67.93	68.15	2.92	2.90
14th cycle	65.15	66.61	2.49	2.39
17th cycle	63.64	64.73	2.14	2.10
20th cycle	62.37	64.21	1.88	1.79
25th cycle	61.89	65.11	1.53	1.40

*Capacity retention when compared with the 2nd cycle discharge capacity

*Decay per cycle = [Capacity at nth cycle - Capacity at 2nd cycle] x 100 / [Capacity of 2nd cycle x Cycle number, that is, n]

A comparative study between the low (0.2 A g^{-1}) and high currents (1 A g^{-1}) is given in **Table 4.1**, for the initial 25 cycles. The results in **Table 4.1** confirm that at a low current, the steep

capacity retention was in the same order as that of at a high current rate. The capacity decay rate was also in the same order for both high and low current rates. Several studies have shown that the steep capacity fading, cycling stability, and rate performance can be improved by exfoliation[23] and by assimilating Mo-based chalcogenides with other nanostructure metal oxides[24] and carbonaceous conducting materials such as graphene, carbon nanotubes, and the like[25,26] The addition of these materials in the composite structure could enhance the chemical stability of electronic conductivity and reduce the aggregation of discharge products, which significantly improve the Li-ion mobility and result in the enhancement of electrochemical properties.[22] The high reversibility of the material was further verified by the long-term cycling performance, as shown in **Figure 4.7b**. A discharge capacity of 291 mAh g^{-1} was observed over 260 cycles, which showed capacity retention of 73.5 % (when compared with the second cycle discharge capacity) at a high current rate of 1 A g^{-1}.

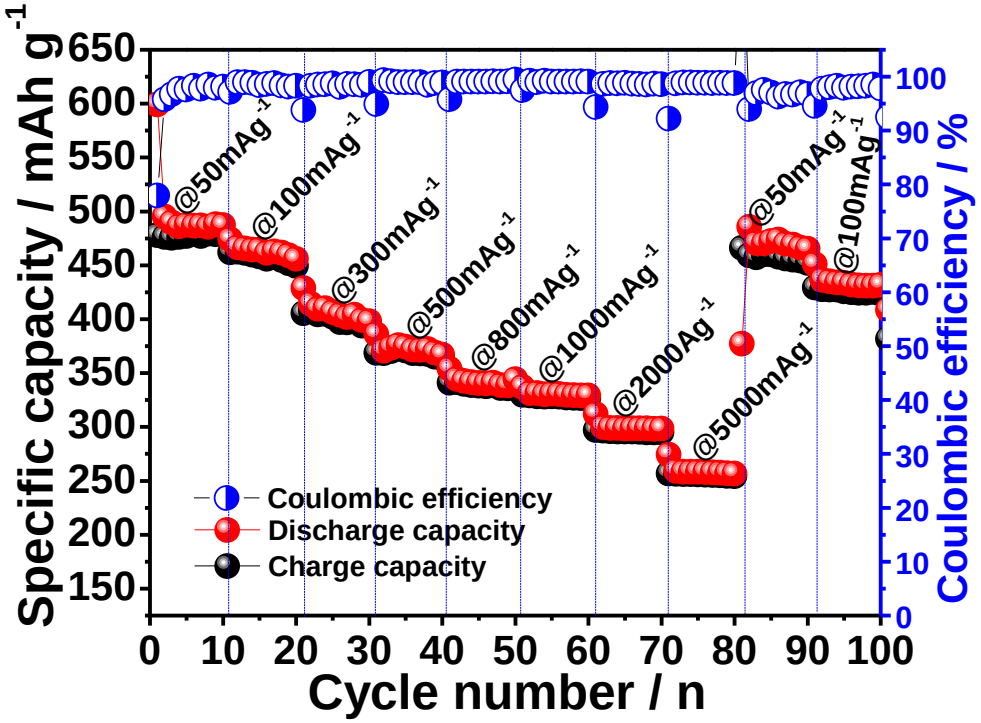

Figure 4.9 Rate performance along with the Coulombic efficiencies of the $MoTe_2$ anode in a half-cell configuration at different rates.

Figure 4.9 shows the rate capability of the half-cell configuration. The $MoTe_2$ exhibited specific capacities of 488, 465, 410,375, 342, 330, 298, and 258 mAh g^{-1} at respective current densities of 50 mA g^{-1}, 100 mA g^{-1}, 300 mA g^{-1}, 500 mA g^{-1}, 800 mA g^{-1}, 1 A g^{-1}, 2 A g^{-1}, and 5 A g^{-1}, which confirmed the suitability of the $MoTe_2$ anode at various currents. **Table 4.2** shows a comparison between our 2H-$MoTe_2$ pristine anode (without further surface

modification or a carbon additive) and the conventional Mo-based anode materials (MoO_3, Mo chalcogenides, and composites) that have been reported in the literature. The pristine 2H-$MoTe_2$ showed superior specific capacity and stability at a higher current rate. The results presented in **Table 4.2** strongly suggest the superiority of using the $MoTe_2$ as the anode for LIBs in terms of capacity and stability, which are two critical aspects of LIBs. It may be noted that the observed reversible specific capacity of the $MoTe_2$ electrode is much higher than the theoretical capacity, which is calculated by assuming 4 mols of Li^+ for 1 mol of $MoTe_2 \approx 305.4$ mAh g^{-1}.[7,9,12] This is despite the fact that, in the case of other TMDs, the same trend of a higher specific capacity than the theoretical capacity is observed.[7,9,12,27] There are a number of possible reasons for this discrepancy.

Table 4.2 A comparison of the conventional layered anode and our $MoTe_2$ anode configuration.

Anode Material	**Current rate**	**Discharging Capacity (mAh g^{-1})**	**Cycling retention**	**Reference**
Pristine MoO_3	0.1 A g^{-1}	650	50	28
Carbon-based MoO_3 nanostructures	0.75 C	373	400	29
SWNT-bridged MoO_3 structure	0.1 A g^{-1}	865	100	30
MoO_2-porous carbon hollow spheres	0.05 A g^{-1}	640	80	31
MoO_2–carbon nanowires	0.2 A g^{-1}	500	20	32
MoS_2@$Ti_3C_2T_x$	1 A g^{-1}	132	275	33
MoS_2/partially oxidized $Ti_3C_2T_x$	0.5 A g^{-1}	230	50	34
Hierarchical MoS_2 microspheres	1A g^{-1}	353	70	35
$MoSe_2$/C	0.1 A g^{-1}	576	50	36
Pristine $MoTe_2$	**1 A g^{-1}**	**432**	**260**	**(Present work)**

The most likely reasons are the pseudocapacitive behavior of TMDs at lower potentials,[7,9,16,37] and the job-sharing mechanism between Mo nanoparticles and Li during conversion reaction.[9,15] The formation of the gel-like polymer film (shown in **Figure 4.10b**, for the

electrode after full-discharge) due to a high surface area and more active sites causes the decomposition of electrolytes during the electrochemical reaction. The possible interfacial sites and vacancies in the $MoTe_2$ blocks (shown in **Figure 4.5e**) further enhance the electrochemical reactions.[9,38] The morphology of the pristine material and the presence of tellurium vacancies may have an impact during electrochemical cycling, because they provide more active sites due to exfoliation of the parent structure.[9,27] These results show that $MoTe_2$ is a strong potential candidate in LIB applications.

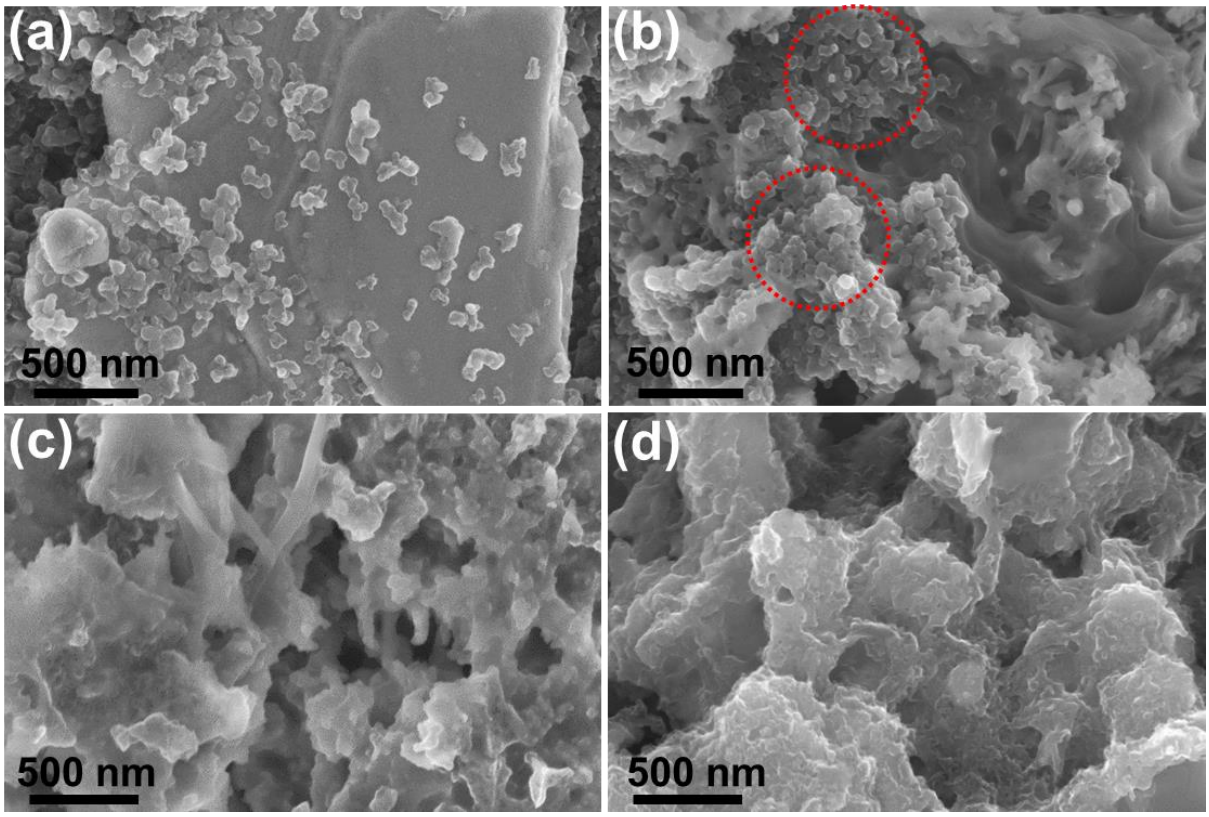

Figure 4.10 FESEM image of (a) $MoTe_2$ as-prepared electrode (b) after full discharge (c) after 1st cycle fully charged state (d) after 5th cycle fully charged state.

4.3.3 In situ electrochemical impedance spectroscopy and calculation of Li^+ diffusion coefficients (D_{Li+})

Kinetic Li^+ transport studies of the MoT_2 electrode were performed during the lithiation and delithiation process by CV experiments, which were performed at different scan rates, as shown in **Figure 4.11a**. In order to understand the diffusive and capacitive nature of the $MoTe_2$ electrode, CV experiments were performed at scan rates between 0.01 and 1 mV s^{-1} in the voltage range of 0.01 to 3 V. An increasing trend of peak intensities has been observed at a higher current rate, which corresponds to both anodic and cathodic reactions. Simultaneously,

there is an anodic peak shift toward the higher potentials and a cathodic peak shift toward the lower potentials, as shown in **Figure 4.11a**.

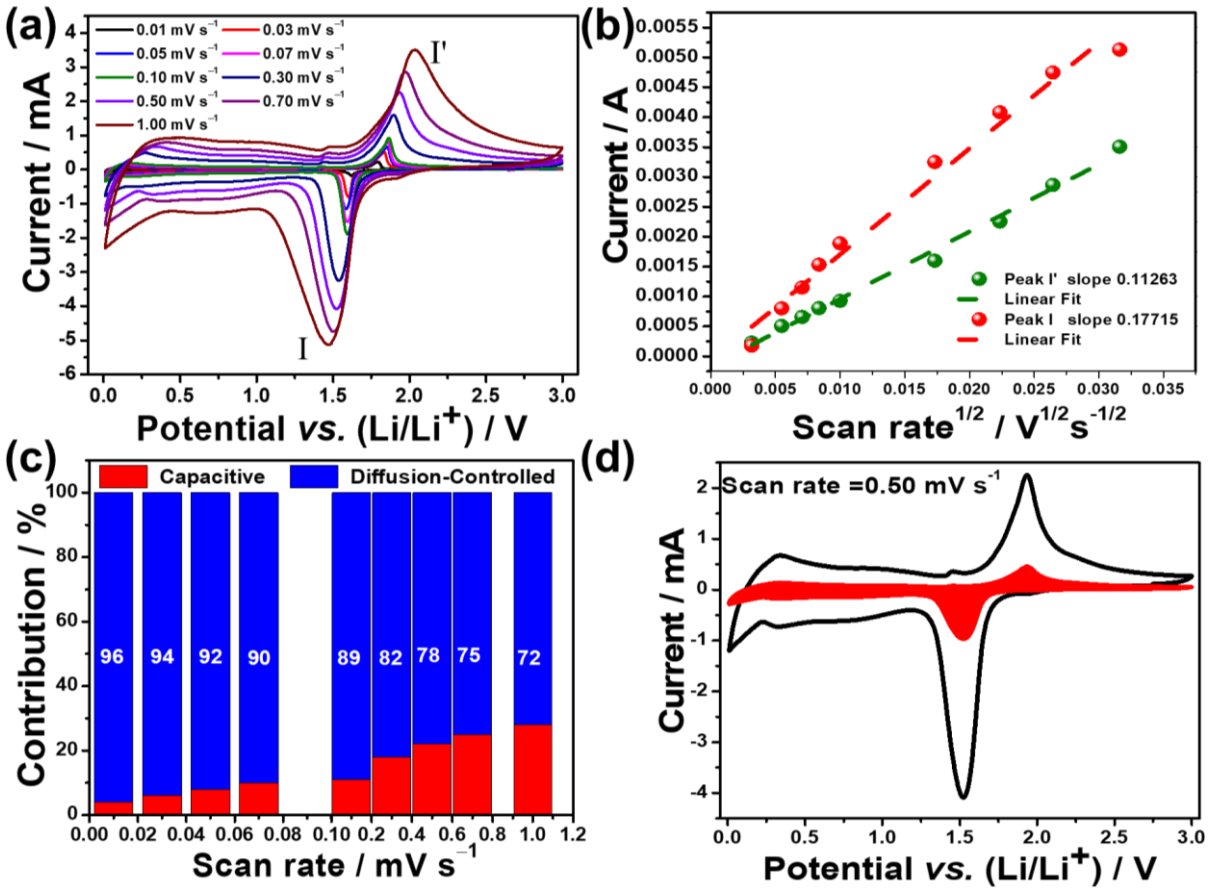

Figure 4.11 Li^+ diffusion coefficients (D_{Li+}), kinetics and quantitative analysis of the storage mechanism of Li^+ in the $MoTe_2$ electrode. (a) The CV of the $MoTe_2$ electrode at different scan rates. (b) The peak current versus the square root of the scan rate of the reduction (I) and oxidation (I') peaks. (c) The ratio of the pseudocapacitive (red) and diffusion-controlled (blue) capacities of the $MoTe_2$ electrode at different scan rates. (d) Fitted pseudocapacitive contribution (red area) of the $MoTe_2$ electrode at 0.50 mV s^{-1}.

The observed features follow the power-law ($i_p = av^b$). From the graph between log i_p versus log v, the obtained values of b are ≈0.5689 and ≈0.6634, which correspond to the redox peaks, I and I', as shown in **Figure 4.15a**. The obtained b-values illustrate the Li^+ storage in the $MoTe_2$ electrode that is dominated by diffusion-controlled reactions as opposed to surface-controlled reactions.[7] At high current, the electrochemical properties show a pseudocapacitance process, as can be seen from rate studies. This is a result of both capacitive and diffusion-controlled Li^+ insertion.[7,26,39]

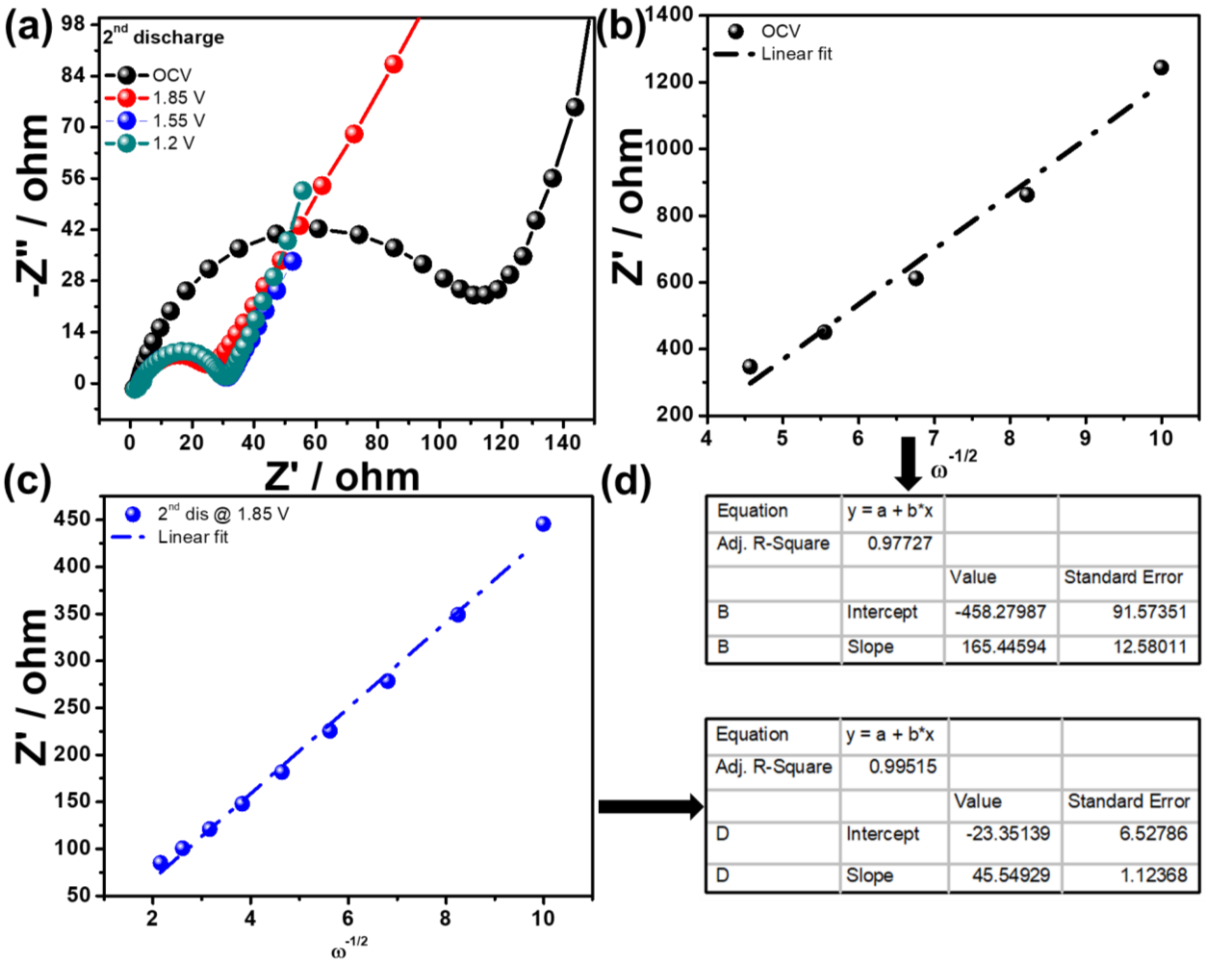

Figure 4.12 Li^+ diffusion coefficients (D_{Li+}), kinetics and quantitative analysis of the storage mechanism of Li^+ in the $MoTe_2$ electrode. (a–f) Nyquist plots and fitting results at different discharge voltages of the $MoTe_2$ electrode during the 2nd cycle of the $MoTe_2$ electrode.

The capacitive and diffusion-controlled Li^+ insertion process has been calculated from the equation, $i(V) = k_1v + k_2v^{1/2}$, where i(V) is related to the total current contributions that can be split into k_1v (capacitive contribution by the surface) and $k_2v^{1/2}$ (diffusion-controlled insertion). From the value of k_1 and k_2 from the straight-line fit between $v^{1/2}$ versus different scanning rates, which corresponded to the reduction peak (I) and the oxidation peak (I'), as shown in **Figure 4.11b**, the values of the diffusive contribution capacity with an increasing scan rate were calculated. At 0.01 mV s^{-1}, the obtained Li^+ capacitive contribution was only ≈4 %, which increased to ≈28 % at 1 mV s^{-1}.

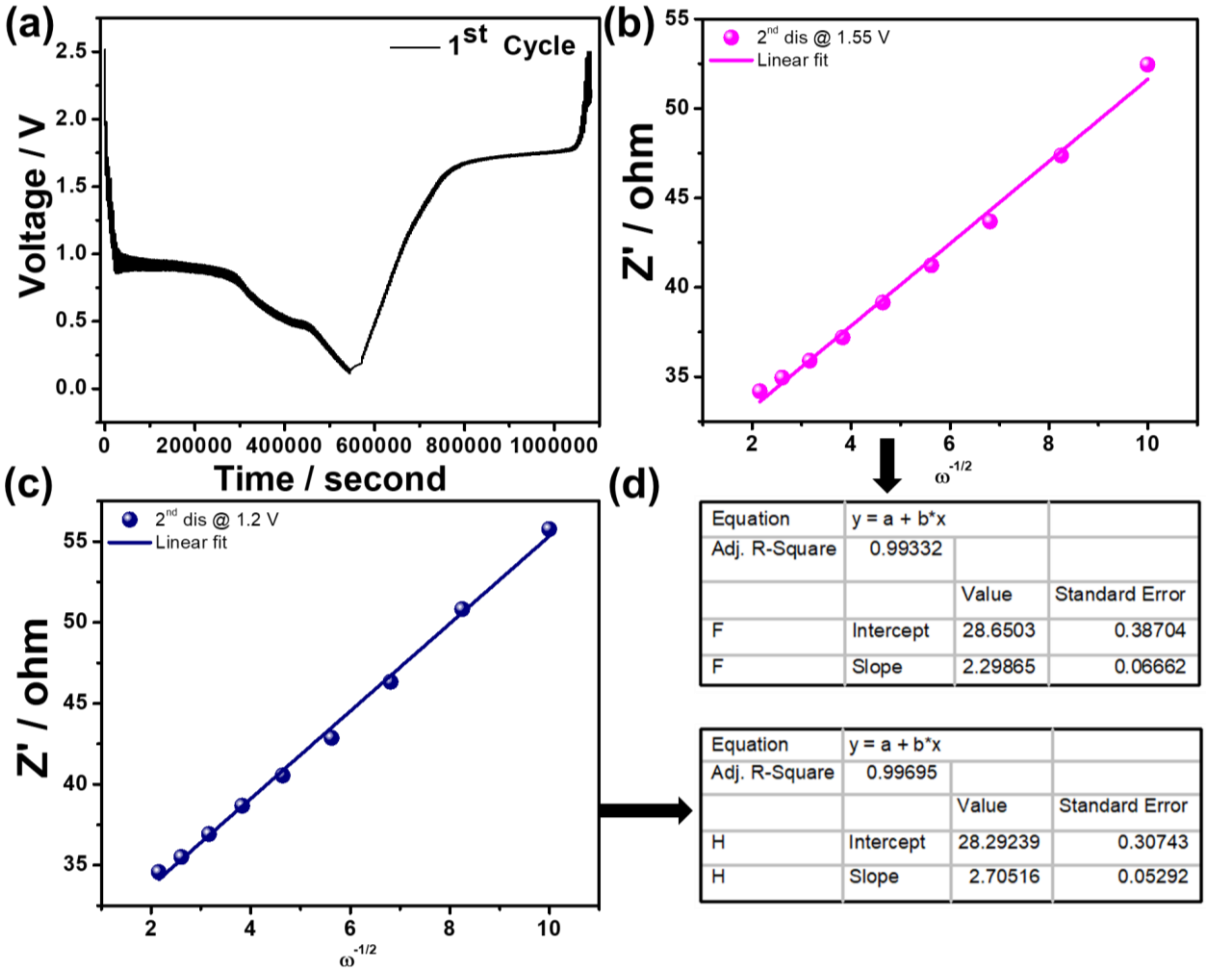

Figure 4.13 Li^+ diffusion coefficients (D_{Li+}), kinetics and quantitative analysis of the storage mechanism of Li^+ in the $MoTe_2$ electrode. (a–f) Nyquist plots and fitting results at different discharge voltages of the $MoTe_2$ electrode during the 2nd cycle of the $MoTe_2$ electrode.

Further, a capacitive contribution of 4 %, 6 %, 8 %, 10 %, 11 %, 18 %, 22 %, 25 %, and 28 % at the scan rates of 0.01, 0.03, 0.05, 0.07, 0.10, 0.30, 0.50, 0.07, and 1.00 mV s^{-1}, respectively, were observed, as revealed in **Figure 4.11c**. These results show the dominance of capacitive contribution at higher currents. **Figure 4.11d** shows the fitted CV curve at a scan rate of 0.05 mV s^{-1}, where the shaded red region (8 %) that indicates the total Li^+ storage capacity arises from the capacitive behavior of the MoT_2 electrode. At higher current, the utilized electrodes require a large volume with a high specific surface area to enhance the capacitance. Subsequently, the reduction in the size of microsupercapacitors led to a great decline in the energy-storage performance.

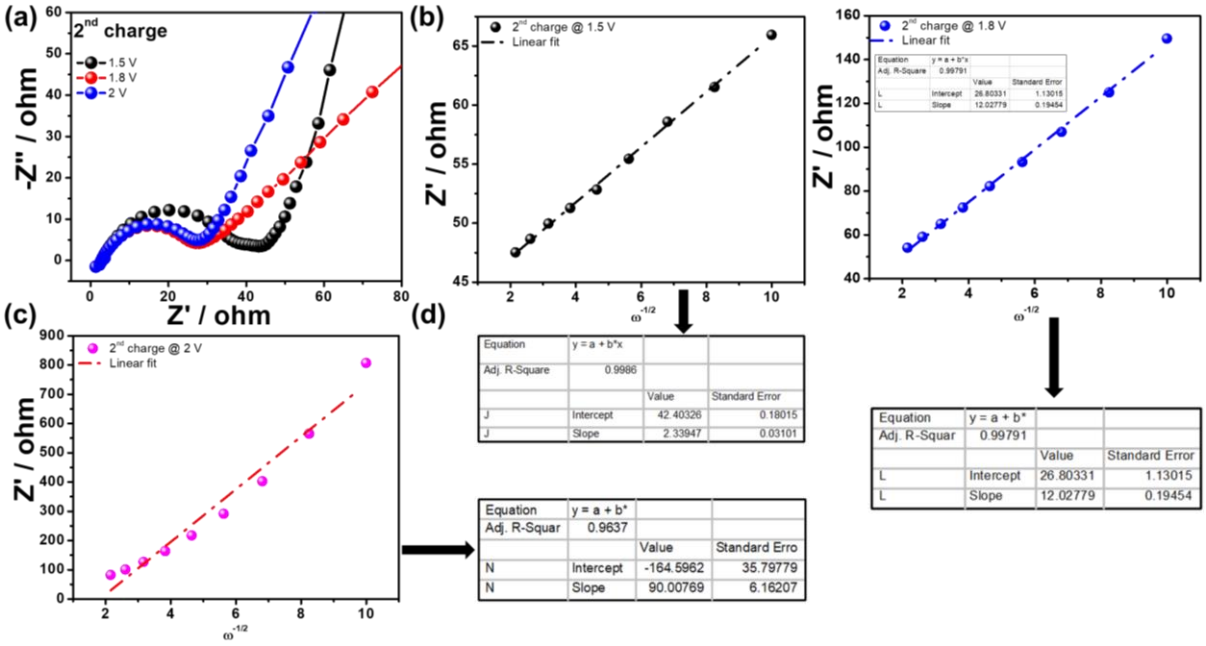

Figure 4.14 Li^+ diffusion coefficients (D_{Li+}), kinetics and a quantitative analysis of the storage mechanism of Li^+ in the $MoTe_2$ electrode. (a–d) Nyquist plots and fitting results at different charge voltages of the $MoTe_2$ electrode during the 2nd cycle of the $MoTe_2$ electrode.

As shown in **Figure 4.11a**, the CV curves of the $MoTe_2$ electrode at various sweeping rates further disclose the cause of the higher rate performance at a lower current rate due to low capacitive contribution. The low capacitive contribution results in higher Coulombic efficiency and less irreversible loss, which enhances the long cycling performance; however, the low capacity contribution restricts the rate capability. The properties discussed at various currents during the insertion of Li^+ into $MoTe_2$ electrodes indicate that the transport, storage, and mobility of the Li^+ are due to the active diffusion-controlled storage, which is related to the challenge to achieve higher energy density at the higher current rate.[40,41] A similar phenomenon was observed in other 2D chalcogenides.[7,26] Further, the Randles–Sevcik equation was implemented to calculate the Li^+ apparent diffusion coefficient (Equation (1)).

$$i_p = 0.4463n^{3/2}F^{3/2}CARF^{-1/2}T^{-1/2}FD_{cv}V^{1/2}F \quad (1)$$

where i_p is the peak current; n is the number of electrons; F corresponds to Faraday's constant (96485 C mol^{-1}); C represents the bulk concentration (mol cm^{-3}); The concentration of Li (C) taken is 1.8359×10^{-2} mole/cm^3. A represents the area of the electrode (cm^2); R represents the gas constant (8.314 J mol^{-1} K^{-1}); T represents the absolute temperature (K), D_{cv}, which is the diffusion coefficient (cm^2 s^{-1}) that corresponds to the Li^+ apparent diffusion coefficient; and V corresponds to the potential scan rate (mV s^{-1}), as shown in **Figure 4.11a, b** and **Figure 4.15a**.

Table 4.3 CV results showing different scan rates of the $MoTe_2$ electrode.

Scan rate ($mV\ s^{-1}$)	Voltage values		
	V(I)	V(I')	V (II') (diff. between anodic and cathodic potential)
0.01	1.793	1.622	0.178
0.03	1.836	1.602	0.801
0.05	1.85	1.583	1.148
0.07	1.8545	1.596	1.53291
0.10	1.865	1.594	1.89
0.30	1.896	1.538	3.251
0.50	1.936	1.519	4.083
0.70	1.971	1.506	4.746
1.00	2.032	1.475	5.131
Diffusion coefficient ($D_{cv}\ Li^+ / Cm^2\ s^{-1}$)	2.11×10^{-9}	5.23×10^{-9}	

The denominations: V(I) is the oxidation peak voltage, V (I') is the reduction peak voltage, and V(II') is the difference between V(I) and V(I').

The values obtained for the Li^+ apparent diffusion coefficients (D_{Li+}) at different anodic and cathodic peaks were in the order of 10^{-9} (within the range of 2.11×10^{-9}– 5.23×10^{-9}), as shown in as shown in **Table 4.3**. This indicates a much greater Li^+ diffusion coefficient in the $MoTe_2$ electrode in comparison to other Mo-based chalcogenides and Mo-based oxides such as $MoSe_2$, MoS_2, WS_2, and MoO_3.[16,39] The GITT for the $MoTe_2$ electrode was performed during the second cycle as a function of time in the voltage range of 0.01 to 2.5 V. The cell was first discharged with a pulse of a few mA for 15 min with a 40 min interruption to allow the cell voltage to arrive at a steady-state value, Es. The corresponding potential versus time plot is given in **Figure 4.13a** and **Figure 4.15c,e**. The value of the diffusion coefficient was calculated at different discharge potentials (1.7 V, 1.6 V, 1.5 V) and charge potentials (1.6 V, 1.7 V, 1.75 V) during the second cycle, according to the equation (2) below:

$$D_{Li^+} = \frac{4}{\pi\tau}\left(\frac{m_B V_M}{M_B A}\right)^2 \left(\frac{\Delta E_s}{\Delta E_\tau}\right)^2 \quad (2)$$

The resulting voltage profile is given in **Figure 4.13a** and **Figure 4.15c,e**. From the results of ΔE_s and ΔE_τ by keeping m_B, V_M, M_B, and A values as constant during cycling, the diffusion coefficient value was obtained, and it is given in **Table 4.4**.

Table 4.4 The diffusion coefficient (GITT).

Discharge Potential	**(D_{cv} Li^+ / Cm^2 s^{-1}) (Discharge potential)**	**log D (Discharge potential)**	**Charge Potential**	**(D_{cv} Li^+ / Cm^2 s^{-1}) (Charge potential)**	**log D (Charge potential)**
1.696	3.38669 x 10^{-11}	-10.47022455	1.74978	3.28 x 10^{-12}	-11.48465611
1.643	3.724 x 10^{-12}	-11.42899033	1.78344	2.24 x 10^{-11}	-10.64901586
1.599	1.025 x 10^{-11}	-10.98927613	1.648	2.55 x 10^{-11}	-10.59381762

Table 4.5 The diffusion coefficient (Impedance)

Voltage (2^{nd} discharge)	**(D_{cv} Li^+ / Cm^2 s^{-1}) (2^{nd}discharge)**	**log (D_{cv} Li^+ / Cm^2 s^{-1}) (2^{nd} discharge)**	**Voltage (2^{nd} charge)**	**(D_{cv} Li^+ / Cm^2 s^{-1}) (2^{nd} charge)**	**log (D_{cv} Li^+ / Cm^2 s^{-1}) (2^{nd} charge)**
OCV (2.5V)	3.83 **x** 10^{-15}	-14.4174			
1.85	5.05 **x** 10^{-14}	-13.2967	1.5	1.91 **x** 10^{-11}	-10.7183
1.55	2.53 **x** 10^{-11}	-10.596	1.8	7.24 **x** 10^{-13}	-12.1404
1.2	1.43 **x** 10^{-11}	-10.8444	2	1.29 **x** 10^{-14}	-13.8887

Figure 4.14c shows the linear relationship between the voltage and the square root of time below at 1.6 V during the discharge process. Electrochemical Impedance Spectroscopy (EIS) was conducted for the $MoTe_2$ electrode before cycling (that is, at OCV) and after the 1^{st}, 2^{nd}, 10^{th}, and 50^{th} cycles (fully charged state) in the frequency range of 10 mHz to 1 MHz, as shown in **Figure 4.16a**. The corresponding Randle circuit model is given in the inset of **Figure 4.16b**.

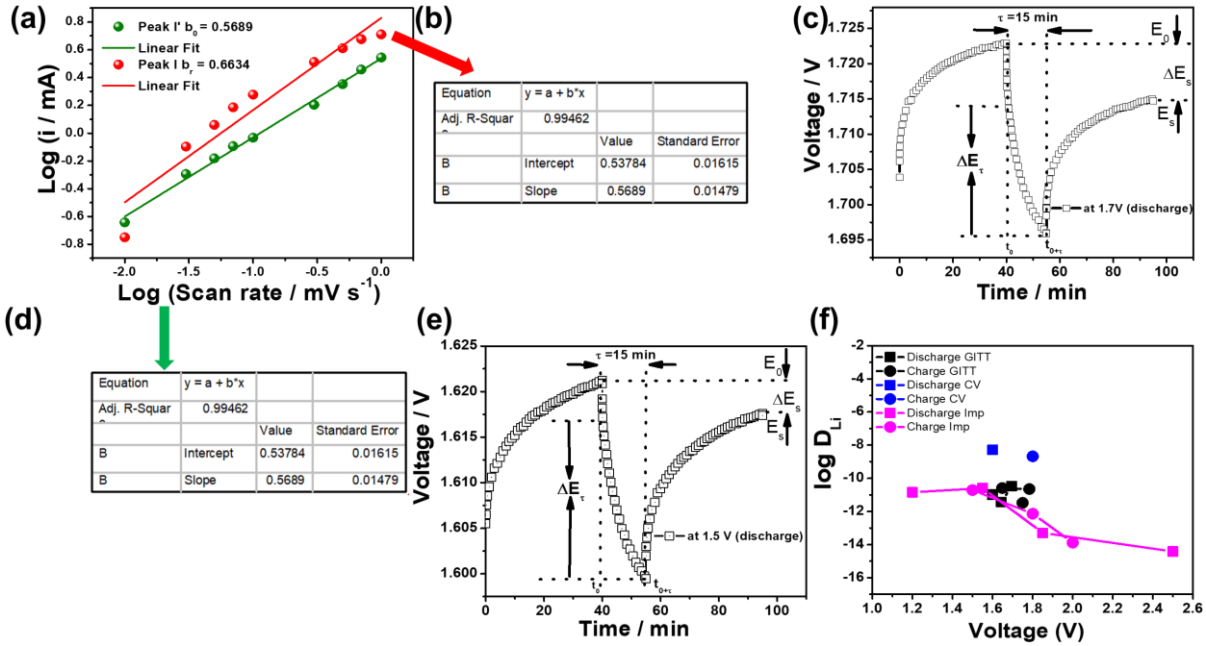

Figure 4.15 Li^+ diffusion coefficients (D_{Li+}), kinetics and a quantitative analysis of the storage mechanism of Li^+ in the $MoTe_2$ electrode. (a) Linear fitting of the log (i) versus log (v) plots of the $MoTe_2$ electrode at different scan rates. (b) The voltage profile before, during, and after a constant current pulse of a single titration at second cycle 1.7 V discharge voltages during GITT measurement with schematic labeling of different parameters of the $MoTe_2$ electrode. (c) The linear relationship between voltages against $\tau^{1/2}$. (d) A plot comparing the calculations of different Li^+ diffusion coefficients (D_{Li+}) from the CV, GITT and EIS results.

The medium-frequency semicircle explains the charge-transfer resistance, and the low-frequency region implies the diffusion coefficient of the lithium-ion in the $MoTe_2$ electrode. **Figure 4.16c** shows the values of R_{ct}, which correspond to different cycling. At OCV, the R_{ct} value is calculated as 108.3 Ω; after the first cycle, it reduces to 21.7 Ω. The high R_{ct} value at OCV shows the initial barrier of Li's reaction to the $MoTe_2$. After the second cycle, the R_{ct} value (21.16 Ω) is almost the same as that after the first cycle. After the 10^{th} and 50^{th} cycles, the value of R_{ct} reduces to 17.51 Ω and 12.45 Ω. After the first cycle, the particles became nanosized, which facilitates Li^+ transfer by decreasing R_{ct}.

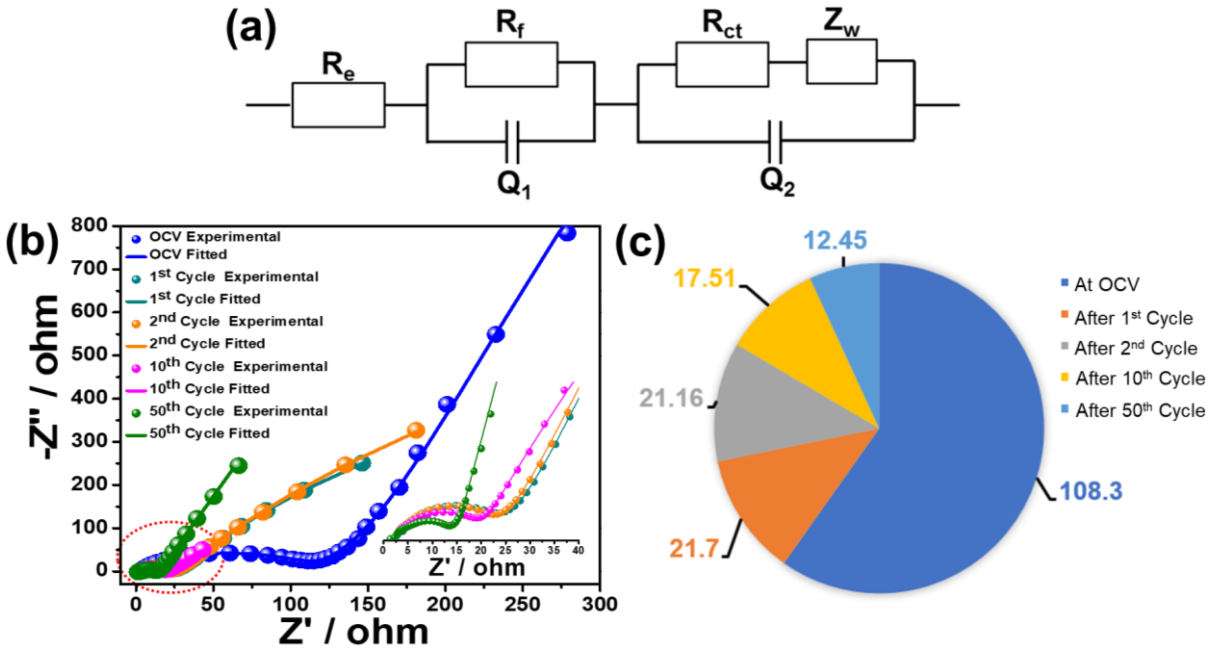

Figure 4.16(a) The equivalent circuit used to fit the EIS spectra during the charge/discharge process. (b) Fitted circuit Nyquist plots and the fitting results at OCV, after 1st, 2nd, 10th, and 50th cycles of the $MoTe_2$ electrode. (c) The fitted Impedance parameters (R_{ct} values) that correspond to the $MoTe_2$ electrode during various cycles.

The continuous decrease of the R_{ct} during cycling proves that faster Li^+ mobility in the $MoTe_2$ electrode leads to low overpotential after the first cycle.[7] Further, the Li^+ diffusion coefficient (D_{Li+}) is calculated from the in situ ElS, which is performed at different discharging and charging potentials of the second cycle, as shown in **Figure 4.12** and **Figure 4.14**. The inclined line at the low-frequency region (**Figure 4.12** and **Figure 4.14**) implies Warburg behavior, which is associated with lithium-ion diffusion within the $MoTe_2$ electrode. The Li^+ diffusion coefficient of the $MoTe_2$ electrode is calculated from the following equation (3).[25]

$$D_{Li+} = (R^2 T^2)/ (2A^2 n^4 F^4 C^2 \sigma^2), \quad (3)$$

where, the related parameters are R (gas constant); T (absolute temperature); A (area of the electrode); n (number of electrons); F (Faraday's constant); and C (concentration of Li^+), respectively. Further σ, which is the Warburg factor, is associated with Z' by the relation, $Z' = R_s + R_{ct} + \sigma\omega^{-1/2}$; R_s and ω represent the ohmic resistance and angular frequency.[42] The value of σ is obtained from the plot between Z' and the reciprocal square root of the angular frequency ($\omega^{-1/2}$) (separately plotted for each potential,) as shown in **Figure 4.12** and **Figure 4.14**. The calculated D_{Li+} of the $MoTe_2$ electrode during different discharge and charge potentials for the second cycle is shown in **Table 4.5**. It has been noted that the D_{Li+} (3.83×10^{-15} cm^2 s^{-1}) for

OCV increases slightly for the different discharge and charge potentials, which proves the facile diffusion process. The value of D_{Li+} lies in the range of (1.43×10^{-11} to 3.83×10^{-15}) during the discharge and charge process. **Figure 4.15f** shows the comparative plot of the diffusion coefficient of Li^+ (D_{Li+}) of the $MoTe_2$ anode, which is calculated from three different studies (CV, GITT, and Impedance) and appears to be in the range of 10^{-9} to 10^{-15}.

4.3.4 In situ XANES analysis upon cycling

Operando XAS studies are useful characterization tools to overcome impurities such as lithium oxide, alkoxide, transition metal oxide, and organometallic components, which are formed on the surface of the anode during the ex situ mode of measurements. The other advantages of operando XAS studies lie in the characterizing of the amorphous or the nanocrystalline phase after the conversion reaction. The best tool for electrode material characterization is XAS, which enables a more precise understanding of the reaction mechanism. To perform the operando studies of the CR2032-type coin-cell battery, a special type of spectrochemical cell-holding setup was designed for operando experiments at the Indus 2 synchrotron facilities in India.[7,43,44] The setup was designed for both XRD and XAS (XANES and EXAFS) measurements. For XAS, the setup can be used both in transmission and fluorescence modes of measurements. The spectrochemical cell-holding setup was used to carry out the operando XAS experiment for the first time at the Indus 2 synchrotron facilities in India. A patent application for this setup has been filed in the Indian patent office, and its application number is 201921023104.[45] In the 2032-type of coin cell, windows of a diameter of 5 mm were covered by a Kapton tape of a thickness of 100 μm to allow the X-ray to pass through. To perform the experiment, the electrochemical cell-holding setup including the potentiometer, was connected directly to the beamline and provided with electrical connections as shown in **Figure 4.17**.

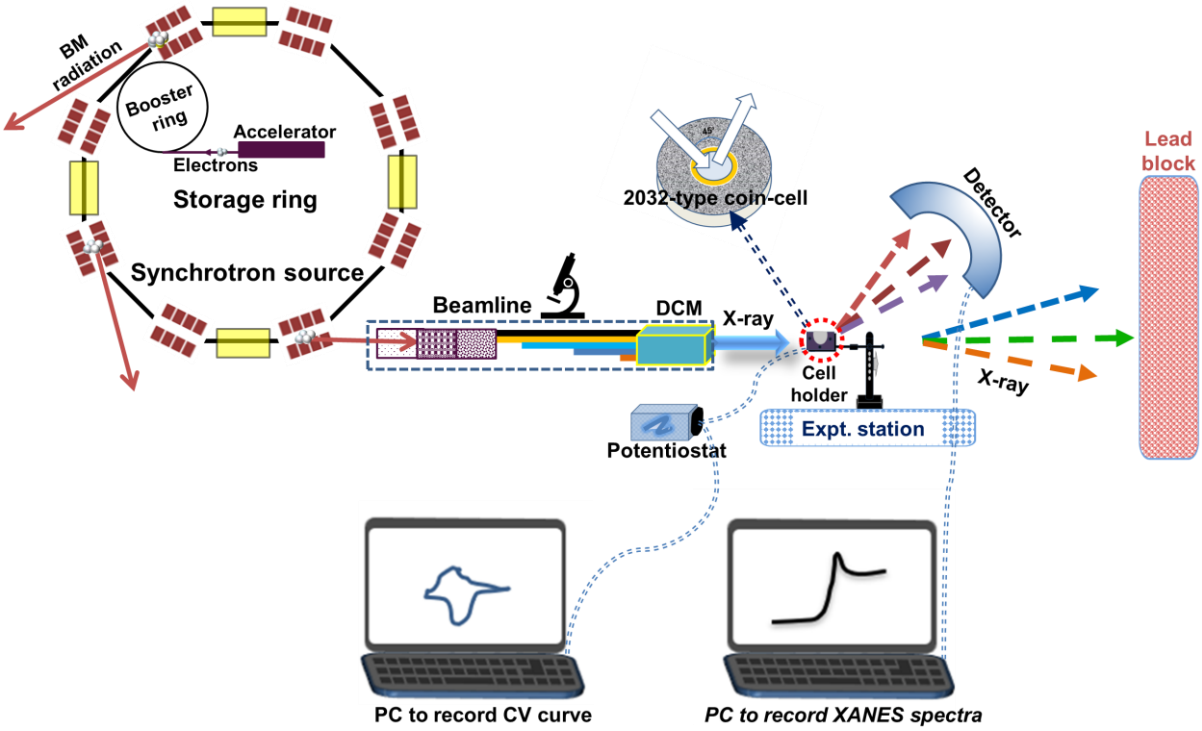

Figure 4.17 (a) Schematic of the in situ XAS cell-holder setup used for in situ XANES experiments at the synchrotron radiation (SR) source. Monochromatic X-rays are focused on the CR2032-type coin cell. (b) Different parts of the coin cell. The coin cell is positioned with a stage that is capable of rotation and three-axis translation in the beam path; a series of in situ XANES spectra are recorded over the investigated energy range.

The assembled 2032-type coin cell along with the various parts that are attached with the setup has been described schematically in **Figure 4.17**. During the measurement, the electrochemical cell was discharged/charged, that is, the insertion/deinsertion of lithium into the $MoTe_2$ host structure was allowed at a very slow rate (0.05 mV s^{-1}). The spectra were recorded at the Mo K-edge (20,000 eV) in the fluorescence mode with a step size of 1 eV. The recording of each spectrum took approximately 50 min. The variations in the local structure, charge state, and phase reversibility were monitored during the lithium insertion/deinsertion process.

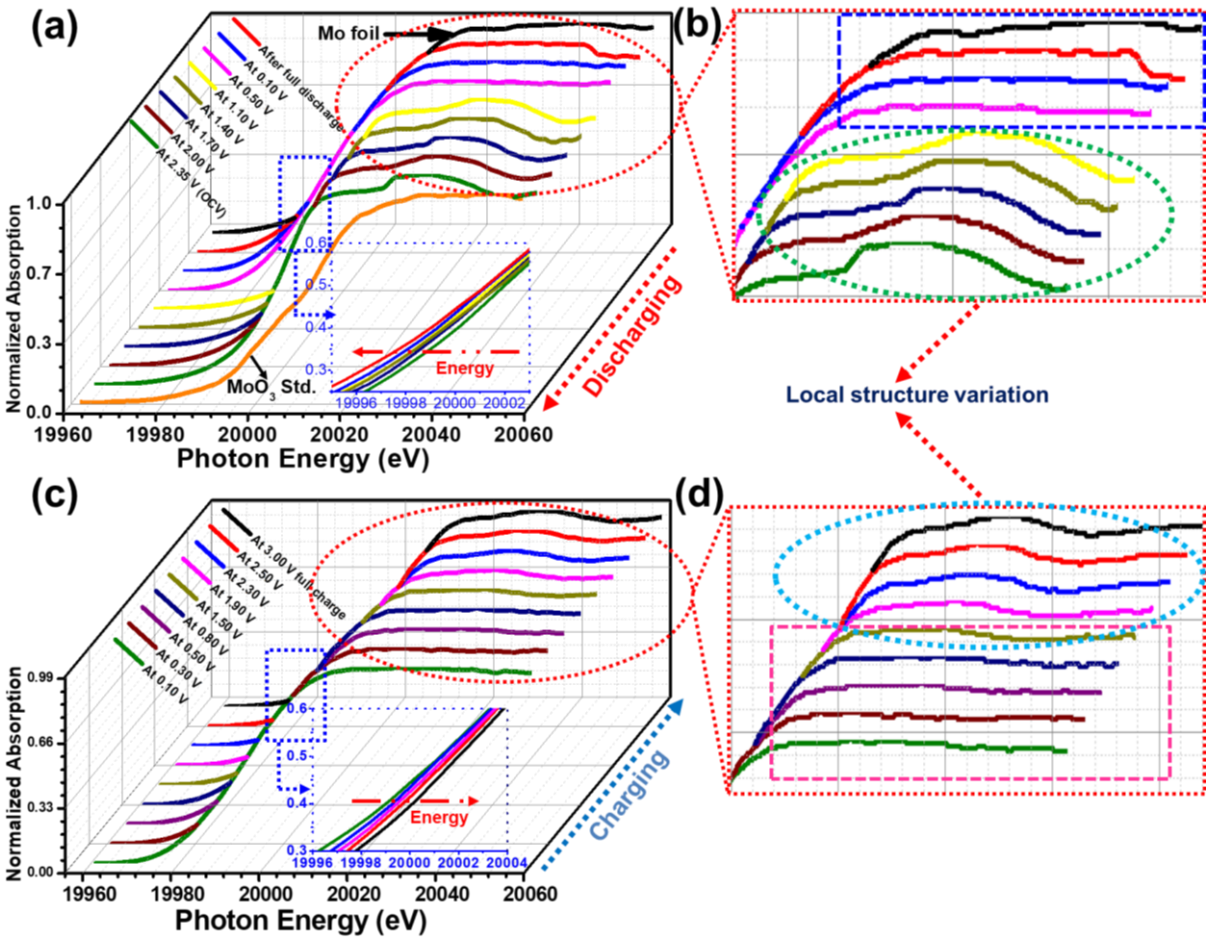

Figure 4.18 Structure evolution of lithium-storage in the $MoTe_2$ electrode. (a) In situ XANES spectra at the Mo K-edge of the $MoTe_2$ electrode collected at various applied potentials of first discharge states. (b) The magnified view of in situ XANES spectra, showing the variation in the local structure during the discharge process. The features are clearly distinguished by the circle and rectangular denomination. (c) In situ XANES spectra at the Mo K-edge of the $MoTe_2$ electrode, collected at various applied potentials of first charge states. (d) The magnified view of in situ XANES spectra, showing the variation in the local structure during the charging process. The features are clearly distinguished by the circle and rectangular denomination.

The XANES spectra provide information about the coordination geometry, and the charge states and are categorized by different features. These features are pre-edge (transition from 1s to the 3d bound state);[7,43,44,46] main edge, due to the transition of photoelectrons resonance from 1s to continuum multiple scattering;[7,43,44,47–49] and post-edge, above the main edge with the typical wiggles/oscillatory features, which provide information about the nearest neighbors and the local chemistry.[48] The CV curve (shown in **Figure 4.6a**) at which, during the first discharge, two broad peaks are seen in between 1.5 and 0.9 V, which correspond to

the intercalation of lithium into the $MoTe_2$ host lattice to form the Li_xMoTe_2 structure. There is a sharp peak at 0.72 V, which is followed by a small peak at 0.4 V during Li^+ insertion; additionally, a sharp oxidation peak at 1.82 V during the removal of Li^+ is observed. These observations were compared with the Mo K-edge XANES spectra during the first discharge/charge process, as shown in **Figure 4.18a–d**.

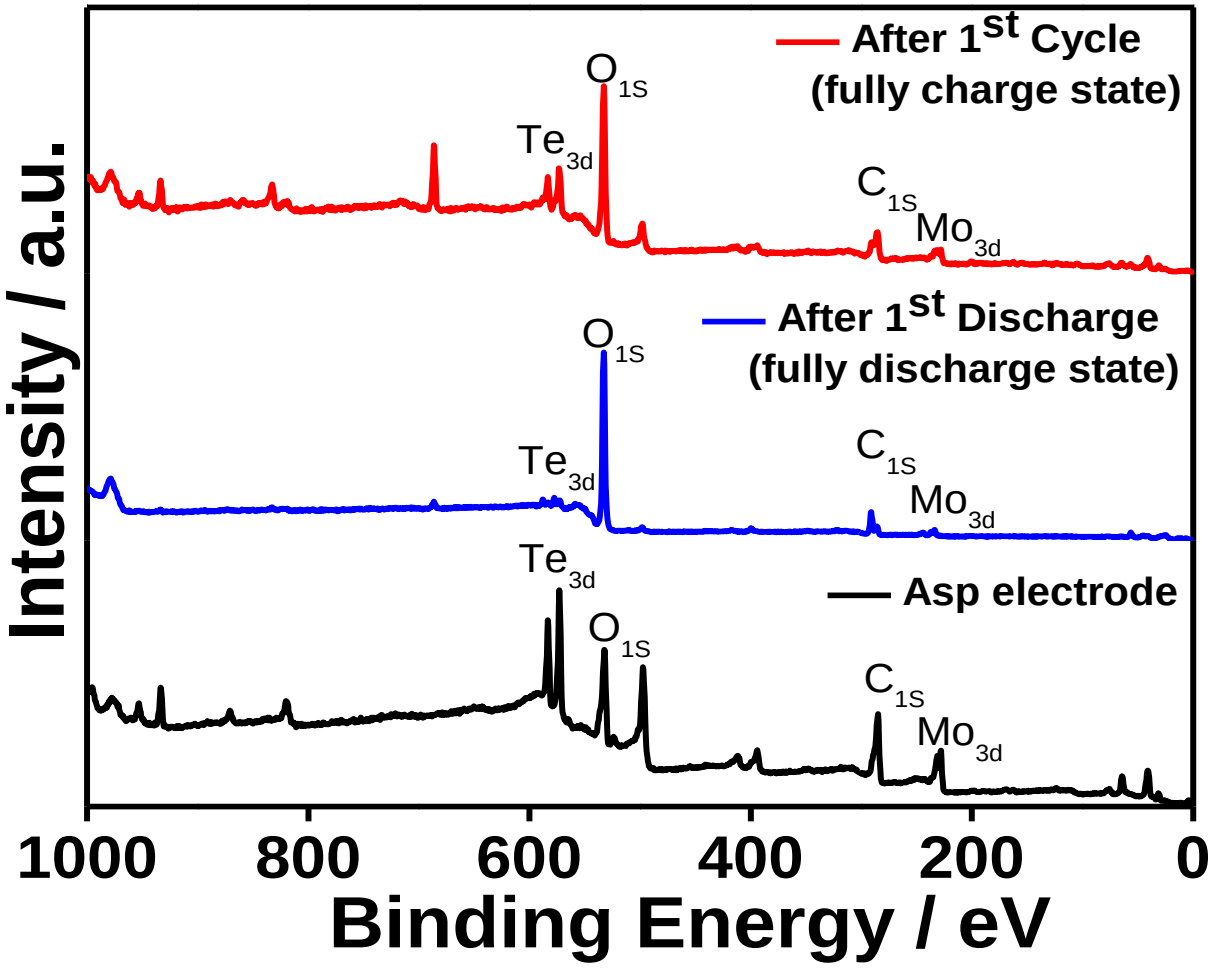

Figure 4.19 Survey XPS spectra for (a) as-prepared (b) after 1st discharge (fully discharged) and (c) after 1st cycle (fully charged state) of $MoTe_2$ electrodes.

The in situ XANES spectra, as shown in **Figure 4.18a**, which is taken during the discharge process that takes place during the insertion of the Li^+ into the $MoTe_2$ structure, can be written as $xLi^+ + MoTe_2 = Li_xMoTe_2$. The variation of the features of the Mo K-edge shows the active participation of the $MoTe_2$ and the charge state modification of Mo during the electrochemical reaction.[7,10] The absorption energy shifts toward the lower energy that was observed during the discharge process, with reference to that of the XANES spectra before cycling, that is, at OCV. A shift toward the lower energy (inset of **Figure 4.18a**) of the

absorption edge of Mo indicates the reduction of the Mo charge state progressively with an increase in the concentration of Li^{+}.[10]

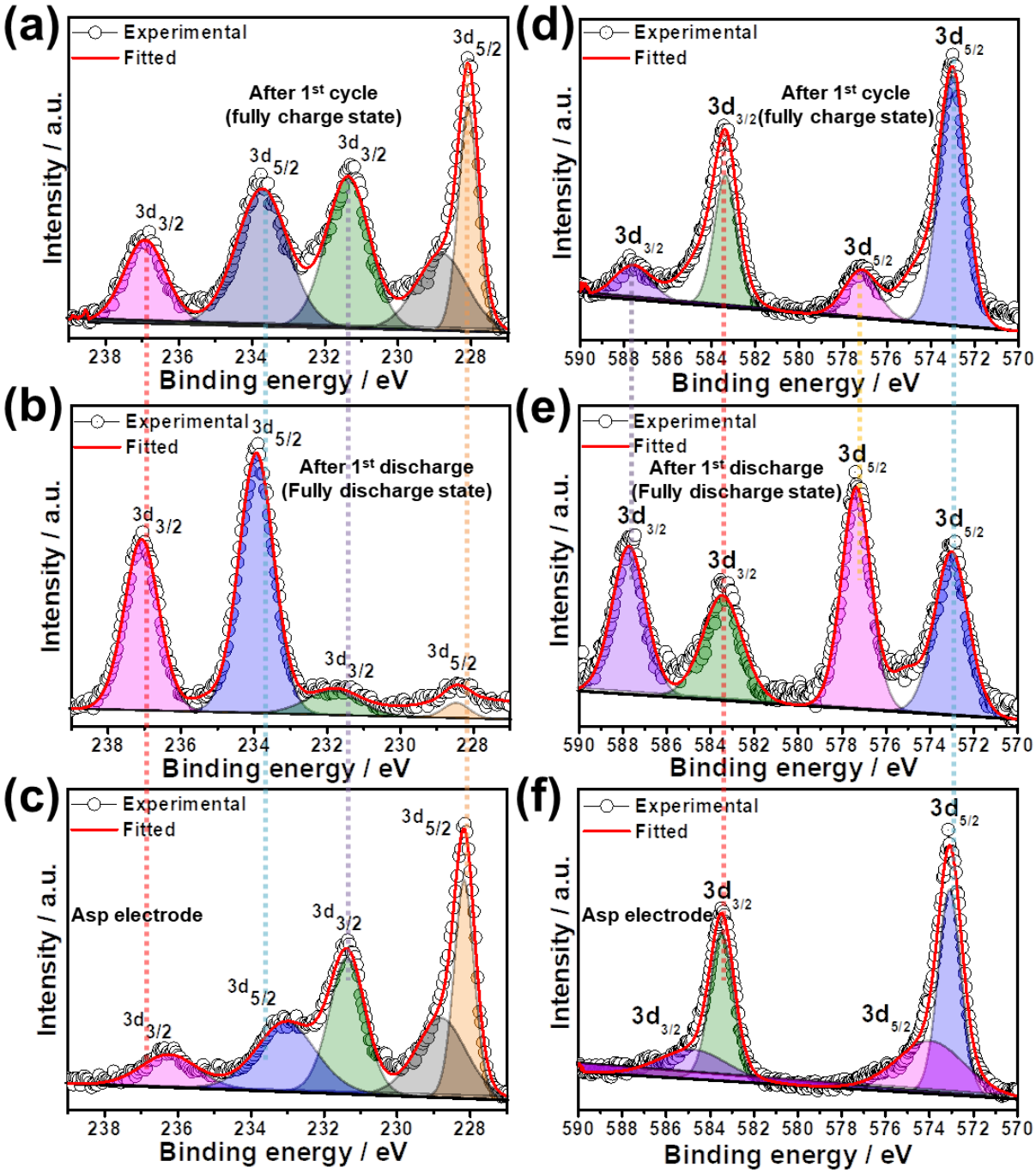

Figure 4.20 (a–f) Deconvoluted Mo and Te HRXPS spectra of as-prepared, after 1st discharge (fully discharged) and after 1st cycle (fully charged state) of $MoTe_2$ electrodes.

Figure 4.18b shows the magnified post-edge regions of the discharged XANES spectra, where two distinct features have been observed; the denoted circular region shows oscillatory behavior, which confirms the interaction between Mo and Te atoms. The oscillation gradually

reduces with the increase in the concentration of Li^+, which is shown by the spectral marked with a rectangular region in **Figure 4.18b**. The presence of oscillations in the region after the absorption edge is associated with the structural order within short distances.[7,47,48,50] From 0.5 V discharge voltage onward, the features are similar to the standard Mo foil. During the discharge process, due to a decrease of interaction between Mo and Te atoms, the oscillation gradually diminishes with the increase in the concentration of Li^+ and, finally, the feature matches with that of the Mo foil (**Figure 4.18b**). Similarly, during the charging process, a shift of the absorption edge to higher energies (inset of **Figure 4.18c**) has been observed in the Mo K-edge XANES. This observation indicates the progressive increase of Mo charge during lithium removal. In the spectral regions between those denoted by the rectangular and circular provinces, as shown in **Figure 4.18d**, the feature of the XANES spectra matches with that of the $MoTe_2$ structure, and there is a gradual increase in the oscillations in the observed post-edge region. The oscillatory features become stronger after the fully charged state at 3.00 V, which resembles the XANES spectra of OCV (**Figure 4.18d**). The XANES spectra during the charging process show a reversal of the order observed during the discharge process. This confirms the reversibility and structural stability of the $MoTe_2$ structure during the lithiation/delithiation process, which is in accord with the other TMDs.[7,12,21]

The FESEM image of the as-prepared electrode shows the carbon and the additives that are coated on the bulk MoT_2 structure electrode. The morphology of the electrode after full discharge indicates the formation of a gel-like polymer film (shown in **Figure 4.10b**) due to a high surface area and more active sites, which are a result of the formation of Mo nanoparticles that cause the decomposition of electrolytes during the electrochemical reaction.[7,9,12] The BF-TEM image of the electrode after full discharge reveals a fairly uniform set of morphologies, with networks of crystalline nanoparticles. The nanoparticles appear to be of a size of mostly 10–20 nm (with the occasional larger crystal), as shown in **Figure 4.21a,d**, which is consistent with the FESEM results. The FESEM image of the electrode after the first cycle and the fifth cycles at a full-charge state shows the amorphous sheets of morphology due to the exfoliation of the bulk structure during electrochemical cycling. The BF-TEM image shown in **Figure 4.22a,d**, further verifies the observation from the FESEM image, that is, the amorphous phase is attributed to the formation of ultrafine $MoTe_2$ nanocrystals by the repeated lithiation/ delithiation process of the cycled electrodes. The FESEM image of the electrode after the first cycle and the fifth cycles at a full-charge state shows the amorphous sheets of morphology due to the exfoliation of the bulk structure during electrochemical cycling. The BF-TEM image

shown in **Figure 4.22a,d**, further verifies the observation from the FESEM image, that is, the amorphous phase is attributed to the formation of ultrafine $MoTe_2$ nanocrystals by the repeated lithiation/ delithiation process of the cycled electrodes.

The discharge sample show a fairly uniform set of morphologies, with networks of crystalline nanoparticles. The nanoparticles appear to be of a size of mostly 10–20 nm (with the occasional larger crystal), as shown in **Figure 4.21**. A High-resolution transmission electron microscopy (HRTEM) image and SAED patterns of the electrodes after full discharge at two different observed locations are shown in **Figure 4.21**. The SAED pattern of the fully discharged electrode sample is matched with the metallic Mo and the Li_2Te phases.

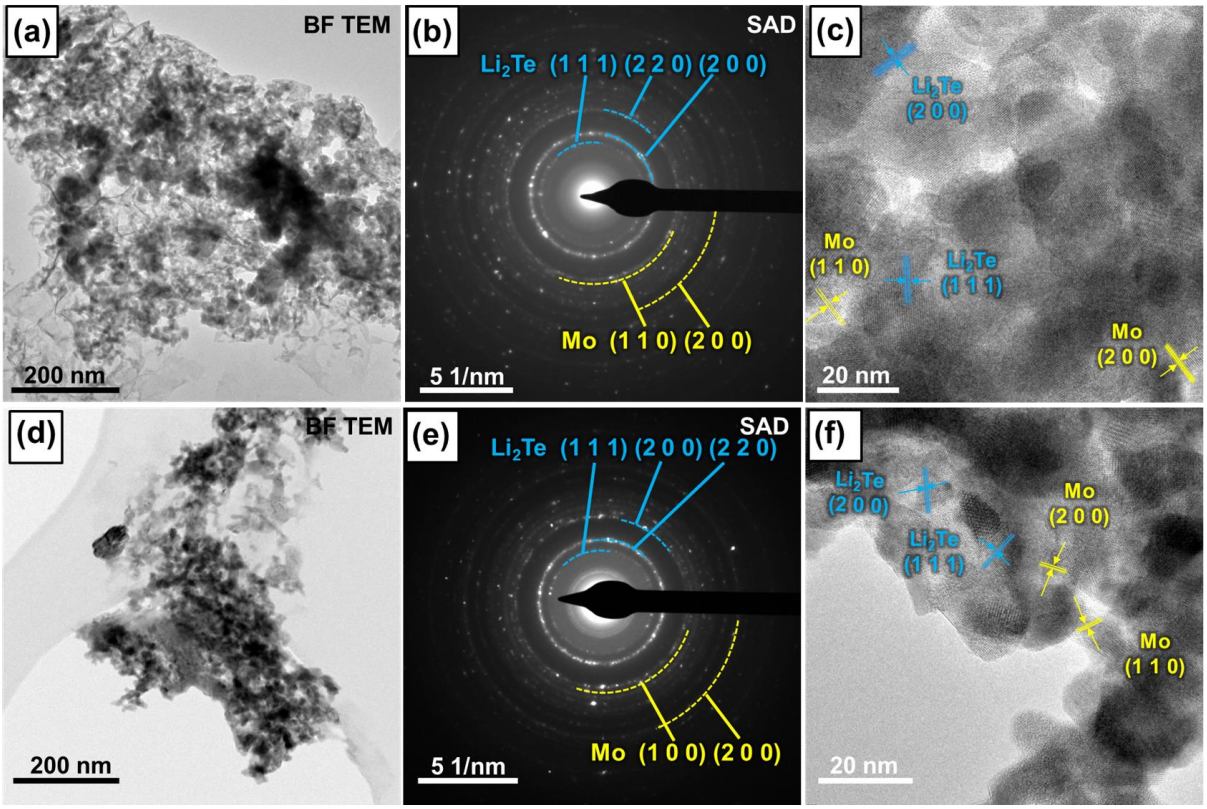

Figure 4.21 BF images, SAD patterns, and HRTEM images of the $MoTe_2$ electrodes after the full-discharge process at two different locations. (a–c) The BF-TEM image and SAD pattern from the designated area, and HRTEM images after the full-discharge process. (d–f) The BF-TEM image and SAD pattern from the indicated area, and the HRTEM image after the full-discharge process at different locations.

Figure 4.21a,d shows that the BF image and the SAED patterns were taken from a very large area, as indicated in **Figure 4.21a,d**. **Figure 4.21c,f** show the lattice fringes of 0.157 nm and 0.22 nm, respectively, which correspond to the (200) and (110) planes of the metallic Mo

nanoparticles. The lattice fringes of 0.32 nm and 0.38 nm correspond to the (200) and (111) planes of the Li_2Te phases, respectively. The planes observed above were fully consistent with the diffraction ring patterns of the SAED pattern, as shown in **Figure 4.21b,e**. The electrode in the fully charged state shows the amorphous phase (different from the discharge electrodes) as shown in **Figure 4.22**. The BF-TEM shows highly disordered types of amorphous morphologies, which are observed from two separate imaging locations. The observed lattice fringes of 0.21, 0.29, 0.3, and 0.35 nm are well-matched with the conforming planes of (105), (101), (100), and (004) of the $MoTe_2$ phase, respectively.

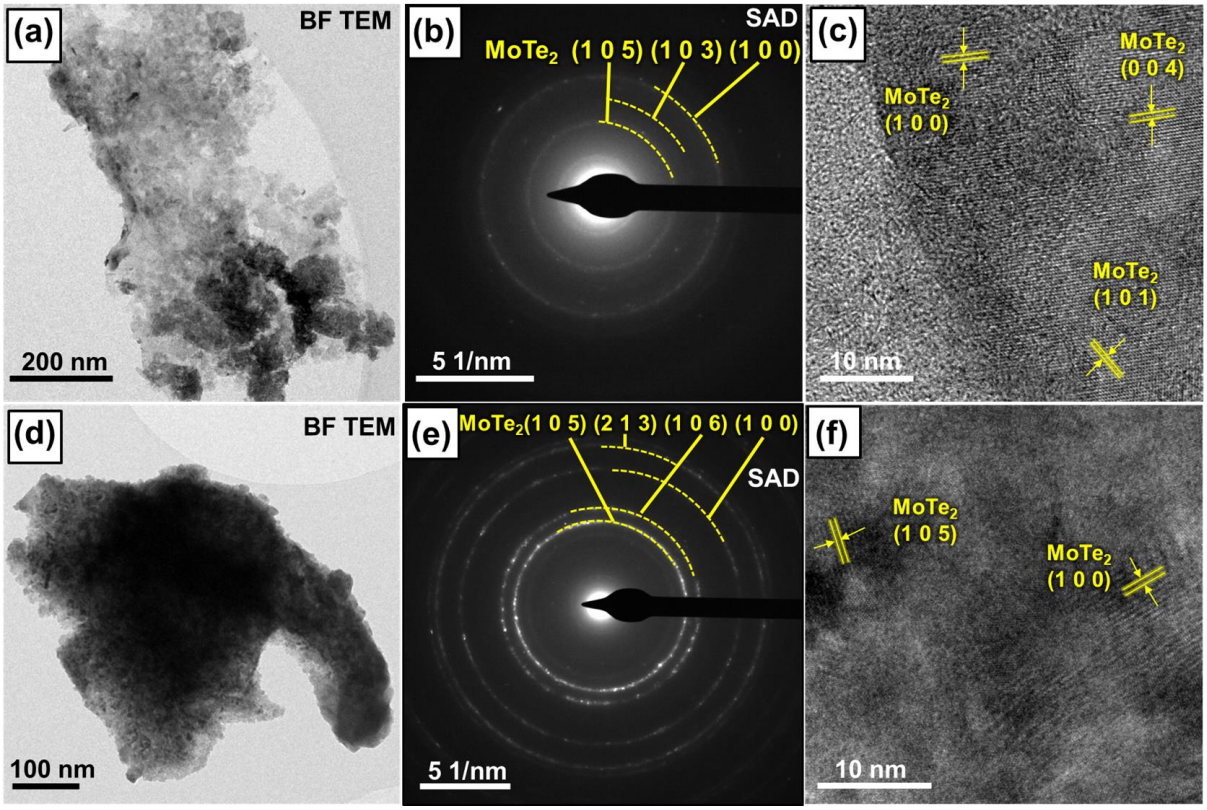

Figure 4.22 Bright field images, SAD patterns, and HRTEM images of the $MoTe_2$ cycled electrodes at two different locations. (a–c) The BF-TEM image and SAD pattern from the indicated area, and HRTEM images after the full-charge process. (d–f) BF-TEM image and SAD pattern from the indicated area, and the HRTEM image after the full-charge process at different locations.

The diffraction ring patterns of the SAED pattern, which were recorded from a very large area, as shown in **Figure 4.22b,e**, are quite consistent with the observed planes that correspond to the $MoTe_2$ phase. The amorphous phase, which is attributed to the formation of ultrafine $MoTe_2$ nanocrystals by the repeated lithiation/delithiation process of the cycled electrodes, is quite

clear from the SAED patterns. The above consequences are consistent with in situ XANES and DFT results and the reported literature.[7,9,12]

Further ex situ XPS measurements of cycled electrode samples have been performed to monitor the charge states of Mo and Te along with the as-prepared electrode sample. Two separate cells have been developed, and the XPS spectra of both electrodes have been recorded. The spectrum of one electrode was recorded after full discharge, and that of the other, after the first cycle at a fully charged state. The corresponding survey spectra, which show Mo, Te, C, and O, are presented in **Figure 4.19a–c**. The Mo-3d spectrum of the ASP electrode (**Figure 4.20c**) at binding energies of ≈228.15 eV and ≈231.36 eV for Mo $3d_{5/2}$ and Mo $3d_{3/2}$, and the peaks at ≈573.07 and ≈583.45 eV for Te $3d_{5/2}$ and Te $3d_{3/2}$, as shown in **Figure 4.20f**, respectively, confirms the 2H-$MoTe_2$ phase.[7,12–14] The Mo 3d peaks (≈233.03 eV and ≈236.23 eV for Mo $3d_{5/2}$ and Mo $3d_{3/2}$, respectively) are due to the MoO_3 phase, and the peaks that correspond to Te-3d (573.95 eV and 584.78 eV for Te $3d_{5/2}$ and Te $3d_{3/2}$, respectively) are due to the TeO_2 phases, since the as-prepared electrode sample was exposed to air.[7,12,14] The Te HRXPS spectra of the electrode after first discharge (**Figure 4.20e**) showed no drastic changes for peak positions that result from Te (573.01 eV and 583.47 eV for Te $3d_{5/2}$ and Te $3d_{3/2}$, respectively); whereas, was noticed that the Mo-3d peaks (**Figure 4.20b**) that corresponded to the 2H-$MoTe_2$ showed negligible intensities (what resulted from the 2H-$MoTe_2$ phase that did not react). The dominant Mo-3d (**Figure 4.20b**) peaks (at ≈233.94 eV and 237.08 eV for Mo $3d_{5/2}$ and Mo $3d_{3/2}$, respectively) confirm the formation of metallic Mo nanoparticles when fully discharged. This reflects as MoO_3 due to the reaction of metallic Mo nanoparticles with atmospheric air during the ex situ XPS experiment. The reconstitution of the 2H-$MoTe_2$ phase has been confirmed by examining the HRXPS spectra of Mo and Te elements of the electrode after the first cycle at a fully charged state, as shown in **Figure 4.20a,d**. The Mo-3d HRXPS peaks that are present at ≈228.07 eV and ≈231.36 eV along with the Te-3d XPS spectrum ≈572.94 eV and ≈583.35 confirm the representative peaks of the 2H-$MoTe_2$ phase;[7,12–14] whereas, the extra peaks for Mo-3d (233.71 eV and 236.92 eV for Mo $3d_{5/2}$ and Mo $3d_{3/2}$, respectively) are characteristics of the MoO_3 phase, and the peaks that correspond to Te-3d (577.18 eV and 587.54 eV for Te $3d_{5/2}$ and Te $3d_{3/2}$, respectively) are attributed to the presence of the TeO_2 phases. The additional metal oxide phases are due to the presence of the highly reactive nanophase when exposed to atmospheric oxygen while performing the ex situ XPS experiment.[7,12,14] Although the results from XPS and in situ XANES are not strictly comparable, a good agreement has generally been achieved.

4.3.5 First-principles DFT calculations of $MoTe_2$ polymorphs; understanding changes in the crystal structure with cycling

In situ and ex situ experiments give us an insight into the final properties and the exterior kinetics while using these materials in LIB systems; however, they offer little insight into the actual mechanisms involved at the atomic scale. We employed DFT to provide an atomistic perspective to the experimental results. To simulate the lithiation process, we considered a 2 x 2 x 1 supercell of $MoTe_2$, as discussed in the computational section (**section 3.5**).

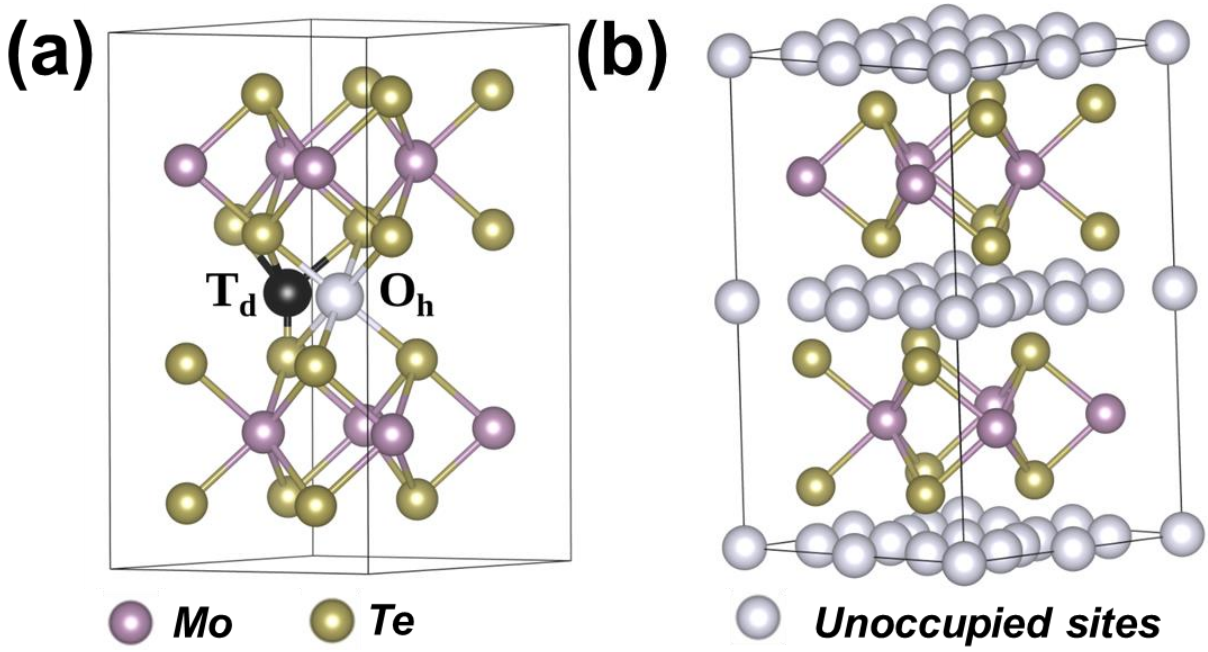

Figure 4.23 Augmented structures of pristine $MoTe_2$. (a) The octahedral (O_h) site above the center of a hexagon, which is denoted by the white sphere; and the tetrahedral T_d site above a Te atom, which is denoted by the black sphere. (b) Represents all possible O_h and T_d sites between the interlayer spaces of the $MoTe_2$ structure, for Li-intercalation in the 2H–$MoTe_2$ structure. The green, purple, and yellow spheres denote Li, Mo, and Te atoms, respectively.

We study the evolution of the electronic and geometric structure of Li_xMoTe_2 by varying the Li concentration (x) in the interlayer spacing. The possible non-equivalent distinct sites for intercalation of the Li atoms belong to two categories (**Figure 4.23**): 1) an Octahedral (O_h) site, in which the intercalated Li atom makes six bonds with the Te atoms (three per layer), and 2) a tetrahedral (T_d) site in which the intercalated atom makes four bonds with the Te atoms (one with the Te atom in the lower layer, and three bonds are with the Te atoms that belong to the upper layer). We find that O_h is the most favorable site for intercalation; it has a binding energy (refer to Equation (4) below) that is lower by 0.22 eV when compared to that of the tetrahedral

site. This observation agrees well with the previous studies, which report the preference of the octahedral site for Li atom intercalation in the case of the MoS_2 structure that has a 2H symmetry.[51,52]

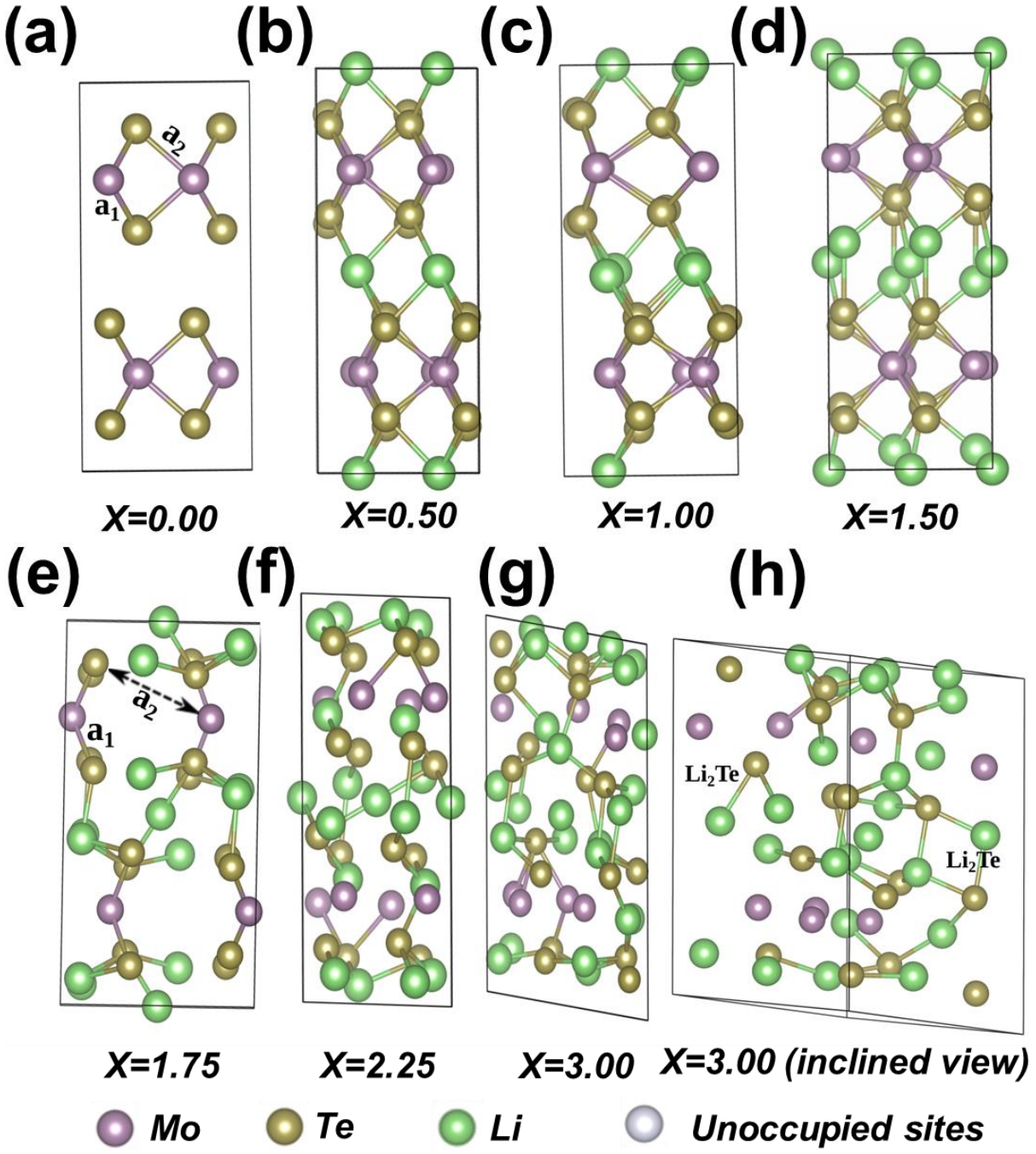

Figure 4.24 Augmented structures of lithiated $MoTe_2$ for different concentrations of Li. (a–h) Front view (in the x-z plane) of lowest energy structure for the various concentrations of the Li atom in Li_xMoTe_2 over a range of $0 \leq x \leq 3.0$. For x = 3.00, the structure is additionally shown in the inclined view, where a clear signature of Li_2Te + Mo formation can be seen. The green, purple, and yellow spheres denote Li, Mo, and Te atoms, respectively.

The location of the various sites at which Li atoms have been intercalated is shown in **Figure 4.23a,b**. For each concentration, we generate non-equivalent symmetrical configurations that follow the intercalation of Li atoms between the two $MoTe_2$ layers. Using a combination of coarse- and fine-DFT methods, as discussed in the computational section (**section 3.5**), we identified the lowest energy structure for each value of x. Further, to establish the energetic stability of the lowest energy structures, we calculated the binding energy of the system per Li atom (E_b) by using the following equation (4):

$$E_b = \frac{E_{LixMoTe2} - E_{MoTe2} - nE_{Li}}{n}, \quad (4)$$

where $E_{LixMoTe2}$ is the ground state energy of the Li atom-intercalated system, E_{MoTe2} is the ground state energy of the pristine 2H–$MoTe_2$ structure, E_{Li} is the energy of an isolated atom of Li, and n is the number of Li atoms intercalated into the interlayer spacing of the $MoTe_2$ structure. We find that the binding energy of the system for each polymorph is negative, which indicates that all these systems are energetically stable. For more details, see **Figure 4.25b**, where the binding energy values are plotted as a function of x. Next, we discuss the geometrical structure of the lowest energy configurations for each concentration.

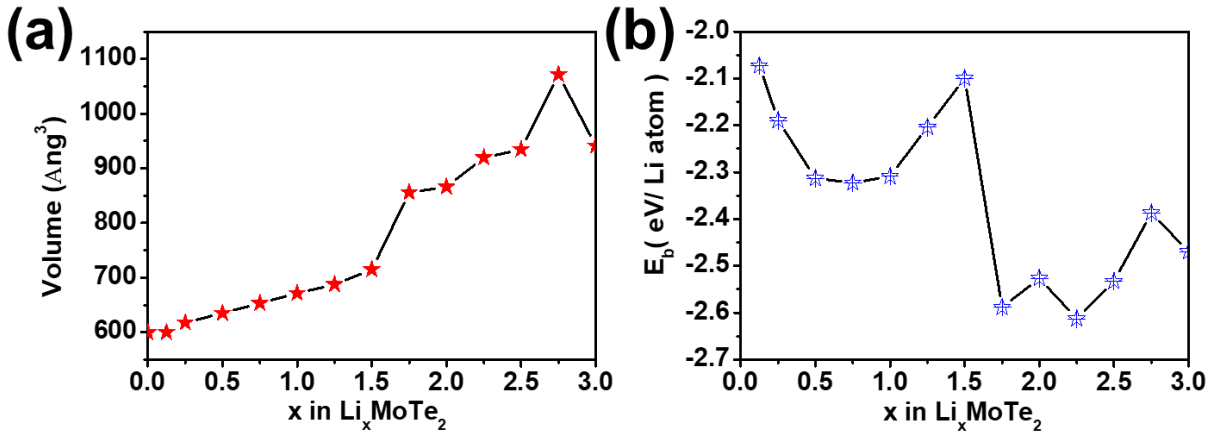

Figure 4.25 (a) Calculated volume of the lowest energy structure of the modeled supercell of Li_xMoTe_2 over the complete range of compositions ($0 < x \leq 3$) used in this study. (b) Calculated binding energies per Li atom for various concentrations of Li atoms in Li_xMoTe_2 for the lowest energy structure, over the range of $0 < x \leq 3$.

Figure 4.25 shows the lowest energy structures for x = 0, 0.5, 1.0, 1.5, 1.75, 2.25, and 3.0. We find that when the Li atoms are intercalated in $MoTe_2$, at lower concentrations ($0 < x \leq 1.5$,), the Li atom tends to occupy octahedral positions. This range of concentrations leads to small but non-negligible changes in the bonding between Mo and Te atoms when compared to that

of pristine $MoTe_2$. However, at higher concentrations ($1.5 < x \leq 3.0$), unambiguous identification of the sites is not possible because of the distortion that is produced in the structure by the intercalated Li atoms. It has been found that the higher the concentration, the higher the tendency toward the formation of the Li_2Te compound in the system. This may be attributed to the breaking of the intra-layer covalent bonding between the Mo and Te atoms. It can be observed from **Table 4.6** that the bond distance between the Mo and Te atoms ($d_{Mo–Te}$) increases gradually in the range of a Li concentration of $0 < x \leq 1.5$. The maximum change in the bond distance between the Mo and Te atoms is found to be about 6 % (for $x = 1.5$) when compared to $d_{Mo–Te}$, which is observed in the case of the pristine $MoTe_2$ structure.

Table 4.6 Lattice parameters of the optimized lowest energy structure of the lithiated $MoTe_2$ anode for various Li concentrations over a range of $0 \leq x \leq 3.0$. The last column corresponds to the bond length ($d_{Mo–Te}$) between the Mo and Te atoms, when all the bonds have the same bond length (below $x = 1$). On the other hand, a range of the bond lengths ($d_{Mo–Te}$) between Mo and Te atoms is given, when the bond lengths are different (from $x = 1$).

x	a Å	b Å	c Å	α °	β °	γ °	$d_{Mo–Te}$ Å
0.000	7.04	7.04	13.93	90.00	90.00	120.00	2.73
0.125	7.02	7.02	14.19	90.00	82.95	119.99	2.74
0.250	7.04	7.04	14.37	90.00	90.00	119.98	2.75
0.500	6.91	6.91	14.69	90.00	90.00	118.97	2.76
0.750	6.93	6.93	14.88	88.75	90.00	118.74	2.78
1.000	7.19	7.19	14.83	90.00	90.00	119.06	2.73-2.84
1.250	7.30	7.00	15.48	96.84	81.06	118.50	2.73-2.89
1.500	7.38	7.09	15.74	90.00	90.00	118.23	2.75-2.88
1.750	9.07	7.33	14.60	90.00	90.00	118.35	2.68-5.65
2.000	9.54	7.36	14.53	90.00	90.00	122.03	2.84-5.53
2.250	7.55	9.91	15.02	86.94	90.15	125.10	2.89-5.35
2.500	8.57	9.13	14.71	77.32	98.78	123.69	3.10-5.88
2.750	8.68	9.07	14.97	90.00	90.00	114.87	3.11-6.23
3.000	9.06	8.15	14.91	87.29	98.97	120.08	3.10-7.23

On the other hand, for a higher range of concentrations ($1.5 < x \leq 3.0$), some of the bonds between Mo and Te start to break (referred to as a_2-type bonds in **Figure 4.24g** for $x = 1.75$). We note from **Table 4.6** that, for $x = 1.75$, a drastic change in the values of bond distances ($d_{Mo–Te}$) is observed. For example, at this concentration, the values of $d_{Mo–Te}$ lie in the range of

2.68 to 5.65 Å. However, for x = 3.0, it is observed that the bonds between Mo and Te atoms break, the Te atoms tend to bind with the Li atoms, and some of these eventually form molecular Li_2Te (indicated in **Figure 4.24h**). We note here that some of the bond lengths between Li and Te (d_{Li-Te}) and Li-Te-Li angles are found to be 2.83 Å and 71.02º, respectively. These values match very well with the corresponding values of 2.82 Å and 70.52º, which are observed in the case of bulk Li_2Te. Additionally, some of the Mo atoms are found to be no longer bound with the Te atoms (**Figure 4.24h**).

Table 4.7 Charge on Mo, Te and Li atoms after lithiation for various Li concentrations using the Bader charge analysis. A range of the charges is given when the charge on all the atoms of a particular type of element is not the same; on the other hand, when the charge on the same type of elements is similar, the charge on only one of the atoms is presented here.

N	ΔQ_{Mo} (e)	ΔQ_{Te} (e)	ΔQ_{Li} (e)
0.000	0.53	-0.26	0.00
0.125	0.53	-0.40 to -0.26	0.85
0.250	0.52	-0.40 to-0.29	0.85
0.500	0.52	-0.53 to -0.42	0.86
0.750	0.52	-0.70 to -0.41	0.86
1.000	0.50-0.53	-0.77 to -0.65	0.86-0.87
1.250	0.50-0.51	-0.91 to -0.67	0.82-0.86
1.500	0.48-0.52	-0.90 to -0.83	0.82-0.85
1.750	0.36-0.46	-0.95 to -0.93	0.84-0.88
2.000	0.31-0.52	-1.12 to -0.87	0.82-0.86
2.250	0.33-0.45	-1.20 to -1.08	0.85-0.88
2.50	0.29-0.36	-1.34 to -1.13	0.83-0.88
2.750	0.24-0.36	-1.45 to -1.22	0.84-0.87
3.000	0.00-0.12	-1.56 to -1.21	0.83-0.85

It can be observed from **Table 4.6** that the lattice parameters expand due to the insertion of Li atoms. When we analyze the concentration of intercalated Li atoms in the range of $0 < x \leq 1.5$, we observe that the maximum differences do not exceed 0.012 Å and 1.5 Å for lattice constants a (and b) and c, respectively, when compared to those of the pristine $MoTe_2$. However, at higher concentrations ($1.5 < x \leq 3.0$), the values of the lattice constant start to increase significantly in the x and y directions as well. We observe that the values of the lattice constant, a and b, increase by a maximum of about 2.8 Å when compared to those of the pristine case. Therefore,

we observe that the volume of the supercell slowly increases for the composition range of $0 < x \leq 1.5$, when compared with the volume of the pristine 2H –$MoTe_2$ supercell. On the other hand, for a higher range of concentrations ($1.5 < x \leq 3.0$), the volume expansion is found to be much larger. For example, for x = 3.0, the volume of the supercell expands by ≈ 57 % when compared to the volume of the pristine 2H–$MoTe_2$ supercell (shown in **Figure 4.25a**). Further, we observe that the interlayer spacing increases as we increase the concentration of the Li atom.

To understand the changes in the charge density of the system following lithiation, we have carried out the Bader charge analysis[53,54] for the Li-intercalated lowest energy structure over the range, $0 < x \leq 3.0$, as well as for the Li_2Te crystal structure. From the Bader charge analysis for the Li_2Te crystal structure, we find that the charges on Te and Li atoms are ≈1.72 and 0.86e, respectively, which indicates that the Li atoms behave like an electron donor, and Te atoms act as the acceptor of the electronic charge.

The result above is also consistent with the difference in the electronegativity between the Li and Te atoms. For the lithiated systems, we observe from **Table 4.7** that Te atoms gain charge from Li atoms, and as we increase the concentration of Li atoms, this tendency of gaining charge increases. Finally, at x = 3.0, the values of charge on Te and Li atoms are the same as the corresponding values in the pristine Li_2Te compound. One can additionally note from **Table 4.7** that the Mo atoms behave like neutral atoms at a concentration of x = 3.0. Therefore, the Bader charge analysis validates the Li_2Te formation and the separation of the Mo atom from Te in the lithiated system at a concentration of x = 3.0.

We conclude here from the DFT calculations that at lower concentrations ($0 < x \leq 1.5$) of Li atoms in Li_xMoTe_2, geometrical and electronic properties change moderately and a Li_xMoTe_2-intercalated structure is formed. On the other hand, at higher concentrations ($1.5 < x \leq 3.0$), the conversion reaction begins, which shows the signature of the formation of an Li_2Te + Mo type of structure at a Li concentration of about x = 3.0. A similar conversion reaction has been reported in a previous study, in which Li and Na atoms have been intercalated in 2H-MoS_2.[10,55]

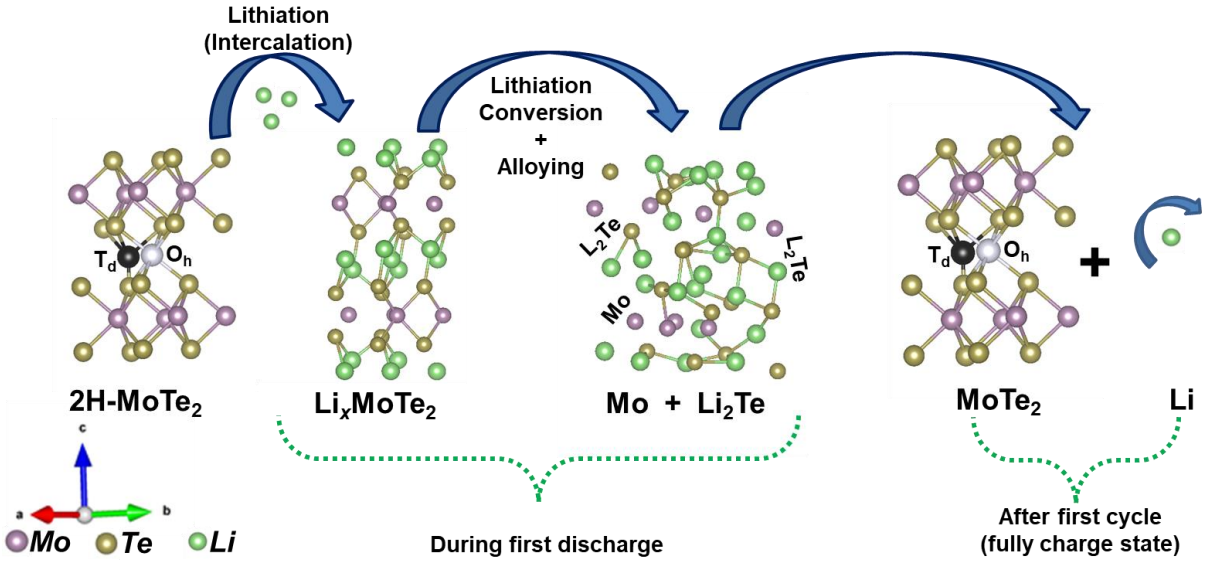

Figure 4.26 Schematic of a reversible Li storage mechanism in the $MoTe_2$.

From the in situ XANES study, we observe phase reversibility of the $MoTe_2$ structure after the completion of the first cycle of charging (fully charged state). This observation matches well with the existing literature on $MoTe_2$ structures.[7,9,12] The reversible lithium-storage mechanism in the $MoTe_2$ structure has been presented schematically in **Figure 4.26**. From the DFT results, it is observed that at a lower concentration ($0 < x \leq 1.5$) of Li atoms in Li_xMoTe_2, the optimized structure after removal of Li atoms exhibits a symmetry that is similar to that of the initial structure. Therefore, our results on the delithiation process, which are obtained through DFT calculations, match well with the reversible nature of the reaction pathway, up to a concentration of $x = 1.5$, as observed from the in situ XANES experiments. At higher concentrations ($1.5 < x \leq 3.0$) of Li, our results show a signature of segregation of the Mo layer and a formation of molecular Li_2Te; this is elucidated in **Figure 4.24h** for an Li concentration of $x = 3.0$. However, the delithiation process for higher concentrations (x above 1.5) does not exhibit a reversible nature. To simulate the delithiation process by using the first-principles method is a task that is nearly impossible, specifically at higher concentrations when a substantially distorted lithiated structure is present. In such a case, the study of the delithiation process requires a large number of computational resources. There is also a chance that, after geometry optimization, we may obtain a structure that is metastable or at a local minima state.

4.3.6 $MoTe_2$ versus LCO full-cell study

A full-cell LIB was fabricated by coupling our $MoTe_2$ anode and the LCO cathode. By observing the electrochemical performance of both the $MoTe_2$ anode and the LCO cathode, the

weight ratio of the anode ($MoTe_2$) to the cathode (LCO) was fixed at 1:3 to monitor the performance of the $MoTe_2$//LCO full cell. The ratio of $MoTe_2$ (anode) and LCO (cathode) active materials were decided based on the half-cell specific capacity of $MoTe_2$ (~375 mAh g^{-1}) at 500 mA g^{-1}, LCO (~140 mAh g^{-1}) at 500 mA g^{-1} and the initial cycles lithium loss during charging of full cell was also under consideration.

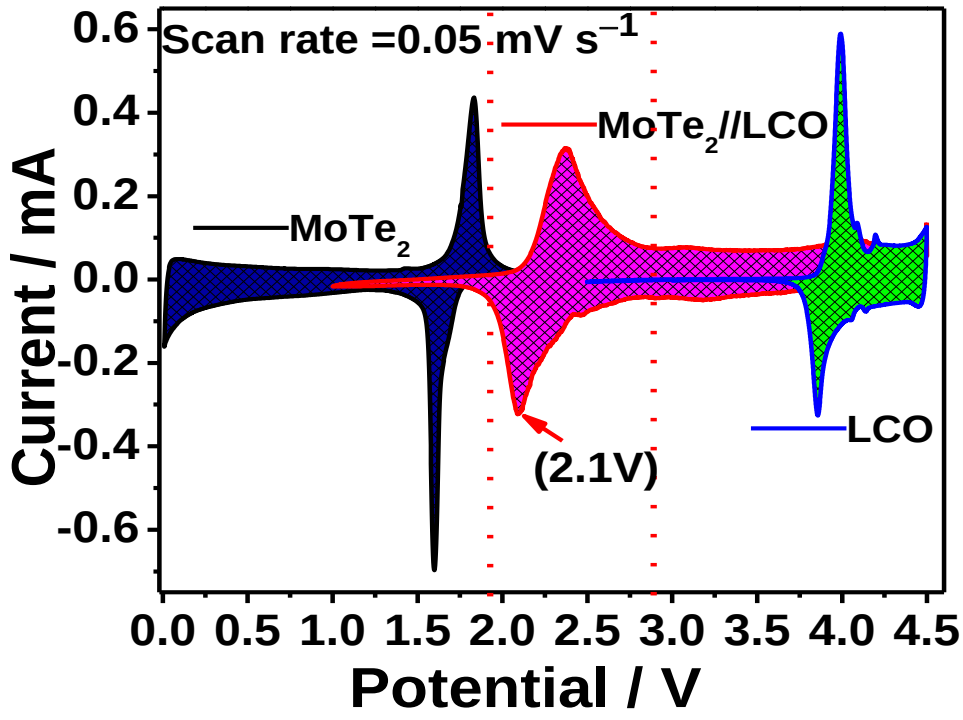

Figure 4.27 Combined CV of the anode and the cathode in a half-cell configuration (against lithium metal), and the $MoTe_2$//LCO full-cell system at a voltage range between 0.1 and 4.5 V.

Figure 4.27 shows the combined CV curve of the $MoTe_2$ anode, the LCO cathode, and the $MoTe_2$//LCO full cell at a scan rate of 0.05 mv s^{-1}. The CV curve of the $MoTe_2$//LCO full cell shows a sharp reduction peak of nearly ≈2.10 V, which shows that the nominal voltage of the $MoTe_2$//LCO full cell is approximate ≈2.10 V. The galvanic charge/discharge curve of the $MoTe_2$//LCO full cell is shown in **Figure 4.28a** in the voltage window of 1.8−3.8 V. A charge capacity of 228 mAh g^{-1} and a corresponding discharge capacity of 216 mAh g^{-1} have been observed along with Coulombic efficiency of 95 % in the second cycle at a current rate of 0.5 A g^{-1}. The $MoTe_2$//LCO full cell has a capacity retention of 80 % over 100 cycles, as shown in **Figure 4.28b**.

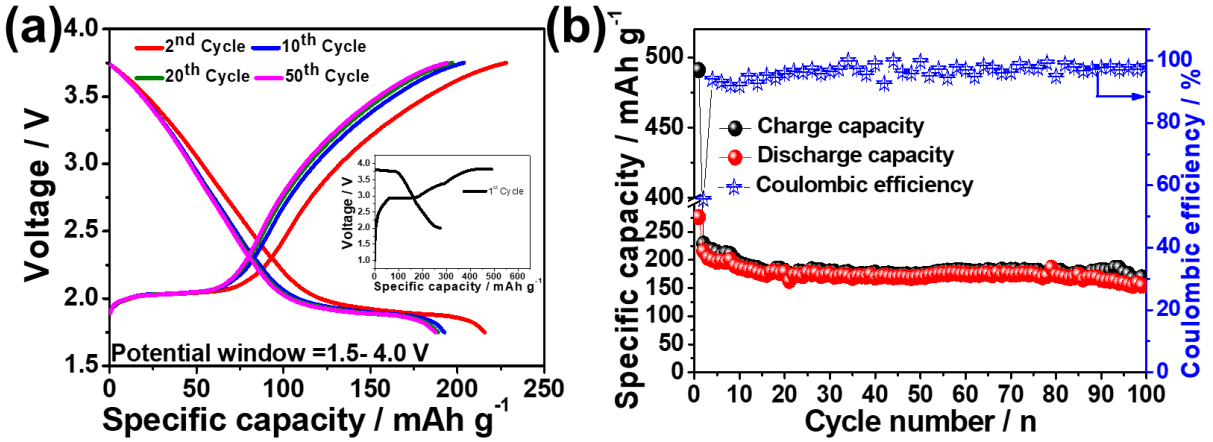

Figure 4.28 The electrochemical performance of the full-cell system, coupled with $MoTe_2$ as the anode and LCO as the cathode; the specific capacities were evaluated on the mass of $MoTe_2$. (a) Galvanostatic charge/discharge curves versus specific capacity at 0.5 A g^{-1} of the $MoTe_2$ and LCO full-cell type in the voltage range of 1.8 to 3.8 V. (b) Cycling performance of the full-cell system during 100 cycles at 0.5 A g^{-1}.

In the case of the $MoTe_2$//LCO full cell, a better cycle performance is observed for initial cycles, because the potential window is restricted between 1.8 to 3.8 V. Such-a-small potential window results in the minimization of the conversion reaction and the halting of the excessive formation of Mo nanoparticles during the discharge process[9,22], which helps to slow down the electrolyte reduction reaction. Hence, we observe better cycle performance for initial cycles in the case of the $MoTe_2$//LCO full cell. By considering the intercalation mechanism between the $MoTe_2$ anode and the Li/Li^+, and by combining both the half-cell reactions of the $MoTe_2$ anode and the LCO cathode, the possible electrochemical reactions that occur at both positive and negative electrodes is shown in equation (5a) and (5b) below:

Cathode:

$$LiCoO_2 \leftrightarrow CoO_2 + xLi^+ + xe^- \quad (5a)$$

Anode:

$$MoTe_2 + xLi^+ + xe^- \leftrightarrow Li_xMoTe_2 \quad (5b)$$

The $MoTe_2$//LCO full cell shows a high energy density of 454 Wh kg^{-1} (based on the $MoTe_2$ mass) and capacity retention of 80 % over 100 cycles. Here we ignore the weight of the separator, electrolyte, and cell pack components while calculating the energy density of the full cell. We believe reporting the energy density based on anode mass is more suitable in this current stage of development.

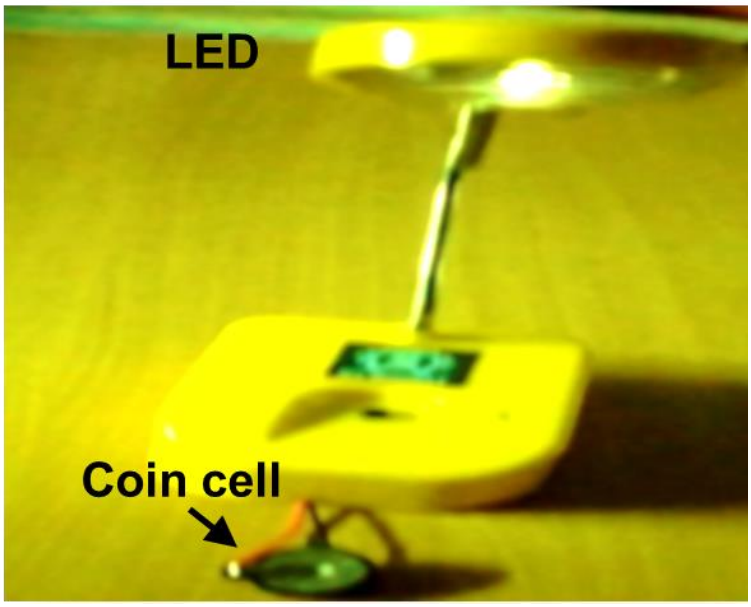

Figure 4.29 A prototype demonstration of the $MoTe_2$ and the LCO full-cell system, showing the lighting of an LED table lamp powered by a coin cell.

A practical demonstration has been carried out to light a study lamp (light-emitting diode, (LED) of 2 V) by using a single coin cell, as shown in **Figure 4.29**. The outcomes of the electrochemical performances discussed above indicate that $MoTe_2$ has great potential as an anode material for future LIBs.

4.4 Conclusions

In summary, the 2H-$MoTe_2$ anode has been successfully prepared by a simple solid-state method. The hexagonal structure of the material along with a 2H-type symmetry is confirmed by HRSTEM and XRD results. The $MoTe_2$ electrode without any in situ coating of conductive carbon additives shows an initial specific capacity of 432 mAh g^{-1} at a current density of 1.0 A g^{-1}. Further, it exhibits an excellent reversible specific capacity of a value of 291 mAh g^{-1} after 260 cycles of operation. The lithium-storage mechanism during lithiation/delithiation has been investigated by in situ XANES, which is complemented by first principle DFT calculations and which confirms the electrochemical reversibility and structural stability of the $MoTe_2$ anode. Moreover, the capacitive Li^+ storage transport mechanism and Li^+ diffusion coefficients have been determined by quantitative electrochemical kinetic calculations. The $MoTe_2$//LCO full cell shows a high energy density of 454 Wh kg^{-1} and capacity retention of 80 % over 100 cycles, which suggests that the $MoTe_2$ can serve as an efficient anode for LIBs. The present study demonstrates that 2H-$MoTe_2$ can be used as an efficient electrode material in LIBs applications.

4.5 References

(1) Qi, Y.; Naumov, P. G.; Ali, M. N.; Rajamathi, C. R.; Schnelle, W.; Barkalov, O.; Hanfland, M.; Wu, S. C.; Shekhar, C.; Sun, Y.; Süß, V. Superconductivity in Weyl Semimetal Candidate $MoTe_2$. *Nat. Commun.* **2016**, 7, 1–7.

(2) Keum, D. H.; Cho, S.; Kim, J. H.; Choe, D. H.; Sung, H. J.; Kan, M.; Kang, H.; Hwang, J. Y.; Kim, S. W.; Yang, H.; Chang, K. J.; Bandgap Opening in Few-Layered Monoclinic $MoTe_2$. *Nat. Phys.* **2015**, 11, 482–486.

(3) Pradhan, N. R.; Rhodes, D.; Feng, S.; Xin, Y.; Memaran, S.; Moon, B. H.; Terrones, H.; Terrones, M.; Balicas, L. Field-Effect Transistors Based on Few-Layered α-$MoTe_2$. *ACS nano* **2014**, 8, 5911–5920.

(4) Deng, K.; Wan, G.; Deng, P.; Zhang, K.; Ding, S.; Wang, E.; Yan, M.; Huang, H.; Zhang, H.; Xu, Z.; Denlinger, J. Experimental Observation of Topological Fermi Arcs in Type-II Weyl Semimetal $MoTe_2$. *Nat. Phys.* **2016**, 12, 1105–1110.

(5) Liu, M.; Wang, Z.; Liu, J.; Wei, G.; Du, J.; Li, Y.; An, C.; Zhang, J. Synthesis of Few-Layer 1T′-$MoTe_2$ Ultrathin Nanosheets for High-Performance Pseudocapacitors. *J. Mater. Chem. A* **2017**, 5, 1035–1042.

(6) Panda, M. R.; Bao, Q.; Mitra, S. $MoTe_2$, A Novel Anode Material for Sodium Ion Battery. *AIP Conf. Proc.* **2018**, 1942, 140078.

(7) Panda, M. R.; Ghosh, A.; Kumar, A.; Muthuraj, D.; Sau, S.; Yu, W.; Zhang, Y.; Sinha, A. K.; Weyland, M.; Bao, Q.; Mitra, S. Blocks of Molybdenum Ditelluride: A High Rate Anode for Sodium-Ion Battery and Full Cell Prototype Study. *Nano Energy* **2019**, 64, 103951.

(8) Li, W.; Li, J. Ferroelasticity and Domain Physics in Two-Dimensional Transition Metal Dichalcogenide Monolayers. *Nat. Commun.* **2016**, 7, 1–8.

(9) Ma, N.; Jiang, X. Y.; Zhang, L.; Wang, X. S.; Cao, Y. L.; Zhang, X. Z. Novel 2D Layered Molybdenum Ditelluride Encapsulated in Few-Layer Graphene as High-Performance Anode for Lithium-Ion Batteries. *Small* **2018**, 14, 1703680.

(10) Sen, U. K.; Johari, P.; Basu, S.; Nayak, C.; Mitra, S. An Experimental and Computational Study to Understand the Lithium Storage Mechanism in Molybdenum Disulfide. *Nanoscale* **2014**, 6, 10243–10254.

(11) Luo, Z.; Zhou, J.; Wang, L.; Fang, G.; Pan, A.; Liang, S. Two-Dimensional Hybrid Nanosheets of Few Layered $MoSe_2$ on Reduced Graphene Oxide as Anodes for Long-Cycle-Life Lithium-Ion Batteries. *J. Mater. Chem. A* **2016**, 4, 15302–15308.

(12) Cho, J. S.; Ju, H. S.; Lee, J. K.; Kang, Y. C. Carbon/Two-Dimensional $MoTe_2$ Core/Shell-Structured Microspheres as an Anode Material for Na-Ion Batteries. *Nanoscale* **2017**, 9, 1942–1950.

(13) Zhou, L.; Xu, K.; Zubair, A.; Liao, A. D.; Fang, W.; Ouyang, F.; Lee, Y. H.; Ueno, K.; Saito, R.; Palacios, T.; Kong, J. Large-Area Synthesis of High-Quality Uniform Few-Layer $MoTe_2$. *J. Am. Chem. Soc.* **2015**, 137, 11892–11895.

(14) Vishwanath, S.; Sundar, A.; Liu, X.; Azcatl, A.; Lochocki, E.; Woll, A. R.; Rouvimov, S.; Hwang, W. S.; Lu, N.; Peng, X.; Lien, H. H.; Weisenberger, J.; McDonnell, S.; Kim, M. J.; Dobrowolska, M.; Furdyna, J. K.; Shen, K.; Wallace, R. M.; Jena, D.; Xing, H. G. MBE Growth of Few-Layer 2H-$MoTe_2$ on 3D Substrates. *J. Cryst. Growth* **2018**, 482, 61–69.

(15) Zhu, C.; Mu, X.; van Aken, P. A.; Yu, Y.; Maier, J. Single-Layered Ultrasmall Nanoplates of MoS_2 Embedded in Carbon Nanofibers with Excellent Electrochemical Performance for Lithium and Sodium Storage. *Angew. Chem.* **2014**, 126, 2184–2188.

(16) Zhang, S.; Wang, G.; Jin, J.; Zhang, L.; Wen, Z.; Yang, J. Robust and Conductive Red $MoSe_2$ for Stable and Fast Lithium Storage. *ACS nano* **2018**, 12, 4010–4018.

(17) Zhou, L.; Yan, S.; Pan, L.; Wang, X.; Wang, Y.; Shi, Y. A Scalable Sulfuration of WS_2 to Improve Cyclability and Capability of Lithium-Ion Batteries. *Nano Res.* **2016**, 9, 857–865.

(18) Yang, W.; Wang, J.; Si, C.; Peng, Z.; Zhang, Z. Tungsten Diselenide Nanoplates as Advanced Lithium/Sodium Ion Electrode Materials with Different Storage Mechanisms. *Nano Res.* **2017**, 10, 2584–2598.

(19) Wang, J.; Chen, L.; Zeng, L.; Wei, Q.; Wei, M. In Situ Synthesis of WSe_2/CMK-5 Nanocomposite for Rechargeable Lithium-Ion Batteries with a Long-Term Cycling Stability. *ACS Sustain. Chem. Eng.* **2018**, 6, 4688–4694.

(20) Srinivaas, M.; Wu, C. Y.; Duh, J. G.; Hu, Y. C.; Wu, J. M. Multi-Walled Carbon-Nanotube-Decorated Tungsten Ditelluride Nanostars as Anode Material for Lithium-Ion Batteries. *Nanotechnology* **2019**, 31, 035406.

(21) Hong, M.; Li, J.; Zhang, W.; Liu, S.; Chang, H. Semimetallic 1T′ WTe_2 Nanorods as Anode Material for the Sodium Ion Battery. *Energy Fuels* **2018**, 32, 6371–6377.

(22) Shu, H.; Li, F.; Hu, C.; Liang, P.; Cao, D.; Chen, X. The Capacity Fading Mechanism and Improvement of Cycling Stability in MoS_2-Based Anode Materials for Lithium-Ion Batteries. *Nanoscale* **2016**, 8, 2918–2926.

(23) David, L.; Bhandavat, R.; Barrera, U.; Singh, G. Polymer-Derived Ceramic Functionalized MoS_2 Composite Paper as a Stable Lithium-Ion Battery Electrode. *Sci. Rep.* **2015**, 5, 9792.

(24) Chen, Y.; Song, B.; Tang, X.; Lu, L.; Xue, J. Ultrasmall Fe_3O_4 Nanoparticle/MoS_2 Nanosheet Composites with Superior Performances for Lithium Ion Batteries. *Small* **2014**, 10, 1536–1543.

(25) Kong, D.; He, H.; Song, Q.; Wang, B.; Lv, W.; Yang, Q. H.; Zhi, L. Rational Design of MoS_2@Graphene Nanocables: Towards High Performance Electrode Materials for Lithium Ion Batteries. *Energy Environ. Sci.* **2014**, 7, 3320–3325.

(26) Kang, J.; Su, Q.; Feng, H.; Huang, P.; Du, G.; Xu, B. $MoSe_2$ Nanosheets-Wrapped Flexible Carbon Cloth as Binder-Free Anodes for High-Rate Lithium and Sodium Ion Storages. *Electrochim. Acta* **2019**, 301, 29–38.

(27) Sahu, T. S.; Mitra, S. Exfoliated MoS_2 Sheets and Reduced Graphene Oxide An Excellent and Fast Anode for Sodium-Ion Battery. *Sci. Rep.* **2015**, 5, 12571.

(28) Garcia, A. M.; Thapa, A. K.; Dharmadasa, R.; Nguyen, T. Q.; Jasinski, J.; Druffel, T. L.; Sunkara, M. K. High Rate and Durable, Binder Free Anode Based on Silicon Loaded MoO_3 Nanoplatelet. *Sci. Rep.* **2015**, 5, 10530.

(29) Ding, J.; Abbas, S. A.; Hanmandlu, C.; Lin, L.; Lai, C. S.; Wang, P. C.; Li, L. J.; Chu, C. W.; Chang, C. C. Facile Synthesis of Carbon/MoO_3 Nanocomposites as Stable Battery Anodes. *J. Power Sources* **2017**, 348, 270–280.

(30) Sun, H.; Hanlon, D.; Dinh, D. A.; Boland, J. B.; Castillo, A. E. D. R.; Giovanni, C. D.; Ansaldo, A.; Pellegrini, V.; Coleman, J. N.; Bonaccorso, F. Carbon Nanotubes-Bridged Molybdenum Trioxide Nanosheets as High Performance Anode for Lithium Ion Batteries. *2D Mater.* **2018**, 5, 015024.

(31) Gao, H.; Liu, C. L.; Liu, Y.; Liu, Z. H.; Dong, W. S. MoO_2-Loaded Porous Carbon Hollow Spheres as Anode Materials for Lithium-Ion Batteries. *Mater. Chem. Phys.* **2014**, 147, 218–224.

(32) Gao, Q.; Yang, L.; Lu, X.; Mao, J.; Zhang, Y.; Wu, Y.; Tang, Y. Synthesis, Characterization and Lithium-Storage Performance of MoO_2/Carbon Hybrid Nanowires. *J. Mater. Chem.* **2010**, 20, 2807–2812.

(33) Shen, C.; Wang, L.; Zhou, A.; Zhang, H.; Chen, Z.; Hu, Q.; Qin; G. MoS_2-Decorated Ti_3C_2 MXene Nanosheet as Anode Material in Lithium-Ion Batteries. *J. Electrochem. Soc.* **2017**, 164, A2654–A2659.

(34) Zheng, M.; Guo, R.; Liu, Z.; Wang, B.; Meng, L.; Li, F.; Li, T.; Luo, Y. MoS_2 Intercalated p-Ti_3C_2 Anode Materials with Sandwich-Like Three Dimensional Conductive Networks for Lithium-Ion Batteries. *J. Alloy Compd.* **2018**, 735, 1262–1270.

(35) Ding, S.; Zhang, D.; Chen, J. S.; Lou, X. W. Facile Synthesis of Hierarchical MoS_2 Microspheres Composed of Few-Layered Nanosheets and Their Lithium Storage Properties. *Nanoscale* **2012**, 4, 95–98.

(36) Liu, Y.; Zhu, M.; Chen, D.; Sheet-like $MoSe_2$/C Composites With Enhanced Li-Ion Storage Properties. *J. Mater. Chem. A* **2015**, 3, 11857–11862.

(37) Bissetta, M. A.; Worralla, S. D.; Kinloch, I. A.; Dryfea, R. A.W. Comparison of Two-Dimensional Transition Metal Dichalcogenides for Electrochemical Supercapacitors *Electrochim. Acta* **2016**, 201, 30–37.

(38) Wang, J.; Liu, J.; Chao, D.; Yan, J.; Lin, J.; Shen, Z. X. Self-Assembly of Honeycomb-Like MoS_2 Nanoarchitectures Anchored into Graphene Foam for Enhanced Lithium-Ion Storage. *Adv. Mater.* **2014**, 26, 7162–7169.

(39) Brezesinski, T.; Wang, J.; Tolbert, S. H.; Dunn, B. Ordered mesoporous α-MoO_3 with Iso-Oriented Nanocrystalline Walls for Thin-Film Pseudocapacitors. *Nat. Mater.* **2010**, 9, 146–151.

(40) Da, Y.; Liu, J.; Zhou, L.; Zhu, X.; Chen, X.; Fu, L. Engineering 2D Architectures Toward High-Performance Micro-Supercapacitors. *Adv. Mater.* **2019**, 31, 1802793.

(41) Kyerematen, N. A.; Brousse, T.; Pech, D. Microsupercapacitors as Miniaturized Energy-Storage Components for On-Chip Electronics. *Nat. Nanotechnol.* **2017**, 12, 7–15.

(42) Kisu, K.; Iwama, E.; Onishi, W.; Nakashima, S.; Naoi, W.; Naoi, K. Ultrafast Nano-Spherical Single-Crystalline $LiMn_{0.792}Fe_{0.198}Mg_{0.010}PO_4$ Solid-Solution Confined Among Unbundled Interstices of SGCNTs. *J. Mater. Chem. A* **2014**, 2, 20789–20798.

(43) Panda, M. R.; Bhowmik, R. N.; Singh, H.; Singh, M. N.; Sinha, A. K. Air Annealing Effects on Lattice Structure, Charge State Distribution of Cations, and Room Temperature Ferrimagnetism in the Ferrite Composition $Co_{2.25}Fe_{0.75}O_4$. *Mater. Res. Express* **2015**, 2, 036101.

(44) Bhowmik, R. N.; Panda, M. R.; Yusuf, S. M.; Mukadam, M. D.; Sinha, A. K. Structural Phase Change in $Co_{2.25}Fe_{0.75}O_4$ Spinel Oxide by Vacuum Annealing and Role of Coexisting CoO Phase on Magnetic Properties. *J. Alloys Compd.* **2015**, 646, 161–169.

(45) Panda, M. R.; Sau, S.; Mitra, S.; Spectroelectrochemical Cell Holding Set-up for In-Situ/Operando Synchrotron-Based Measurements *IN Patent App.* 201921023104, **2019**.

(46) Joseph, D.; Yadav, A. K.; Jha, S. N.; Bhattacharyya, D. Chemical shift of Mn and Cr K-edges in X-ray Absorption Spectroscopy with Synchrotron Radiation. *Bull. Mater. Sci.* **2013**, 36 1067–1072.

(47) Lytle, F. W. The EXAFS Family Tree: A Personal History of the Development of Extended X-ray Absorption Fine Structure. *J. Synchrotron Radiat.* **1999**, 6, 123–134.

(48) Mastelaro, V. R.; Zanotto, E. D. X-Ray Absorption Fine Structure (XAFS) Studies of Oxide Glasses a 45-Year Overview. *Materials* **2018**, 11, 204.

(49) Singh, S.; Panda, M. R.; Sen, R.; Johari, P.; Sinha, A. K.; Meena, S. S.; Mitra, S. Study of Higher Discharge Capacity, Phase Transition, and Relative Structural Stability in Li_2FeSiO_4 Cathode upon Lithium Extraction Using an Experimental and Theoretical Approach and Full Cell Prototype Study. *ACS Appl. Energy Mater.* **2019**, 2, 6584–6598.

(50) Stern, E. A. Theory of the Extended X-Ray-Absorption Fine Structure. *Phys. Rev. B* **1974**, 10, 3027.

(51) Shuai, J.; Yoo, H. D.; Liang, Y.; Li, Y.; Yao, Y.; Grabow, L. C. Density Functional Theory Study of Li, Na, and Mg Intercalation and Diffusion in MoS_2 with Controlled Interlayer Spacing. *Mater. Res. Express* **2016**, 3, 064001.

(52) Enyashin, A. N.; Seifert, G. Density-Functional Study of Li_xMoS_2 Intercalates (0<=x<=1). *Comput Theor Chem* **2012**, 999, 13–20.

(53) Sanville, E.; Kenny, S. D.; Smith, R.; Henkelman, G. Improved Grid-Based Algorithm for Bader Charge Allocation. *J. Comput. Chem.* **2007**, 28, 899–908.

(54) Yu, M.; Trinkle, D. R. Accurate and Efficient Algorithm for Bader Charge Integration. *J. Chem. Phys.* **2011**, 134, 064111.

(55) Li, Q.; Yao, Z.; Wu, J.; Mitra, S.; Hao, S.; Sahu, T. S.; Li, Y.; Wolverton, C.; Dravid, V. P. Intermediate Phases in Sodium Intercalation into MoS_2 Nanosheets and Their Implications for Sodium-Ion batteries. *Nano Energy* **2017**, 38, 342–349.

CHAPTER 5

An excellent and fast anode for lithium-ion batteries based on 1T'–$MoTe_2$ phase material

"The 1T'-phase of $MoTe_2$ that is synthesized by a solid-state route as a fast anode for LIBs is discussed in this chapter. Ex situ X-ray absorption near-edge structures are used to reveal the unique lithium reaction pathway and storage mechanism of 1T'-phase of $MoTe_2$ anode, which is further complemented by DFT calculations along with the full-cell prototype study."

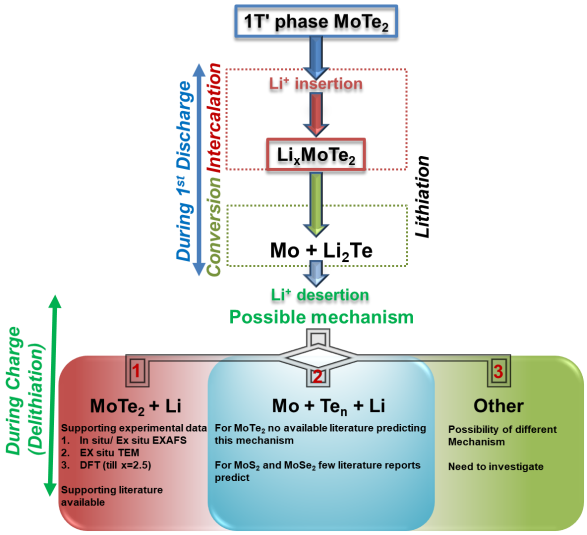

*An excerpt from this chapter is under review.

5.1 Introduction

Two-dimensional (2D) layered transition-metal dichalcogenides (TMDs) those have both the hexagonal (2H) phase with trigonal prismatic coordination and semiconducting characteristics as well as the monoclinic (1T') phase that has metallic or semimetallic characteristics are gaining attention of the researchers as an energy storage material for both battery and supercapacitor applications.[1–4] In the area of energy storage applications, among other 2D materials, $MoTe_2$ has shown greater applicability due to its lower bandgap, weak van der Waals interaction between the layers, unique interlayer vibrational behaviors and unique structure and higher-layer d-spacing. These properties are expected to help faster intercalation/deintercalation of both Li^+ and Na^+, while implementing $MoTe_2$ as an anode material in LIB and SIB applications. From our study, discussed in chapter 4 of this thesis, where we have implemented the 2H phase of $MoTe_2$ as an anode for LIB application, we show that the 2H phase of $MoTe_2$ has faster Li^+ diffusion properties than shown by other researchers where the 2H phase of $MoTe_2$ has been used as an anode material for LIB/SIB application.[5–7]

Understanding and manipulating the transitions between the 2H and 1T' structures is an active research area. The 1T' phase of $MoTe_2$ is semimetallic (60 me V bandgap) and has shown higher carrier mobility.[6] Apart from energy storage applications due to its tunable bandgap, the higher magnetoresistance of the1T' phase of $MoTe_2$ has made it useful in optoelectronic, field-effect transistor, and sensor applications.[8–13] The energy difference between the metallic 1T' phase and the semiconducting 2H phase is minimal ($\Delta E < 50$ meV), which makes $MoTe_2$ a promising material among other TMDs for phase engineering.[14–16] Many studies show various processes, such as strain engineering, doping, controlled chemical vapor deposition (CVD) through laser irradiation and the like, which are used to convert the 2H phase of $MoTe_2$ to the metallic 1T' phase[15,17,18] The arrangement of the Te atom is the specific reason for the structural variation between the 2H and the 1T'–$MoTe_2$ phase.[16]

Further, it is known that, the semimetallic 1T'–$MoTe_2$, which has higher electronic conductivity, enhances electrochemical performances without any carbon additives.[6] Therefore, in this chapter, we report the 1T' phase of the $MoTe_2$ as an anode material for the LIB and the related electrochemical mechanism and full-cell studies. In this work, 1T'–$MoTe_2$ has been prepared through the solid-state route has been reported as an anode material in LIB applications. The as-prepared 1T'–$MoTe_2$ layered material has shown better electrochemical performance without any carbonaceous additives or surface modifications. In the 1T'–$MoTe_2$

it has been observed that the presence of Te vacancy, higher electronic conductivity, higher carrier mobility, and defects have played an active role in higher Li^+ diffusion.[6] To gain further understanding of the Li^+ storage mechanism in 1T'–$MoTe_2$ during the Li^+ insertion and desertion process, we have carried out detailed studies including ex situ XANES measurements and analyses that is supported by density functional theory (DFT) calculations.

5.2 Synthesis of the 1T' phase of molybdenum ditelluride

A 1T'–$MoTe_2$ polycrystalline powder was prepared by mixing a stoichiometric amount of molybdenum (Sigma–Aldrich, 99.999 %) and tellurium (Sigma–Aldrich, 99.999 %) powders. The Mo powder was pre-sintered at 600 °C in an argon atmosphere for 8 h. Subsequently, the Mo powder was uniformly mixed with tellurium powder by hand-grinding in an argon atmosphere to obtain a precursor for 1T'–$MoTe_2$ synthesis.

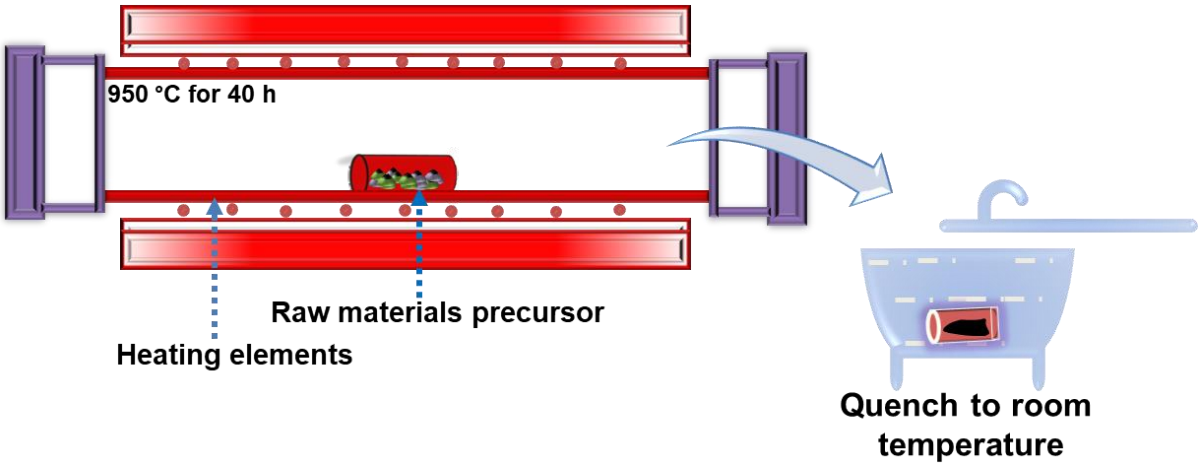

Figure 5.1 Schematic representation of the preparation of 1T'–$MoTe_2$.

The mixed powder was then sealed under vacuum (10^{-5} torr of pressure) in a quartz ampoule of an inner diameter of 12 mm. The ampoule that contained the precursors was purged under argon several times before evacuation to remove additional oxygen. After sealing the precursor powder, the precursors inside the ampoule were spread horizontally and placed inside the furnace. The temperature of the furnace was increased slowly from room temperature to 950 °C. The temperature was maintained at 950 °C for 40 h to complete the alloying reaction.[7,19,20] The temperature was quenched to room temperature by an ice bath to capture the 1T' phase of the $MoTe_2$ (**Figure 5.1**). After cooling to room temperature, a black powder of 1T'–$MoTe_2$ was obtained, which was ground in an inert atmosphere before further characterization.

5.3 Results and discussion

After successfully synthesizing the material, various characterization techniques such as XRD, XPS, FESEM and HRTEM were used for phase confirmation, in finding the chemical compositions, and to observe the morphologies of the as-prepared 1T'–$MoTe_2$ powder sample. Ex situ XANES techniques were used to monitor the electrochemical reaction mechanism. Moreover, conventional electrochemical measurements have been performed to monitor the electrochemical performance and Li^+ storage mechanisms. To support the experimental study and for understanding of the process of lithiation/delithiation, calculations employing DFT were performed to study the structural evolution during the lithiation/ delithiation process.

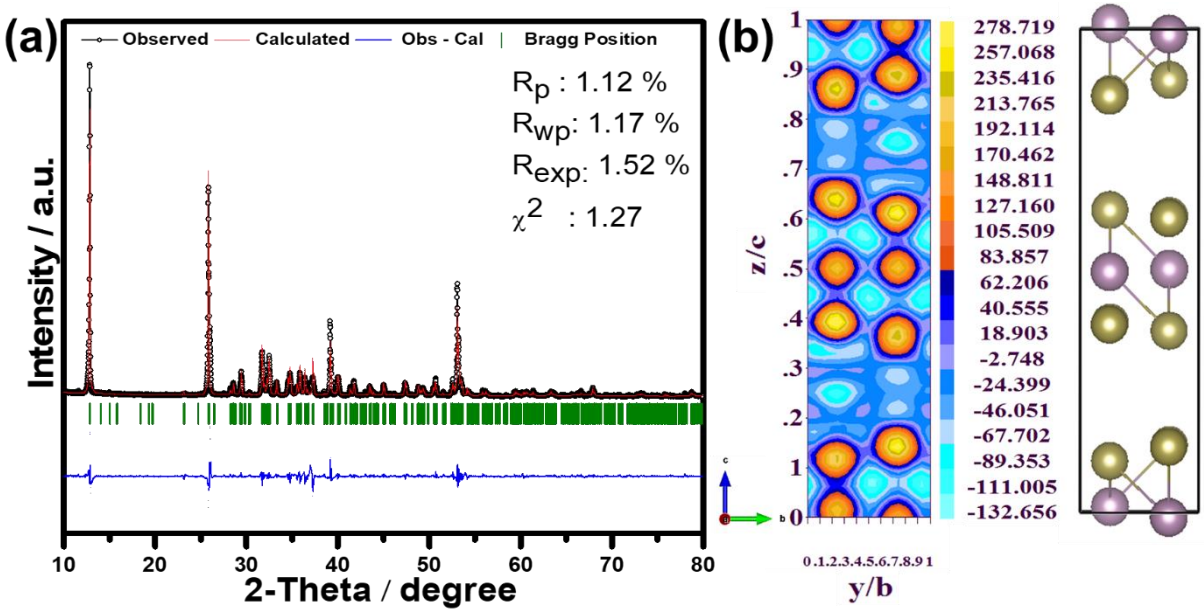

Figure 5.2 (a) The XRD pattern of the as-prepared 1T' phase of the $MoTe_2$ powder, and the Rietveld refinement plot along with the fitted parameters, and (b) The electronic structure of the as-prepared 1T' phase of the $MoTe_2$ powder, showing the electron density distribution.

5.3.1 Structural characterization of as-prepared 1T'–$MoTe_2$

Figure. 5.2a represents the typical XRD pattern of the as-prepared 1T' phase of the $MoTe_2$ powder sample. The XRD pattern was analyzed using the Rietveld refinement program. The inset of **Figure 5.2a** shows the obtained fitting parameters from Rietveld refinement, such as R_p (1.12 %), R_{wp} (1.17 %), R_{exp} (1.52 %) and χ^2 (1.27), and all these values are found to lie in a reasonable range. This confirms the acceptable quality of the Rietveld refinement and the phase purity of the 1T'–$MoTe_2$structure. The XRD peaks have been indexed with the phase of

the monoclinic structure with the space group, $P2_1/m$. **Figure 5.2b** illustrates the electron density distribution of the as-prepared 1T' phase of the $MoTe_2$.

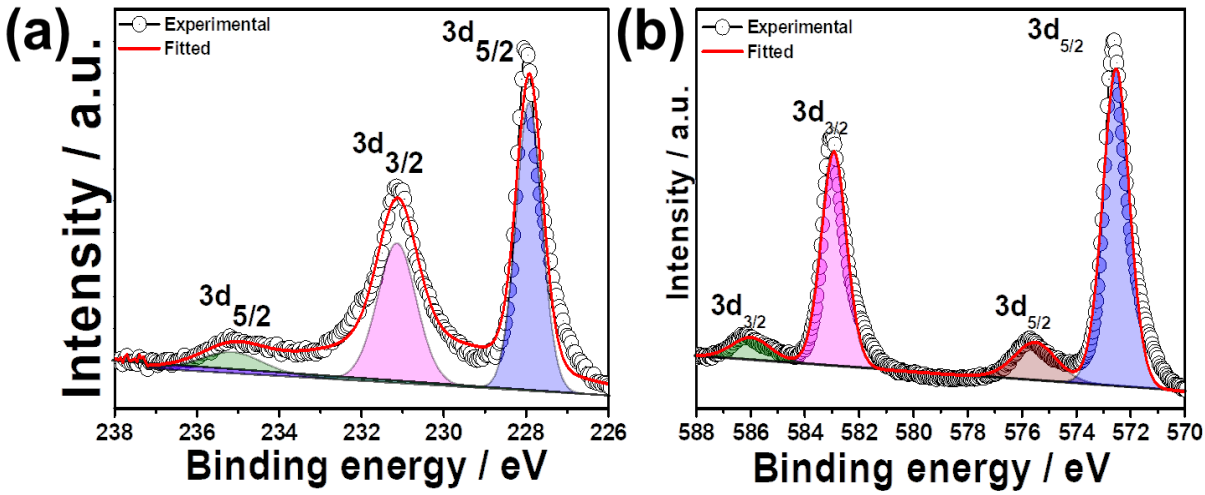

Figure 5.3 HRXPS spectra of (a) Mo 3d and (b) Te 3d of pristine 1T'–$MoTe_2$ powder.

To obtain the surface chemical composition and the charge state of the as-prepared 1T'–$MoTe_2$ sample, XPS measurements were performed. **Figure 5.3a** shows the HRXPS peaks of Mo $3d_{5/2}$ at 227.88 eV and $3d_{3/2}$ at 231.12 eV, which is a result of the 1T'–$MoTe_2$ phase. The HRXPS peaks of Te $3d_{5/2}$ and $3d_{3/2}$ at 572.54 eV and 582.93 eV are shown in **Figure 5.3b**, respectively. These results confirm the phase purity of the 1T'–$MoTe_2$ sample.[21,22] The two additional peaks of Te at 576.53 eV and 586.08 eV with lower intensities are due to the TeO_2 phase from the oxidation of the high-activity surface of the 1T'–$MoTe_2$ sample. The HRXPS peak of Te, which corresponds to Te^{4+}, further shows a shift from the original position. This confirms the possibility of molybdenum vacancy in the as-prepared $MoTe_2$ powders, as observed in the literature.[5–7,20] Our obtained results show that the Mo and Te HR peaks downshift by ~0.5 eV from the Mo and Te HR peaks of 2H phase of $MoTe_2$. These observations are in good agreement with the existing literature and further confirm the phase purity of the 1T'–$MoTe_2$ sample.[21,22]

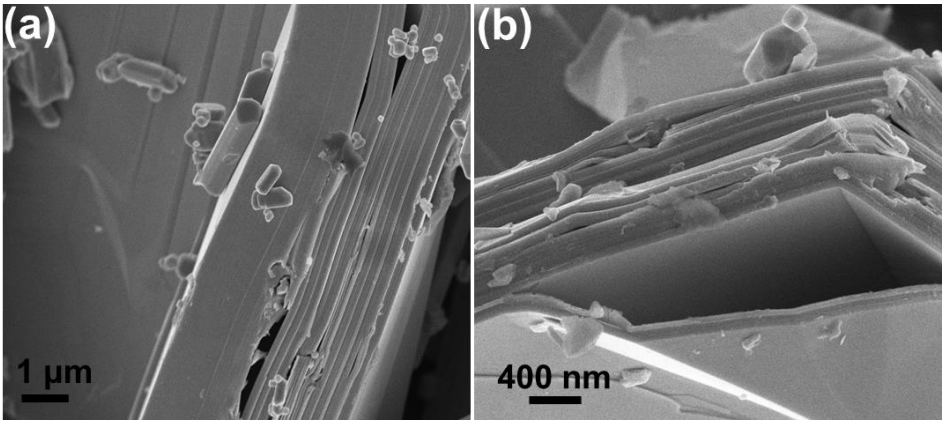

Figure 5.4 (a–b) Field-Emission Scanning Electron Microscope (FESEM) images of the as-prepared 1T'–$MoTe_2$ powder.

The pristine $MoTe_2$ powder, which can be seen in FESEM images, shows the bulk-layer morphology with an abundance of folds and cracks (**Figure 5.4**). The morphology of the sample shows a bulky sheet structure that has several fine plane folds and cracks.

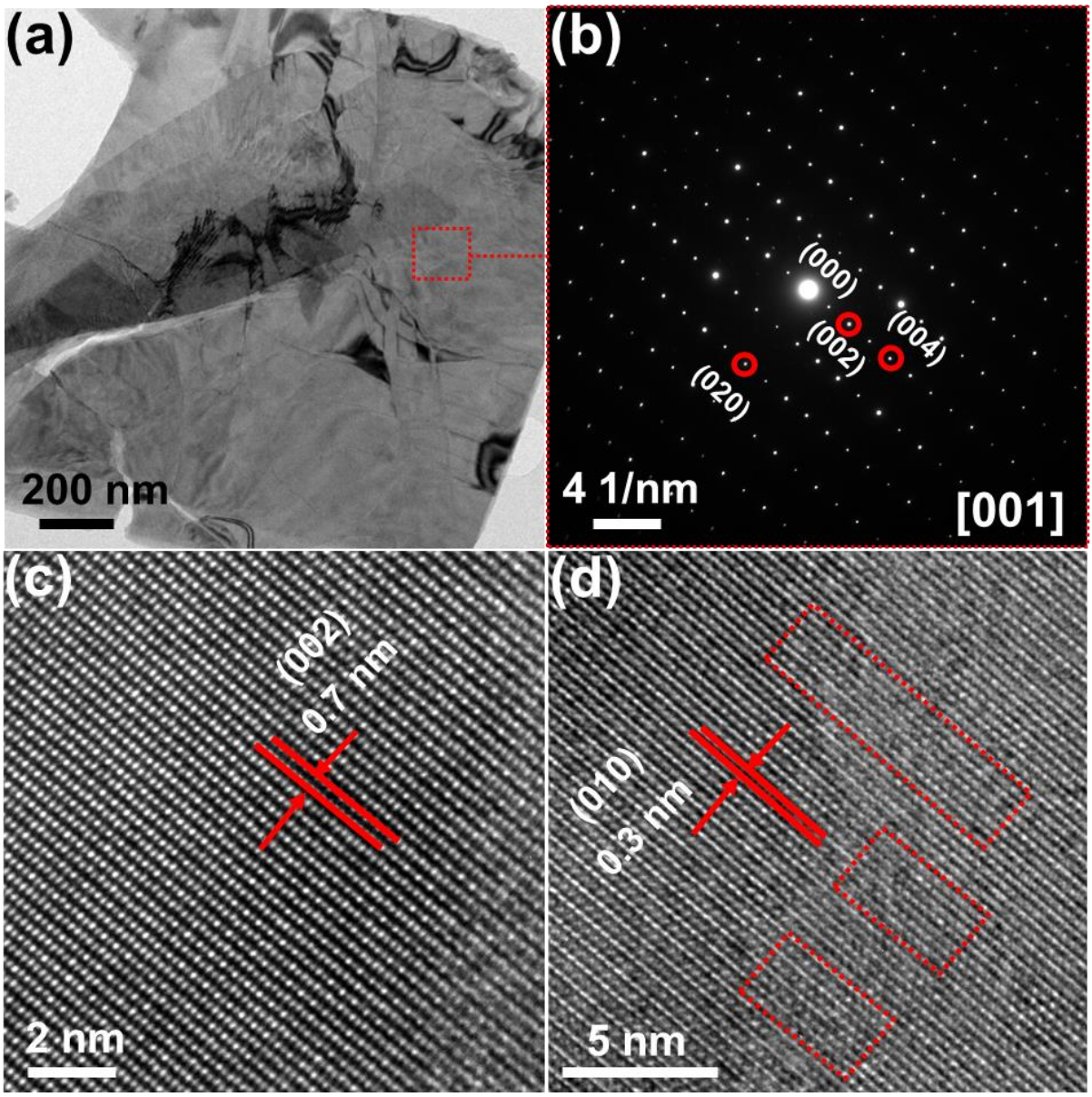

Figure 5.5 Electron microscopy studies of the as-synthesized $MoTe_2$ sample. (a) Bright-field TEM (BFTEM) image of a flat crystal. (b) SAED pattern of the BFTEM image along the [001] direction, indicated in a). (c–d) HRTEM images, showing the corresponding planes of the 1T'-$MoTe_2$ sample. Inset of (d) shows occasional missing layers.

A few small rod-shaped particles have been observed on the surface of the plane folds. **Figure 5.5** shows the HRTEM image and SAED patterns, which present results of the investigations of the atomic arrangement of $MoTe_2$ and confirm the 1T' structure. **Figure 5.5a** shows the BFTEM image of a flat thin crystal, the electron diffraction of the same has been used to identify the preferential crystal and the related planes. The BFTEM image confirms that the crystal has a few layers of 1T'–$MoTe_2$ flakes from the single crystal in the 1T' phase. **Figure 5.5b** shows the corresponding SAED patterns along the [001] direction. The HRTEM images,

as shown in **Figure 5.5c**, match well with the corresponding d-spacing of 0.7 nm of the (002) plane. **Figure 5.5d** shows a d-spacing of 0.3 nm, which matches with the (010) plane. Rectangular insets in **Figure 5.5d** show a few defects, which are possibly due to the Mo or Te vacancy in the 1T' phase. The presence of these native vacancies or defects is expected to improve the efficient diffusion of Li^+ in the 1T'–$MoTe_2$ structure.[6,7]

5.3.2 Half-cell electrochemical measurements

Electrochemical performances were carried out to evaluate the storage properties of Li^+ and the relevant lithiation/delithiation mechanisms of 1T' $MoTe_2$. To investigate the storage mechanism of Li^+, recent literature on $MoTe_2$[5–7,20] and related types of TMDs, namely, MoS_2[23], $MoSe_2$[24], WS_2[25], WSe_2[26], and WTe_2[27] were considered as references. We employed ex situ XANES measurements to understand the phase reversibility and its relation to the lithiation/delithiation process.

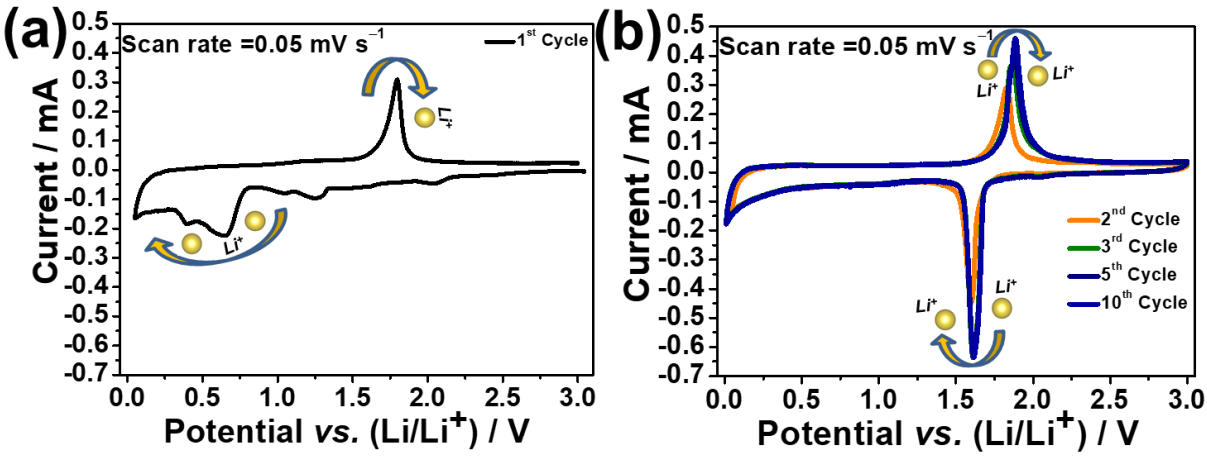

Figure 5.6 The CV curve of the 1T' phase of the $MoTe_2$ (used as electrode) vs. lithium metal. (a) First cycle and (b) Second, third, fifth, and tenth cycles of the $MoTe_2$ electrode at 0.05 mV s^{-1} in the voltage range of 0.01–3.00 V, using 1 M $LiPF_6$ in the EC/DMC (1:1vol./vol.) electrolyte in a half-cell configuration at 20±2 ºC.

Figure 5.6 shows the CV curve of 1T'–$MoTe_2$ against lithium at 0.05 mV s^{-1} in the potential window between 0.01 V and 3.00 V versus lithium with 1 M $LiPF_6$ in the EC/DMC (1:1vol./vol.) electrolyte in a half-cell configuration. It is clear that the reaction between $MoTe_2$ and Li^+ is quite different in the 1st cycle in comparison to the consecutive cycles. The electrochemical performance of the 1T'–$MoTe_2$ electrode against lithium metal in a half-cell configuration was checked. The cyclic voltammogram of the 1T'–$MoTe_2$ half cell (in comparison to Li/Li^+) showed a few redox peaks during the first lithiation process at 2 V, 1.3

V, and 1.0 V potentials along with a sharp peak at 0.64 V. The peaks at 2 V, 1.3 V, and 1.0 V, respectively, are due to the intercalation of Li into the $MoTe_2$ lattice structure, which forms the Li_xMoTe_2 structure in which x corresponds to different concentrations of lithium.[6,7] With the increase in the concentration of Li^+, the lattice disorder of $MoTe_2$ begins at 0.64 V. A sharp peak is observed along with a small peak at 0.39 V. The observed lower lithiation voltage peaks are due to the formation of Mo and Li_2Te ($MoTe_2 + 4Li^+ + 4e^- \rightarrow Mo + 2Li_2Te$), which are a result of the conversion of $MoTe_2$ and the construction of a solid electrolyte interphase (SEI).[5–7,20] This discussion agrees well with the existing literature, which reports that the cathodic peak (1.1–0.9 V) that is known for the intercalation and is in the range of (0.3–0.5 V) is indicative of a conversion reaction in case of MoS_2 and $MoSe_2$ electrodes.[23,24] From the 2nd cycle onwards, the reduction peak at 1.58 V results due to the distortion of the $MoTe_2$ lattice and electronic polarization.[6,7] The repeated reduction and oxidation peaks of the CV during the lithiation/delithiation process at higher cycles confirm the structural stability of the $MoTe_2$ anode.[5–7,20] The structural stability of the $MoTe_2$ anode compared with lithium is also seen in the existing literature on $MoTe_2$.[6,7]

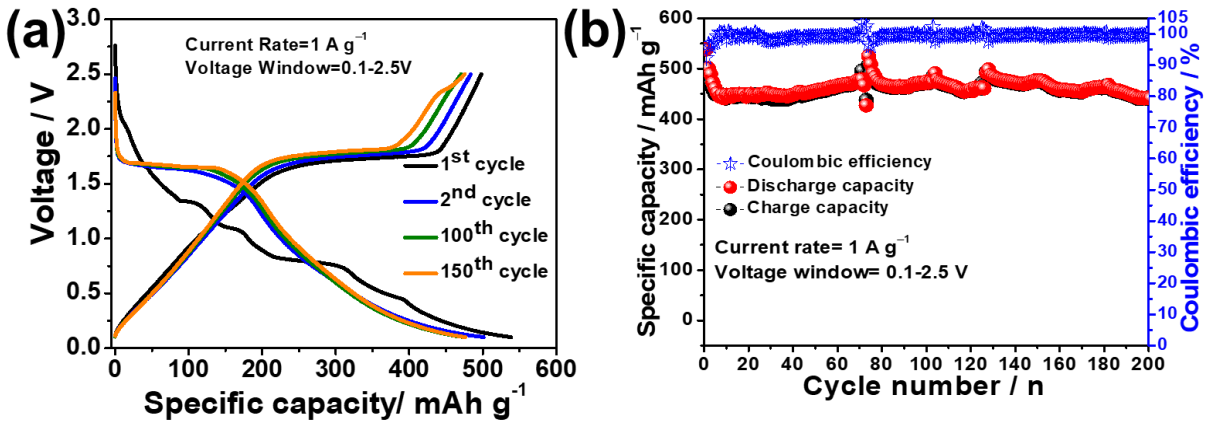

Figure 5.7 Half-cell configuration (1T'–$MoTe_2$ versus lithium metal) electrochemical performance at 1 A g^{-1} in the voltage window of 0.01–2.8 V. (a) Galvanostatic charge/discharge profile of $MoTe_2$. (b) Long-term cycling performance over 260 cycles.

Figure 5.7 shows the galvanostatic charge/discharge of the $MoTe_2$ electrode against lithium at 1 A g^{-1}. The observed plateaus during the first cycle followed the CV curve, as shown in **Figure 5.7a**. An initial discharge capacity of 538 mAh g^{-1}, with a charge capacity of 498 mAh g^{-1}, is observed during the first cycle. The nature of the broad discharge plateau in the 1st discharge process is due to the conversion reaction that is a result of the formation of Mo nanoparticles and SEI due to the decomposition of the electrolyte at a lower potential.[6,20,28,29] The shifting of reduction peaks to higher potentials from the second cycle onward is due to the decrease in

electrochemical polarization, which is a result of the reduction in size of the particles and distortion in the lattice.[6,20,30,31] For the initial five cycles, a stiff capacity degradation has been observed due to the formation of Mo nanoparticles during the lithiation process. The formed nanoparticles are prone to aggregation. This provides more surface area, which enables contact with the electrolyte, resulting in electrolyte degradation and additional SEI formation.[6,7,32,33] This process continues for a few initial cycles, which results in a thick SEI layer and is responsible for the initial loss in capacity.[7,33] From the second cycle onwards, a discharge capacity of 501 mAh g^{-1} and charge capacity of 487 mAh g^{-1} with enhanced Coulombic efficiency of 97 % with reference to the first cycle (92 %) is obtained. The half cell had capacity retention of 91.5 % (with reference to the 2nd cycle) and 99 % of Coulombic efficiency over 200 cycles (**Figure 5.7b**).

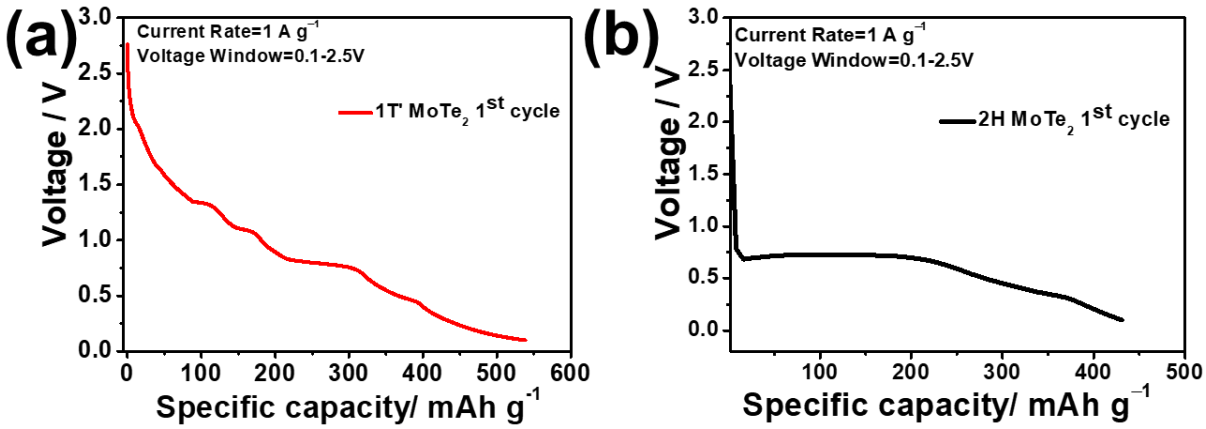

Figure 5.8 The first discharge Galvanostatic charge/discharge curve of (a) 1T'–$MoTe_2$electrode and (b) 2H $MoTe_2$ electrode vs. lithium at 1 A g^{-1} in the voltage range of 0.01–2.5 V.

The first cycles of both the 2H and 1T' $MoTe_2$ have been compared. In 1T'–$MoTe_2$, a few stepwise additional reduction peaks have been noticed at different concentrations of Li^+ in addition to the sharp reduction peak in the range of 0.5 V to 0.56 V (**Figure 5.8a,b**). This may be due to the higher stability and propensity for an electrochemical reaction of the 1T' phase compared to those of the 2H $MoTe_2$ phase. The other possible cause may be the formation of several metastable phases during the lithiation process between Li and $MoTe_2$,[23] which is difficult to observe through conventional ex situ characterization techniques. The broad discharge plateau in the 1st discharge process is due to the conversion reaction; this reaction is a result of the formation of Mo nanoparticles and SEI due to the decomposition of the electrolyte at a lower potential.[28,29] The shifting of reduction peaks to higher potentials is due

to the decrease in electrochemical polarization, which is a result of the reduction in the size of the particle and the distortion in the lattice.[5–7,20,23] In **Figure 5.19**, we have outlined different possibilities for the 1T'–$MoTe_2$–Li reaction. We have performed in situ Electrochemical Impedance Spectroscopy (EIS) study along with XANES measurements to understand the underlying reaction mechanism and the reaction products after discharge-charge cycling.

5.3.3 Electrochemical Impedance Spectroscopy (EIS) study of cycling and the estimation of Li^+ diffusion coefficients (D_{Li+})

The lithium transport kinetics in the 1T'–$MoTe_2$ material during the lithiation/delithiation process have been investigated by CV at different scan rates, as shown in **Figure 5.9a**. There is a noticeable shift of the reduction peak (I) toward the lower potential and the oxidation peaks are shifted toward the higher potentials as the scan rate is increased (0.05 to 1.00 mV s^{-1}). This peak current versus scan rate obeys the power law ($i_p=a\ v^b$)[7,34] in which the log i_p versus log v yields a slope that resembles the b value. The value of b, which is close to 1, specifies a capacitive-controlled ion storage process; whereas, the b value of ~0.5 (**Figure 5.10**) proposes a solid-state diffusion process.[7,34]

For the 1T'–$MoTe_2$ electrode, the observed b values for the reduction I and oxidation I' peaks are 0.65 and 0.63, as seen in **Figure 5.9b**. This shows that the Li^+ transport kinetics in the 1T'–$MoTe_2$ electrode follows both surface-controlled and diffusion-controlled reactions. This observation indicates that the Li^+ transport kinetics of the 1T'–$MoTe_2$ electrode is principally ruled by the pseudocapacitance.[7,21]

The origin of pseudocapacitance may be assigned to the increased surface area through nanostructuring during the phase transformation of 2D materials during the lithiation/delithiation process. Nanostructuring helps to provide an additional surface for electrolyte access, which results in the additional Li^+ storage sites. The other advantage of nanostructuring is that it enables a decrease in the Li^+ diffusion length, which results in a high rate capability.[35] The electrodes that display capacitive behavior are less dominant than those that display diffusion-controlled behavior (**Figure 5.9c**) and have dominant Li^+ storage sites, which are contributed by the surface; therefore, the charging rate is relatively rapid and surface-controlled. These advantages make layered anodes a potential candidate for use as high-rate LIB anodes.[36]

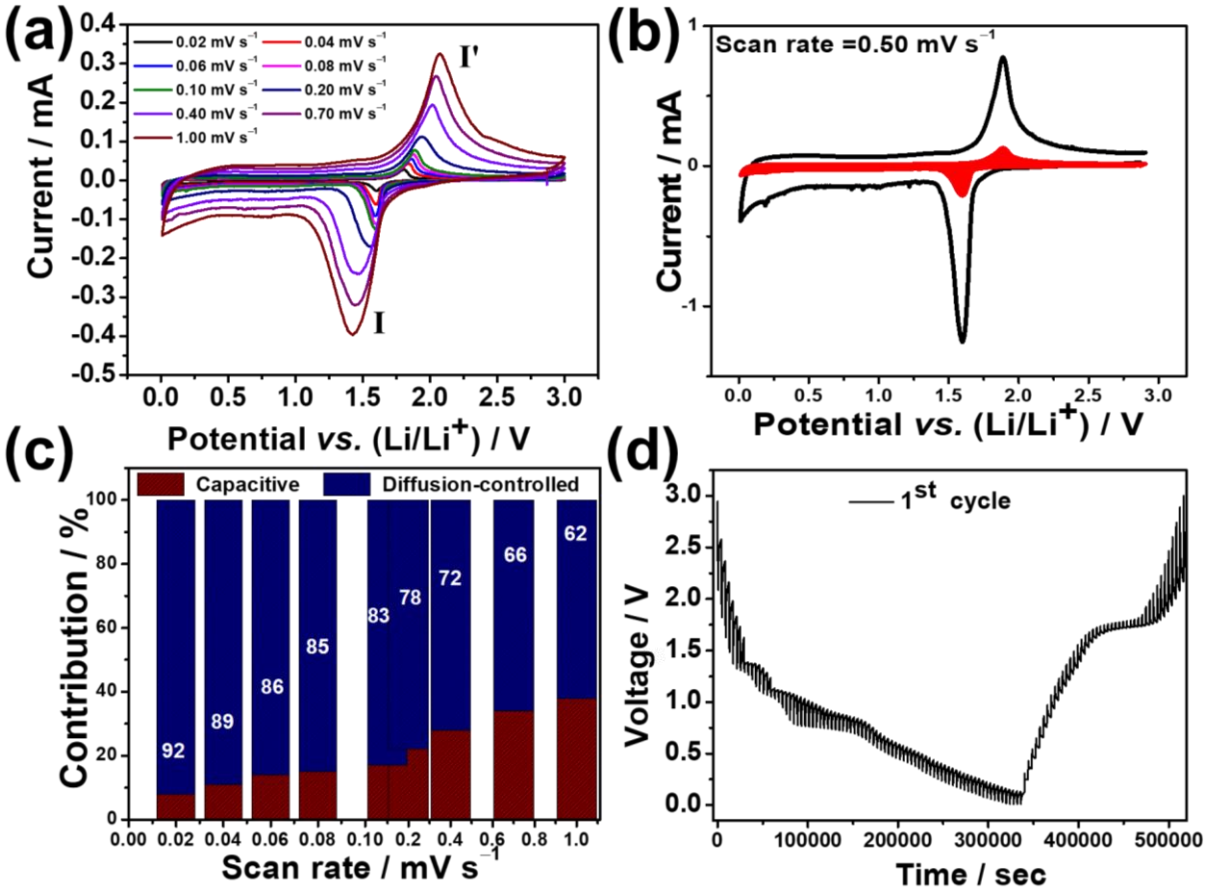

Figure 5.9 Kinetics study and quantitative analysis of the Li^+ storage mechanism in the $MoTe_2$ (a) CV of the different scan rates of the 1T'–$MoTe_2$ electrode. (b) Fitted CV curve, showing pseudocapacitive-contribution (red area) at 0.50 mV s^{-1}. (c) The ratio of the pseudocapacitive (red) and diffusion-controlled (blue) capacities of the 1T'–$MoTe_2$ electrode at different scan rates. (d) Voltage profile at a constant current pulse of the 1T' $MoTe_2$ electrode during the first cycle.

The current that is obtained through the CV of different scan rates corresponds to a particular potential that arises due to two phenomena: the surface-contributed capacitive effect and the diffusion-controlled insertion process.[7,20,21] These two processes can be designated quantitatively by the different sweep rates of the obtained CV results according to the equation, $i(v)=k_1v + k_2v^{1/2}$. Here, i(v) is associated with the total current contributions, which can be split by k_1v and $k_2v^{1/2}$. They are designated as the capacitive contribution of the surface and the diffusion-controlled insertion process, as shown in **Figure 5.9c**. The fitted CV curve (**Figure 5.9b**) represents the contribution of the capacitive current in the shaded red region in comparison to the total current at a scan rate of 0.1 mV s^{-1} of the 1T'–$MoTe_2$ electrode. From the analysis, it has been observed that the majority contribution (83 %) of the total Li^+ storage capacity was by the diffusion-controlled insertion process. The 1T'–$MoTe_2$ electrode shows 92

%, 89 %, 86 %, 85 %, 83 %, 78 %, 72 %, 66 %, and 62 % of diffusion-controlled insertion contributions at scan rates of 0.02, 0.04, 0.06, 0.08, 0.10, 0.20, 0.40, 0.70, and 1.00 mV s^{-1} (**Figure 5.9c**).

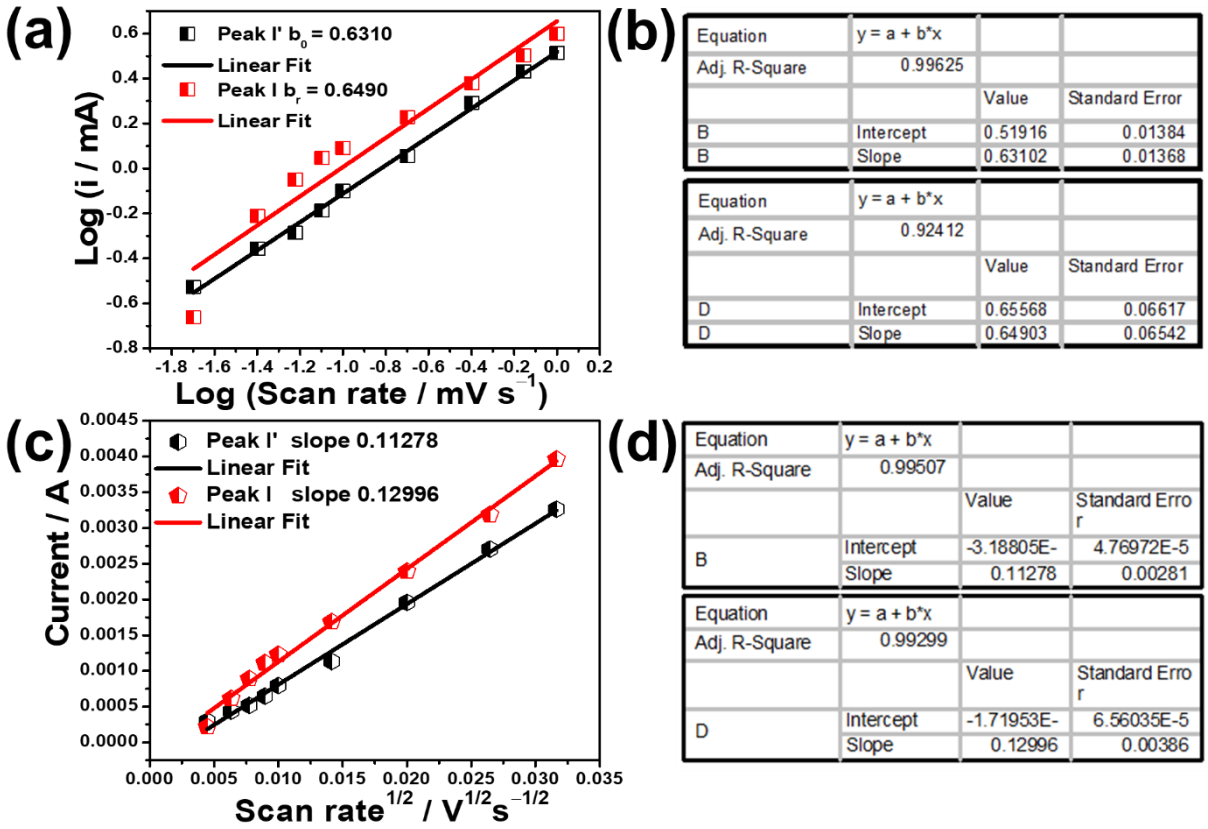

Equation	y = a + b*x		
Adj. R-Square	0.99625		
		Value	Standard Error
B	Intercept	0.51916	0.01384
B	Slope	0.63102	0.01368

Equation	y = a + b*x		
Adj. R-Square	0.92412		
		Value	Standard Error
D	Intercept	0.65568	0.06617
D	Slope	0.64903	0.06542

Equation	y = a + b*x		
Adj. R-Square	0.99507		
		Value	Standard Error
B	Intercept	-3.18805E-	4.76972E-5
	Slope	0.11278	0.00281

Equation	y = a + b*x		
Adj. R-Square	0.99299		
		Value	Standard Error
D	Intercept	-1.71953E-	6.56035E-5
	Slope	0.12996	0.00386

Figure 5.10 Li^+ kinetics study and quantitative analysis of the 1T'–$MoTe_2$ anode. (a) Peak current vs. scan rates of the lithiation (I) and delithiation (I') peaks. (b) Table showing corresponding fitted parameters. (c) Peak current versus the square root of the scan rate of the reduction (I) and oxidation (I') peaks. (d) Table showing corresponding fitted parameters.

Further, the Randles–Sevcik equation has been used to estimate the Li^+ diffusion coefficient. It has been observed that the Li^+ apparent diffusion coefficients that correspond to both reduction and oxidation peaks are of the order of $10^{-9}$$cm^2$ s^{-1}, as shown in **Table 5.1** (between 2.09×10^{-9} and 2.82×10^{-9}). The obtained result shows that the Li^+ diffusion coefficient of the 1T'–$MoTe_2$ electrode is much superior to other Mo-based chalcogenides such as MoS_2 and $MoSe_2$.[37–39]

Figure 5.9d shows the voltage profile at a constant current pulse of the 1T' $MoTe_2$ electrode during the first cycle, illustrating different potential steps during the insertion and removal of Li^+ within the 1T'–$MoTe_2$ structure.

Table 5.1 Calculation of the diffusion coefficient from CV at different scan rates of the 1T'–$MoTe_2$ electrode.

Scan rate ($mV\ s^{-1}$)	**V(I')**	**I(I')**	**V(I)**	**I(I)**
0.02	1.800	0.297	1.606	0.218
0.04	1.839	0.439	1.601	0.615
0.06	1.858	0.517	1.598	0.893
0.08	1.873	0.649	1.597	1.115
0.10	1.885	0.795	1.597	1.232
0.20	1.943	1.134	1.556	1.689
0.40	2.011	1.958	1.456	2.394
0.70	2.046	2.706	1.437	3.188
1.00	2.073	3.264	1.421	3.966
Diffusivity ($cm^2\ s^{-1}$)		$2.09*10^{-9}$		$2.82*10^{-9}$

The used denominations are V(I') and I (I'), oxidation peak voltage and current, V(I) and I (I), reduction peak voltage and current, respectively.

To gain deeper insight into the Li^+ storage performance of the 1T'–$MoTe_2$ electrode, EIS was carried out for the initial 50 cycles. This is a relevant technique, which enables comprehension of the electrochemical kinetics of the electrode and the electrolyte.[7,20,23]

Electrochemical impedance spectroscopy spectra were taken after full-discharge and -charge states of the initial 50 cycles to observe the changes that occurred in the cell during the discharge–charge cycling. It has been observed that the EIS spectra for the discharge process are different from the charge process. **Figure 5.11** shows the EIS spectra of the initial 50 cycles after the discharge process. The EIS spectra show two distinct semicircles after the full-discharge states of each cycle. The two semicircles are present possibly because of the two phases, Mo and Li_2Te, which occur after full discharge. After a few cycles, the EIS spectra of the discharge process remain unchanged, which confirms that the lithiation reaction is stable after a few cycles.[23]

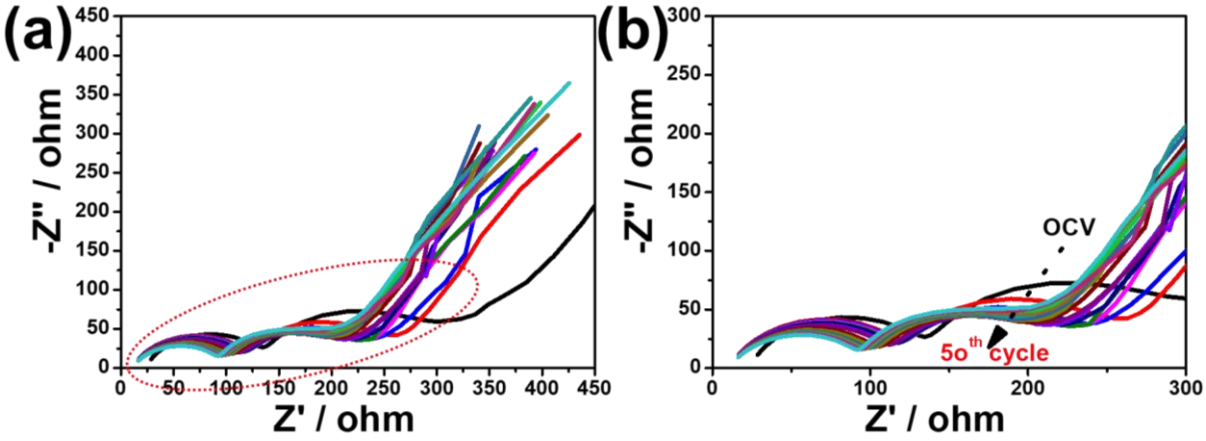

Figure 5.11 Nyquist plots of 1st to 50th cycle after the full-discharge state of the 1T'–$MoTe_2$ electrode *vs.* Li/Li^+.

Figure 5.12 shows the Nyquist plots at OCV and after cycling (1st to 50th cycle) through the full-charge states of the 1T'–$MoTe_2$ electrode. The diameter of the semicircle of the 1T'–$MoTe_2$ (in the observed Nyquist plots) is smaller than the diameter of the OCV in the high-to-medium frequency region of the electrode after a few cycles. This observation confirms that the 1T'–$MoTe_2$ electrode possesses lower-order contact and charge-transfer resistances after a few cycles.[40] The observed R_{ct} value decreases continuously and becomes stable after 10 cycles due to the transformation of the 1T'–$MoTe_2$ into amorphous nanocrystals during the continuous charge/discharge process.[5–7,20] The decrease in the R_{ct} values refers to the increasing ionic conductivity of the 1T'–$MoTe_2$ electrode along with the increase in Li^+ insertion, which generates an additional conducting 1T'–$MoTe_2$ phase. After 10 cycles, the unchanged values of R_{ct} and other parameters, which result from the EIS spectra, confirm the structural stability of the cycled 1T'–$MoTe_2$ electrode during the repeated lithiation and delithiation processes.

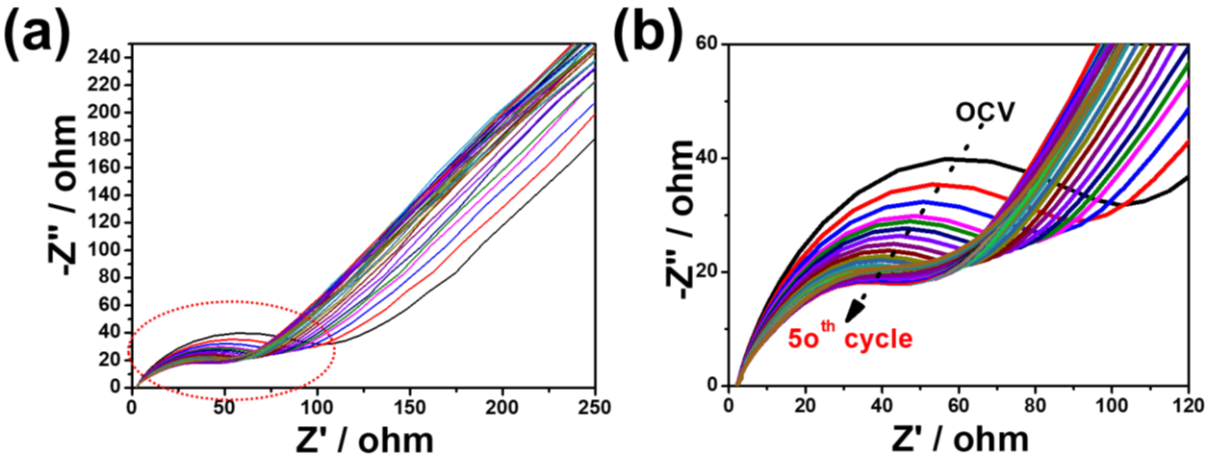

Figure 5.12 Nyquist plots at OCV, after the 1st to 50th cycle (full-charge state) of the 1T' $MoTe_2$ electrode vs. Li/Li^+.

The EIS results are in good agreement with the results of XANES and, possibly, mechanism 1. (**Figure. 5.19**). This confirms the possible conversion reaction, the existence of two phases after the full-discharge process, and the reversibility of 1T'–$MoTe_2$ after the charging process.

The ex situ XANES technique has been employed to understand the reaction mechanism in ex situ mode of the 1T'–$MoTe_2$ material when compared with lithium in a half-cell configuration. When a battery is in a working condition, XANES is the best spectroscopy technique to track the phase evolution, because it is more sensitive to local chemical and electronic changes in the studied material.[6,20,41] It has been observed that, during cycling in the different stages of discharge and charge potentials, chemical evolution may take place in a particular direction. However, when the concentration of Li^+ is increased, that is, at higher discharge/charge potentials, chemical evolution may occur in all directions throughout the bulk of the active material. To investigate the phase transformation at the bulk level more accurately and to obtain all possible intermediate phases during phase evolution, XANES is the most suitable technique. Due to the element-specific properties of the XANES technique, it can provide insight into the mechanism of phase changes that occurs inside the battery due to the strain on the materials during cycling; it also provides insight into the variations in the charge state of the element under investigation.[6,15,41–43]

5.2.4 Ex situ XANES studies of cycled electrodes

Ex situ XANES was performed at the Mo K-edge of different electrode samples to understand the electrochemical mechanism during the lithiation/delithiation process. The XANES technique is useful in monitoring the charge state of Mo and in investigating the structural variation of 1T'–$MoTe_2$ during the lithiation/delithiation process of the 1T'–$MoTe_2$ electrode. The technique also provides information about coordination geometry and other relevant features that are associated with different regions, namely, pre-edge, rising-edge, post-edge, and the like.[6,20,41–43] The normalized Mo K-edge XANES spectra for $MoTe_2$ electrodes at various discharge/charge cycles (as-prepared, after the 1^{st} and 5^{th} discharged states, and after the 1^{st} and 5^{th} cycles in a charged condition) are shown in **Figure 5.13**, with Mo metal foil as the reference.

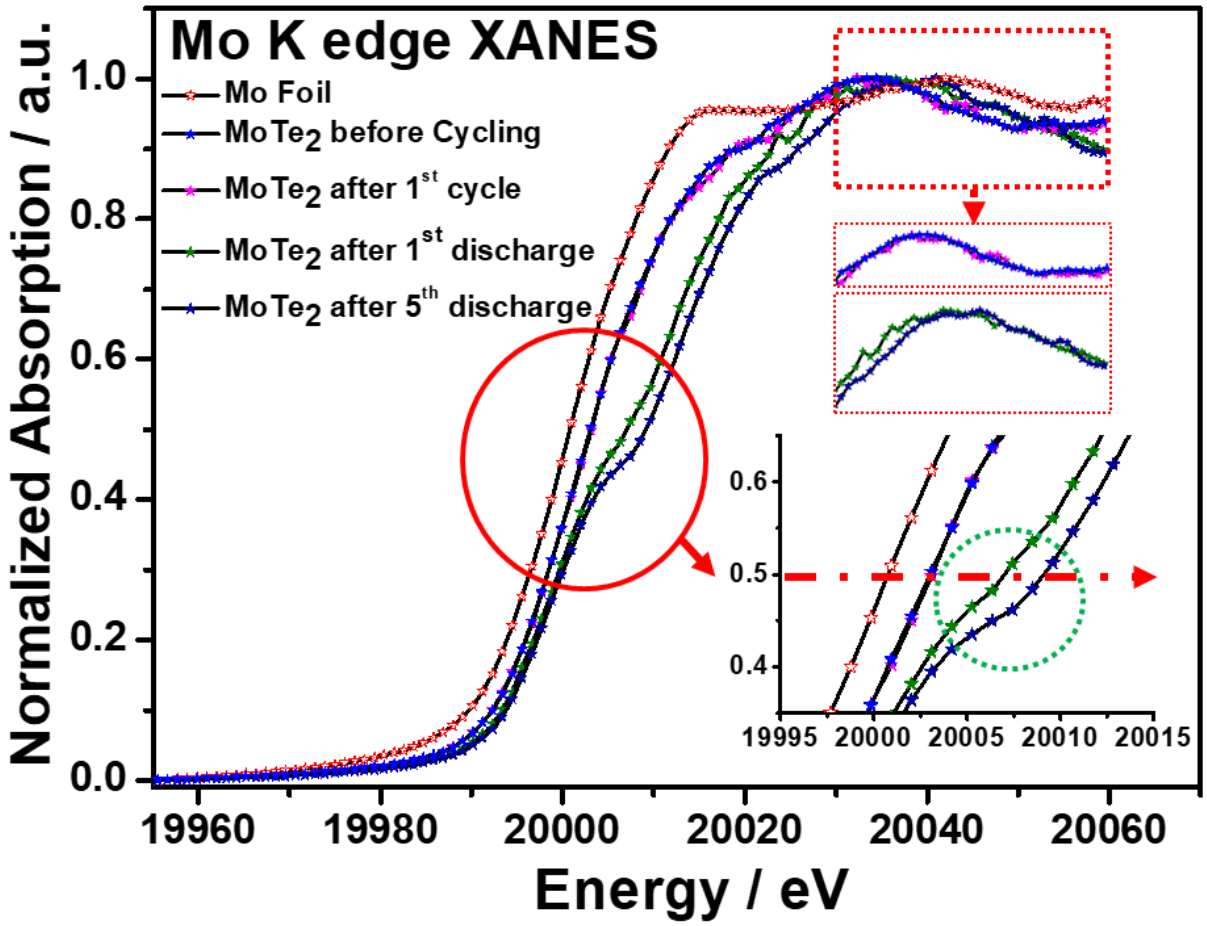

Figure 5.13 Ex-situ XANES measurements of 1T'–$MoTe_2$ electrodes before cycling and at various discharge/charge states, and (b) Normalized Mo K-edge XANES spectra of 1T'–$MoTe_2$ electrodes before cycling, after 1st and 5th discharged states, after the 1st cycle in a charged state, and the Mo foil reference spectra. Inset: zoomed-in region showing edge and post-edge regions.

The binding energy shift (ΔE) of the electrodes obtained by the maxima of the first derivative of the absorption edge region of Mo XANES spectra corresponds to the variation of the charged state of Mo.[6,20,41–43] The Mo metal foil that corresponds to the zero-charge state of Mo is used as a reference; any value of energy shift (ΔE) toward the right corresponds to an increase in the charge state of Mo, whereas any value of energy shift (ΔE) toward the left corresponds to a decrease in the charge state of Mo. Above the rising-edge with typical wiggles/oscillatory features, the post-edge region offers information about the nearest neighbors and the local chemistry.[7,41,43]

It has been observed that the edge-step normalized energies of the as-prepared samples and the samples after the 1st cycle are in the same order, whereas the 1st discharge and 5th discharge electrode samples are in a different order. The oxidation states of Mo for the as-prepared

samples and for samples of the electrode after the 1st cycle at a charged state are +4, and the energies that correspond to the charge state of Mo is +4, which confirms the $MoTe_2$ structure. The edge-step normalized energies for the 1st and 5th discharged state electrode samples are observed at a higher energy, which corresponds to the increase in the core electron binding energy with a distinct pre-edge peak (inset of **Figure 5.13**). This observation results from the as-formed Mo nanoparticles that oxidize to a highly stable oxide (that is, MoO_3). The distinct pre-edge features for the electrodes after the 1st discharge and the 5th discharge correspond to the local symmetry around Mo atoms, which results in the transition from the core 1s level to the unoccupied 4d orbitals.[7,23,41,43] The presence of pre-edge peaks and the energy shift (ΔE) toward the higher value confirms that the charge state of Mo for the electrodes after the 1st and 5th discharge states are close to +6, which corresponds to the MoO_3 structure and agrees well with the reported literature.[20,23] It has been observed that for the as-prepared electrode and after the 1st cycle, electrodes above the rising-edge have similar wiggles/oscillatory features (inset of **Figure 5.13**). Similarly, for the electrodes after the 1st and 5th discharge states, we find similar wiggles/oscillatory features (inset of **Figure 5.13**), which further confirms that the structure and the charge state of Mo are the same for the as-prepared electrode, for electrodes after the 1st cycle; similarly, for the electrodes after the 1st and 5th discharge states offer similar information.

Figure 5.14 shows the morphology of the electrodes after full discharge and after the 1st cycle at full-charge states along with the as-prepared electrodes. The morphology of the as-prepared electrode (**Figure 5.14a**) shows carbon coating on the surface of the broken pieces of the 1T'–$MoTe_2$ electrode samples, which is a result of the slurry-making process. After the 1st discharge at the full-discharge state, the morphology of the electrodes has been observed to be highly porous and consists of sheets of the agglomerated phase. It may be noted that the morphology changes to a flower-type morphology (**Figure 5.14a,b**) due to the exfoliation and agglomeration of the sheets that are formed in the discharge process. The flower-type morphology provides additional surface area for greater electrolyte access and enhanced electrochemical reaction during the lithiation/delithiation process.

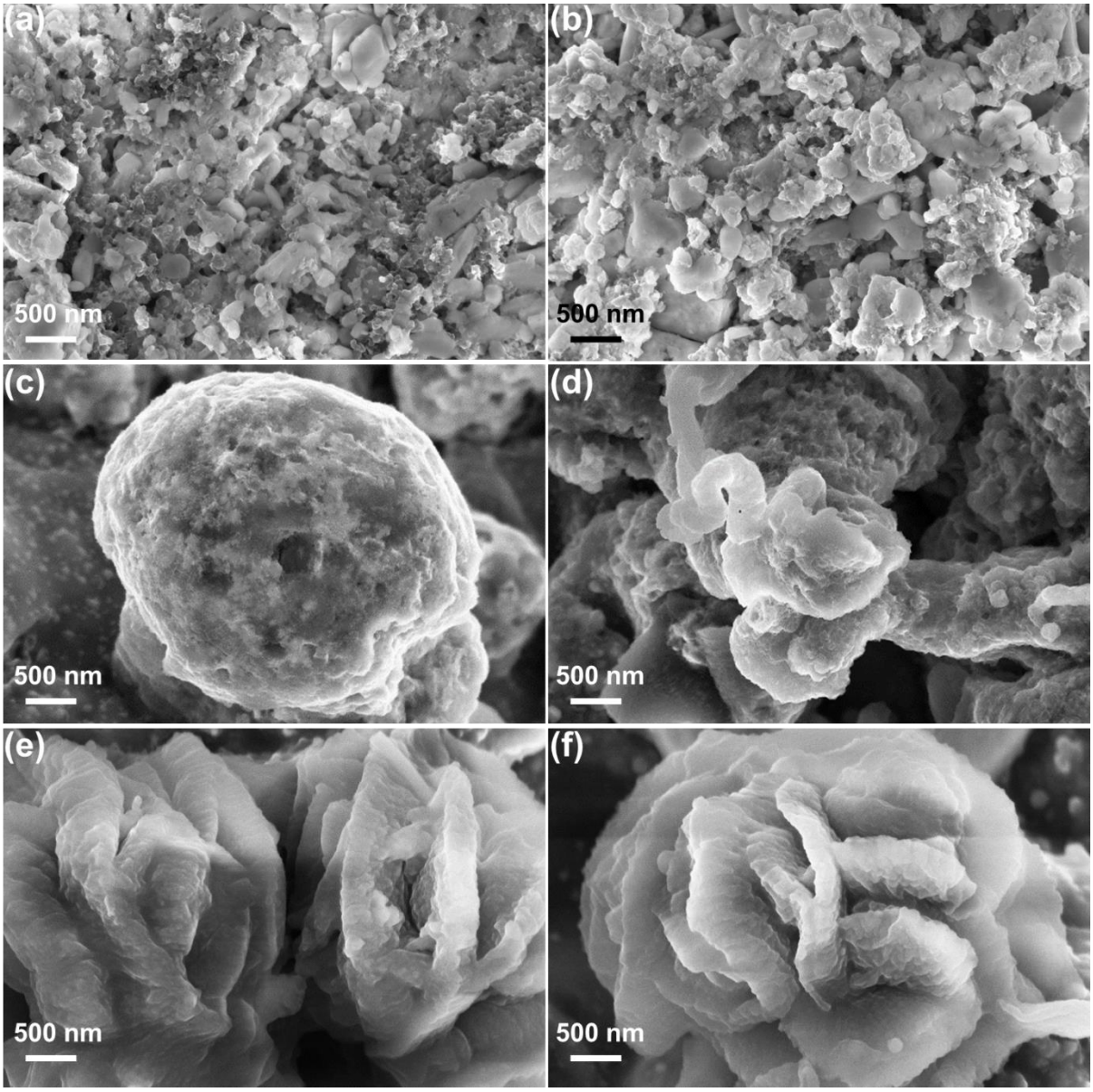

Figure 5.14 Morphology evolution of the 1T'–$MoTe_2$ electrode during lithiation/delithiation process. (a–b) FESEM image of the 1T'–$MoTe_2$ as-prepared electrode. (c–d) Electrode after full discharge. (e–f) electrode after 1st cycle (charge state).

5.3.5 First-principles DFT calculations for lithium intercalation in 1T'–$MoTe_2$

In this section, we discuss the lithiation in 1T'–$MoTe_2$ with varying Li concentrations. To simulate the Li-intercalated 1T'–$MoTe_2$, we construct a 1 x 2 x 1 supercell. For the lithiation process, we probe the probable non-equivalent sites for the intercalation of Li atoms. The possible sites are shown in **Figure 5.15a**: (1) the T_{Mo} site, in which the intercalated Li atom is placed on top of Mo atoms, and (2) the T_{Te} site, in which the intercalated atom is positioned above the Te atoms. Further, the concentration, x, of Li atoms over the range, $0 < x \leq 3.0$, with

the step of x = 0.25 has been considered for the lithiation process, with x = 3 being the maximum concentration of the Li atoms to be intercalated.

We wish to mention here that the 1 x 2 x 1 supercell of the pristine 1T'–$MoTe_2$ has a total of 8 Mo and 16 Te atoms. Thus, x = 3 case corresponds to full coverage (complete occupancy) of the T_{Mo} and T_{Te} sites by the Li atoms, leading to a total of 24 Li atoms (x = 3 case) in the 1T'–$MoTe_2$ supercell (**Figure 5.15b**). For lower concentrations, we find that the T_{Mo} site is energetically more favorable than the T_{Te} site. Hence, we proceed with the lithiation process by first occupying the T_{Mo} site, followed by the filling of the T_{Te} positions. This observation agrees well with our previous studies of Li intercalation in 2H–$MoTe_2$.[7]

First of all, we calculate the binding energy per Li atom (E_b) of the system to account for the energetic stability of the lithiated systems with various concentrations using the formula

$$E_b = \frac{E_{LixMoTe2} - E_{MoTe2} - nE_{Li}}{n} \quad (1)$$

where $E_{LixMoTe2}$ corresponds to the total energy of the Li atom-intercalated system, Li_xMoTe_2. E_{MoTe2} represents the energy of the pristine 1T'–$MoTe_2$ system, and E_{Li} refers to the energy of an isolated Li atom. The symbol, n, signifies the number of Li atoms employed for the intercalation (lithiation) in between the two layers of 1T'–$MoTe_2$. The results of the binding energy of all the lithiated systems are found to be negative, which indicates that all the systems are energetically stable (**Figure 5.16**).

The optimized structures are displayed in **Figure 5.15**, and various geometrical parameters that characterize these structures are compiled in **Table 5.2**. The figure displays the optimized structures for Li-intercalated 1T'–$MoTe_2$ for the concentrations, x = 0, 1.0, 1.5, 2.0, 2.25, 2.50, 2.75, and 3.0. From the figure, we observe that for lower concentrations, the Li atoms prefer to reside at the T_{Mo} site. However, with the increasing number of Li atoms per layer, the intercalated atoms prefer to occupy positions other than the T_{Mo} site as well.

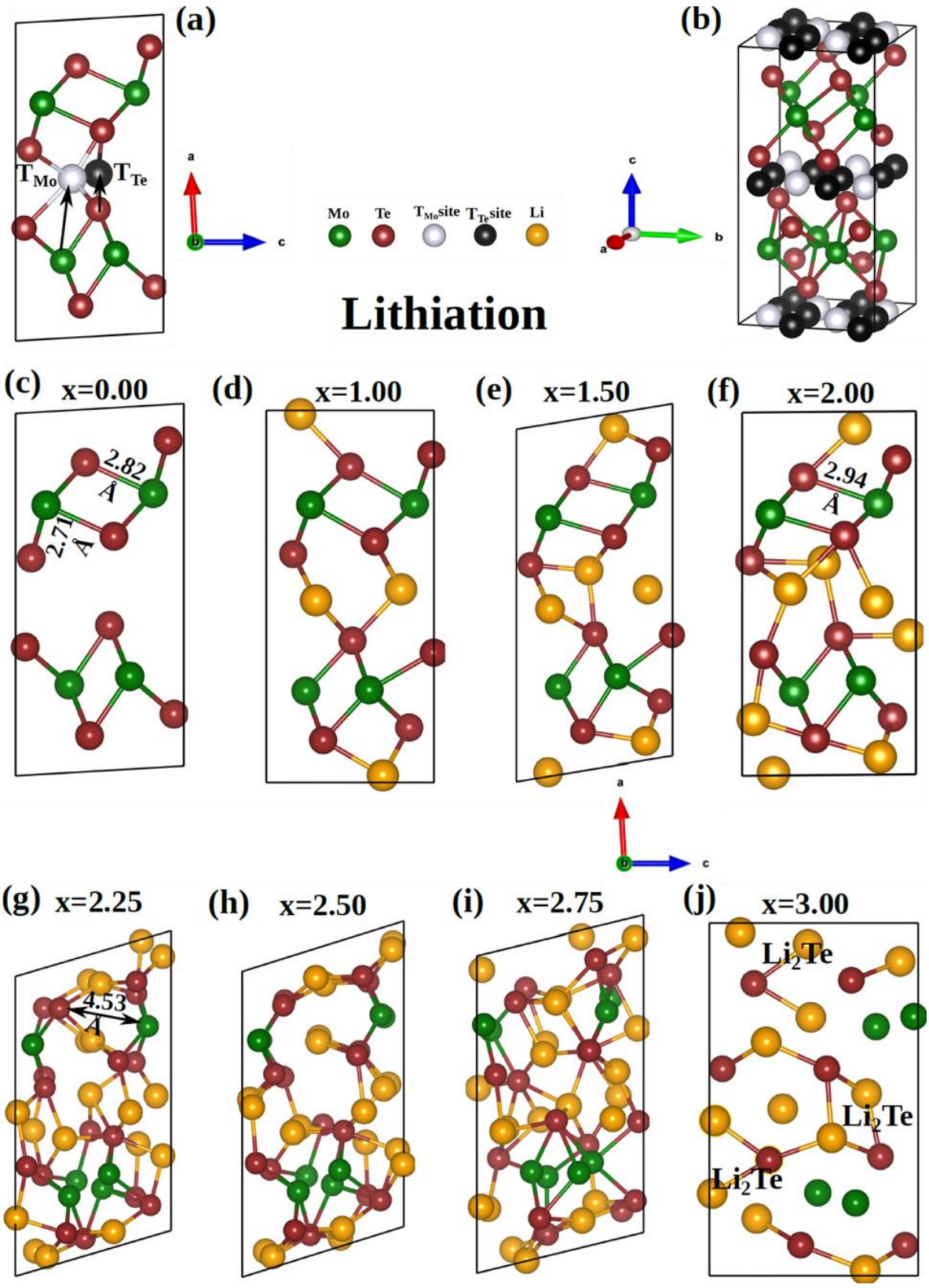

Figure 5.15 (a) The probable sites, T_{Mo} and T_{Te}, between the interlayer space for Li intercalation in the 1T'–$MoTe_2$ supercell structure. (b) Represents full occupancy of all possible sites in the supercell. (c)–(j) show the optimized structures for various Li concentrations in Li_xMoTe_2 over a range of $0 < x \leq 3.0$.

From **Table 5.2**, we note the enhancement in the lattice constants upon insertion of Li atoms. For the Li concentration in the range of $0 < x \leq 1.5$, we note that the maximum change (increment) in the lattice constants, a and b, is around 5.2 %, whereas it is around 8.5 % for lattice constant, c. As we move to x = 1.75 and x = 2, lattice increments of around 1.6 % and 25 % have been observed along the a and b directions, respectively, with compression along the c direction and a maximum change of 1.75 %. The combined influence of change in the lattice constants in all three directions results in an overall volume expansion for the composition range of $0 < x \leq 2.0$ (**Figure 5.17**). We observe a gradual change in the volume for this concentration range, with the maximum being 24.7 % when compared to that of the corresponding parent 1T'–$MoTe_2$ supercell.

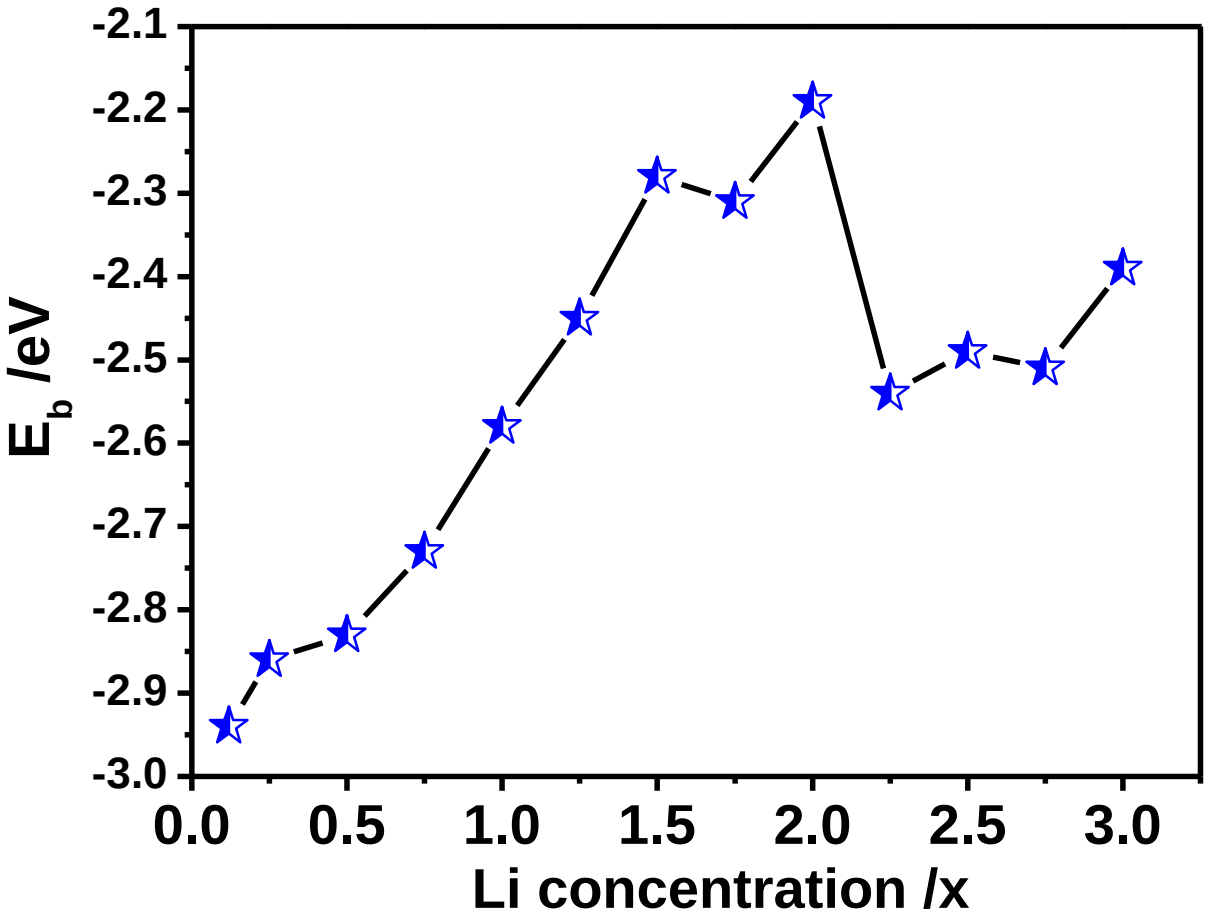

Figure 5.16 Binding energy per atom (E_b) for various concentrations of Li intercalation in the 1T'–$MoTe_2$ structure.

The rate of change of volume between x = 2.0 to x = 2.25 is around 3.6 times that of x = 1.75 to x = 2.0. Further, for x = 2, the lithiated system does not retain the basic symmetry of the 1T'–$MoTe_2$, as is evident from the change in the bond angles (α, β, and γ) (**Table 5.2**).

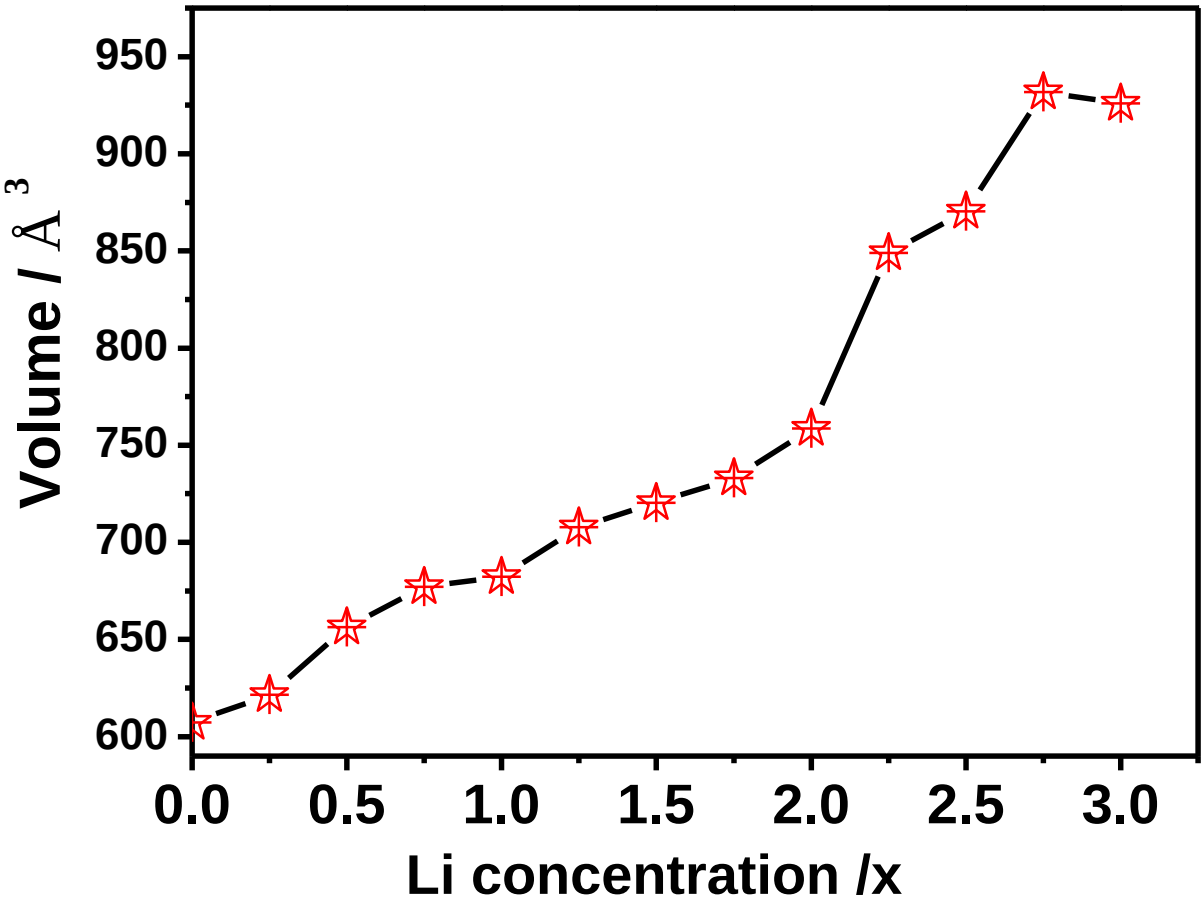

Figure 5.17 Volume of the supercell as a function of various concentrations (x) of Li intercalation in the 1T'–$MoTe_2$ structure.

Along with the variation in the lattice parameters and, consequently, the volume, we additionally notice that there is an increment in the Mo-Te bond lengths ($d_{Mo–Te}$). From **Table 5.2**, it is evident that $d_{Mo–Te}$ values increase slowly for the Li concentration in the range of $0 < x \leq 2$. The maximum increment in this range is found to be about 4.25 %, in comparison to that for the pristine 1T'–$MoTe_2$ structure. In contrast to this, at a higher range of concentration ($2 < x \leq 3$), some of the bonds between Mo and Te begin to break (**Figure 5.15g** for x = 2.25). Further, the process of the formation of bonds between Te and Li atoms sets in, leading to the formation of Li_2Te compounds (**Figure 5.15g** for x = 3.0). In addition to this, Mo atoms are no longer found to be bound to the Te atoms. We wish to point out here that some of the bond lengths between Li and Te ($d_{Mo–Te}$) and the angles, Li-Te-Li, are found to be 2.70 Å and 66.7º, respectively. These are very close to the corresponding values of 2.82 Å and 70.52º, which are observed in the case of bulk Li_2Te.[7] Thus, we conclude that for a higher concentration of Li atoms, there is a tendency of the formation of the Li_2Te compound, along with a separate Mo layer in the system.

Table 5.2 Lattice parameters of the optimized structure of the lithiated 1T'–$MoTe_2$ anode for various Li concentrations over a range of $0 < x \leq 3.0$. The range of bond lengths between Mo and Te, $d_{Mo–Te}$, is given.

x	a [Å]	b [Å]	c [Å]	α [°]	β [°]	γ [°]	$d_{Mo–Te}$ [Å]
0.00	6.36	6.97	13.70	90.00	93.34	90.00	2.71 to 2.82
0.25	6.38	6.89	14.31	90.38	99.50	90.25	2.67 to 2.82
0.50	6.45	6.99	14.61	89.72	95.53	90.01	2.67 to 2.85
0.75	6.46	7.24	14.57	89.91	82.98	90.52	2.67 to 2.88
1.00	6.49	7.27	14.42	90.00	90.01	90.00	2.64 to 2.88
1.25	6.62	7.33	14.69	90.00	97.22	90.00	2.69 to 2.91
1.50	6.69	7.33	14.87	90.00	99.28	90.00	2.71 to 2.89
1.75	6.30	8.70	13.38	90.00	93.07	90.00	2.65 to 2.99
2.00	6.46	8.71	13.46	90.00	90.53	90.00	2.64 to 2.94
2.25	8.14	7.31	15.02	96.10	106.88	84.06	2.66 to 4.53
2.50	8.31	7.49	14.82	90.84	107.30	80.94	2.66 to 5.15
2.75	8.15	7.93	14.95	88.98	103.44	82.42	2.71 to 5.14
3.00	8.52	7.54	14.41	90.00	90.01	90.00	3.00 to 6.92

To understand the nature of the bonding that is prevalent in the system because of lithiation, we perform the Bader charge analysis.[44–47] For the lithiated systems, we observe from **Table 5.3** that Te atoms gain charge from Li atoms, and as we increase the concentration of Li atoms, this tendency of gaining charge also increases. Finally, at x = 3.0, the charge on Te atoms is somewhat close to that of the Te atom in the pristine Li_2Te compound,[7] which is around –1.72 e for Te. The charge on the Li atom is the same as that on the Li atom in the pristine Li_2Te compound (0.86 e).[7] One can additionally note from **Table 5.3** that with the increase in Li concentration, the (positive) charge on Mo atoms gradually decreases, and these atoms behave like a neutral atom at a concentration of x = 3.0. Therefore, the Bader charge analysis validates the signature of the formation of Li_2Te and the disappearance of bonding between Mo and Te atoms. We wish to mention here that a similar analysis has already been performed for 2H-$MoTe_2$,[7] and it is observed that at the lower concentration ($0 < x \leq 1.5$) of Li atoms in Li_xMoTe_2, the geometrical structure and the charge distribution changes moderately, leading to the formation Li_xMoTe_2-intercalated structures. However, at a higher concentration ($1.5 < x \leq 3.0$), the weakening of Mo and Te bonds is observed along with subsequent a signature of the formation of Li_2Te + Mo at an Li concentration of approx. x = 3. The bulk 1T'-$MoTe_2$ shows

the characteristic signature of accommodating more Li atoms (up to x = 2.0) without the dissociation of Mo-Te bonds, although the 1T'-$MoTe_2$ has a smaller interlayer distance (6.85Å) than 2H-$MoTe_2$ (7.10Å).[7,48]

Table 5.3 Charge on Mo, Te, and Li atoms after lithiation for various Li concentrations using the Bader charge analysis; a range of charges is given when the atoms of a particular type of element do not possess the same charges. On the other hand, when the charges are identical, a single value is reported.

x	ΔQ_{Mo} **[e]**	ΔQ_{Te} **[e]**	ΔQ_{Li} **[e]**
0.00	0.52	-0.26	
0.25	0.52 to 0.54	-0.24 to -0.44	0.85
0.50	0.52 to 0.54	-0.29 to -0.64	0.85
0.75	0.53 to 0.56	-0.28 to -0.78	0.83 to 0.85
1.00	0.53	-0.62 to -0.74	0.84
1.25	0.50 to 0.56	-0.52 to -0.95	0.80 to 0.85
1.50	0.48 to 0.51	-0.69 to -0.99	0.79 to 0.84
1.75	0.36 to 0.45	-0.85 to -1.02	0.79 to 0.84
2.00	0.29 to 0.44	-0.73 to -1.16	0.76 to 0.85
2.25	0.22 to 0.43	-0.84 to -1.38	0.81 to 0.85
2.50	0.16 to 0.33	-0.86 to -1.40	0.80 to 0.84
2.75	0.10 to 0.32	-0.87 to -1.50	0.81 to 0.86
3.00	0.11 to 0.20	-1.20 to -1.50	0.81 to 0.85

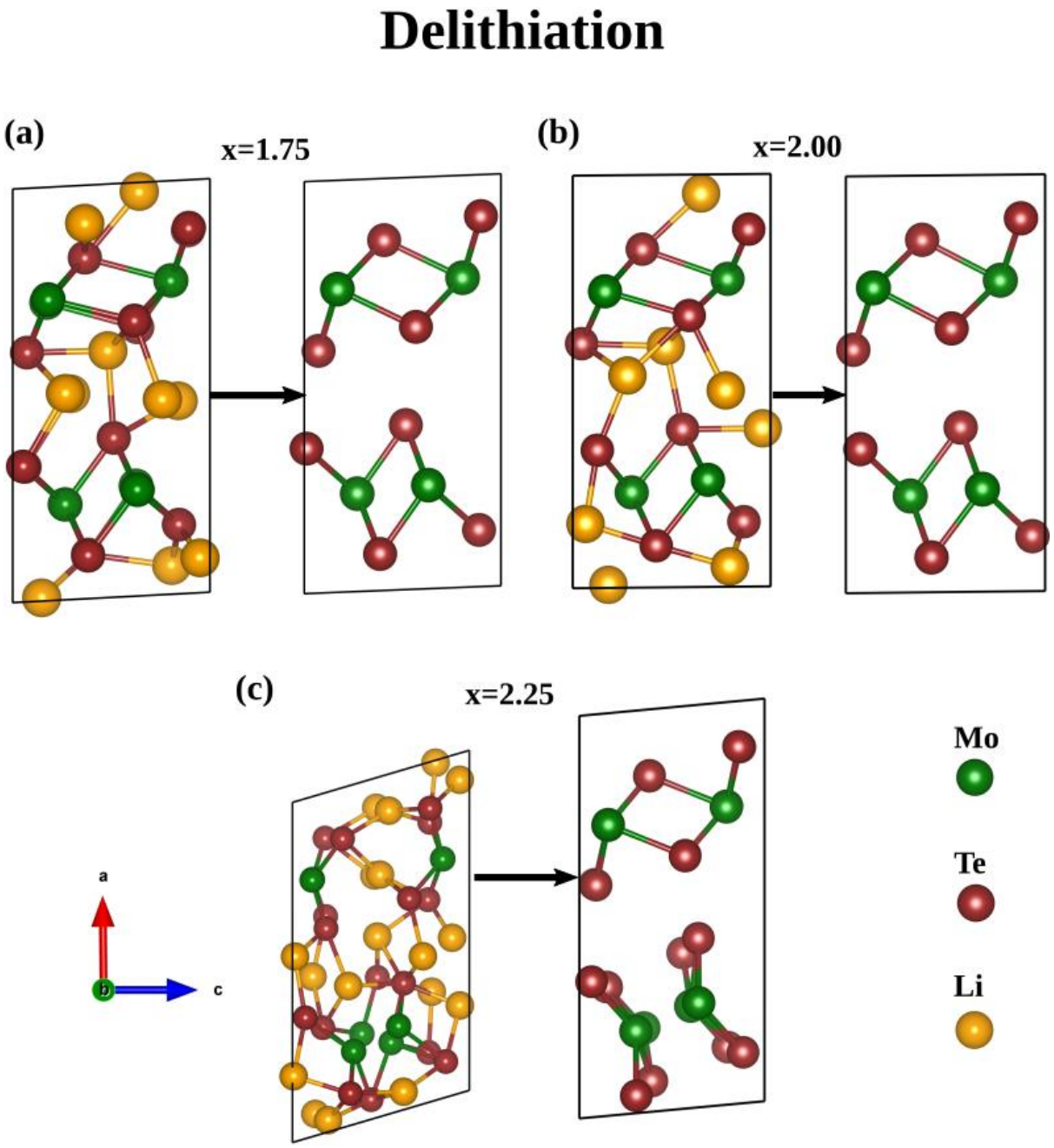

Figure. 5.18 Delithiation of Li_xMoTe_2 for x = 1.75, x = 2.00, and x = 2.25, signifying that the process retains the parent 1T'–$MoTe_2$ structure until a concentration of x = 2.00.

From the lithiation results, we find that up to the concentration of $x \leq 2$, Li atoms are considered to be intercalated with moderate changes in the $MoTe_2$ geometry, and the bonding between Mo and Te is retained in Li_xMoTe_2. Thus, the delithiation (removal of Li atoms from Li_xMoTe_2) at these concentrations leads to the original bulk structure of the 1T'–$MoTe_2$ (**Figure 5.18**). However, for x>2, where the system has been observed to be distorted significantly, the original 1T'–$MoTe_2$ structure is not achieved after the delithiation process. Thus, the delithiation process may be predicted to be an irreversible process for x>2. However, we wish to mention

here that simulating the delithiation process for a higher concentration (for x>2) using an ab initio method is a difficult task. In these cases, static DFT calculations may provide some metastable states or a local minimum. Therefore, at a higher concentration (for x>2), our DFT calculations may not be able to predict the delithiation process accurately.

We conclude from the results of DFT calculations that at lower concentrations ($0 < x \leq 2$) of Li atoms in Li_xMoTe_2, geometrical parameters and the charge distribution change moderately, and a Li_xMoTe_2-intercalated structure forms. On the other hand, at higher concentrations ($2 < x \leq 3.0$), it is expected that the conversion reaction will begin, which leads to the formation of Li_2Te +Mo at about a concentration Li of approx. x = 3.

5.3.6 Discussion

We have investigated the Li^+ storage mechanism in the 1T'–$MoTe_2$ during the Li^+ insertion and desertion process. The reason for the change of discharge profile after the 1st discharge/charge process, the high observed capacity, and the polarization loss is discussed through experimental observations. The reaction mechanism that occurs in the first discharge/charge and after a few cycles, and the discharge/charge process of the 1T'–$MoTe_2$ is thoroughly investigated by the ex situ XANES study. **Figure. 5.19** shows a schematic representation of the possible mechanisms during the lithiation/delithiation of the 1T'–$MoTe_2$ with lithium. From our experimental findings, we observe that during the Li^+ insertion at the initial concentration, the mechanism followed the intercalation process. As the Li^+ insertion concentration increases, the reaction pathway changes to the conversion process at the end of the 1st discharge process. At the end of the discharge process, the followed conversion reaction results in Mo nanoparticles with lithium telluride (Li_2Te).

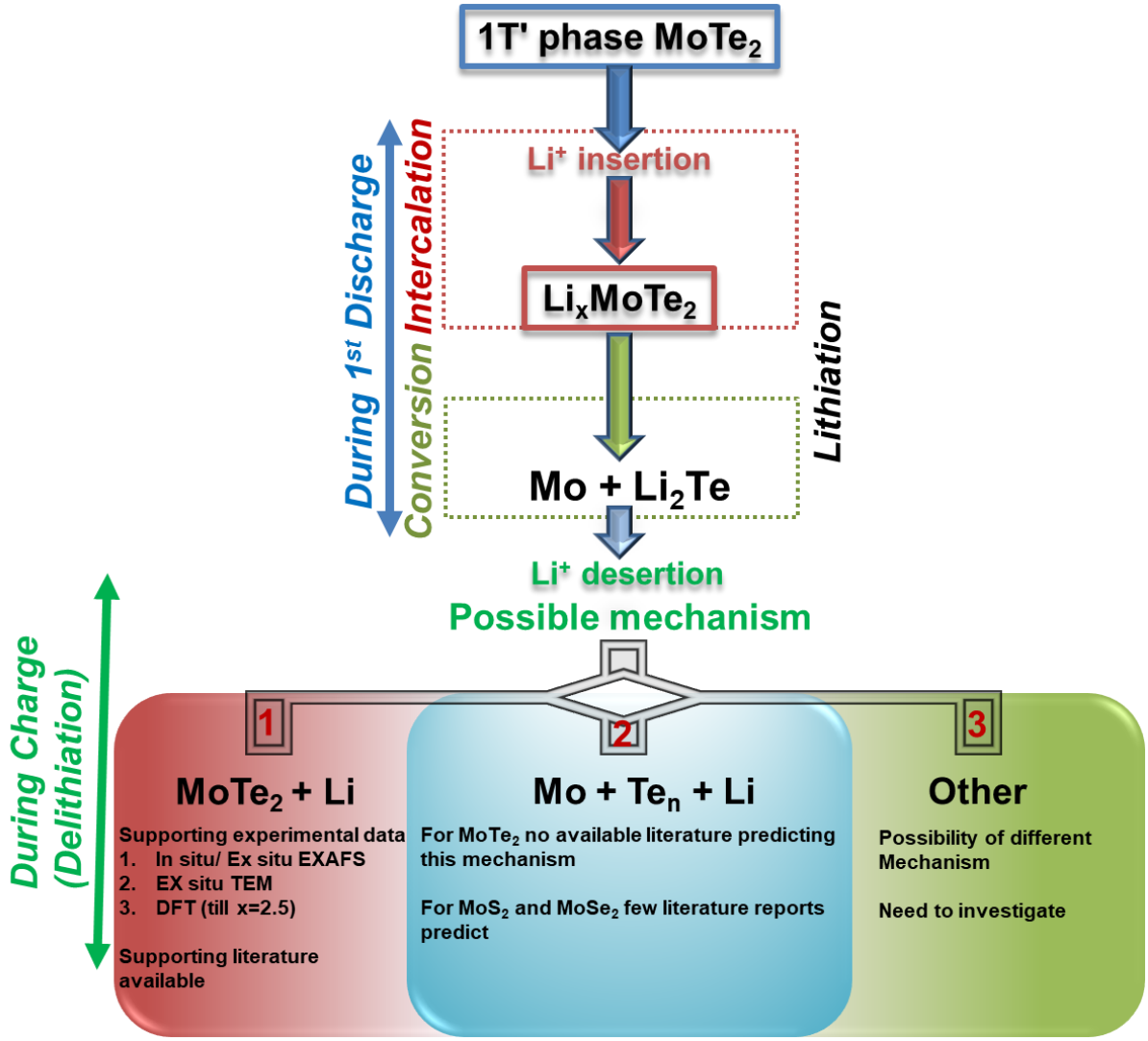

Figure. 5.19 The possible electrochemical mechanism of the Li^+ insertion/desertion process of the 1T' phase of the $MoTe_2$.

Our observation from the ex situ XANES experimental findings during the 1st discharge process followed intercalation, which was followed by the conversion reaction that was observed in the case of MoS_2, $MoSe_2$, and other chalcogenides.[23,24,49] During the delithiation process, that is, at the end of the charging process, this mechanism is observed from the ex situ XANES data. The experimental observation shows that the delithiation process is highly reversible, and the observed features match with the as-prepared 1T'–$MoTe_2$ electrode. The theoretical study employing DFT indicates that the reaction is reversible for a specific concentration of Li ($x \leq 2$). However, it is to be noted that, the DFT study may have limitations in the simulating of the delithiation process and hence the calculations at a higher concentration (for $x>2$) obtained using the ab initio method may yield metastable states or a local minimum.

Therefore, it is expected that for higher concentrations (for x>2), our DFT calculations may not be able to predict the delithiation process accurately.

The nature of the broad discharge plateau in the 1st discharge process is due to the conversion reaction that results in the formation of Mo nanoparticles and SEI due to the decomposition of the electrolyte at a lower potential.[6,23,28,29] The shifting of reduction peaks to higher potentials is due to the decrease of electrochemical polarization, which is a result of the reduction in the particle size and destruction of the lattice.[6,23,30,31]Our experimental and theoretical findings show that the Li^+ insertion/deinsertion process in the $MoTe_2$ possibly follows mechanism 1. (**Figure. 5.19**), which agrees with the previous literature on 2H–$MoTe_2$, which was used for LIBs and SIBs.[6,7]

5.3.7 1T'–$MoTe_2$versus lithium cobalt oxide full cell

To evaluate its practical applicability, a full-cell lithium-ion battery is structured by coupling the studied 1T'–$MoTe_2$ anode with lithium cobalt oxide (LCO) as the cathode. To fabricate the full-cell, borosilicate glass fiber (GF/D, Whatman) is used as the separator, which is soaked with 1 M $LiPF_6$ in EC/DMC (1:1 vol./vol.) and 3 wt % of additive, fluoroethylene carbonate (FEC). The anode-to-cathode mass ratio has been set as 1:3 (optimized for the full-cell) by observing the electrochemical performances of both the 1T'–$MoTe_2$ anode and the LCO cathode.[6,7] Here, we have not considered the weight of the electrolyte, the separator, and the components of the cell pack in calculating the energy density. The specific capacity of the 1T'–$MoTe_2$//LCO full cell is calculated based on the mass of the anode active material, that is, the mass of the 1T'–$MoTe_2$. The improving of the overall performance of the full-cell, balancing of the specific weight, and incorporating of strategies to stabilize the cells are under investigation. **Figure 5.20a** shows a schematic representation of the 1T'−$MoTe_2$//LCO full-cell configuration that has various components. The zoomed portions of both electrodes represent the atomic structures of the anode and the cathode active materials. **Figure 5.20b** presents the CV of the 1T'−$MoTe_2$//LCO full-cell configuration, which further confirms that the full cell's nominal voltage is 2.2 V. **Figure 5.20c** shows the three charge/discharge curves (2nd, 10th, 20th, and 50th cycles) of the full battery in a voltage range of 1−4 V. The initial charge/discharge capacities were ≈606.2 and ≈411.6 mAh g^{-1} at 100 mA g^{-1} (estimated on the mass of the $MoTe_2$), with a Coulombic efficiency of 68.0 %.

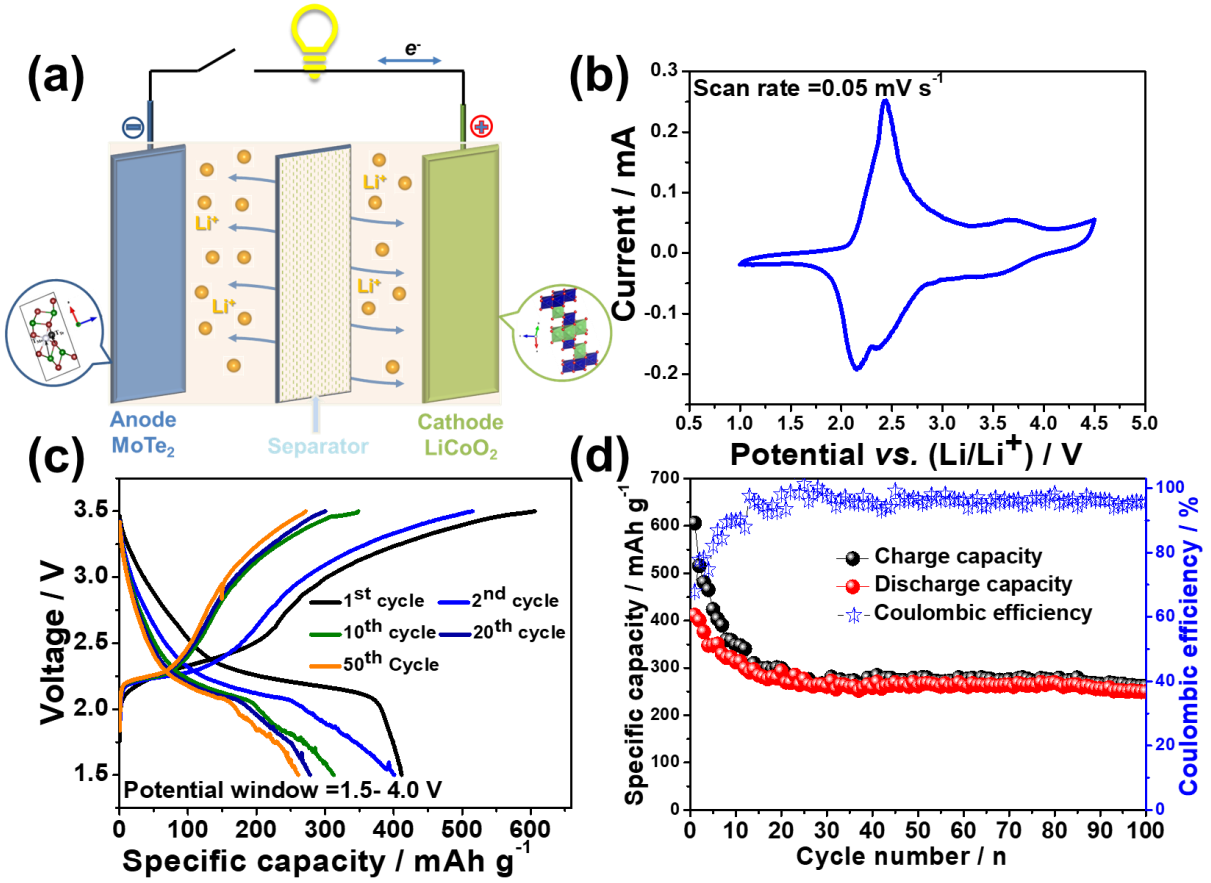

Figure 5.20 The electrochemical performance of the 1T'–$MoTe_2$ anode and the LCO as the cathode full-cell system; the specific capacities were estimated on the mass of the 1T'–$MoTe_2$. (a) Schematic representation of the 1T'–$MoTe_2$ anode and the LCO as the cathode full-cell configuration. (b) CV of the 1T'–$MoTe_2$//LCO full-cell configuration at a voltage window of 1.0–4.5 V. (c) Galvanostatic charge/discharge curves versus specific capacity at 100 mA g^{-1} of the $MoTe_2$ and the LCO full cell. (d) Long-term cycling performance of the full-cell system during 100 cycles at 100 mA g^{-1}.

The 1T'–$MoTe_2$//LCO full battery displayed a reversible capacity of 388.4 mAh g^{-1} at 100 mA g^{-1} for 100 cycles. The 1T'–$MoTe_2$//LCO full cell is able to retain 74 % of its initial capacity (with reference to the 2nd cycle) with ≈96 % of Coulombic efficiency over 100 cycles, as shown in **Figure 5.20d**.

5.4 Conclusions

The 1T'–$MoTe_2$ anode material was successfully synthesized by a solid-state method. The phase purity of the material was confirmed by XRD, XPS, and HRTEM with SAED patterns. A discharge capacity of 501 mAh g^{-1} was obtained with a Coulombic efficiency of 97 %. The

half cell showed capacity retention of 91.5 % (with reference to the 2nd cycle) and 99 % of Coulombic efficiency over 200 cycles. Ex situ XANES complemented by first-principle DFT calculations revealed the lithiation/delithiation mechanism and its reversible nature in the 1T'–$MoTe_2$ anode during cycling. Quantitative electrochemical kinetic analyses were performed to analyze the charge storage mechanism and Li^+ diffusion coefficients. The 1T'–$MoTe_2$//LCO full battery displayed a reversible capacity of 388.4 mAh g^{-1} at 100 mA g^{-1} for 100 cycles. The 1T'–$MoTe_2$//LCO full cell retained 74 % of its initial capacity (with reference to the 2nd cycle) with a Coulombic efficiency of ≈96 %. These studies confirm the potential of the 1T'−$MoTe_2$ anode including its use in LIBs.

5.5 References

(1) Lee, C. H.; Lee, G. H.; Van Der Zande, A. M.; Chen, W.; Li, Y.; Han, M.; Cui, X.; Arefe, G.; Nuckolls, C.; Heinz, T. F.; Guo, J. Atomically Thin p–n Junctions with Van Der Waals Heterointerfaces. *Nat. Nanotechnol.* **2014**, 9, 676–681.

(2) Gong, C.; Zhang, Y.; Chen, W.; Chu, J.; Lei, T.; Pu, J.; Dai, L.; Wu, C.; Cheng, Y.; Zhai, T.; Li, L. Electronic and Optoelectronic Applications Based on 2D Novel Anisotropic Transition Metal Dichalcogenides. *Adv. Sci.* **2017**, 4, 1700231.

(3) Zheng, C.; Zhang, Q.; Weber, B.; Ilatikhameneh, H.; Chen, F.; Sahasrabudhe, H.; Rahman, R.; Li, S.; Chen, Z.; Hellerstedt, J.; Zhang, Y. Direct Observation of 2D Electrostatics and Ohmic Contacts in Template-Grown Graphene/WS_2 Heterostructures. *ACS nano* **2017**, 11, 2785–2793.

(4) Zhou, T.; Pang, W. K.; Zhang, C.; Yang, J.; Chen, Z.; Liu, H. K.; Guo, Z. Enhanced Sodium-Ion Battery Performance by Structural Phase Transition from Two-Dimensional Hexagonal-SnS_2 to Orthorhombic-SnS. *Acs Nano* **2014**, 8, 8323–8333.

(5) Cho, J. S.; Ju, H. S.; Lee, J. K.; Kang, Y. C. Carbon/Two-Dimensional $MoTe_2$ Core/Shell-Structured Microspheres as an Anode Material for Na-Ion Batteries. *Nanoscale* **2017**, 9, 1942–1950.

(6) Ma, N.; Jiang, X. Y.; Zhang, L.; Wang, X. S.; Cao, Y. L.; Zhang, X. Z. Novel 2D Layered Molybdenum Ditelluride Encapsulated in Few-Layer Graphene as High-Performance Anode for Lithium-Ion Batteries. *Small* **2018**, 14, 1703680.

(7) Panda, M. R.; Gangwar, R.; Muthuraj, D.; Sau, S.; Pandey, D.; Banerjee, A.; Chakrabarti, A.; Sagdeo, A.; Weyland, M.; Majumder, M.; Bao, Q.; Mitra, S. High

Performance Lithium-Ion Batteries Using Layered 2H-$MoTe_2$ as Anode *Small* **2020**, 16, 2002669.

(8) Pradhan, N. R.; Rhodes, D.; Feng, S.; Xin, Y.; Memaran, S.; Moon, B. H.; Terrones, H.; Terrones, M.; Balicas, L. Field-Effect Transistors Based on Few-Layered α-$MoTe_2$. *ACS Nano* **2014**, 8, 5911–5920.

(9) Yamamoto, M.; Wang, S. T.; Ni, M.; Lin, Y. F.; Li, S. L.; Aikawa, S.; Jian, W.B.; Ueno, K.; Wakabayashi, K.; Tsukagoshi, K. Strong Enhancement of Raman Scattering from a Bulk-Inactive Vibrational mode in Few-Layer $MoTe_2$. *ACS Nano* **2014**, 8, 3895–3903.

(10) Lin, Y. F.; Xu, Y.; Wang, S. T.; Li, S. L.; Yamamoto, M.; Aparecido-Ferreira, A.; Li, W.; Sun, H.; Nakaharai, S.; Jian, W.B.; Ueno, K. Ambipolar $MoTe_2$ Transistors and their Applications in Logic Circuits. *Adv. Mater.* **2014**, 26, 3263–3269.

(11) Roy, A.; Movva, H. C.; Satpati, B.; Kim, K.; Dey, R.; Rai, A.; Pramanik, T.; Guchhait, S.; Tutuc, E.; Banerjee, S.K. Structural and Electrical Properties of $MoTe_2$ and $MoSe_2$ Grown by Molecular Beam Epitaxy. *ACS Appl. Mater. Interfaces* **2016**, 8, 7396–7402.

(12) Choi, K.; Lee, Y. T.; Kim, J. S.; Min, S. W.; Cho, Y.; Pezeshki, A.; Hwang, D. K.; Im, S. Non-Lithographic Fabrication of All-2D α-$MoTe_2$ Dual Gate Transistors. *Adv. Funct. Mater.* **2016**, 26, 3146–3153.

(13) Deng, K.; Wan, G.; Deng, P.; Zhang, K.; Ding, S.; Wang, E.; Yan, M.; Huang, H.; Zhang, H.; Xu, Z.; Denlinger, J. Experimental Observation of Topological Fermi arcs in type-II Weyl Semimetal $MoTe_2$. *Nat. Phys.* **2016**, 12, 1105–1110.

(14) Duerloo, K. A.; Li, Y.; Reed, E. J. Structural Phase Transitions in Two-Dimensional Mo- and W-Dichalcogenide Monolayers, *Nat. Commun.* **2014**, 5, 4214.

(15) Cho, S.; Kim, S.; Kim, J. H.; Zhao, J.; Seok, J.; Keum, D. H.; Baik, J.; Choe, D.; Chang, K. J.; Suenaga, K.; Kim, S. W.; Lee, Y. H.; Yang, H. Phase Patterning for Ohmic Homojunction Contact in $MoTe_2$. *Science* **2015**, 349, 625–628.

(16) Tan, Y.; Luo, F.; Zhu, M.; Xu, X.; Ye, Y.; Li, B.; Wang, G.; Luo, W.; Zheng, X.; Wu, N.; Yu, Y.; Qin, S.; Zhang, X. Controllable 2H-to-1T' Phase Transition in Few-Layer $MoTe_2$. *Nanoscale* **2018**, 10, 19964–19971.

(17) Song, S.; Keum, D. H.; Cho, S.; Perello, D.; Kim, Y.; Lee, Y. H. Room Temperature Semiconductor-Metal Transition of $MoTe_2$ Thin Films Engineered by Strain. *Nano Lett.* **2016**, 16, 188–193.

(18) Wang, Y.; Xiao, J.; Zhu, H.; Li, Y.; Alsaid, Y.; Fong, K. Y.; Zhou, Y.; Wang, S.; Shi, W.; Wang, Y.; Zettl, A.; Reed, E. J.; Zhang, X. Structural Phase Transition in Monolayer $MoTe_2$ Driven by Electrostatic Doping. *Nature* **2017**, 550, 487–491.

(19) Keum, D. H.; Cho, S.; Kim, J. H.; Choe, D. H.; Sung, H. J.; Kan, M.; Kang, H.; Hwang, J. Y.; Kim, S. W.; Yang, H.; Chang, K. J. Bandgap Opening in Few-Layered Monoclinic $MoTe_2$. *Nat. Phys.* **2015**, 11, 482–486.

(20) Panda, M. R.; Ghosh, A.; Kumar, A.; Muthuraj, D.; Sau, S.; Yu, W.; Zhang, Y.; Sinha, A. K.; Weyland, M.; Bao, Q.; Mitra, S. Blocks of Molybdenum Ditelluride: A High Rate Anode for Sodium-Ion Battery and Full Cell Prototype Study. *Nano Energy* **2019**, 64, 103951.

(21) Liu, M.; Wang, Z.; Liu, J.; Wei, G.; Du, J.; Li, Y.; An, C.; Zhang, J. Synthesis of Few-Layer 1T'-$MoTe_2$ Ultrathin Nanosheets for High-Performance Pseudocapacitors. *J. Mater. Chem. A* **2017**, 5, 1035–1042.

(22) Sun, L.; Ding, M.; Li, J.; Yang, L.; Lou, X.; Xie, Z.; Zhang, W.; Chang, H. Phase-Controlled Large-Area Growth of $MoTe_2$ and $MoTe_{2-x}O_x$/$MoTe_2$ Heterostructures for Tunable Memristive Behavior. *Nanoscale* **2019**, 11, 1887–1900.

(23) Sen, U. K.; Johari, P.; Basu, S.; Nayak, C.; Mitra, S. An Experimental and Computational Study to Understand the Lithium Storage Mechanism in Molybdenum Disulfide. *Nanoscale* **2014**, 6, 10243–10254.

(24) Zhang, S.; Wang, G.; Jin, J.; Zhang, L.; Wen, Z.; Yang, J. Robust and Conductive Red $MoSe_2$ for Stable and Fast Lithium Storage. *ACS nano* **2018**, 12, 4010–4018.

(25) Zhou, L.; Yan, S.; Pan, L.; Wang, X.; Wang, Y.; Shi, Y. A Scalable Sulfuration of WS_2 to Improve Cyclability and Capability of Lithium-Ion Batteries. *Nano Res.* **2016**, 9, 857–865.

(26) Yang, W.; Wang, J.; Si, C.; Peng, Z.; Zhang, Z. Tungsten Diselenide Nanoplates as Advanced Lithium/Sodium Ion Electrode Materials with Different Storage Mechanisms. *Nano Res.* **2017**, 10, 2584–2598.

(27) Srinivaas, M.; Wu, C. Y.; Duh, J. G.; Hu, Y. C.; Wu, J. M. Multi-Walled Carbon-Nanotube-Decorated Tungsten Ditelluride Nanostars as Anode Material for Lithium-Ion Batteries. *Nanotechnology* **2019**, 31, 035406.

(28) Luo, Z.; Zhou, J.; Wang, L.; Fang, G.; Pan, A.; Liang, S. Two-Dimensional Hybrid Nanosheets of Few Layered $MoSe_2$ on Reduced Graphene Oxide as Anodes for Long-Cycle-Life Lithium-Ion Batteries. *J. Mater. Chem. A* **2016**, 4, 15302.

(29) Zhang, Y.; Liu, Z.; Zhao, H.; Du, Y. $MoSe_2$ Nanosheets Grown on Carbon Cloth with Superior Electrochemical Performance as Flexible Electrode for Sodium Ion Batteries. *RSC Adv.* **2016**, 6, 1440.

(30) Zhang, J.; Xiang, J.; Dong, Z.; Liu, Y.; Wu, Y.; Xu, C.; Du, G. Biomass Derived Activated Carbon with 3D Connected Architecture for Rechargeable Lithium−Sulfur Batteries. *Electrochim. Acta* **2014**, 116, 146–151.

(31) Rui, K.; Wen, Z.; Lu, Y.; Jin, J.; Shen, C. One-Step Solvothermal Synthesis of Nanostructured Manganese Fluoride as an Anode for Rechargeable Lithium-Ion Batteries and Insights into the Conversion Mechanism. *Adv. Energy Mater.* **2015**, 5, 1401716.

(32) Zhu, C.; Mu, X.; van Aken, P. A.; Yu, Y.; Maier, J. Single-Layered Ultrasmall Nanoplates of MoS_2 Embedded in Carbon Nanofibers with Excellent Electrochemical Performance for Lithium and Sodium Storage. *Angew. Chem. Int. Ed.* **2014**, 126, 2184–2188.

(33) Shu, H.; Li, F.; Hu, C.; Liang, P.; Cao, D.; Chen, X. The Capacity Fading Mechanism and Improvement of Cycling Stability in MoS_2-based Anode Materials for Lithium-Ion Batteries. *Nanoscale* **2016**, 8, 2918–2926.

(34) Kisu, K.; Iwama, E.; Onishi, W.; Nakashima, S.; Naoi, W.; Naoi, K. Ultrafast Nano-Spherical Single-Crystalline $LiMn_{0.792}Fe_{0.198}Mg_{0.010}PO_4$ Solid-Solution Confined Among Unbundled Interstices of SGCNTs. *J. Mater. Chem. A* **2014**, 2, 20789–20798.

(35) Kim, J. W.; Augustyn, V.; Dunn, B. The Effect of Crystallinity on the Rapid Pseudocapacitive Response of Nb_2O_5. *Adv. Energy Mater.* **2012**, 2, 141.

(36) Jiang, Y.; Liu, J. Definitions of Pseudocapacitive Materials: A Brief Review. *Energy Environ. Mater.* **2019**, 2, 30–37.

(37) Li, Y.; Chang, K.; Shangguan, E.; Guo, D.; Zhou, W.; Hou, Y.; Tang, H.; Lia, B.; Chang, Z. Powder Exfoliated MoS_2 Nanosheets with Highly Monolayer-Rich Structures as High-Performance Lithium-/Sodium-Ion Battery Electrodes. *Nanoscale* **2019**, 11, 1887–1900.

(38) Hu, S.; Jiang, Q.; Ding, S.; Liu, Y.; Wu, Z.; Huang, Z.; Zhou, T.; Guo, Z.; Hu, J. Construction of Hierarchical $MoSe_2$ Hollow Structures and Its Effect on Electrochemical Energy Storage and Conversion. *ACS Appl. Mater. Interfaces* **2018**, 10, 25483–25492.

(39) Kang, J.; Su, Q.; Feng, H.; Huang, P.; Du, G.; Xu, B.; $MoSe_2$ Nanosheets-Wrapped Flexible Carbon Cloth as Binder-Free Anodes for High-Rate Lithium and Sodium Ion Storages. *Electrochim. Acta* **2019**, 301, 29–38.

(40) Liu, Y.; Zhua, M.; Chen, D.; Sheet-like $MoSe_2$/C Composites with Enhanced Li-Ion Storage Properties. J. *Mater. Chem. A* **2015**, 3, 11857–11862.

(41) Mastelaro, V. R.; Zanotto, E. D. X-ray Absorption Fine Structure (XAFS) Studies of Oxide Glasses a 45-Year Overview. *Materials* **2018**, 11, 204.

(42) Singh, S.; Panda, M. R.; Sen, R.; Johari, P.; Sinha, A. K.; Meena, S. S.; Mitra, S. Study of Higher Discharge Capacity, Phase Transition, and Relative Structural Stability in Li_2FeSiO_4 Cathode Upon Lithium Extraction Using an Experimental and Theoretical Approach and Full Cell Prototype Study. *ACS Appl. Energy Mater.* **2019**, 2, 6584–6598.

(43) Stern, E. A. Theory of the Extended X-Ray-Absorption Fine Structure. *Phys. Rev. B* **1974**, 10, 3027.

(44) Tang, W.; Sanville, E.; Henkelman, G. A Grid-Based Bader Analysis Algorithm Without Lattice Bias. *J. Phys. Condens. Matter* **2009**, 21, 084204.

(45) Sanville, E.; Kenny, S. D.; Smith, R.; Henkelman, G. Improved Grid-Based Algorithm for Bader Charge Allocation. *J. Comput. Chem.* **2007**, 28, 899–908.

(46) Henkelman, G.; Arnaldsson, A.; Jónsson, H. A Fast and Robust Algorithm for Bader Decomposition of Charge Density. *Comput. Mater. Sci.* **2006**, 36, 354–360.

(47) Yu, M.; Trinkle, D. R. Accurate and Efficient Algorithm for Bader Charge Integration. *J. Chem. Phys.* **2011**, 134, 064111.

(48) Kim, E. K.; Yoon, S. J.; Bui, H. T.; Patil, S. A.; Bathula, C.; Shrestha, N. K.; Im, H.; Han, S. H. Epitaxial Electrodeposition of Single Crystal $MoTe_2$ Nanorods and Li^+ Storage Feasibility. *J. Electroanal. Chem.* **2020**, 878, 114672.

(49) Roy, A.; Ghosh, A.; Kumar, A.; Mitra, S. A High-Performance Sodium Anode Composed of Few-Layer $MoSe_2$ and N, P Doped Reduced Graphene Oxide Composites. *Inorg. Chem. Front.* **2018**,5, 2189–2197.

CHAPTER 6

Blocks of molybdenum ditelluride: A high-rate anode for sodium-ion battery and full-cell prototype study

"This chapter provides information about the use of as-synthesized $MoTe_2$ as an active material for SIB without any further surface modification or conductive coating. Synchrotron X-ray diffraction and XANES are used to detect phase changes during the sodiation/desodiation process to explore the sodium storage mechanism. Finally, a full-cell SIB has been demonstrated using the $MoTe_2$ anode and sodium vanadium phosphate (NVP) as the cathode to investigate numerous practical energy-storage applications."

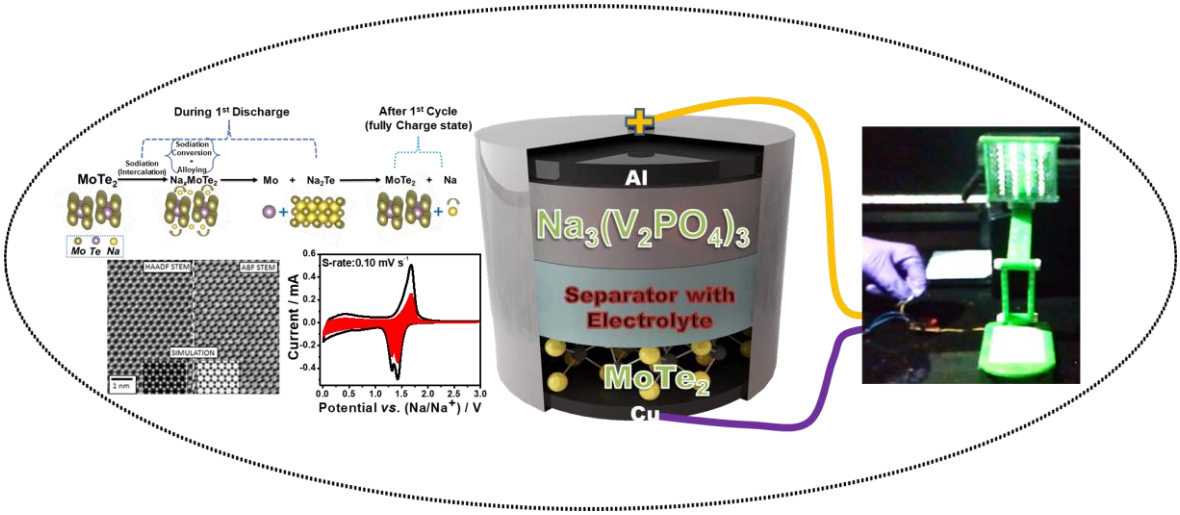

* An excerpt from this chapter has been published in *Nano Energy*, 64, 2019, 103951.

6.1 Introduction

In previous chapters, we studied the 2H and 1T' $MoTe_2$ phases in LIB applications and the associated lithiation/delithiation mechanism. After the successful investigation of the novel $MoTe_2$ against lithium, we extended our study to the layered structured 2H phase of the $MoTe_2$ as anode SIBs. In this chapter, $MoTe_2$ has been applied in SIBs in bulk for the first time without any further surface modification or the use of any conductive-coating carbonaceous material. The new candidate, the layered $MoTe_2$ phase, has been investigated as a unique anode material for SIBs. The crystal structure of the $MoTe_2$ is layered, which allows facile insertion/extraction of Na^+ ions into/from the host.[1,2] Molybdenum ditelluride is composed of alternately stacked layers of Mo and Te (Te–Mo–Te), which are held together by weak van der Waals interactions.[2,3] The interlayer spacing of $MoTe_2$ is about 0.70 nm, which is considerably larger than that of graphite (0.335 nm); the layer gaps are expected to allow the efficient diffusion of Na^+ ions without any significant disturbance to the crystal structure. Moreover, tellurium has a comprehensively higher electronic conductivity (2×10^2S m^{-1}), which results in higher utilization of active materials than in sulfur (5×10^{-13}S m^{-1}) and selenium (1×10^{-3}S m^{-1}).[2,3] Hence, $MoTe_2$ can be considered an intercalation host and a promising electrode material for SIBs. The present study highlights the potential of $MoTe_2$ as an anode material in SIB application.

This study revealed the detailed mechanism of $MoTe_2$ with respect to sodium metal during the first discharge and the subsequent charge/discharge cycles. In addition, we investigated the structural stability of $MoTe_2$ electrode using ex situ Synchrotron X-ray diffraction (SXRD), HRTEM, XPS and XANES analysis. Finally, considering our optimum goal, a full cell is fabricated by combining the $MoTe_2$ as an anode and (NVP) as a cathode. The ($MoTe_2$//NVP) full cell shows high specific capacity with high-rate capability (207 mA h g^{-1} at a high current rate of 0.5 A g^{-1}, which is based on the mass of the $MoTe_2$) and outstanding cycling stability (that is, 88 % reversible capacity retention after 150 cycles). Our sodium-ion full cell, which operates at 2 V, delivers a high energy density of 414 W h kg^{-1}. When the high structural stability of the $MoTe_2$ structure and its performance in the full-cell configuration as an anode material is taken into account, it is observed that the two-dimensional layer material, $MoTe_2$, could be a potential anode material in high-performance sodium-ion batteries in the near future.

6.2 Material synthesis

6.2.1 Synthesis of $MoTe_2$ powder

The $MoTe_2$ polycrystalline powder was prepared by mixing a stoichiometric amount of molybdenum (Sigma–Aldrich, 99.999 %) and tellurium (Sigma–Aldrich, 99.999 %) powders. The Mo powder was pre-sintered at 600 °C in an argon atmosphere for 8 h. Subsequently, the powder was uniformly mixed with tellurium powder by hand-grinding in an argon atmosphere to obtain a precursor for $MoTe_2$ synthesis. The mixed powder was then sealed in a 150-mm-long quartz ampoule (15 mm inner diameter) under vacuum at a pressure of 10^{-5} torr. The ampoule was vibrated for ten minutes and purged under an argon atmosphere five times while evacuating it to eliminate more oxygen. After sealing the precursor powder, it was spread along the length of the horizontal ampoule and introduced into a furnace (**Figure 6.1a**). The temperature was increased slowly from room temperature to 800 °C, the temperature was maintained at 800 °C for 20 h to complete the alloying reaction.[4] Slow heating avoids a possible explosion due to the strongly exothermic reaction between the elements. The heating and cooling rate during the annealing process was maintained at a ramping rate of 1 °C/min. After cooling to room temperature, a black powder of the $MoTe_2$ was obtained, which was further ground in an inert atmosphere before further characterization.

6.2.2 Preparation of $Na_3V_2(PO_4)_3$ (NVP)

A simple two-step process that comprised a solid-state reaction followed by the carbothermal reduction route has been followed to obtain a nearly phase-pure $Na_3V_2(PO_4)_3$. In the first step, a stoichiometric amount of NH_4VO_3 (Sigma–Aldrich, ≥ 99 %) and $NaH_2PO_4.2H_2O$ (Sigma–Aldrich, ≥ 99 %) were mixed with 20 % of sucrose in 20 ml of ethanol medium. This mixture was subjected to ball mill for 24 h at 300 rpm. After ball milling, the obtained mixture was dried at 100 °C in air; it was then crushed to a powder. In the second step, two-step heating of the precursor was carried out to obtain a calcined powder. During the two-step heating process, the powder was initially kept at 350 °C for 3 h, which was followed by final calcinations at 800 °C in an N_2/H_2 (95:5) atmosphere for 8 h, with a ramp rate of 5 °C/min to obtain the desired pure-phase $Na_3V_2(PO_4)_3$ material.[5]

6.3 Results and discussion

6.3.1 Physiochemical characterization of $MoTe_2$

Figure 6.1a shows the schematic of the successful preparation of the $MoTe_2$ powder sample. **Figure 6.1b** represents the typical SXRD pattern of the as-prepared $MoTe_2$ powder sample. The SXRD pattern was analyzed using the Rietveld refinement program. The inset of **Figure 6.1b** shows that the fit parameters such as R_p (1.02 %), R_{wp} (1.07 %), R_{exp} (1.32 %) and χ^2 (0.87), which were obtained from the Rietveld refinement, lie in a reasonable range; this confirms the acceptable quality of the Rietveld refinement and the phase purity of the $MoTe_2$ structure.

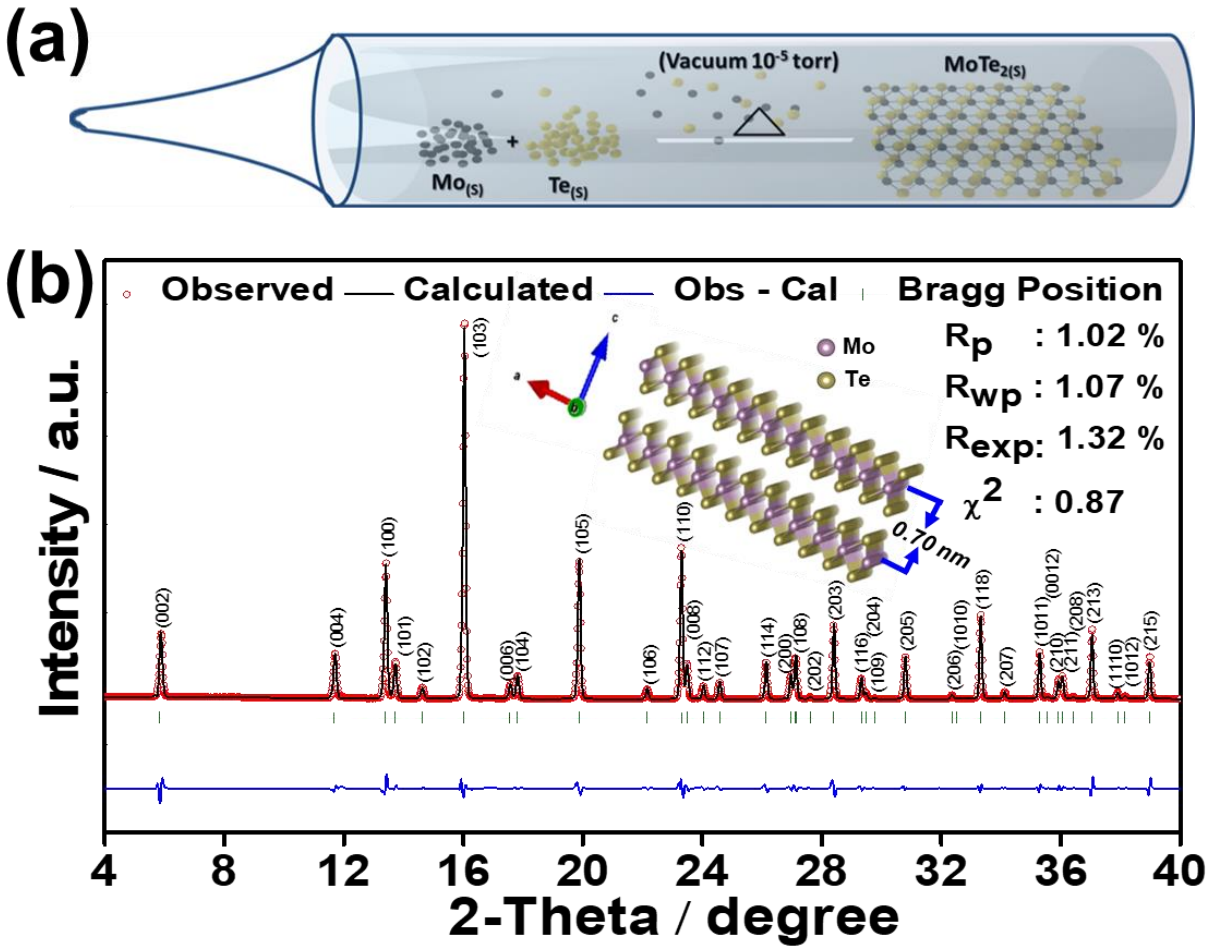

Figure 6.1 Synthesis and structural characterization of the $MoTe_2$ powder sample. (a) Schematic presentation of the solid-state preparation route of the $MoTe_2$ powder. (b) Powder SXRD pattern of the as-prepared $MoTe_2$ powder, and the Rietveld refinement plot along with the fitted parameters; the inset shows the layer structures that have interlayer spacing in the order of ~ 0.70 nm.

The SXRD peaks have been indexed with the phase of the hexagonal structure with the space group, $P6_3/mmc$. The inset of **Figure 6.1b** schematically shows the layer structure of the $MoTe_2$ with an interlayer spacing of 0.70 nm. The obtained lattice parameters are a= b= 3.526 Å and c= 13.989 Å, which is in good agreement with the previously reported literature.[6] The grain size of the $MoTe_2$ is estimated using the Debye–Scherer formula, $\langle d \rangle = (0.89 \times \lambda)/ (\beta \times \cos \theta)$, in which β (FWHM in Radians) and θ (half of the peak position in the 2θ scale) use the Gaussian fit of the prominent SXRD peaks (103, 100, 105). Thus, the estimated grain size is ~120 nm.

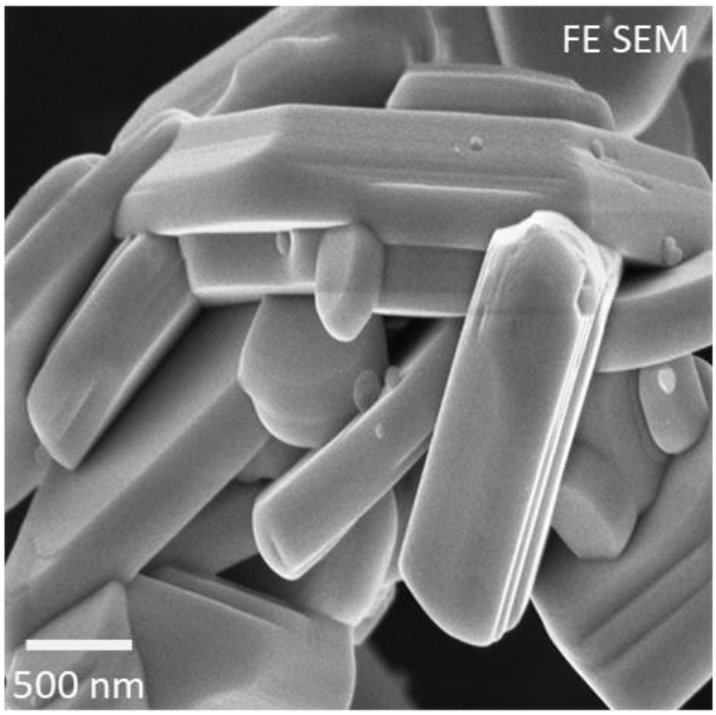

Figure 6.2 Electron microscopy studies of the as-prepared $MoTe_2$ sample. FESEM image of the as-prepared $MoTe_2$ sample.

The FESEM image in **Figure 6.2** indicates a block type of $MoTe_2$ crystal morphology with a length of ~ 2 µm, and a breadth and thickness of ~0.5 µm. The atomic arrangement of the $MoTe_2$ was studied by examining areas of a thin crystal (**Figure 6.3a**) that have delaminated or separated from the larger crystals (the thickness and the high atomic number of the majority of the crystals preclude imaging in transmission).

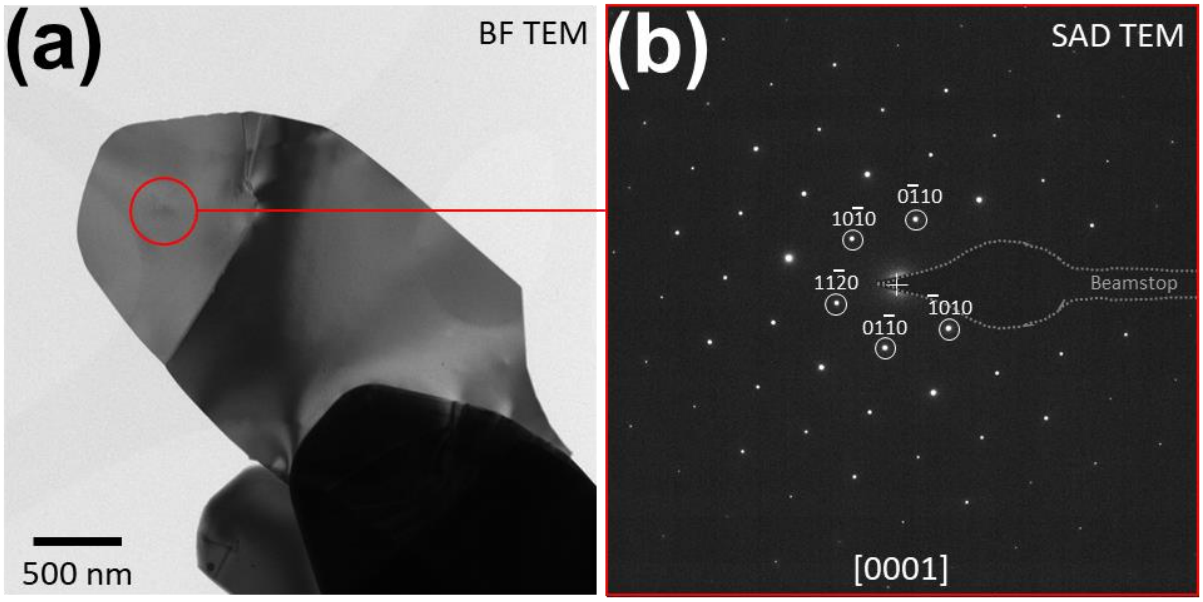

Figure 6.3 Electron microscopy studies of the as-prepared $MoTe_2$ sample. (a) A BFTEM image of a thin area of a flat crystal. (b) A SAD pattern from the indicated area.

The SAD pattern in **Figure 6.3b**, from the area indicated in **Figure 6.3a**, is consistent with a single-crystal of $MoTe_2$, which is orientated along with the [0001] axis and is perpendicular to the direction in which the layers are stacked.

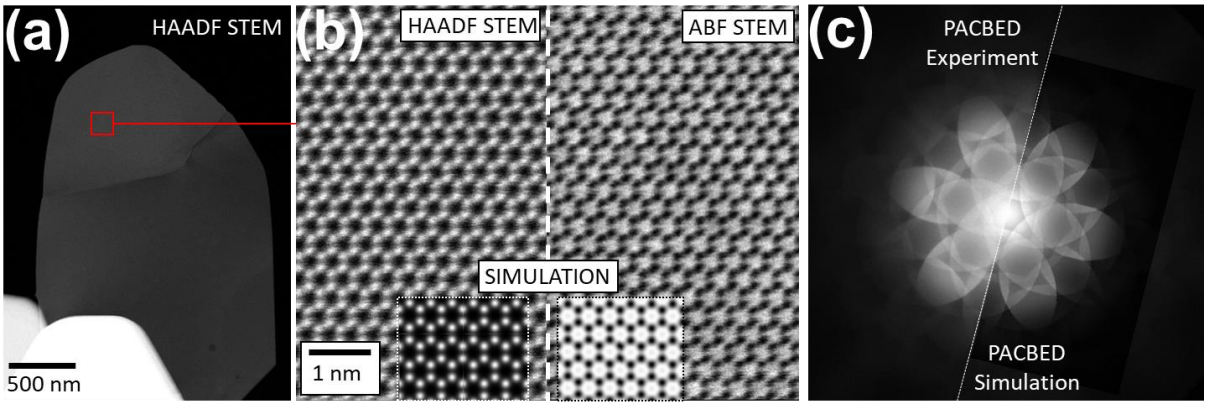

Figure 6.4 Electron microscopy studies of the as-prepared $MoTe_2$ sample. (a–c) Low magnification HAADF STEM, atomic resolution HAADF, and ABF STEM images at the [0001] zone axis; the inset shows the simulation images for the same thickness and orientation. (c) PACBED experimental patterns for the area in a) and the simulated pattern for 24 nm.

The HAADF and ABF STEM images, **Figure 6.4a** also indicate that this is a single-crystal. Any disorder in the 2H stacking would be present as additional spots in the SAD and as a reduction or removal of all contrast in the STEM images. The PACBED pattern (**Figure 6.4c**) is an excellent match for a crystal thickness of 24 nm. Simulations of the HAADF and ABF

STEM images at this thickness (box out of **Figure 6.4b**) are consistent with the image contrast. (The given experimental data is unsmoothed, and all specimens have at least 1–2 nm of amorphous surface contaminants.)

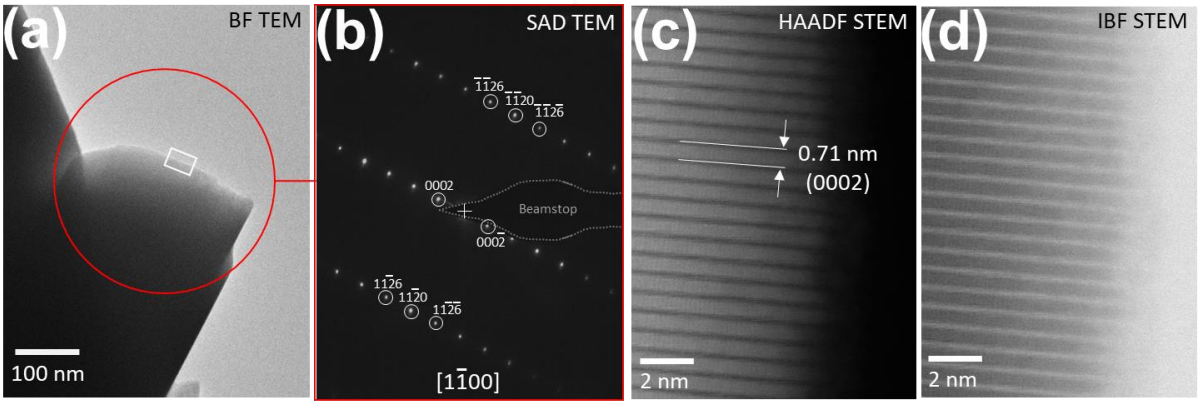

Figure 6.5 Electron microscopy studies of the as-prepared $MoTe_2$ sample. (a) A BFTEM image of the end of an edge of a crystal. (b) A SAD pattern from the area that is indicated in a). (c–d) HAADF and IBF STEM images, taken from a marked box in image a), along the [0002] direction, showing interlayer spacing in the order of 0.71 nm.

Shown in **Figure 6.5a** is an area of a crystal-orientated edge-on; the very edge of the crystal is thin enough to be electron transparent. The SAD of the indicated area (**Figure 6.5a**) is consistent in the aspects of shape and spacing distance with the $MoTe_2$ that is orientated toward the [$\mathbf{1\bar{1}00}$] direction. Higher magnification images of the edge (**Figure 6.5c,d**) of the specimen through HAADF and IBF STEM show the distinctive 0.71-nm interlayer spacing between successive chalcogenide layers, which is ideal for intercalation by Na ions. The thickness (estimated at >200 nm), even at the edge of the specimen, precludes the useful application of ABF STEM, BF-STEM or PACBED. This also prevents column imaging, which is possible in the [0001] direction. Enough information is present in both these directions, however, to conclude that the $MoTe_2$ crystals conform completely to the standard 2H-$MoTe_2$ structure.

6.3.2 Electrochemical performance study

6.3.3 $MoTe_2$ versus Na metal half cell

The electrochemical performance of the $MoTe_2$ powder has been tested against sodium metal in a coin-cell configuration at 20 °C with an accuracy of ± 2 °C. The CV performance of pure $MoTe_2$ for the first five cycles at a voltage scan rate of 0.05 mV s^{-1}, between the voltages of 0.01 and 3.00 V, is shown in **Figure 6.6a**. A small reduction peak, which is positioned at ~ 0.86 V and is observed at a slow scan rate (0.02 mV s^{-1}), as shown in **Figure 6.6b**, corresponds

to the intercalation of Na^+ into the $MoTe_2$ host structure according to the intercalation reaction, $MoTe_2 + xNa^+ + xe^- \leftrightarrow Na_xMoTe_2$; this forms Na_xMoTe_2.

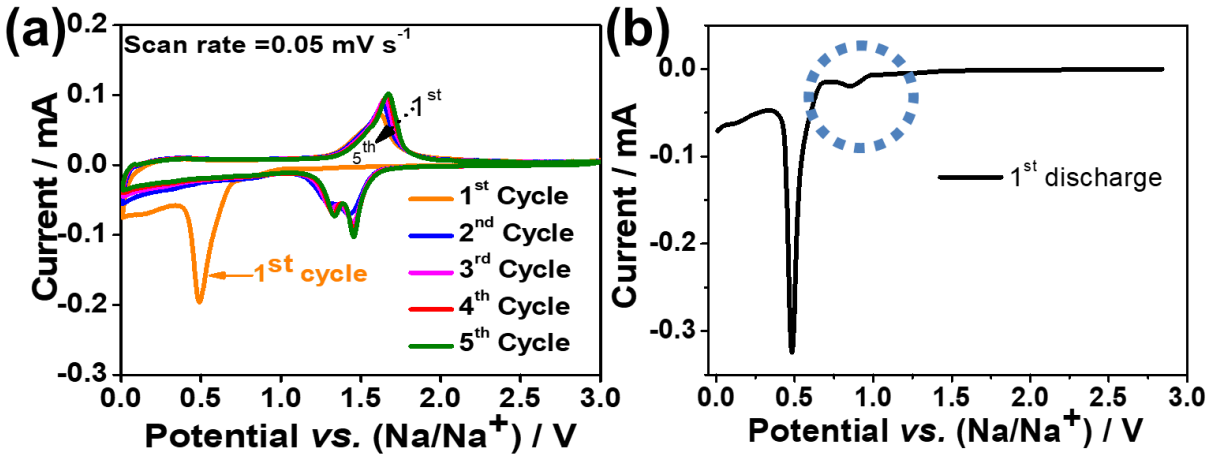

Figure 6.6 The electrochemical performance of $MoTe_2$ electrodes with a typical loading of the active material at 2.0 mg cm^{-2} at 20 ± 2 ºC for sodium storage in a half-cell configuration.(a) Cyclic voltammogram of the $MoTe_2$ electrode at a scan rate of 0.05 mV s^{-1} in the potential window, 0.01–3.00 V. (b) First discharge CV profile of the $MoTe_2$ electrode at a scan rate 0.02 mV s^{-1} between the potential windows of 0.01 and 3.00 V versus Na/Na^+.

The sharp peak, ~0.49 V, which is present in the first cathodic scan of the $MoTe_2$ sample, is attributed to the combined effect of the formation of a SEI, metallic Mo nanocrystals, and Na_2Te according to the conversion reaction between $MoTe_2$ and Na ions, as shown below (1):

$$MoTe_2 + 4Na^+ + 4e^- \rightarrow Mo + 2Na_2Te \qquad (1)$$

The subsequent reduction peaks at ~1.43 V and ~1.30 V, from the second cycle onward, are attributed to the Na_2Te alloy and de-alloy phases.[2,3,7] The intensity of these reduction peaks progressively increases after the second cycle ends. There is also a small shift toward higher potentials. The reason for the shift could be the formation of ultrafine $MoTe_2$ nanocrystals and the periodic intercalation and de-intercalation of Na^+ ions into the host lattice structure of $MoTe_2$.[2,3,7] The oxidation peak that is located at ~1.61 V in the anodic scans can be ascribed to the re-formation of $MoTe_2$.

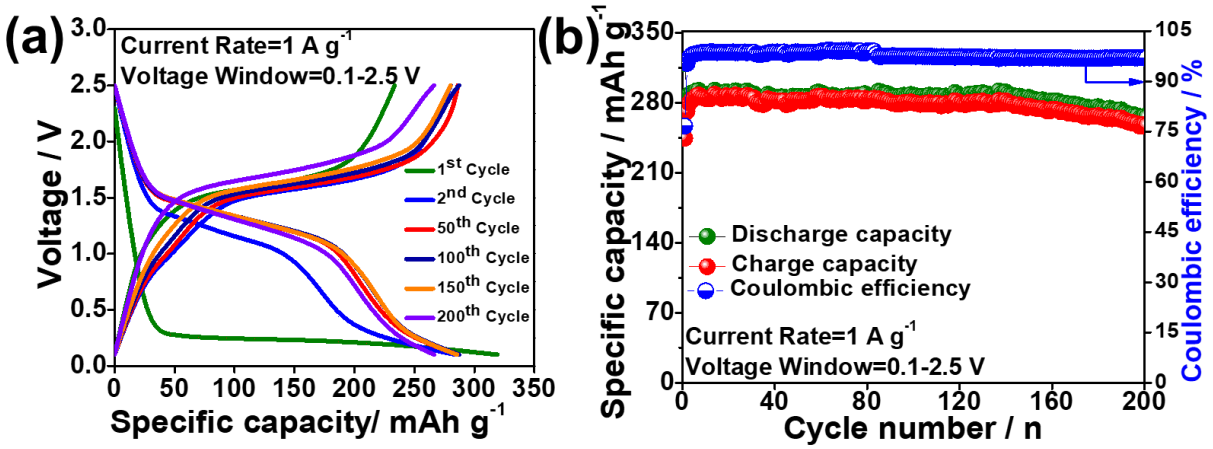

Figure 6.7 The electrochemical performance of $MoTe_2$ electrodes that have a typical loading of the active material at 2.0 mg cm^{-2} at 20 ± 2 ºC for sodium storage in a half-cell configuration. (a) Galvanostatic charge/discharge curves versus specific capacity of $MoTe_2$ electrodes for different cycles at a current rate of 1 A g^{-1} in the potential window, 0.1–2.5 V. (b) Cycling performance with Coulombic efficiency during 200 cycles at a current rate of 1 A g^{-1}.

Further, to check the Na^+-storing ability of the $MoTe_2$ anode, galvanostatic charge/discharge was performed at a higher current rate of 1 A g^{-1} within the potential range, 0.01–2.5 V; the cyclic performance is shown in **Figure 6.7a**. The discharge profile of the first cycle shows an extended plateau at ~0.31 V due to the conversion reaction of $MoTe_2$, which is associated with the formation of SEI. However, after completing the initial two cycles, the working potential of the $MoTe_2$ electrode becomes highly stable at ~1.5 V. A cycling study was carried out to compare the long-term cycling performance of the material and Na/Na^+ at 1 A g^{-1} for 200 cycles (**Figure 6.7b**). The $MoTe_2$ electrode delivered an initial discharge capacity of ~ 320 mAh g^{-1} with Coulombic efficiency of 76 %. The observed initial capacity mismatch could be attributed to the formation of an SEI layer, which is associated with the irreversible consumption of Na^+ ions during initial discharge. However, from the second cycle onward, the $MoTe_2$ anode delivers a stable discharge capacity of 290 mAh g^{-1} with an excellent Coulombic efficiency of > 99 %. The $MoTe_2$ sample exhibits an excellent cycling performance till 200 cycles, retaining a reversible specific capacity of 267 mAh g^{-1}.

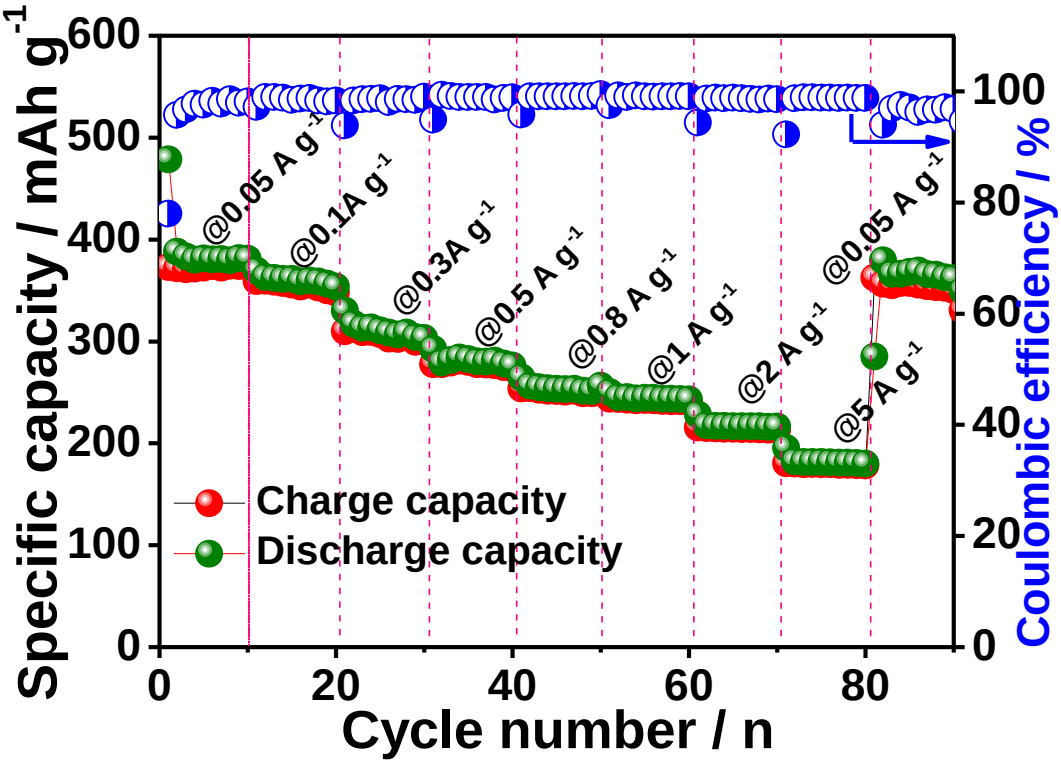

Figure 6.8 The rate performance of $MoTe_2$ electrodes at various rates at 20 ± 2 ºC for sodium storage in a half-cell configuration.

The rate capability of the half-cell is shown in **Figure 6.8**. The **Figure 6.8** reveals that the $MoTe_2$ exhibits specific capacities, 383 mAh g^{-1}, 364 mAh g^{-1}, 320 mAh g^{-1}, 289 mAh g^{-1}, 260 mAh g^{-1}, 251 mAh g^{-1}, 216 mAh g^{-1}, and 185 mAh g^{-1}at corresponding current densities of 0.05 A g^{-1}, 0.1 A g^{-1}, 0.3 A g^{-1}, 0.5 A g^{-1}, 0.8 A g^{-1}, 1.0 A g^{-1}, 2.0 A g^{-1} and 5.0 A g^{-1}, respectively. Although the theoretical capacity of the $MoTe_2$ is 305 mAh g^{-1} (calculated based on 4 mol of Na^+ for 1 mol of $MoTe_2$),[2,3] the excess specific capacity that is observed at 0.05 A g^{-1} might be due to the interfacial Na^+ storage and the formation of the Na_2Te alloy; a similar phenomenon has been observed in other TMDs.[2,3,8–10]

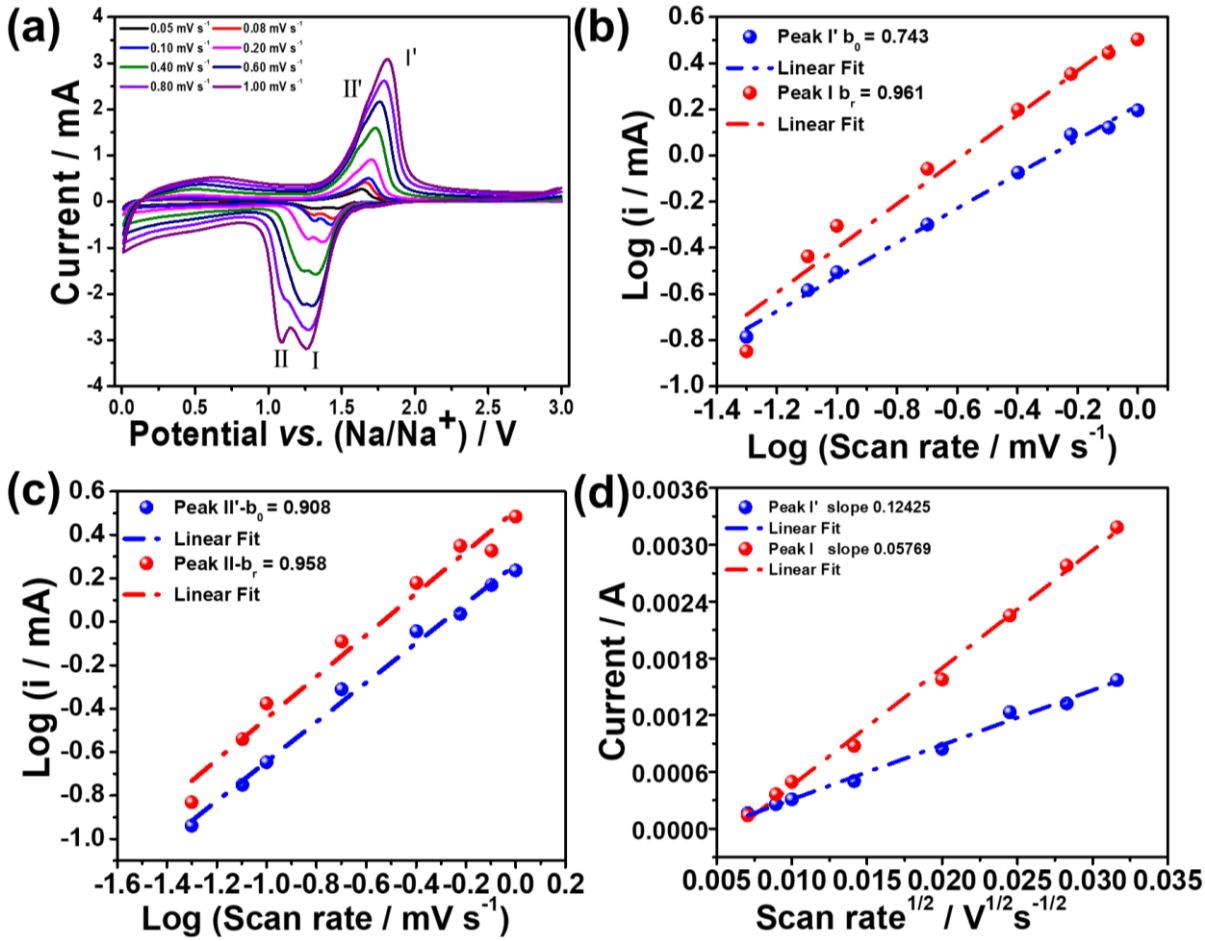

Figure 6.9 Kinetics and quantitative analysis of the Na^+ storage mechanism in the $MoTe_2$ electrode. (a) Cyclic voltammogram of the $MoTe_2$ electrode at different scan rates within the potential window, 0.01–3.00 V. (b–c) Linear relationship between Log i (logarithm peak currents) and log V (logarithm scan rate) of the reduction peaks (I and II) and oxidation peaks (I' and II') at different scan rates (0.05, 0.08, 0.10, 0.20, 0.40, 0.60, 0.80, and 0.10 mV s^{-1}). (d) Linear fitting of the peak current versus the square root of the scan rate of the reduction (I) and oxidation (I') peaks.

Further, we studied the transport kinetics mechanism of the $MoTe_2$ during sodiation and desodiation processes, and we performed CV experiments at different scan rates, as shown in **Figure 6.9a**. A peak shift toward the lower potential, starting from 0.05 to 1.00 mV s^{-1}, was observed when there was an increase in the current rate; this obeys the power-law according to the equation, $i_p = av^b$. The plot of $logi_p$ versus $logv$ produces a slope that corresponds to the values of b. The b value of ~ 1 indicates a capacitive-controlled ion-storage process in the electrode, which was governed by the capacity reaction; whereas, the b value, ~ 0.5, suggests a solid-state diffusion reaction.[11] The calculated *b*-values for the pair of redox peaks, II and II', are 0.958 and 0.908, respectively, as shown in **Figure 6.9c**, which suggests a capacitive-

controlled reaction. Similarly, the obtained *b*-values of the pair of redox peaks, I and I', are estimated to be 0.743 and 0.961, as shown in **Figure 6.9b**, which suggests both surface-controlled and diffusion-controlled reactions in the $MoTe_2$ electrode.

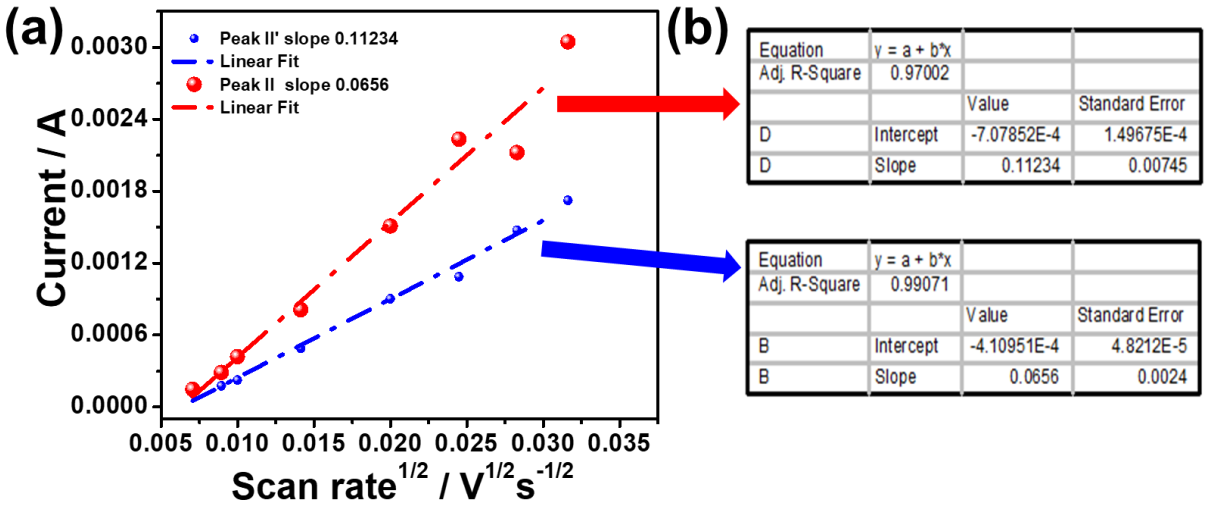

Figure 6.10 Kinetics and quantitative analysis of the Na^+ storage mechanism in the $MoTe_2$ electrode. (a–b) Linear fitting of the peak current versus the square root of the scan rate of the reduction (II) and oxidation (II') peaks.

Therefore, the kinetic analysis suggests that the $MoTe_2$ electrode is primarily governed by the pseudocapacitance process. The above observations could be further related to the superior performance of the $MoTe_2$ electrode at a higher current density, as observed from the rate capability study. The obtained current corresponds to a particular potential that is contributed by two phenomena, namely, the surface-contributed capacitive effect and the diffusion-controlled insertion process.[11–13] The two processes can be described quantitatively by the different sweep rates of the obtained CV results according to the equation, $i(V) = k_1v + k_2v^{1/2}$. Here $i(V)$ is related to the total current contributions that are split by k_1v and $k_2v^{1/2}$, which is a result of the capacitive contribution by the surface and the diffusion-controlled insertion process, respectively. The $\frac{i(V)}{v^{1/2}}$ versus $v^{1/2}$plot at different scanning rates results in a straight line, which fits a slope that corresponds to the value of k_1 and the intercept, k_2, respectively, as shown in **Figure 6.9d** and **Figure 6.10a** corresponding to the reduction peaks (I, II) and oxidation peaks (I' and II').

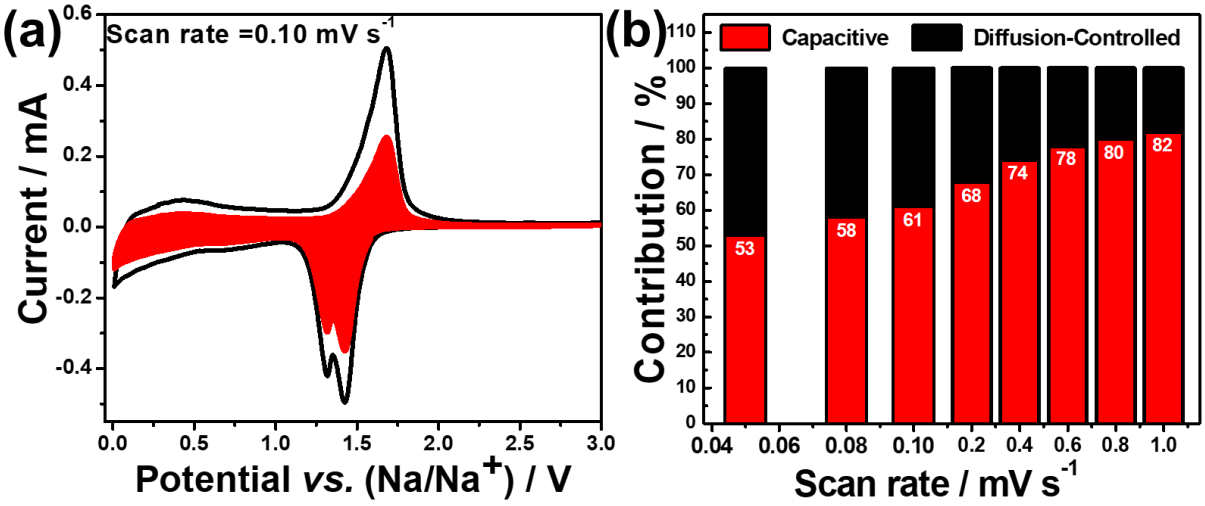

Figure 6.11 Kinetics and quantitative analysis of the Na^+ storage mechanism in the $MoTe_2$ electrode. (a) Fitted pseudocapacitive contribution (red area) of the $MoTe_2$ electrode at a scan rate of 0.10 mV s^{-1} in the potential window, 0.01–3.00 V. (b) Ratio of pseudocapacitive (red) and diffusion-controlled (black) capacities at various scan rates of $MoTe_2$ electrodes.

Figure 6.11a shows the fitted CV curve, in which the capacitive current is denoted by the shaded red region in comparison to the total current that is obtained from the $MoTe_2$ electrode at a scan rate of 0.1 mV s^{-1}. From the fitted curve, it is clear that the major contribution (61 %) to the total Na^+ storage capacity arises from the capacitive behavior of the MoT_2 electrode. The MoT_2 electrode exhibits 53 %, 58 %, 61 %, 68 %, 74 %, 78 %, 80 %, and 82 % of capacitive contributions at the scan rates, 0.05, 0.08, 0.10, 0.20, 0.40, 0.60, 0.80, and 1.00 mV s^{-1}, respectively, as shown in **Figure 6.11b**. The observed results further confirm that the capacitive contribution of the $MoTe_2$ electrode becomes predominant at higher current densities. The phenomenon mentioned above relates the sluggish transport and storage of Na^+ to its larger ionic radius. A phenomenon that is similar to that in MoS_2 and $MoSe_2$ is observed for other 2D chalcogenides.[11] Further, we have used the Randles–Sevcik equation to calculate the Na^+ apparent diffusion coefficient (equation 2):

$$i_p = 0.4463n^{3/2}F^{3/2}CARF^{-1/2}T^{-1/2}FD_{cv}V^{1/2}F \ldots\ldots\ldots\ldots\ldots\ldots \quad (2),$$

where i_p is the peak current, n corresponds to the number of electrons, F corresponds to Faraday's constant (96485 C mol^{-1}), C represents the bulk concentration (mol cm^{-3}), A represents the area of the electrode (cm^2), R represents the gas constant (8.314 J mol^{-1} K^{-1}), T represents the absolute temperature (K), D_{cv} diffusion coefficient (cm^2 s^{-1}) corresponds to the Na^+ apparent diffusion coefficient, and V corresponds to the potential scan rate (mV s^{-1}) as

shown in **Figure 6.9**. The obtained values for the Na^+ apparent diffusion coefficients at different anodic and cathodic peaks are in the order of 10^{-9} (within the range of 1.1×10^{-9} – 5.4×10^{-9}), as shown in **Table 6.1**. This indicates a much better Na^+ diffusion coefficient in the $MoTe_2$ electrode than in other Mo-based chalcogenides such as $MoSe_2$ and MoS_2.[11,14]

Table 6.1 CV results showing different scan rates of the $MoTe_2$ electrode.

Scan rate ($mV\ s^{-1}$)	**Voltage values**					
	V(I')	**V(II')**	**V(I)**	**V(ll)**	**V (I'I) (diff. between anodic and cathodic potential)**	**V (II'II) (diff. between anodic and cathodic potential)**
0.05	1.6327	1.5508	1.47589	1.32187	0.15681	0.22893
0.08	1.6581	1.5668	1.44287	1.31585	0.21523	0.25095
0.10	1.6784	1.5851	1.42686	1.31487	0.25154	0.27023
0.20	1.7041	1.6099	1.37187	1.27486	0.33223	0.33504
0.40	1.7339	1.6339	1.32777	1.24776	0.40613	0.38614
0.60	1.7562	1.6521	1.30582	1.24281	0.45038	0.40929
0.80	1.7950	1.6899	1.2748	1.11879	0.5202	0.57111
1.00	1.8174	1.7109	1.26679	1.0878	0.55061	0.6231
Diffusion coefficient ($D_{cv}\ Na^+ / Cm^2\ s^{-1}$)	1.149 $x10^{-9}$	1.4855 $x10^{-9}$	5.329 $x10^{-9}$	4.356 $x10^{-9}$		

The denominations that were used are: V(I) and V (II) for the reduction peak voltage, V(I') and V (II') for the oxidation peak voltage, V(I'I) for the difference between V(I) and V(I'), and V (II'II) for the difference between V(II) and V(II').

6.3.4 In situ impedance analysis of $MoTe_2$ versus Na metal half cell

To analyze the improved electrochemical performance of the $MoTe_2$ anode, a detailed EIS experiment was carried out at OCV, after the first discharge and consecutive discharge/charge cycles (after 1^{st}, 5^{th}, 10^{th}, 20^{th}, 50^{th} and 100^{th} cycles) of the $MoTe_2$ electrode samples that were between 10 mHz to 1 MHz. **Figure 6.12** shows the Nyquist plots of all the electrodes. The Nyquist plots of the $MoTe_2$ cell before cycling and after the 1^{st}, 5^{th}, 20^{th}, 50^{th}, and 100^{th} cycles were obtained by deconvolution with the equivalent-circuit model, as shown in **Figure 5a**. The equivalent-circuit model describes the electrochemical reaction steps, including Na^+ migration through the SEI layers, the charge-transfer reaction, and the diffusion kinetics throughout the active materials. In **Figure 6.12**, different EIS spectra of the $MoTe_2$ electrode during the cyclic process are shown.

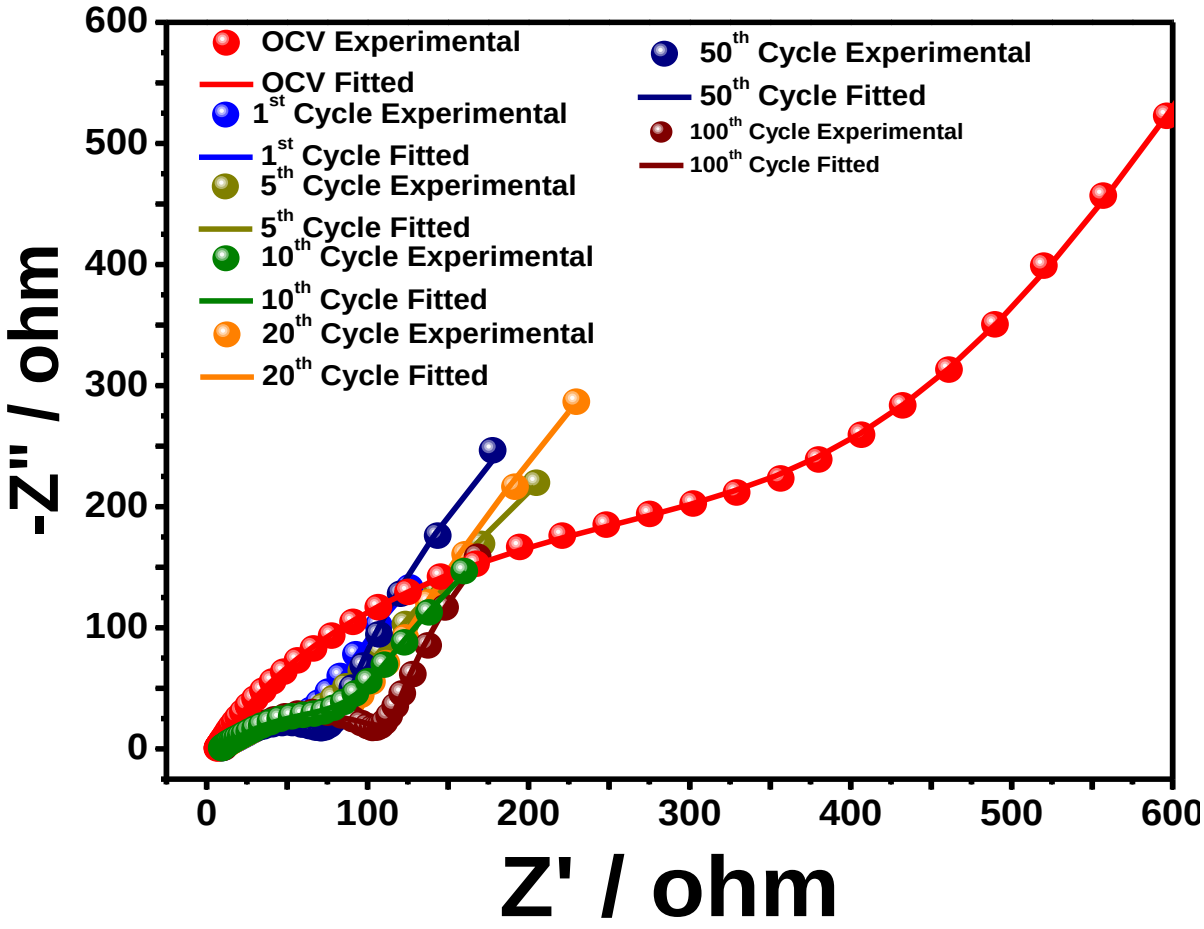

Figure 6.12 EIS spectra of the $MoTe_2$ anode in a half-cell configuration between 10 mHz and 1 MHz, showing Nyquist impedance plots before the cycle, and after the 1st, 5th, 10th, 20th, 50th, and 100th cycles at 20 ± 2 °C.

At OCV, the $MoTe_2$ electrode sample exhibited the maximum charge-transfer resistance in the cycling cell. Significantly, it is observed that the Nyquist graphs for all observations show discrete semicircles at a high frequency, which is a result of the impedance of surface film passivation, electrolyte resistance, and the sodium intercalation process.[15–17] In **Figure 6.12**, except for OCV, where the R_{ct} value is very high ~ 66, which further decreases abruptly after the 1st cycle, this could be due to the transformation of the $MoTe_2$ crystals into ultrafine nanocrystals during the 1st cycle.[16] The R_{ct} values of the $MoTe_2$ sample that is shown in **Table 6.2** remain almost unchanged (10–13 ohms) after the 1st cycle, which shows that the Na^+ diffusion and the stability of the discharge/charge capacity of the cycled electrode remain the same. This phenomenon is a result of the increasing ionic conductivity of the $MoTe_2$ during Na^+ insertion or when an additional conducting $MoTe_2$ phase is generated. The results of the EIS analyses are evidence of the structural stability of the cycled electrode during the repeated sodiation and desodiation processes.

Table 6.2 Impedance fitted parameters for different cycled electrode samples.

Cycle No	R_e (Ohm)	R_f (Ohm)	R_{ct} (Ohm)
Before cycling	8.504	380.8	65.86
1st	9.137	42.26	10.25
5th	8.612	48.04	11.84
10th	9.045	60.42	14.09
20th	8.668	73.5	12.78
50th	8.812	60.05	10.57
100th	8.663	94.26	12.55

6.3.5 Understanding the reaction mechanism of the $MoTe_2$ anode

To understand the reaction mechanism and the phase change during the conversion reaction in the 1st cycle, SXRD, HRTEM with SAD, XPS, and XANES were performed on the cycled $MoTe_2$ electrodes in the ex situ mode. For this, three identical half-cell configuration cells were made after the electrochemical cycle of the $MoTe_2$ electrode against sodium metal.

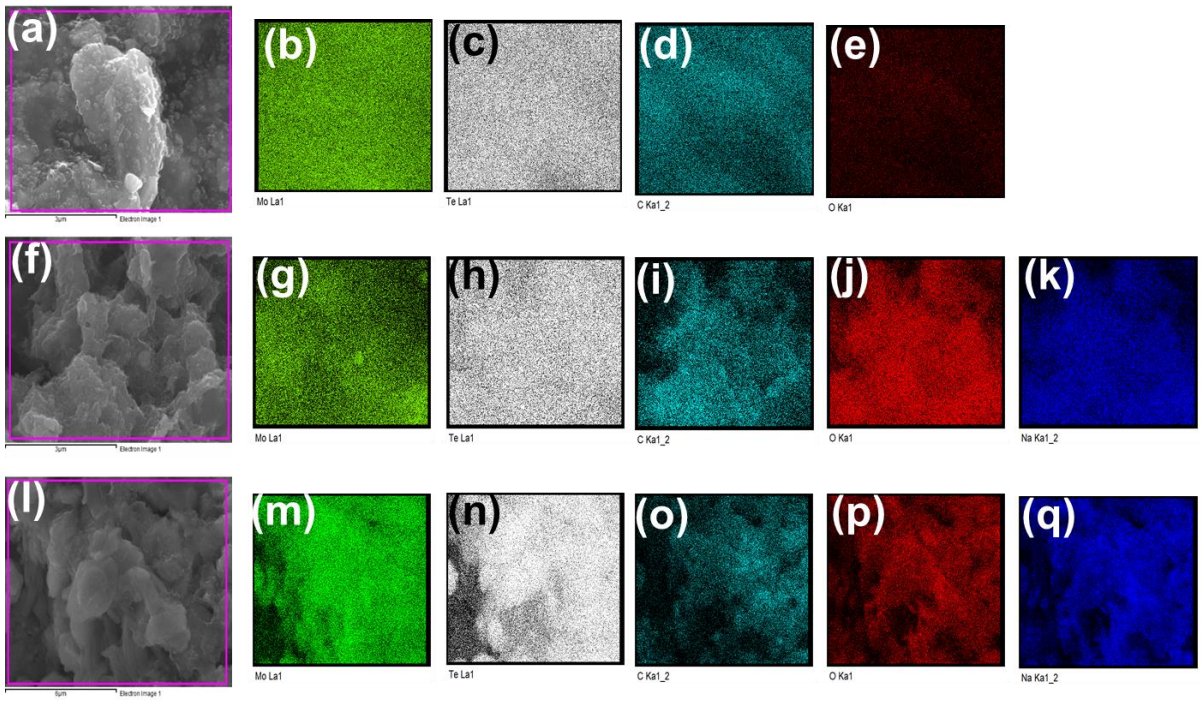

Figure 6.13 EDS mapping of the $MoTe_2$ electrode sample, showing the presence of Mo, Te, C, O, and Na elements. (a–e) As-prepared electrode. (f–l) After 1st discharge. (m–r) After the 5th cycle of the $MoTe_2$ electrode in a fully charged state.

After cycling, the cells were disassembled inside an Ar-filled glove box, and the electrodes were washed well to avoid residual salt (if any). In order to investigate the morphology of the cycled electrode, ex situ SEM characterization was performed. The SEM images revealed that the block-type morphology of the $MoTe_2$ changed to highly disordered shapes after first discharge (**Figure 6.13**). The elemental mapping showed a homogeneous distribution of Mo and Te on the surface of the cycled electrodes, indicating the presence of an active material in the anode, as shown in **Figure 6.13**. However, the morphology of the $MoTe_2$ electrode did not change much after the first cycle of the discharge/charge process, which confirmed the possible structural stability of the $MoTe_2$ electrode after cycling.

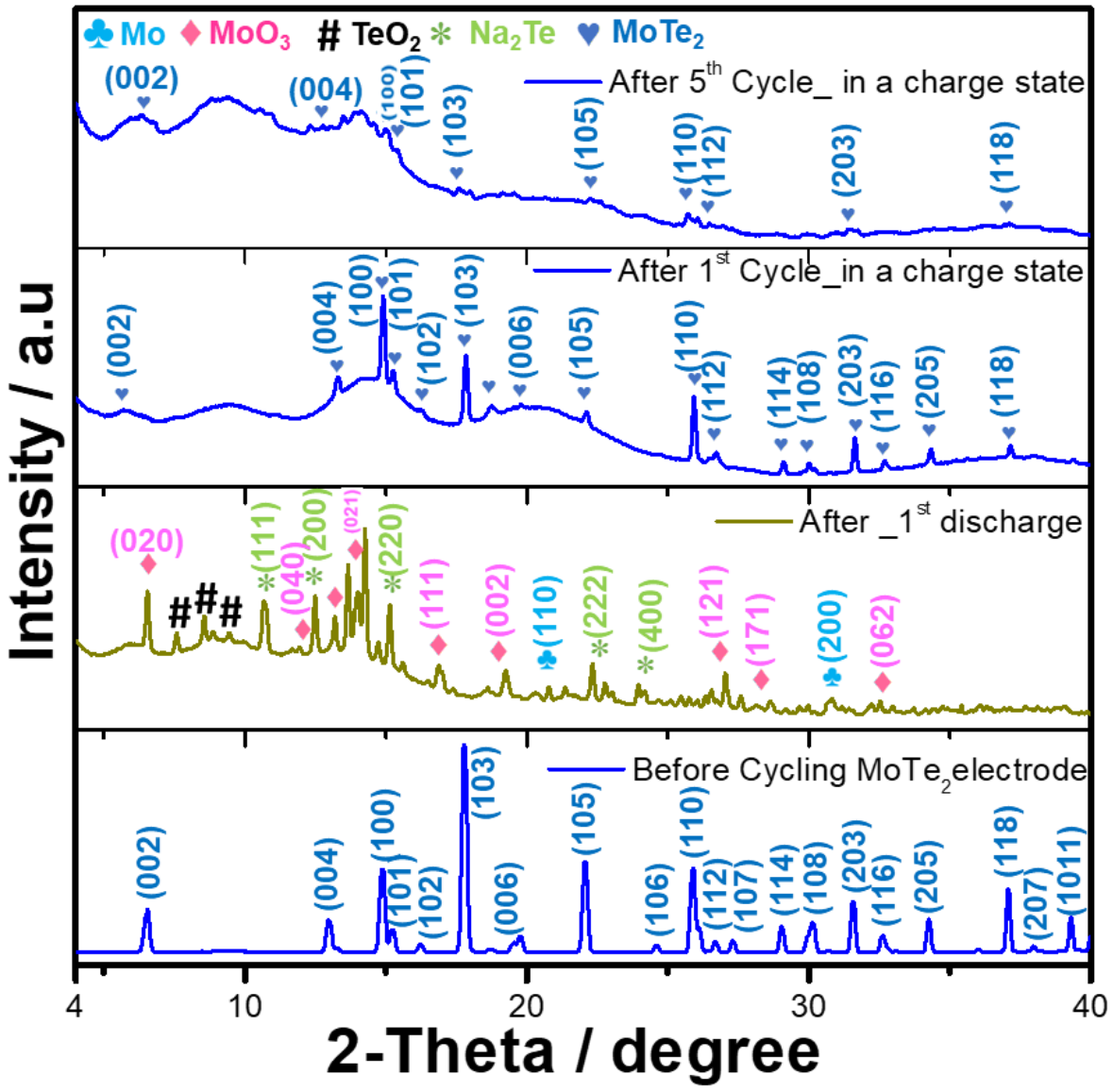

Figure 6.14 Ex situ SXRD of the $MoTe_2$ cycled electrodes, showing before cycling, after 1st discharge, and after the 1st and 5th cycles in a fully charged state. The inset shows symbolic notations that correspond to the related phases.

The ex situ SXRD of the $MoTe_2$ electrode before cycling, after first discharge and after the 1st and 5th cycles (maintained in a charged state) are shown in **Figure 6.14**. The peaks that correspond to different phases are denoted by different notations such as heart (♥) for $MoTe_2$, club (♣) for Mo, diamond (♦) for MoO_3, octothorpe (#) for TeO_2, and star (*) for Na_2Te. During the discharge process, the diffraction peaks of the $MoTe_2$ begin to disappear, which indicates the insertion of Na^+ into the $MoTe_2$ host structure to form Na_xMoTe_2. From the SXRD pattern after the first discharge, the $MoTe_2$ peaks completely disappear and the observed peaks match with the Mo (pdf# 00-001-1205), MoO_3 (pdf# 00-005-0506) and Na_2Te (pdf# 00-023-0442) peaks. A few minor peaks match with TeO_2 (pdf# 00-021-1204) due to the formation of the oxide phase in Mo and Te due to the atmospheric oxygen, when the ex situ experiments are performed. A similar phenomenon has been observed in the results from XPS and XANES. The characteristic peaks of the $MoTe_2$ have been observed during the completion of the 1st cycle, as shown in **Figure 6.14**. However, the observed peak intensity mismatch in comparison to that of the $MoTe_2$ structure might be due to the increased amorphousness after the 1st cycle. Similarly, after the 5th cycle, that is, in the charged state, no sharp $MoTe_2$ peaks have been detected, which confirms that the $MoTe_2$ turns highly amorphous during the discharge/charging process.[2,3]

Further, the HRTEM image and SAD patterns of the 1st discharge, after the 1st, 5th, and 200th cycles in a fully charged state are shown in **Figure 6.15**. The SAD pattern of the first discharged electrode sample is matched with metallic Mo and Na_2Te phases. **Figure 6.15a, d, g, and j** show the BF image, which is indicated by a shaded circle for the location at which the SAD pattern was taken. The SAD and HRTEM displayed in **Figure 6.15c** show lattice fringes of (0.16 nm) and (0.22 nm), which correspond to the (200) and (110) planes of the Mo metal, respectively; and (0.18nm) and (0.26 nm), which correspond to the (400) and (220) planes of the Na_2Te, respectively, and are consistent with the ring patterns that are observed from the SAD pattern (**Figure 6.15b**) After the 1st cycle in a charged state, the lattice fringes of (0.21 nm), (0.25 nm) and (0.30nm) correspond to the (105), (103) and (100) planes of the $MoTe_2$ phase, respectively, and have consistent ring patterns, as observed from the SAD pattern (**Figure 6.15e–f**). For the electrode after the 5th cycle in a charged state, the observed lattice fringes of (0.20 nm) and (0.30 nm) match the corresponding planes of (105) and (100) of the $MoTe_2$ structure (**Figure 6.15i**), whereas the SAD pattern (**Figure 6.15h**) shows increased amorphousness, which could be ascribed to the formation of ultrafine $MoTe_2$ nanocrystals by the repeated sodiation/ desodiation process.[2,3] **Figure 6.15l** shows the lattice fringes of (0.30

nm) that correspond to the (100) plane of the $MoTe_2$ structure. However, after 200 cycles, no obvious change in the SAD pattern was observed, which further attests to the formation of the amorphous phase of $MoTe_2$ in the electrode (**Figure 6.15k**).[2]

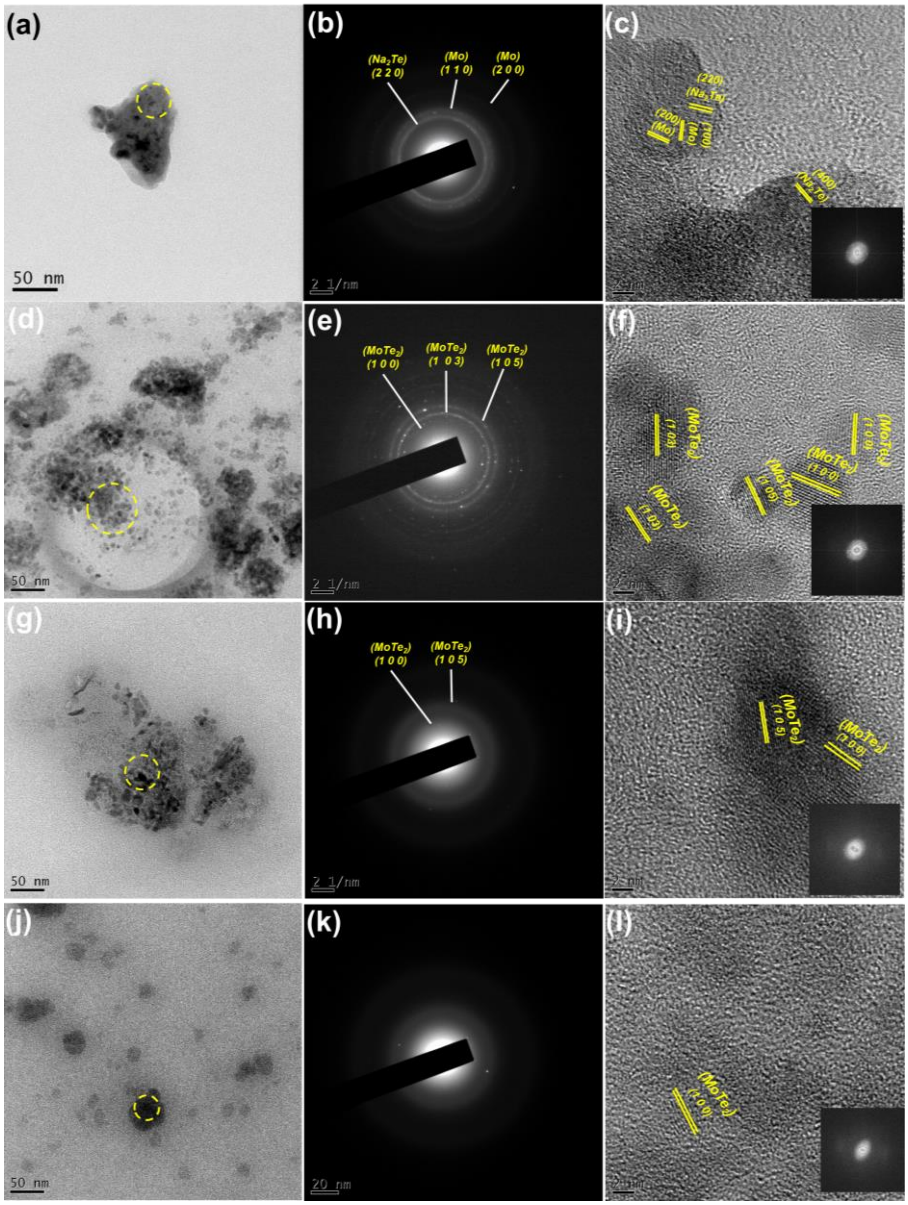

Figure 6.15 Bright field images, SAD patterns, and HRTEM images of the $MoTe_2$ cycled electrodes (inset shows all FFT patterns). (a–c) A BF-TEM image and SAD pattern from the indicated area, and HRTEM images after the 1st discharge process. (d–f) A BF-TEM image and SAD pattern from the indicated area, and an HRTEM image after the 1st cycle in a fully charged state. (g–i) A BF-TEM image and SAD pattern from the indicated area, and an HRTEM image after the 5th cycle in a fully charged state. (j–l) A BF-TEM image and SAD pattern from the indicated area, and an HRTEM image after the 200th cycle in a fully charged state.

In order to identify the charge states of the existing elements for the cycled $MoTe_2$ electrode at OCV after the 1st discharge and after the 1st cycle (that is, when kept in a charged state), were characterized through Te and Mo HRXPS spectra, as shown in **Figure 6.17a, b**.

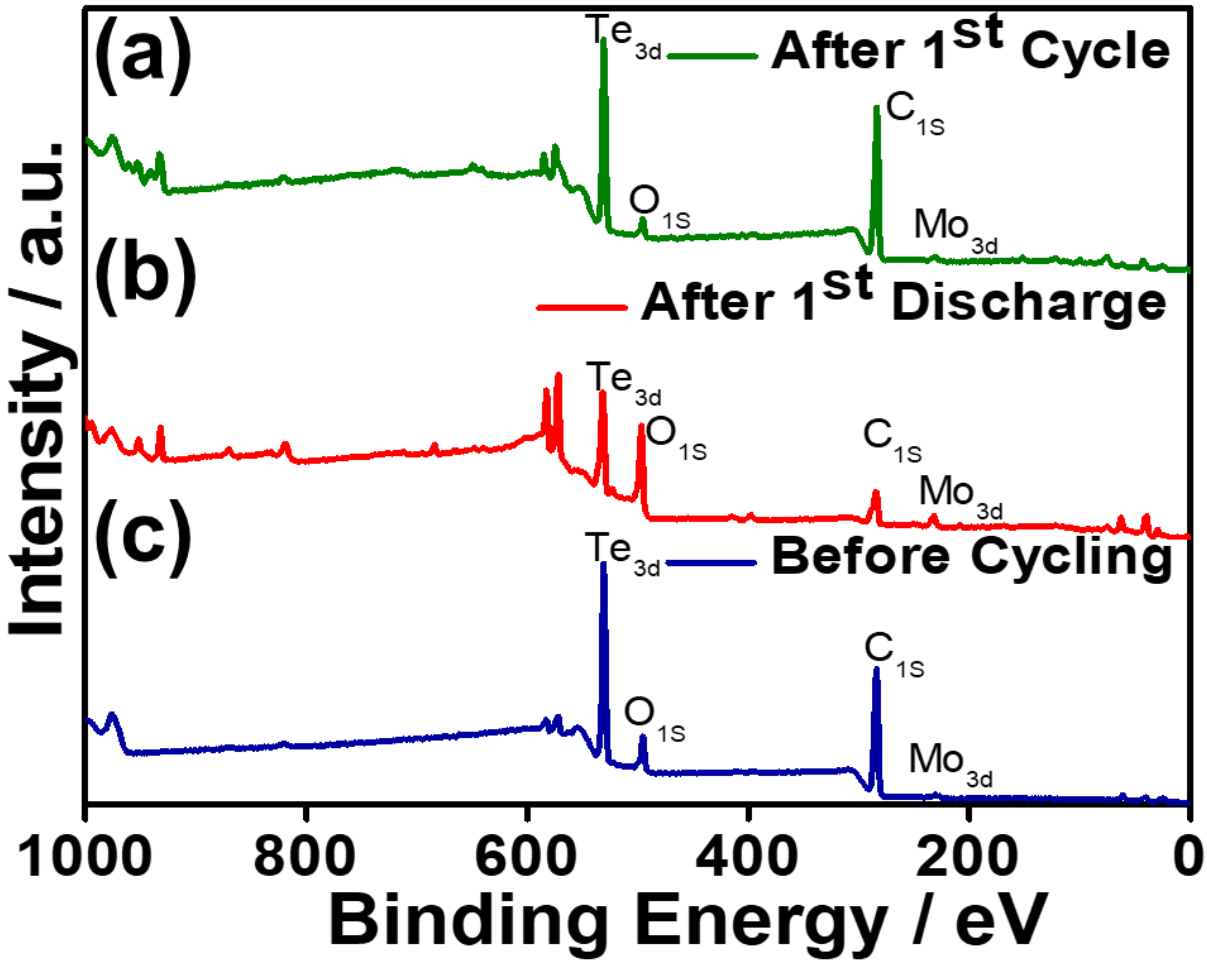

Figure 6.16 Full-scan X-ray photoelectron spectra of $MoTe_2$ electrode samples. (a) After 1st cycle in a fully charged state. (b) After 1st discharge. (c) Before cycling.

The survey XPS spectra given in **Figure 6.16 a–c** indicate the presence of Mo, Te, C, and O in all the electrode samples. In the Mo-3d spectrum of the electrode samples in **Figure 6.17b**, the prominent peaks are located at binding energies of ~231.4 eV for Mo $3d_{3/2}$ and ~227.8 eV for Mo $3d_{5/2}$; the presence of these two major peaks are representative of the $MoTe_2$ phase.[18,19] The minor peak that is situated near ~235.2 eV is recognized as the Mo $3d_{5/2}$ peak, which corresponds to MoO_3, indicating partial oxidation of the sample.[20]

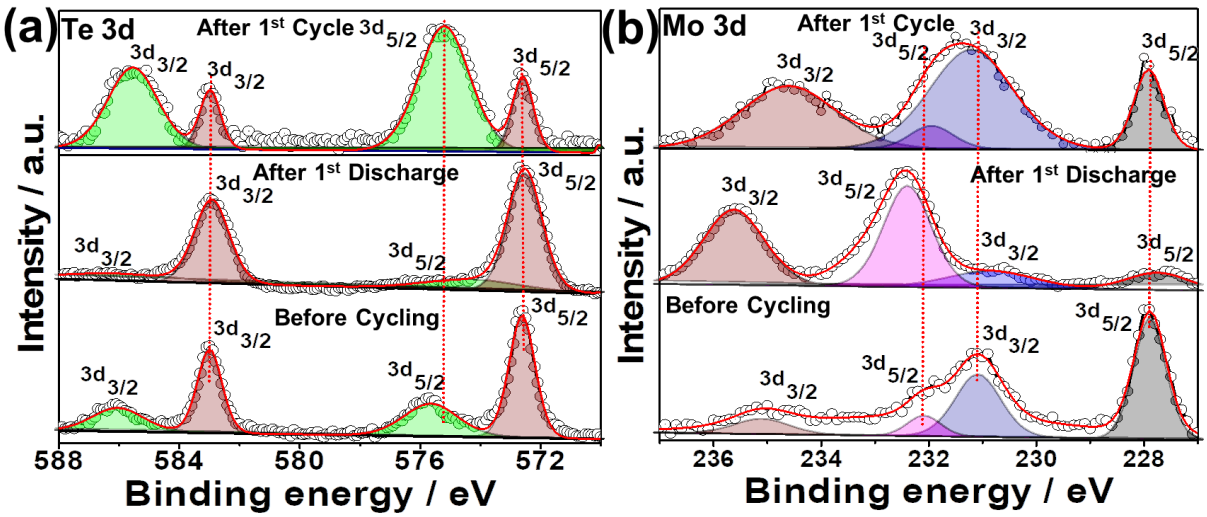

Figure 6.17 (a–b) Deconvoluted Te and Mo HRXPS spectra of $MoTe_2$ electrodes at OCV after 1st discharge and 1st cycle of the $MoTe_2$ electrodes.

In the Te-3d spectrum (**Figure 6.17a**), the peaks at ~572.6 and ~583.0 eV correspond to Te $3d_{5/2}$ and Te $3d_{3/2}$, respectively, which are characteristic of the $MoTe_2$ phase. In addition, two peaks are present at 575.64 and 586.05 eV, which are attributed to the presence of TeO_2 because of oxidation by air. The Mo HRXPS spectra for the electrode after the 1st discharge shows the presence of MoO_3 phase peaks that are positioned at ~230.47 eV, which correspond to $Mo3d_{3/2}$, and at ~232.48 eV, to Mo $3d_{5/2}$. The presence of MoO_3 is due to the highly reactive nature of the formed metallic Mo nanocrystals react highly to atmospheric oxygen, leading to the presence of MoO_3. The Te HRXPS spectrum of the first discharge electrode, and the peaks at 572.52 eV and ~582.92 eV, which correspond to Te $3d_{5/2}$ and $3d_{3/2}$, respectively, represent the Na_2Te phase.[21]To analyze the reversibility of the $MoTe_2$ structure, the XPS spectra that are collected after the 1st cycle electrode sample show two characteristic peaks for $Mo3d_{3/2}$ (~230.47 eV) and $Mo3d_{5/2}$ (~227.78 eV); whereas, the Te-3d XPS spectrum shows Te $3d_{5/2}$ (~572.58 eV) and $3d_{3/2}$ (~582.97), which confirms the characteristic peaks of the $MoTe_2$ phase.[18] Moreover, the additional MoO_3 peaks that are present at 231.94 eV, 234.61 eV, and TeO_2 (575.19 eV and 585.54 eV for Te $3d_{5/2}$ and Te $3d_{3/2}$, respectively) are due to the formation of the oxide phase of Mo and Te due to atmospheric oxygen. Therefore, the XPS analysis that is mentioned above illustrates the formation of metallic Mo nanocrystals by the end of the first discharge process, which is followed by the reversible intercalation mechanism of Na with Te during subsequent cycling. However, XPS is a surface-sensitive technique, which cannot provide information at a bulk level

for the cycled electrodes. Therefore, to cross-check the phenomenon that is mentioned above more carefully, XANES was carried out for a different set of electrode samples to understand and confirm the mechanism. Although we performed an ex situ SXRD analysis to observe the phase change of the $MoTe_2$, the formation of nanocrystalline, and the amorphous phase nature of the $MoTe_2$ electrodes after the discharge/charge process, due to the inability of XRD to identify the oxidation states of Mo, XANES is a better technique to justify the results.

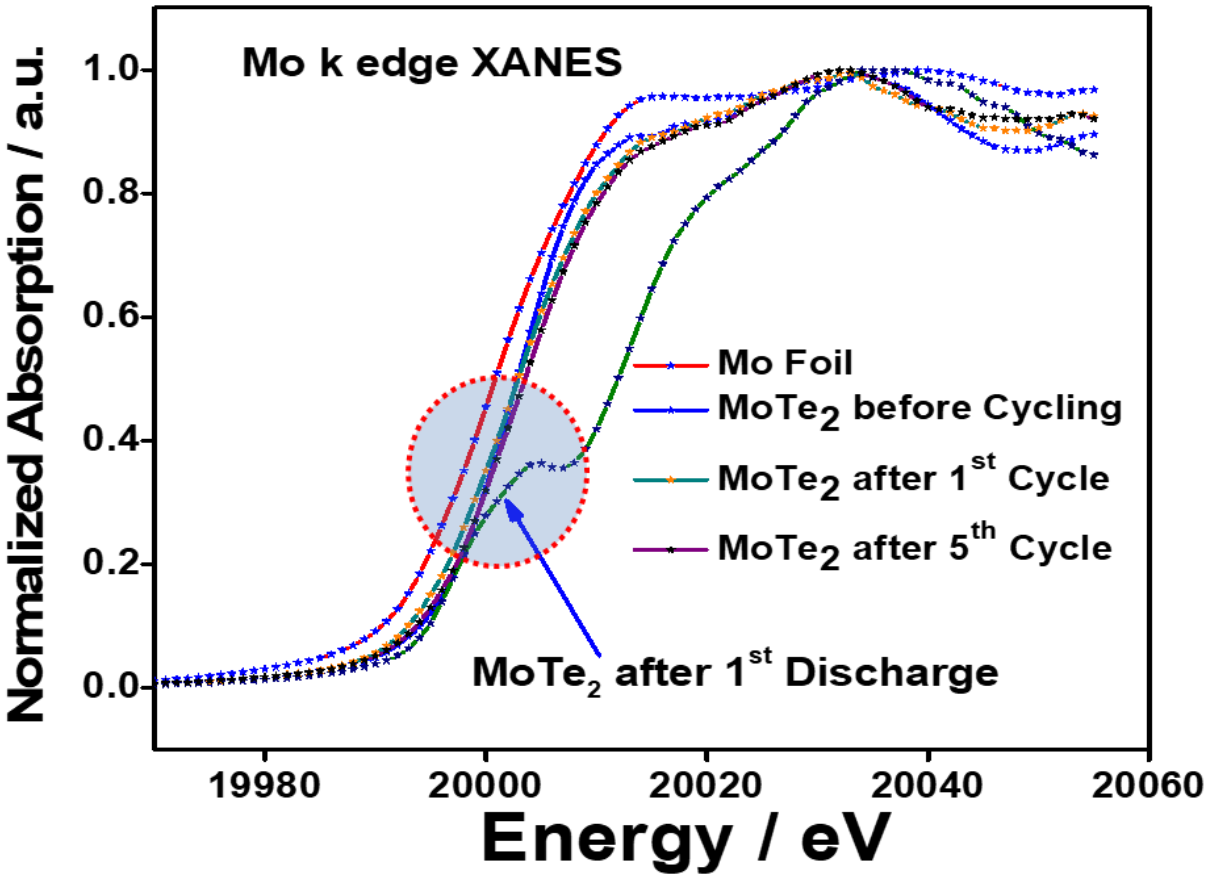

Figure 6.18 Normalized Mo K-edge XANES spectra of $MoTe_2$ electrodes before cycling, and after 1st discharge, 1st cycle, and 5th cycle. (A standard Mo foil is used as a reference.)

Figure 6.18 shows the Mo K-edge normalized XANES spectra for $MoTe_2$ cycled electrodes, that is, the XANES spectra of as-prepared, after first discharge, and after consecutive discharge/charge cycles (1st and 5th cycles kept in a charged state) along with Mo metal foil. The Mo metal foil refers to a zero-valence state of the molybdenum. The extent of the shift of the binding energy (that is, ΔE) can be obtained by the maxima of the first derivative of the edge, which increases toward the higher values with a further increase in the oxidation state of the molybdenum.[5,22–24] The edge-step normalized

energies of all the samples are in the range of 3 to 4 eV, which is higher than those of the Mo foil except for the first discharge electrode (shown in **Table 6.3**).

Table 6.3 Mo K-edge energy positions of the samples with respect to the standard Mo metal foil (20000 keV).

Samples	**Mo K-edge energy position E (eV)**	**ΔE (eV)**	**Phase similarity**
Mo foil	20000.00	00.00	-
Before cycle (OCV)	20003.00	03.00	with $MoTe_2$
After 1st discharge	20013.00	13.00	with MoO_3
After 1st cycle (charge state)	20003.46	03.46	with $MoTe_2$
After 5th cycle (charge state)	20003.75	03.76	with $MoTe_2$

The oxidation state of Mo in the as-prepared electrode sample (before cycling) is +4, which confirms the presence of pure-phase $MoTe_2$. For the first discharge electrode sample, the absorption edge is shifted to higher energy due to the increase in the core electron binding energy, which oxidizes the as-formed Mo nanoparticles to their corresponding highly stable oxide, that is, MoO_3. The presence of the pre-edge peak correlates with the local symmetry around Mo atoms. The distortion from an ideal octahedral symmetry removes the inversion center and induces hybridization between p and d orbital. As a consequence, a distinct pre-edge peak occurs due to the transition from the core 1s level to the unoccupied 4d orbital.[25] Therefore, the oxidation state of Mo in this sample is close to +6, and it corresponds to MoO_3. A similar phenomenon is observed in the previously reported literature.[24] Hence, from the above observation, a good correlation was found between the SXRD, HRTEM, XANES, and XPS results, which enabled the understanding of the Na^+ storage mechanism in the $MoTe_2$ host. Although the absorption edge of the sample after the 1st and 5th cycles in fully charged states is shifted slightly toward the higher values, both are in coherence with the XANES pattern of the pristine $MoTe_2$, which confirms the reversible storage of Na^+ in the $MoTe_2$ matrix.

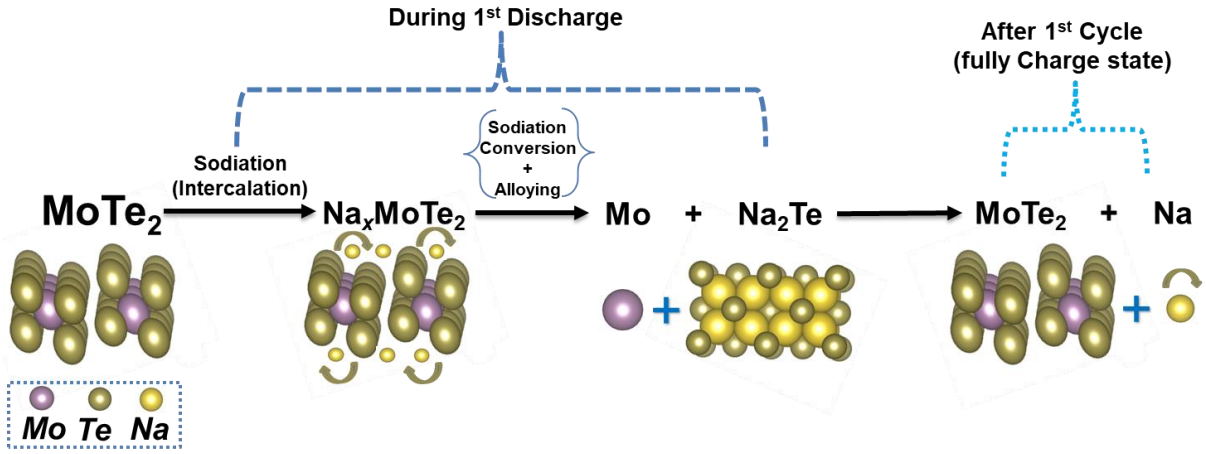

Figure 6.19 Proposed reversible Na^+ storage mechanism of the $MoTe_2$ anode.

In **Figure 6.19**, we propose a schematic illustration of possible electrochemical reactions during the first cathodic and anodic scan. The probable electrochemical mechanism of the $MoTe_2$ host with respect to Na/Na^+ can be divided into two parts (the reaction during the 1st cathodic scan and after the 1st anodic scan). In the electrochemical reaction that occurs during the first discharge cycle, that is, the first cathodic scan, the reduction peak at ~86 V corresponds to the intercalation reaction, $MoTe_2 + xNa^+ \rightarrow Na_xMoTe_2$. The sharp cathode peak at ~0.49 V corresponds to the conversion reaction of the $MoTe_2$ during the formation of metallic Mo nanoparticles and the subsequent alloying reaction between Na and Te to form Na_2Te; this is clear from SXRD, HRTEM, XPS, and XANES and is congruent with the literature.[2,3,26–28] The XANES experiments for the 1st and the 5th cycles that are kept in a fully charged state confirm the reconstitution of the $MoTe_2$ phase and the structural reversibility of the $MoTe_2$ anode. In future work, we hope to provide additional insights into the cycling mechanism by further reducing the influence of unwanted oxygen contact and by developing supporting computational models.

To establish the capability of the $MoTe_2$ as a potential anode material in SIB applications, NVP was established as the cathode material to construct the full-cell prototype. The NVP was synthesized through a simple two-step solid-state reaction route, and it was examined by various physical characterizations such as SXRD, FESEM, HRTEM, and XPS studies, as shown in **Figure 6.20** and **Figure 6.21** confirms the successful preparation of NVP.[5]

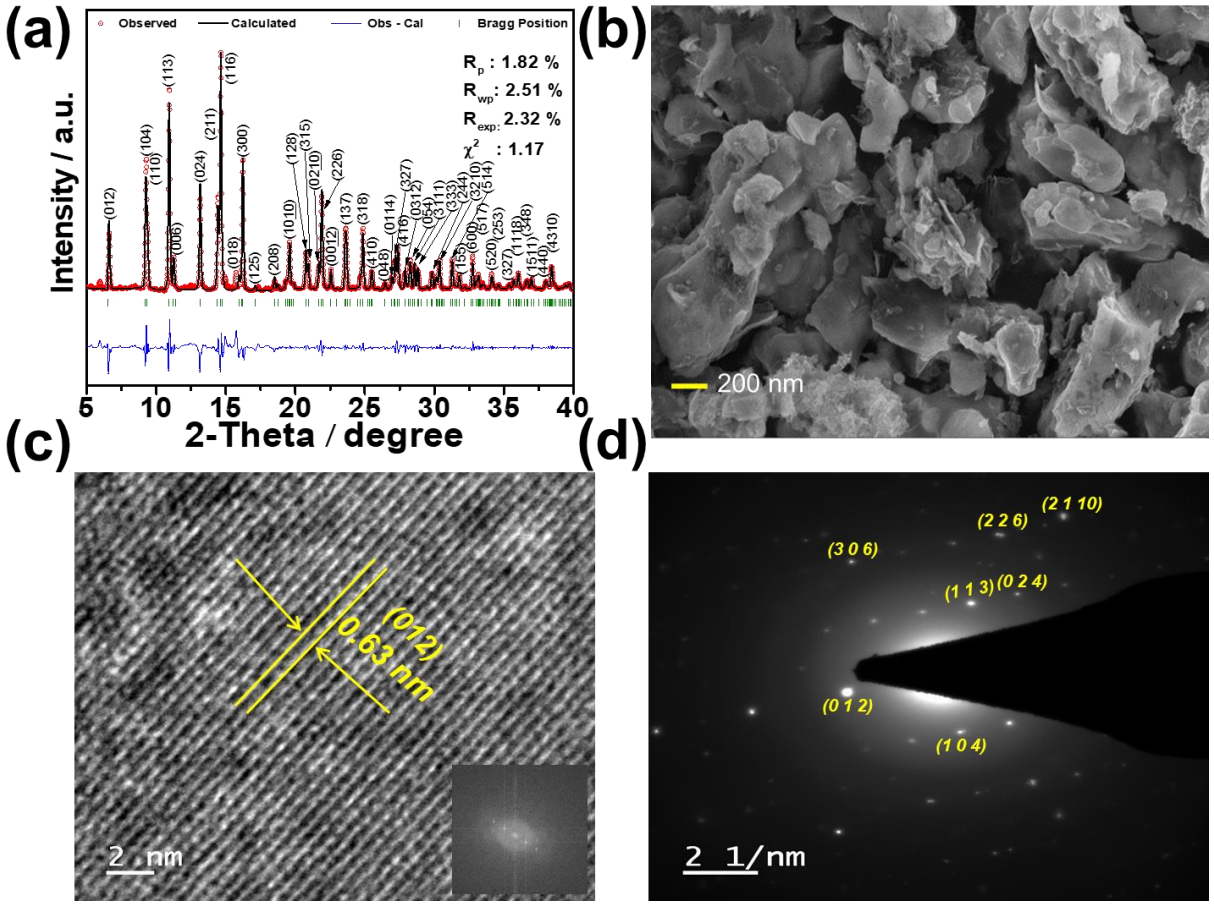

Figure 6.20 Structural and morphological characterization of the as-prepared $Na_3V_2(PO_4)_3$ (NVP) sample. (a) Powder SXRD pattern of the as-prepared NVP powder and the Rietveld refinement plot along with the fitted parameters. (b) An FESEM image of the as-prepared NVP sample. (c) The HRTEM image shows the (012) plane of the NVP material; the inset shows the FFT pattern. (d) An associated SAED (SAD) pattern, showing different planes.

Figure 6.20a shows the SXRD pattern of the as-prepared NVP powder sample along with the fitted Rietveld refinement plot. The fitted SXRD peaks have been indexed with a NASICON structure that has $R\bar{3}C$ space. The fit parameters obtained from the Rietveld refinement, such as R_p (1.02 %), R_{wp} (1.07 %), R_{exp}(1.32 %) and χ^2 (0.87), lie in a reasonable range, which confirms the acceptable quality of the Rietveld refinement and the phase purity of the NVP structure. The obtained lattice parameters such as a=b= 8.745 Å, and c= 21.85 Å are congruent with previously reported literature.[5] The morphology of the NVP material was investigated by FESEM (**Figure 6.20b**) and HRTEM (**Figure 6.20c–d**). It has been observed that the as-prepared NVP sample shows particle sizes in the range of 50–200 nm. The HRTEM image, as shown in **Figure 6.20c**, corresponds to the lattice fringes of ~0.63 nm, which corresponds to

the (012) plane of the NVP phase. The SAD pattern, as shown in **Figure 6.20d**, has been indexed to different planes of the NVP structure.

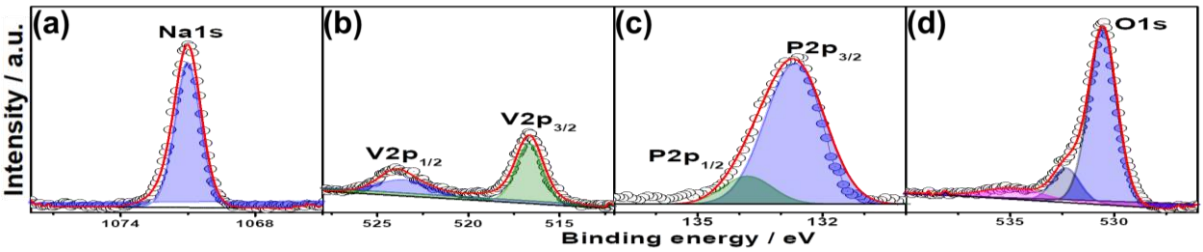

Figure 6.21 Deconvoluted Na_{1s}, V_{2p}, P_{2p}, and O_{1s}HRXPS spectra of the NVP sample.

An XPS study of the NVP sample has been carried out to obtain information about the chemical state of the corresponding elements. The deconvoluted HRXPS spectra of Na_{1s}, V_{2p}, P_{2p} and O_{1s} are shown in **Figure 6.21 a–d**. In **Figure 6.21a**, the HRXPS spectra of Na_{1s} show a peak at ~1071.1 ± 0.1eV, which corresponds to sodium atoms in the NASICON structure. The HR-XSP spectra, which correspond to V_{2p}, have been classified into two asymmetry bands that are divided into two components: 516.6 ± 0.05 eV and 517.4 ± 0.05 eV for V $2p_{3/2}$, and 523.5 ±0.03 eV and 524.06 ± 0.3 eV for V $2p_{1/2}$, as shown in **Figure 6.21b**. In **Figure 6.21c**, the P_{2p} HRXPS spectra show a peak at 133.2 ± 0.2 eV, which can be attributed to the phosphorus in the $Na_3V_2(PO_4)_3$ structure.[5,29,30] Asymmetric profiles of O 1s HRXPS spectra show the presence of two overlapping signals at 530.55± 0.2, 532.3 ± 0.2, and 534.82 ± 0.2 eV (**Figure 6.21d**). These components can be interpreted in terms of the different ionicitis that exist in Na−O−P and V−O−P bonds, which are responsible to affect the electrode-electrolyte interface and to significantly affect the accessibility of sodium ions to the NASICON structure.[5,29,30]

Further, to observe the electrochemical behavior of the synthesized NVP, its half-cell electrochemical characterizations were evaluated against the Na metal before fabricating the full-cell prototype.

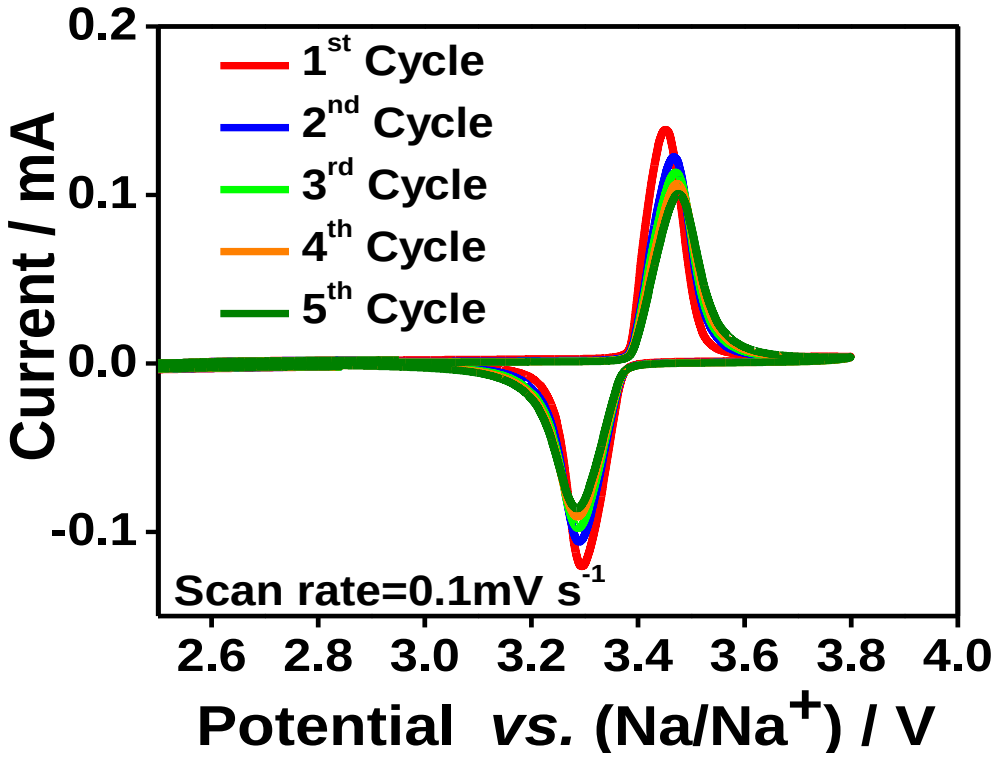

Figure 6.22 The electrochemical performance of NVP electrodes in a half-cell configuration at 20 ± 2 ºC with a typical loading of 5 mg cm^{-2} of active materials. (a) Cyclic voltammogram of the NVP electrode at 0.05 mV s^{-1} in the voltage range of 2.5–3.8 V.

Figure 6.22 shows the CV performance of the NVP material that is at 0.05 mV s^{-1} in the voltage range of 2.5–3.8 V. The CV curve shows a promising oxidation peak at ~3.45 V and a reduction peak at ~3.3 V, which are very stable and can be seen in the subsequent cycles. The cathodic peak at 3.45 V versus Na^+/Na is associated with V^{3+}/V^{4+} redox couples.[5] The Galvanostatic charge/discharge performance of the cell was carried out between the voltages, 2.5–3.8 V, to identify the charge-storage response of the material. A stable charge-discharge plateau at 3.3 V and 3.45 V corresponds to the redox peaks that are observed in CV. Two crystallographic sites accommodate Na^+ ions in the NVP compound, of which the Na (1) site remains totally occupied with one Na^+ ion, while the Na (2) site is active when the sodium content changes from $Na_3V_2(PO_4)_3$ to $NaV_2(PO_4)_3$ in a specialized voltage range.[5] However, the extraction of all three Na^+ ions with a theoretical capacity of 176 mA h g^{-1} is kinetically difficult due to the much lower electronic/ionic conductivity of the end product, $V_2(PO_4)_3$. Therefore, two-thirds of the ions are capable of being reversibly extracted/inserted, which results

in a theoretical capacity of 117 mA h g^{-1} without disturbing the lattice structure of the NVP.

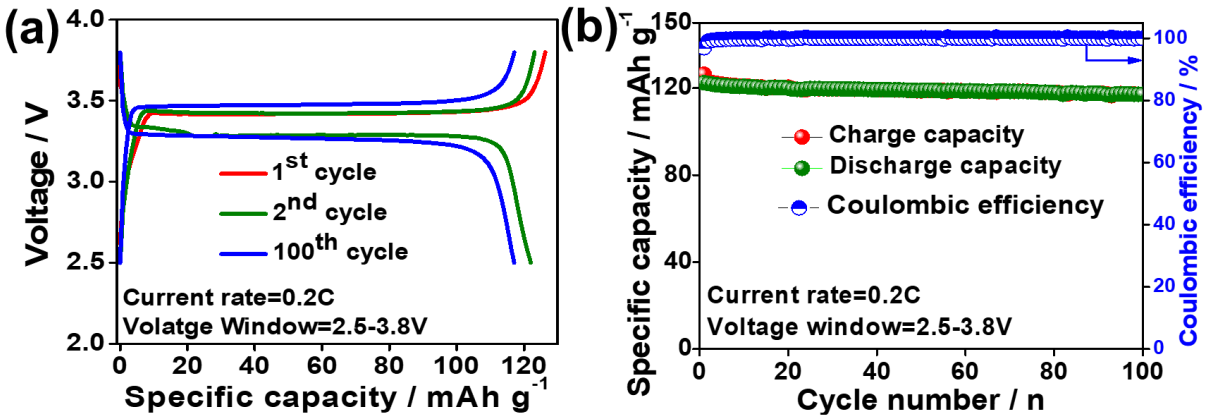

Figure 6.23 The electrochemical performance of NVP electrodes in a half-cell configuration at 20 ± 2 ºC with a typical loading of 5 mg cm^{-2} of active materials. (a) Galvanostatic charge/discharge curves of the NVP electrode at 0.2 C rate for different cycles in the voltage range of 2.5 to 3.8 V. (b) Cycling performance of the NVP electrode at 1 A g^{-1} for 100 cycles.

Figure 6.23a shows an initial charge capacity of 126.4 mA h g^{-1} and a discharge capacity of 122.4 mA h g^{-1}. During the 2nd cycle, a similar charge/discharge capacity of 122 mA h g^{-1} is achieved, which is also the case after the 100th cycle at a discharge capacity of 116 mA h g^{-1} with around 99.5 % Columbic efficiency. Additionally, from **Figure 6.23 a–b**, it can be observed that the behavior of the material in the given window is stable. The power performance of the material is additionally analyzed to check the switchability of the material at various rates. It is evident from **Figure 6.24** that the material is capable of high cycle rates, because it exhibits excellent capacity at various currents. The reversible specific capacities of 117.6 mA h g^{-1}, 113.3 mA h g^{-1}, 101.6 mA h g^{-1}, 92.4 mA h g^{-1}, 75.2 mA h g^{-1}, 50 mA h g^{-1}, and 28.6 mA h g^{-1} are achieved at 0.2C, 0.5C, 1C, 2C, 5C, 10C, and 20C, respectively, with approximately 98 % of Columbic efficiency. In addition, a similar capacity of 90 mA h g^{-1} is achieved when the material switches back from higher rates. This indicates the suitability of NVP as a cathode material in our full-cell prototype.

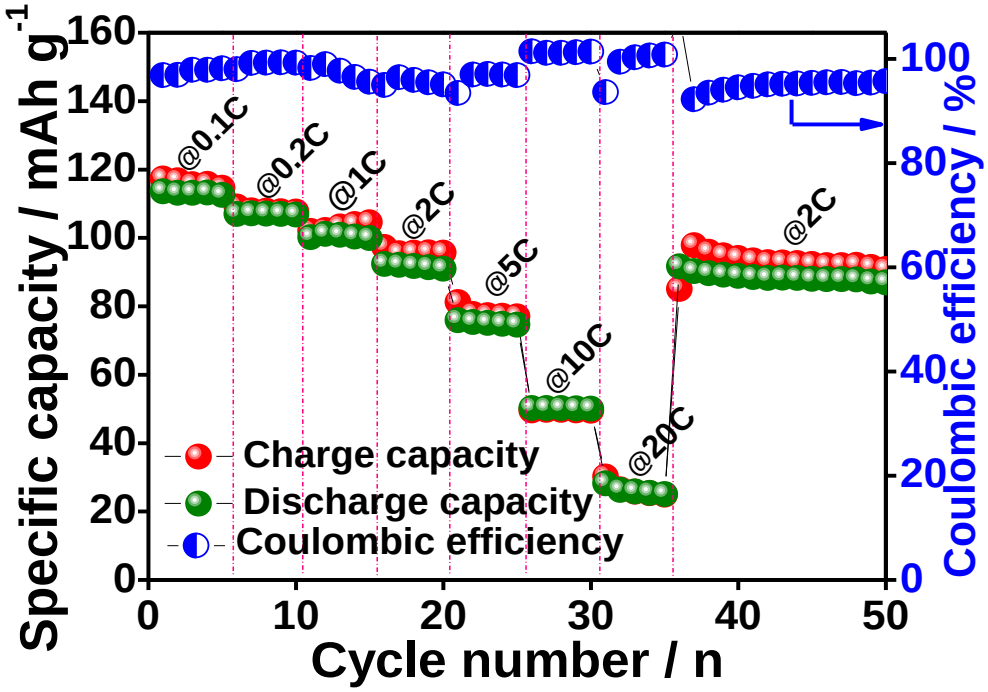

Figure 6.24 Rate performances of the NVP electrode at various rates.

6.3.6 Study of $MoTe_2$ versus NVP full cell

We developed a SIB by comparing our $MoTe_2$ anode with known cathodes for full-cell application. We demonstrate that our anode performs better than sodium-containing cathodes such as ammonium vanadium phosphate (NVP) for full-cell construction. **Figure 6.25–6.28** represents the overall electrochemical results of the sodium-ion full-cell prototype that comprises the $MoTe_2$ anode and the NVP cathode. Borosilicate glass fiber (GF/D, Whatman) is used as the separator, and it is soaked with the electrolyte that is prepared with 1 M of $NaClO_4$ in a mixture of EC and PC (1:1 v/v). An additive at 3 wt % of fluoroethylene carbonate (FEC) is also added. The amount of electrolyte was used 100 µL for the fabrication of full cell Na-ion battery. To fabricate the full cell, the potential window is decided based on the performances of individual electrodes. Based on the practical capacity, the weight ratio of the $MoTe_2$ and NVP is estimated at 1:2, approximately. The ratio of $MoTe_2$ (anode) and NVP (cathode) active materials were decided based on the half-cell specific capacity of $MoTe_2$ (~250 mAh g^{-1}) at 500 mA g^{-1}, NVP (~95 mAh g^{-1}) at 500 mA g^{-1} and the initial cycles sodium loss during charging of full cell was also under consideration. However, specific weight balancing will be required in the future. The full cell is cycled at a current rate of 5 mA g^{-1} with respect to $MoTe_2$ loading in the potential window of 1.0–3.6 V. The specific capacities are evaluated based on the mass loading of $MoTe_2$.

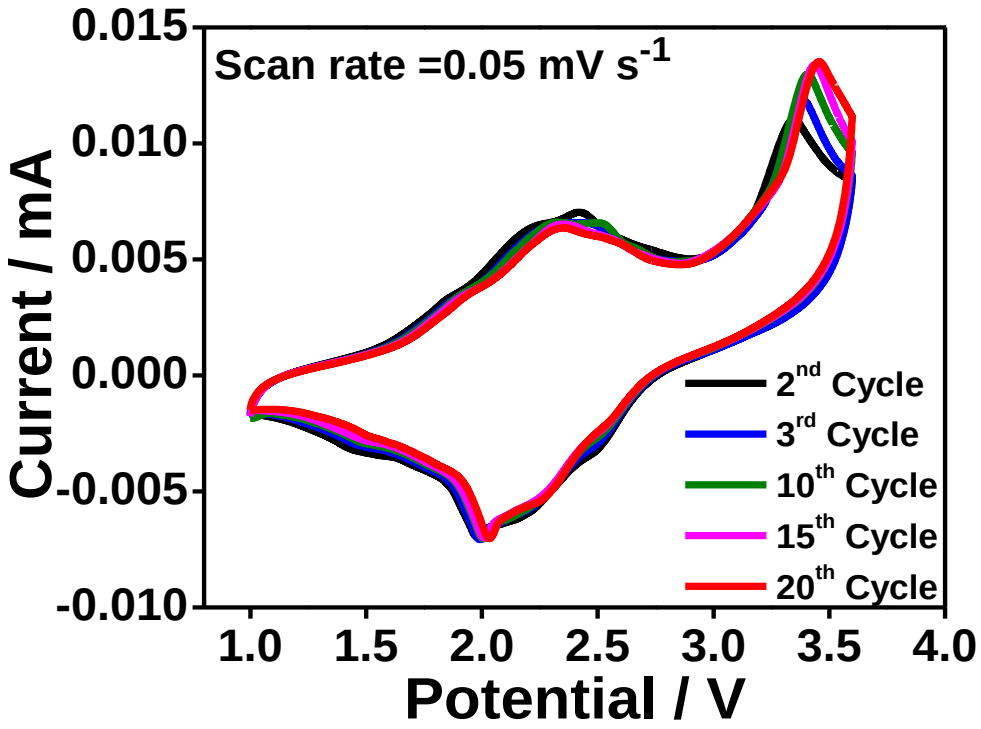

Figure 6.25 The electrochemical performance of the $MoTe_2$//NVP full cell prototype. (a) Cyclic voltammogram at a scan rate of 0.05 mV s^{-1} in the potential window, 1.0–3.6 V.

Figure 6.25 shows the CV curve of the full cell at a scan rate of 0.5 mV s^{-1}. The CV curve shows a prominent reduction peak, ~2.0 V, which corresponds to the range that controls the operational potential of the battery. Since no literature that compares the $MoTe_2$ and the NVP full cell is available, only the NVP-related full cell is used as a reference to investigate the full cell mechanism. According to the intercalation mechanism of $MoTe_2$ versus Na/Na^+, the proposed intercalation mechanism that occurs at the anode and the cathode in the SIB full cell is shown in equations (3a) and (3b) below:

Cathode:

$$Na_3V_2^{3+}(PO_4)_3 \leftrightarrow Na_{3-x}V_{2-x}^{3+}V_x^{4+}(PO_4)_3 + xNa^+ + xe^- \quad (3a)$$

Anode:

$$MoTe_2 + xNa^+ + xe^- \leftrightarrow Na_xMoTe_2 \quad (3b)$$

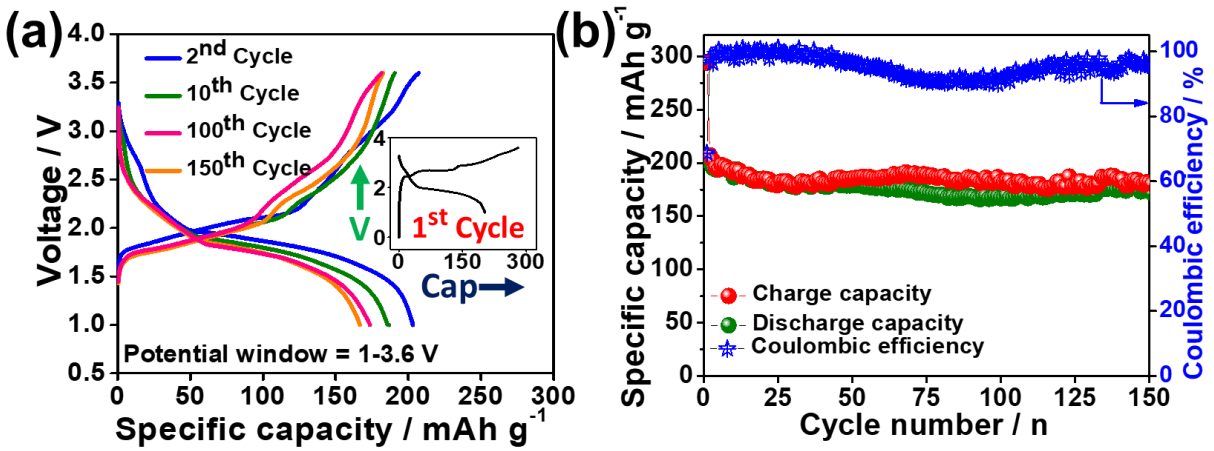

Figure 6.26 The electrochemical performance of the $MoTe_2$//NVP full-cell prototype. (a) Galvanostatic charge/discharge curves at a current rate of 0.5 A g^{-1} for different cycles of the $MoTe_2$//NVP full cell in the voltage range of 1.0 to 3.6 V. (The inset shows the 1st cycle charge/discharge curve.) (b) Cycling performance of the $MoTe_2$//NVP full cell for 150 cycles, at a current rate of 0.5 A g^{-1}.

Figure 6.26a shows the charge/discharge performance of $MoTe_2$//NVP full cell at a current rate of 0.5 A g^{-1} over 150 cycles. The initial charge/discharge capacity is ~294 mA h g^{-1} and ~202 mA h g^{-1}. The 1st cycle shows a lower Coulombic efficiency of 68.7 %, which is mainly due to the polarization and irreversible loss at the anode.

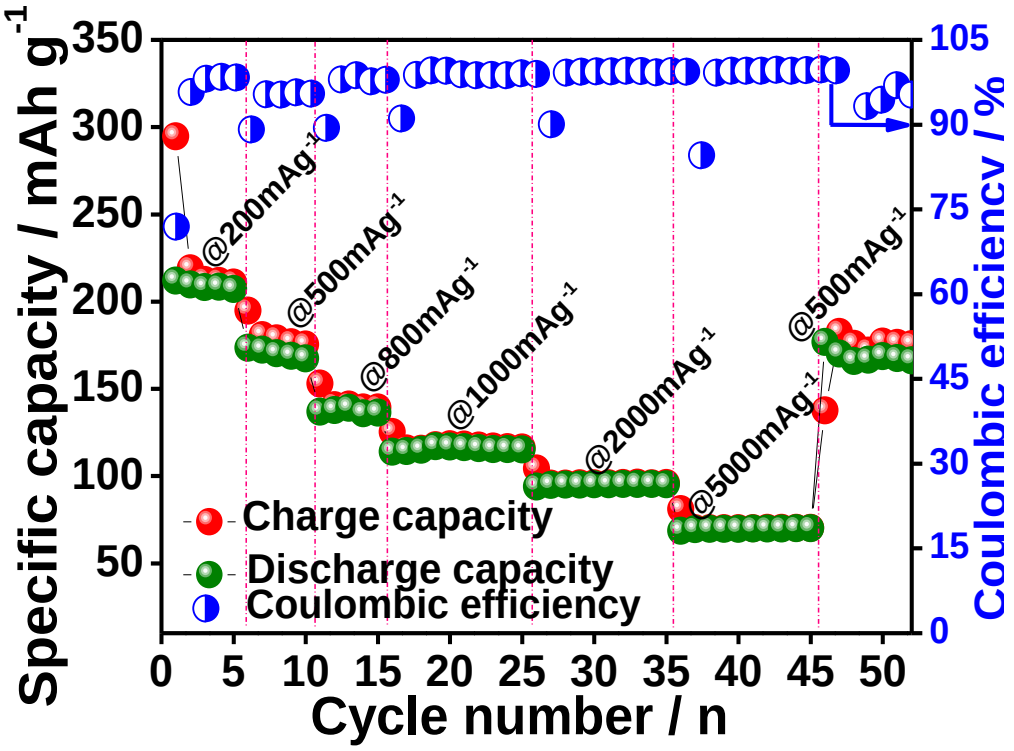

Figure 6.27 Rate performance of the $MoTe_2$//NVP full cell at various current rates.

However, upon cycling, the Coulombic efficiency increases to 98 %, and the charge/discharge capacity is ~207 mA h g^{-1} and ~203 mA h g^{-1}. This $MoTe_2$//NVP full-cell SIB shows a very stable specific discharge capacity of ~182 mA h g^{-1} (~88 % capacity retention) after 150 cycles, as can be seen in **Figure 6.26b**. The versatility of the full-cell rate performance study that is carried out at different current rates (that is, 0.2 A g^{-1}, 0.5 A g^{-1}, 0.8 A g^{-1}, 1 A g^{-1}, 2 A g^{-1}, and 5 A g^{-1}) is seen in **Figure 6.27**. The full cell is able to deliver a discharge capacity of ~230 mA h g^{-1}, ~195 mA h g^{-1}, ~165 mA h g^{-1}, ~140 mA h g^{-1}, ~125 mA h g^{-1}, and ~95 mA h $g^{-1}$with Coulombic efficiency of ~99 %. The cell is able to retain its initial specific capacity when the current rate is switched back to 0.5 A g^{-1}, which indicates a good rate performance of the $MoTe_2$//NVP full cell. Further, to gain a better overview of the total energy that is available at various power densities, a Ragone plot is drawn from the results, as shown in **Figure 6.28a**. The plot elucidates the suitability of the present SIB full-cell prototype to a variety of applications. The reporting$MoTe_2$//NVP full-cell configuration shows an impressive working potential of ~2 V and a specific capacity when compared to other literature reports. A comparison of the conventional SIB full-cell and our full-cell configuration has been presented in **Table 6.4**, which shows a working potential and energy density of ~ 2V and 414 W h kg^{-1}, which is congruent with the literature. We believe reporting the energy density based on anode mass is more suitable in this current stage of development.

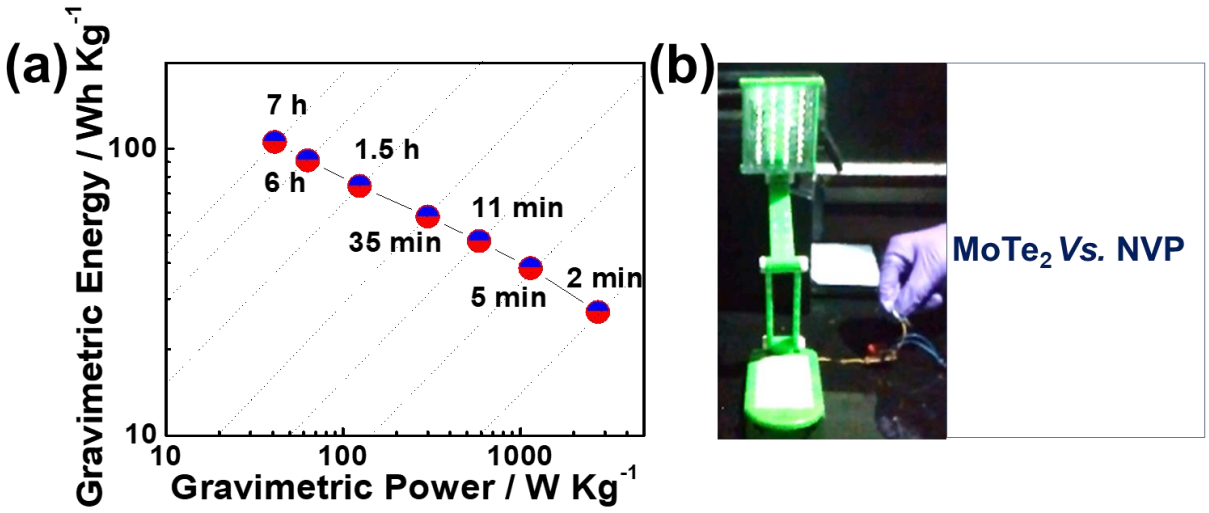

Figure 6.28 The electrochemical performance of the $MoTe_2$//NVP full-cell prototype. (a) Gravimetric power plot for the $MoTe_2$//NVP full cell. (b) Practical demonstration of the $MoTe_2$//NVP full-cell prototype, showing the lighting of an LED table lamp that is powered by a one-coin cell.

Table 6.4 A comparison of the configurations of the conventional SIB full-cell and our full-cell along with their performances, and our present full-cell ($MoTe_2$. versus NVP) combination.

Full cell Configuration	Voltage (V)	Current Rate	Specific Capacity (mA h g^{-1})	Energy Density (Wh kg^{-1})	Capacity Retention
H-$Na_2Ti_3O_7$// $Na_{2/3}(Ni_{1/3}Mn_{2/3})O_2$ [31]	2.7	1 C	182 (anode base)	490	(100^{th} cycle)
XXX (FARADION)	3		162	486	
C//($Na_1Fe_{0.5}Mn_{0.5}O_2$ + 10%Na_3P)[32]	3.2		110	352	81% (20^{th} cycle)
TiO_2 //$Na_2V_2O_5$[33]	2.3	1 C	118	271	76% (350^{th} cycle)
Fe_2O_3, NiO//$Na_3V_2(PO_4)_3$[34]	1.8	C/2	100	180	80% (30^{th} cycle)
Fe_3O_4//$Na_2P_2O_7$[35]	2.28	0.1 C	93	203	93.3%(100^{th} cycle)
Hard carbon//$NaNi_{0.5}Ti_{0.5}O_2$[36]	2.75		95	261	72% (100^{th} Cycle)
$Na[Li_{0.05}Mn_{0.50}Ni_{0.30}Cu_{0.10}Mg_{0.05}]O_2$ //hard carbon[37]	2.9	0.1 C	74	215	98% (200^{th} cycle)
Fe_3O_4@FeS//$Na_3V_2(PO_4)_2O_2F$[39]	2.8	500 mA g^{-1}	157	439	92.3% (50^{th} cycle)
$FePO_4$ // $Na_{0.44}MnO_2$[39]	0.7	3 C	70	49	90% (300^{th} cycle)
$Na_2Fe_2(CN)_6$//Cu INPB[40]	3.11	1 C	108	336	76% (100^{th} cycle)
$MoTe_2$// $Na_3V_2(PO_4)_3$ *(Present work)*	**2**	**500 mA g^{-1}**	**207 (anode base)**	**414**	**88% (150^{th} cycle)**

Moreover, a single coin cell that comprises a $MoTe_2$//NVP full cell is adequate to illuminate an LED lantern study lamp, as illustrated in **Figure 6.28b**. Therefore, the $MoTe_2$//NVP SIB full-cell prototype that contains the $MoTe_2$ anode and the NVP cathode is a potential alternative to conventional LIBs in numerous practical applications.

6.4 Conclusions

Pure layered $MoTe_2$ solid blocks were prepared successfully through a facile solid-state reaction route. Structural and morphological characterizations were carried out by SXRD, FESEM, and HRSTEM. The as-prepared $MoTe_2$ material, for the first time, was applied without any further surface modification or conductive-coating carbon additive as an anode material in a SIB full-cell application against the NVP cathode. The $MoTe_2$ anode showed good electrochemical performance against sodium metal in the half-cell configuration, with an average reversible specific capacity of ~320 mA h g^{-1} (at a current rate of 1 A g^{-1}); the anode also displayed unusual stability and outstanding rate capability. Ex situ SXRD, HRTEM, XPS,

and XANES analyses confirmed the electrochemical mechanism of the $MoTe_2$ anode material versus sodium metal in the half-cell configuration. To construct the full-cell configuration, a crystalline, layered NVP was synthesized through a simple two-step solid-state reaction route to use the NVP as an appropriate cathode against the $MoTe_2$ anode. A systematic study of both the anode and the cathode was carried out to fabricate a high-performance sodium-ion full-cell prototype. The novel sodium-ion full cell ($MoTe_2$//NVP) is able to deliver a nominal cell potential of ~2 V, and it has shown an excellent reversible capacity of 207 mA h g^{-1} at a current rate of 500 mA g^{-1}. Further, the full cell configuration shows a high-rate capability and excellent cycling performance up to 150 cycles, with Coulombic efficiencies of ~ 88 %. This high-performance sodium-ion full cell showed a high energy density of ~414 W h kg^{-1}. The current sodium-ion full cell prototype ($MoTe_2$//NVP) is a potential alternative to conventional LIBs to drive large-scale energy-storage systems.

6.5 References

(1) Deng, K.; Wan, G.; Deng, P.; Zhang, K.; Ding, S.; Wang, E.; Yan, M.; Huang, H.; Zhang, H.; Xu, Z.; Denlinger, J. Experimental Observation of Topological Fermi Arcs in Type-II Weyl Semimetal $MoTe_2$. *Nat. Phys.* **2016**, 12, 1105–1110.

(2) Cho, J. S.; Ju, H. S.; Lee, J. K.; Kang, Y. C. Carbon/Two-Dimensional $MoTe_2$ Core/Shell-Structured Microspheres as an Anode Material for Na-Ion Batteries. *Nanoscale* **2017**, 9, 1942–1950.

(3) Ma, N.; Jiang, X. Y.; Zhang, L.; Wang, X. S.; Cao, Y. L.; Zhang, X. Z. Novel 2D Layered Molybdenum Ditelluride Encapsulated in Few-Layer Graphene as High-Performance Anode for Lithium-Ion Batteries. *Small* **2018**,14, 1703680.

(4) Keum, D. H.; Cho, S.; Kim, J. H.; Choe, D.H.; Sung, H. J.; Kan, M.; Kang, H.; Hwang, J.Y.; Kim, S.W.; Yang, H.; Chang, K. J. Bandgap Opening in Few-Layered Monoclinic $MoTe_2$. *Nat. Phys.* **2015**, 11, 482–486.

(5) Manohar, C. V.; Kar, M.; Forsyth, M.; MacFarlane, D. R.; Mitra, S. Stability Enhancing Ionic Liquid Hybrid Electrolyte for NVP@ C Cathode Based Sodium Batteries. *Sustain. Energy Fuels* **2018**, 2, 566–576.

(6) Roy, A.; Movva, H. C.; Satpati, B.; Kim, K.; Dey, R.; Rai, A.; Pramanik, T.; Guchhait, S.; Tutuc, E.; Banerjee, S. K. Structural and Electrical Properties of $MoTe_2$ and $MoSe_2$ Grown by Molecular Beam Epitaxy. *ACS Appl. Mater. Interfaces* **2016**, 8, 7396–7402.

(7) Hong, M.; Li, J.; Zhang, W.; Liu, S.; Chang, H. Semimetallic 1T' WTe_2 Nanorods as Anode Material for the Sodium Ion Battery. *Energy Fuels* **2018**, 32, 6371–6377.

(8) Sahu, T. S.; Mitra, S. Exfoliated MoS_2 Sheets and Reduced Graphene Oxide-An Excellent and Fast Anode for Sodium-Ion Battery. *Sci. Rep.* **2015**, 5, 12571.

(9) Yang, E.; Ji, H.; Jung, Y. Two-Dimensional Transition Metal Dichalcogenide Monolayers as Promising Sodium Ion Battery Anodes. *J. Phys. Chem. C* **2015**, 119, 26374–26380.

(10) Zhang, Y.; Liu, Z.; Zhao, H.; Du, Y. $MoSe_2$ Nanosheets Grown on Carbon Cloth with Superior Electrochemical Performance as Flexible Electrode for Sodium Ion Batteries. *RSC Adv.* **2016**, 6, 1440–1444.

(11) Kang, J.; Su, Q.; Feng, H.; Huang, P.; Du, G.; Xu, B. $MoSe_2$ Nanosheets-Wrapped Flexible Carbon Cloth as Binder-Free Anodes for High-Rate Lithium and Sodium Ion Storages. *Electrochim. Acta* **2019**, 301, 29–38.

(12) Xiao, Y.; Wang, P. F.; Yin, Y. X.; Zhu, Y. F.; Niu, Y. B.; Zhang, X. D.; Zhang, J.; Yu, X.; Guo, X. D.; Zhong, B. H.; Guo, Y. G. Exposing {010} Active Facets by Multiple-Layer Oriented Stacking Nanosheets for High-Performance Capacitive Sodium-Ion Oxide Cathode. *Adv. Mater.* **2018**, 30,1803765.

(13) Brezesinski, T.; Wang, J.; Tolbert, S. H.; Dunn, B. Ordered Mesoporous α-MoO_3 with Iso-Oriented Nanocrystalline Walls for Thin-Film Pseudocapacitors. *Nat. Mater.* **2010**, 9, 146–151.

(14) Li, Y.; Chang, K.; Shangguan, E.; Guo, D.; Zhou, W.; Hou, Y.; Tang, H.; Li, B.; Chang, Z. Powder Exfoliated MoS_2 Nanosheets with Highly Monolayer-Rich Structures as High-Performance Lithium-/Sodium-Ion-Battery Electrodes. *Nanoscale* **2019**, 11, 1887–1900.

(15) Sarkar, A.; Sarkar, S.; Mitra, S. Exceptionally High Sodium-Ion Battery Cathode Capacity Based on Doped Ammonium Vanadium Oxide and a Full Cell SIB Prototype study. *J. Mater. Chem. A* **2017**, 5, 24929–24941.

(16) Cho, J. S.; Hong, Y. J.; Kang, Y. C. Design and Synthesis of Bubble-Nanorod-Structured Fe_2O_3–Carbon Nanofibers as Advanced Anode Material for Li-Ion Batteries. *ACS nano* **2015**, 9, 4026–4035.

(17) Xu, Y.; Zhu, Y.; Liu, Y.; Wang, C. Electrochemical Performance of Porous Carbon/Tin Composite Anodes for Sodium-Ion and Lithium-Ion Batteries. *Adv. Energy Mater.* **2013**, 3, 128–133.

(18) Bernède, J. C.; Amory, C.; Assmann, L.; Spiesser, M. X-ray Photoelectron Spectroscopy Study of $MoTe_2$ Single Crystals and Thin Films. *Appl. Surf. Sci.* **2003**, 219, 238–248.

(19) Zhou, L.; Xu, K.; Zubair, A.; Liao, A. D.; Fang, W.; Ouyang, F.; Lee, Y. H.; Ueno, K.; Saito, R.; Palacios, T.; Kong, J. Large-Area Synthesis of High-Quality Uniform Few-Layer $MoTe_2$. *J. Am. Chem. Soc.* **2015**, 137, 11892–11895.

(20) Xiong, X.; Luo, W.; Hu, X.; Chen, C.; Qie, L.; Hou, D.; Huang, Y. Flexible Membranes of MoS_2/C Nanofibers by Electrospinning as Binder-Free Anodes for High-Performance Sodium-Ion Batteries. *Sci. Rep*. **2015**, 5, 9254.

(21) Swartz, W.; Hercules, D. M. X-ray Photoelectron Spectroscopy of Molybdenum Compounds. Use of Electron Spectroscopy for Chemical Analysis (ESCA) in Quantitative Analysis. *Anal. Chem.* **1971**, 43, 1774–1779.

(22) Panda, M. R.; Bhowmik, R. N.; Singh, H.; Singh, M. N.; Sinha, A. K. Air Annealing Effects on Lattice Structure, Charge State Distribution of Cations, and Room Temperature Ferrimagnetism in the Ferrite Composition $Co_{2.25}Fe_{0.75}O_4$. *Mater. Res. Express* **2015**, 2, 036101.

(23) Joseph, D.; Yadav, A. K.; Jha, S. N.; Bhattacharyya, D. Chemical Shift of Mn and Cr K-edges in X-ray Absorption Spectroscopy with Synchrotron Radiation. *Bull. Mater. Sci.* **2013**, 36 1067–1072.

(24) Sen, U. K.; Johari, P.; Basu, S.; Nayak, C.; Mitra, S. An Experimental and Computational Study to Understand the Lithium Storage Mechanism in Molybdenum Disulfide. *Nanoscale* **2014**, 6, 10243–10254.

(25) Kang, J. H.; Paek, S. M.; Choy, J. H. In Situ X-ray Absorption Spectroscopic Study for α-MoO_3 Electrode Upon Discharge/Charge Reaction in Lithium Secondary Batteries. *Bull. Korean Chem. Soc.* **2010**, 31, 3675–3678.

(26) Panda, M. R.; Raj K, A.; Bao, Q.; Mitra, S. $MoTe_2$, A Novel Anode Material for Sodium Ion Battery. *AIP Conf. Proc.* **2018**, 1942140078.

(27) Panda, M. R.; Raj K, A.; Sarkar, A.; Bao, Q.; Mitra, S. Electrochemical Investigation of $MoTe_2$/rGO Composite Materials for Sodium-Ion Battery Application. *AIP Conf. Proc.* **2018**, 1961, 2030033.

(28) Panda, M. R.; Raj K, A.; Singh, M. N.; Sagdeo, A.; Sinha, A. K.; Bao, Q.; Mitra, S. Structural and Electrochemical Mechanism Study of Layered $MoTe_2$ Anode Material for Sodium-Ion Battery. *AIP Conf. Proc.* **2019**, 2115, 030615.

(29) Wang, W.; Xu, Q.; Liu, H.; Wang, Y.; Xia, Y. A Flexible Symmetric Sodium Full Cell Constructed Using the Bipolar Material $Na_3V_2(PO_4)$. *J. Mater. Chem. A.* **2017**, 5, 8440–8450.

(30) Aragón, M. J.; Lavela, P.; Ortiz, G. F.; Alcántara, R.; Tirado, J. L. Insight into the Electrochemical Sodium Insertion of Vanadium Superstoichiometric NASICON Phosphate. *Inorg. Chem.* **2017**, 56, 11845–11853.

(31) Fu, S.; Ni, J.; Xu, Y.; Zhang, Q.; Li, L. Hydrogenation Driven Conductive $Na_2Ti_3O_7$ Nanoarrays as Robust Binder-Free Anodes for Sodium-Ion Batteries. *Nano Energy* **2016**, 16, 4544–4551.

(32) Barpanda, P.; Oyama, G.; Nishimura, S. I.; Chung, S. C.; Yamada, A. A 3.8-V Earth-Abundant Sodium Battery Electrode. *Nat. Commun.* **2014**, 5, 4358.

(33) Oh, S. M.; Pilgun Oh, P.; Kim, S. O.; Manthiram, A.; A High-Performance Sodium-Ion Full Cell with a Layered Oxide Cathode and a Phosphorous-Based Composite Anode *J. Electrochem. Soc.* **2017**, 164 (2) A321–A326.

(34) López, M. C.; Aragón, M. J.; Ortiz, G. F.; Lavela, P.; Alcántara, R. High Performance Full Sodium-Ion Cell Based on a Nanostructured Transition Metal Oxide as Negative Electrode. *Chem. Eur. J.* **2015**, 2, 4879–14885.

(35) Ming, J.; Ming, H.; Yang, W.; Kwak, W.; Park, J. A Sustainable Iron-Based Sodium Ion Battery of Porous Carbon–Fe_3O_4/$Na_2FeP_2O_7$ with High Performance. *RSC Adv.* **2015**, 5, 8793–8800.

(36) Wang, H.; Xiao, Y.; Sun, C.; Lai, C.; Ai, X. A Type of Sodium-Ion Full-Cell with a Layered $NaNi_{0.5}Ti_{0.5}O_2$ Cathode and a Pre-Sodiated Hard Carbon Anode. *RSC Adv.* **2015**, 5, 06519–106522.

(37) Deng, J.; Luo, W. B.; Lu, X.; Yao, Q.; Wang, Z.; Liu, H. K.; Zhou, H.; Dou, S. X. Sodium-Ion Batteries: High Energy Density Sodium-Ion Battery with Industrially Feasible and Air-Stable O_3-Type Layered Oxide Cathode. *Adv. Energy Mater.* **2018**, 8, 1701610.

(38) Peng, J.; Wang, J.; Yi, H.; Hu, W.; Yu, Y.; Yin, J.; Shen, Y.; Liu, Y.; Luo, J.; Xu, Y.; Wei, P.; Li, Y.; Jin, Y.; Ding, Y.; Miao, L.; Jiang, J.; Han, J.; and Huang, Y. Sodium Ion Batteries: A Dual-Insertion Type Sodium-Ion Full Cell Based on High-Quality Ternary-Metal Prussian Blue Analogs. *Adv. Energy Mater.* **2018**, 8, 1702856.

(39) Wang, Y.; Feng, Z.; Laul, D.; Zhu, W.; Provencher, M. Ultra-Low Cost and Highly Stable Hydrated $FePO_4$ Anodes for Aqueous Sodium-Ion Battery. *J. Power Sources* **2018**, 374, 211–216.

(40) Rudolaa, A.; Gajjelaa, S. R.; Balaya, P. High Energy Density In-Situ Sodium Plated Battery with Current Collector Foil as Anode. *Electrochem. commun.* **2018**, 86, 157–160.

CHAPTER 7

The impact of crystallite size, morphology, and electrolyte additives on the electrochemical performance of bulk $MoTe_2$ in rechargeable sodium-ion batteries

"This chapter deals with the effect of crystallite size, crystallinity, and additives on the electrochemical performance of sodium-ion batteries. Ex situ/in situ EXAFS/XANES provides the corresponding sodium storage mechanism."

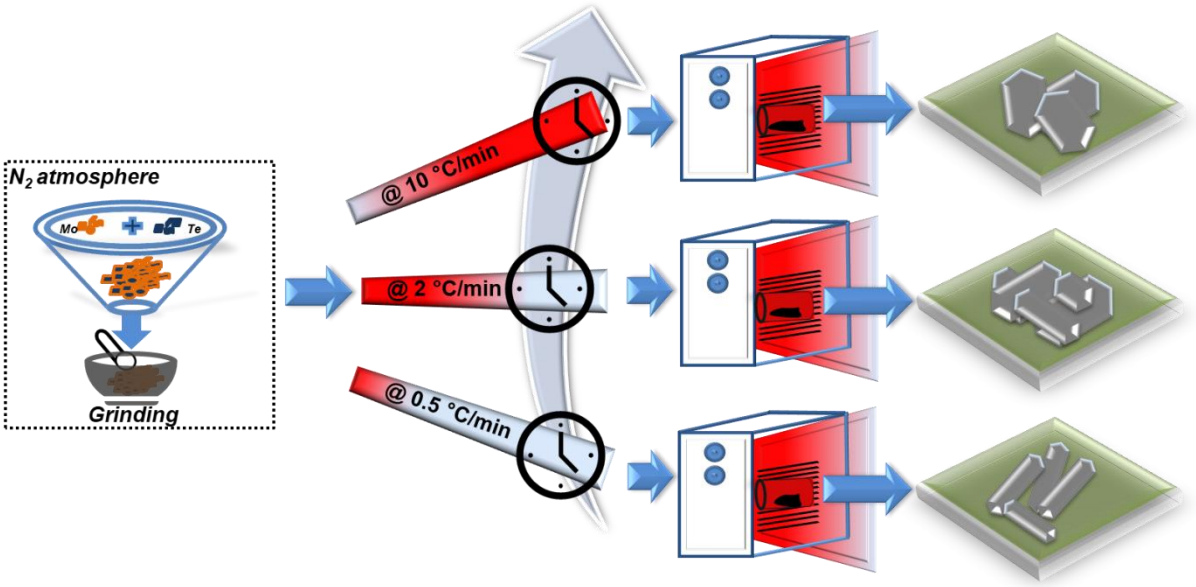

*An excerpt from this chapter is ready to communicate.

7.1 Introduction

Synthesis of materials for sodium-ion batteries (SIBs) with high purity, controllable crystallite size, and various morphologies are crucial.[1–4] The tuning of the crystallite size and morphology of the materials by using conventional preparation methods is challenging. It has been observed from the literature that high heating rates and low sintering temperatures enable grain size retention. On the other hand, for better densification, high annealing temperatures and low heating rates are helpful. An increase in heating rates helps decrease the relative density of the materials, which facilitates the detaining of surface diffusion through coarsening mechanisms, which helps reduce grain size.[5–7]

The effect of the heating rate controls the properties of the material, because the densification rate relates to thermal and electrical conductivity. A high heating rate results in higher thermal gradients, which first sinters the samples' external peripheral rather than the internal peripheral.[5] The effect of the variation in sintered zones of the external and internal regions creates many defects and porosity in the sintered samples due to the lack of particle arrangements.[5–7] As a result, the heating rate and the sintering temperature enable the tuning of the density, crystallinity, porosity, and defects in the material along with the tuning of the thermal and electrical conductivity.[5–8] Electrolyte additives and the morphology of the electrodes also have an impact on the electrochemical performances. The electrolyte with the FEC additive showed better electrochemical performance and better cycle stability due to a stable SEI formed by the electrode surface. These factors are related to the electrochemical performances of the studied materials.

In chapter 6, we present the work on 2H $MoTe_2$ anode against the SIB and the associated sodium storage mechanism; we also study the full cell. Here, we report an approach that allows for large-scale preparation of the $MoTe_2$ electrode with tunable crystallinity and various morphologies, which can be achieved by regulating the synthesis temperature and heating rates. The effect of crystallite size on the electrochemical performance of the $MoTe_2$ electrode was investigated in a half-cell configuration against sodium, and excellent properties were observed even for post-synthesis treatment. It was observed that with an increase in the heating rate in the synthesis of $MoTe_2$, the porosity increased, and the crystallite size decreased. The smaller crystallite size helped shorten the Na^+ diffusion path, which resulted in the enhancement of sodium storage properties. The increased porosity, thermal, and electrical conductivity helped to achieve a higher specific capacity of the high-heating-rate $MoTe_2$ anode,

whereas the sample prepared with a higher heating rate did not show better cycle stability due to the lower-order crystallinity. We finally optimized an optimum heating rate of 2 ºC/min, which is the optimum heating rate for better electrochemical properties. A moderate heating rate that has a smaller crystallite size in $MoTe_2$ enables enhanced sodium storage properties. In the latter part of this chapter, we have briefly discussed the effect of an electrolyte additive on the electrochemical performance of the $MoTe_2$ anode in SIB applications; we have also included full-cell prototype studies.

7.2Material synthesis

A stoichiometric amount of molybdenum (Sigma–Aldrich, 99.999 %) and tellurium (Sigma–Aldrich, 99.999 %) powders have been mixed, and a mixture has been prepared for the synthesis of $MoTe_2$. The mixture was uniformly ground by hand in an argon atmosphere to obtain a precursor to $MoTe_2$ synthesis. The mixed powder was then sealed in three different 150-mm-long quartz ampoules under vacuum at 10^{-5} torr of pressure.[9,10]

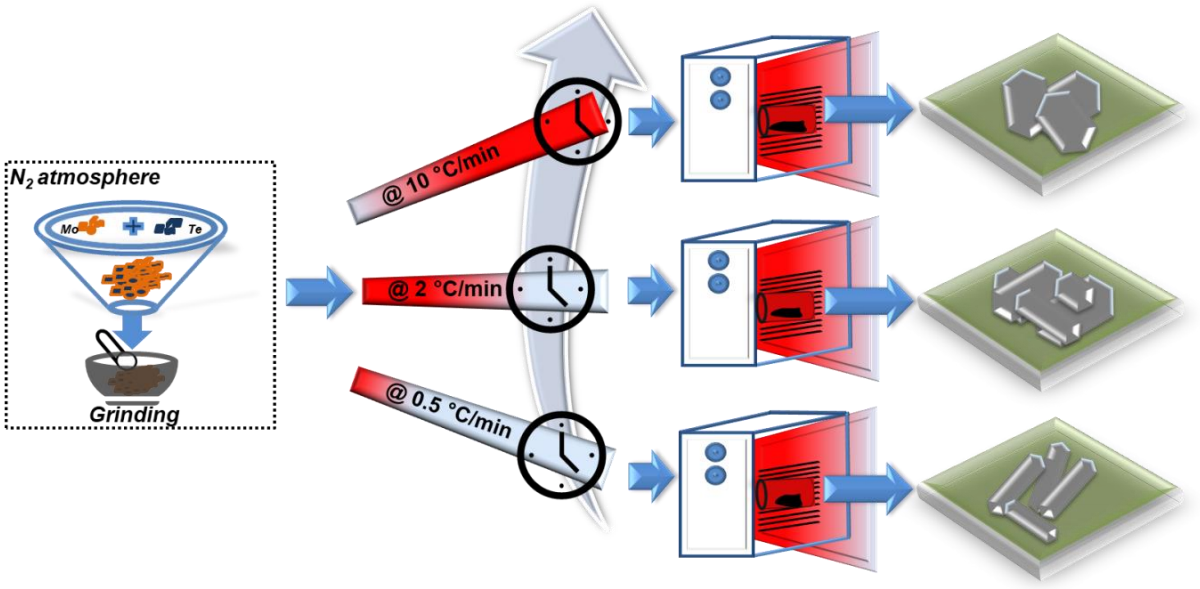

Figure 7.1 Schematic for the preparation of the $MoTe_2$ at different heating rates.

The temperature was increased slowly at three different heating rates (0.5 °C/min, 2°C/min, and 10 °C/min) from room temperature to 810 °C, 820 °C, and 825 °C, respectively (**Figure 7.1**). We have chosen the higher heating rate of 10 °C/min to avoid an exothermic reaction.[10] The higher sintering temperature was limited to 825 °C to retain the phase purity of the 2H-$MoTe_2$ phase. The respective holding temperatures were maintained for 20 h to complete the alloying reaction.[9] After cooling to room temperature, three different black powders of $MoTe_2$

were obtained, which were further ground in an inert atmosphere before further characterization.

7.3 Results and discussion

7.3.1 Crystal structure and morphological study of the as-prepared $MoTe_2$ powders

Figure 7.2a illustrates the Rietveld refinement profile of the SXRD patterns of the $MoTe_2$ electrode, which was annealed at different heating rates at different temperatures. **Figure 7.2b** also shows the magnified view of the major peak of the $MoTe_2$ powder sample, which confirmed the shifting of the peak positions toward the lower 2-theta values.

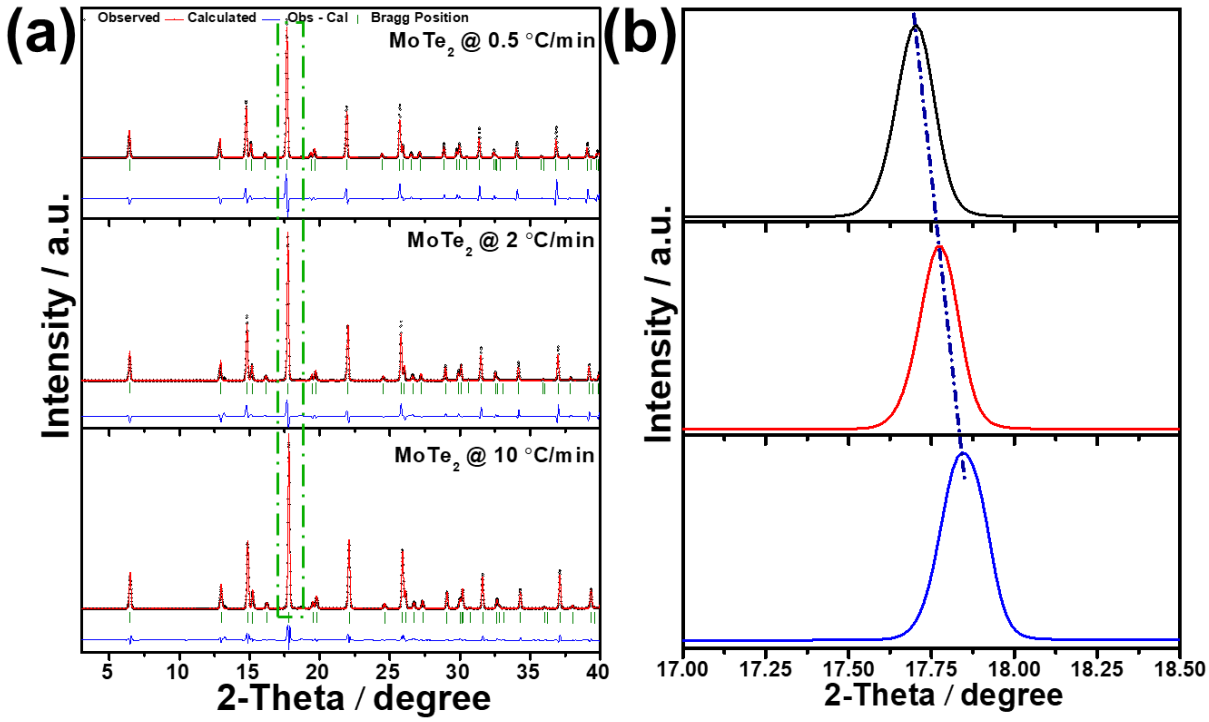

Figure 7.2 (a) Rietveld refinement profile of the SXRD patterns of the $MoTe_2$ electrode annealed at different heating rates at different temperatures. (b) Magnified view of the major peak of the SXRD patterns.

Figure 7.3b displays the variation in the crystallite size and the lattice strain, which was calculated by using the Debye–Scherer formula, $\langle d \rangle = (0.89\times\lambda)/(\beta\times\cos\theta)$, where β(FWHM in Radians) and θ (half of the peak position in 2θ scale) using the Gaussian fit of the prominent SXRD peaks (103, 100, 105).[10] For the sample prepared at 0.5 °C/min of heating rate at 810 °C, a crystallite size of 247.32 nm was observed. For the sample that was prepared at a 2 °C/min of heating rate at 815 °C, a crystallite size of 198.12 nm has been observed. Similarly, for the

sample that was prepared at 10 °C/min of heating rate from room temperature to 825 °C, a crystallite size of 164.51 nm was observed.

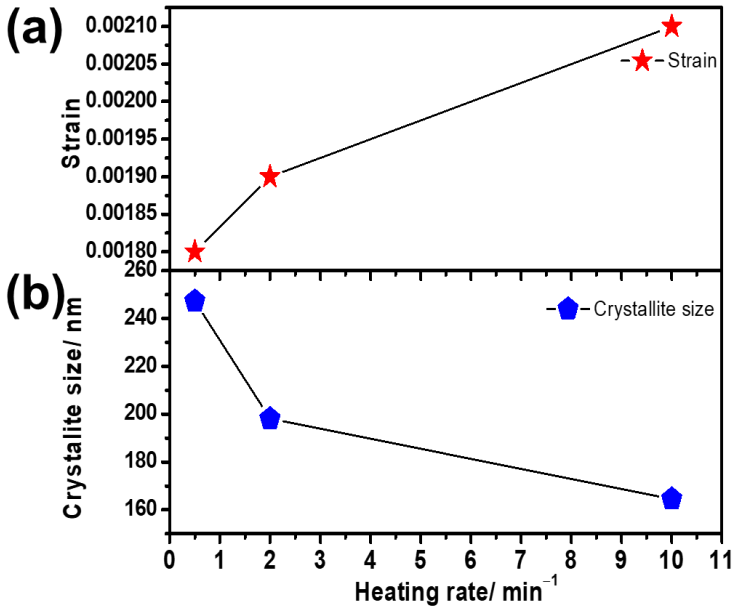

Figure 7.3 (a–b) Variation in the crystallite size and the lattice strain at different heating rates.

The observed strain increased (**Figure 7.3a**) from a lower to a higher value with the increase of the heating rate. The higher heating rate resulted in a higher driving force in the diffusion of grain boundaries within a limited time; therefore, higher heating rates do not provide enough time for surface diffusion, which affects the growth of the grain. The higher heating rate always favors grain boundary diffusion; substantial stresses limit the reduction of the crystallite size due to lack of time that is required to process the growth of the crystallite size.[5–8]

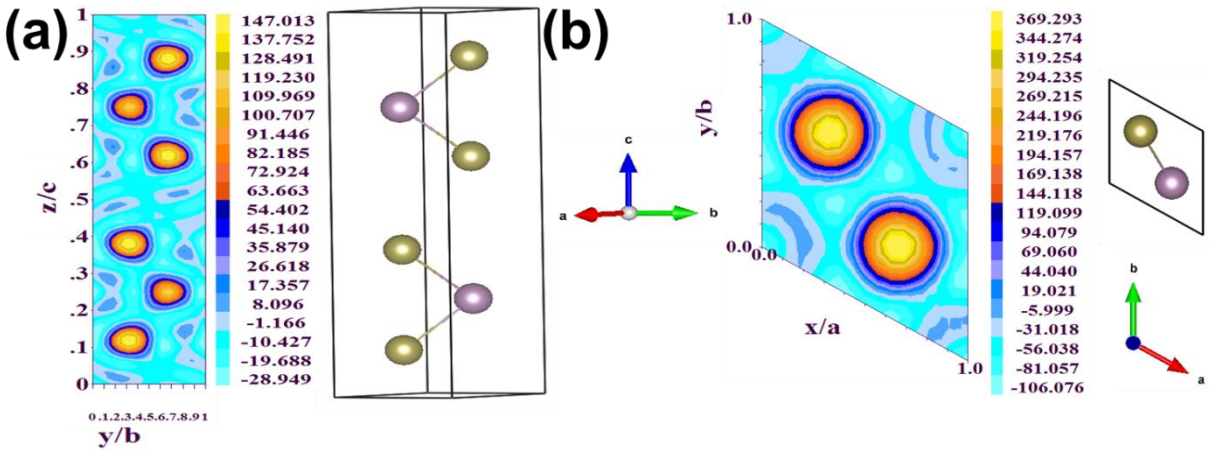

Figure 7.4(a–b) Electronic structure of the as-prepared 2H $MoTe_2$ powder, showing the electron density distribution.

Figure 7.4 (a–b) illustrates the electron distribution of the as-prepared 2H phase of the $MoTe_2$ powder. The observed electron distribution shows the semiconducting nature of the synthesized $MoTe_2$ sample.

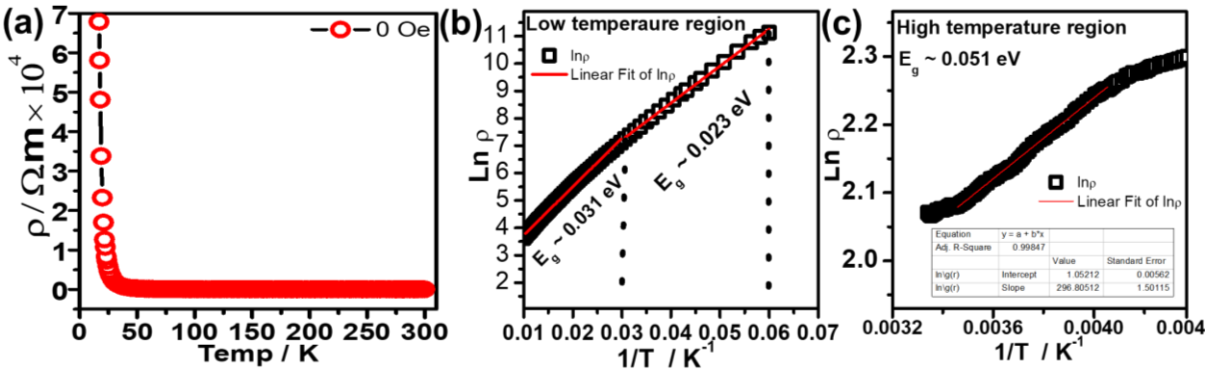

Figure 7.5 Electrical resistivity and temperature relationship. (a) Electrical resistivity as a function of temperature for the 2H $MoTe_2$ sample prepared at a heating rate of 2 ºC/min. (b–c) The linear fit results from the dependence of ln ρ on 1/T for the low-temperature (b) region and (c) the high-temperature regions.

Electrical resistivity was measured using the standard dc-four probe method that comprised 9 T/2 K Quantum Design Cryostat. The measurement was done under zero-field cooling conditions (ZFC). The electron transport properties of the 2H $MoTe_2$ were studied in different temperature regimes. **Figure 7.5a** represents the temperature dependence of the resistivity of the 2H $MoTe_2$. With the increase in the temperature, it has been observed that the resistivity slowly decreases and becomes constant. The experimental feature shows typical semiconductor behavior.[11] Further, we fitted the resistivity data with temperature (ln ρ vs.1/T). **Figure 7.5b, c** shows that the linear fit ln ρ is almost linear to 1/T.[11] The whole data is fitted to the exponential function for the entire temperature region. The three different regions were fitted with three different band gaps. They are marked as a high temperature (**Figure7.5c**) and two low-temperature regions (**Figure7.5b**). The observed bandgap lies in the range of 0.02 to 0.05 eV.

To analyze the local geometrical structure of the absorption atom, Synchrotron-based Extended X-ray Absorption Fine Structure (EXAFS), which is a powerful technique, is used. **Figure7.6** shows the Mo K-edge EXAFS spectra of three different samples. Here we have employed Mo K-edge EXAFS for the three samples to investigate the local structure of the $MoTe_2$ samples. The XAFS spectra of the samples were analyzed by the least-squares fittings of the Mo K-edge XAFS spectra.

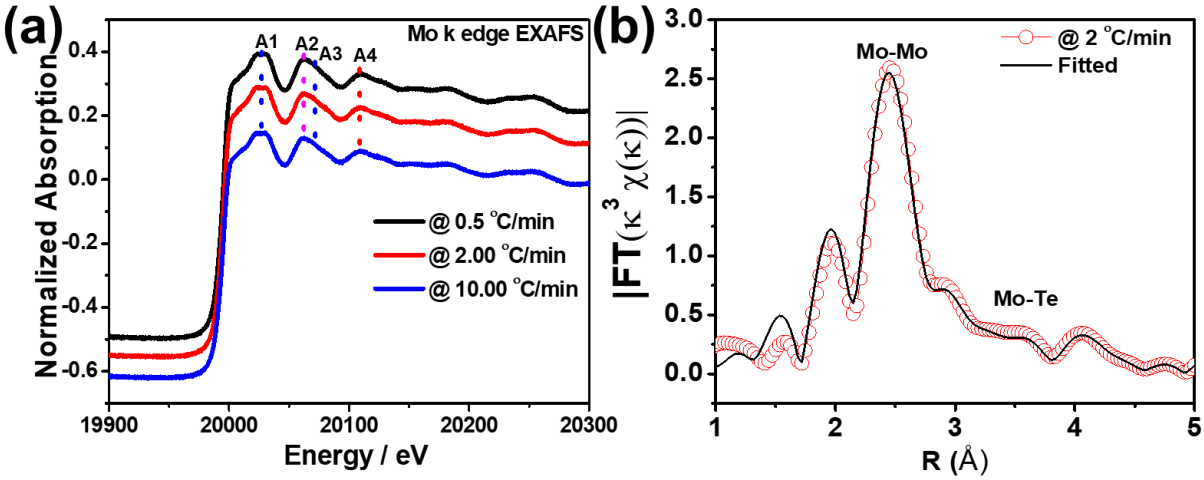

Figure 7.6(a) Mo K-edge XANES of the $MoTe_2$ pristine sample prepared at different heating rates. (b) Fourier-transform of EXAFS spectrum with the fitted simulated spectrum of the sample at a heating rate of 2 ºC/min.

Figure7.6a shows the Mo XANES of the $MoTe_2$ samples at the three heating rates. The features shown in **Figure7.6a**, which are denoted as A1, A2, A3, and A4 are the prominent features of Mo, and they confirm the phase purity of the pristine $MoTe_2$ structure.[10,12,13] **Figure7.6b** shows the equivalent fitted Fourier-transform (FT) spectrum of the sample that was annealed at the heating rate of 2 ºC. The FT spectrum of $MoTe_2$ reveals two peaks at ~2.45 and 3. 54 Å, respectively, which corresponds to the Mo-Te and Mo-Mo bonds.[14] The results of fitting and the observed features provided phase purity and local structure information between Mo and Te atoms in the $MoTe_2$ sample.

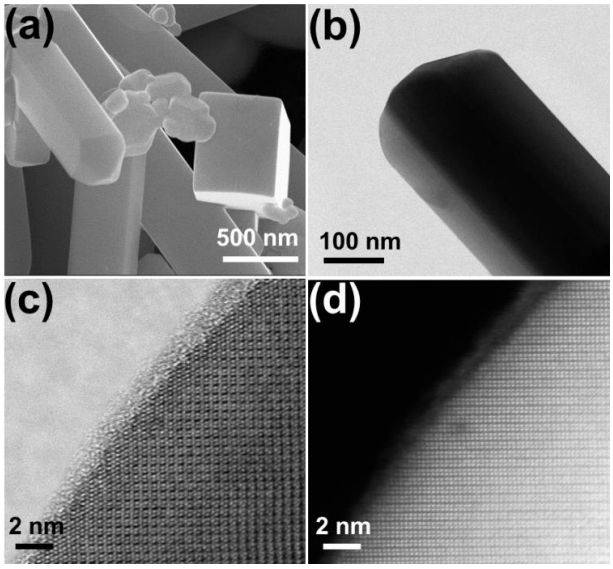

Figure 7.7 (a–d) FESEM and STEM images, showing the morphology variation in $MoTe_2$ powder at a heating rate of 0.5 ºC/min.

The morphological evolution of the samples that were annealed at three different heating rates was investigated by FESEM and STEM techniques. **Figures 7.7, 7.8, and 7.9** show the corresponding morphology of the $MoTe_2$ samples. A solid rod-shaped morphology was observed for the sample that was annealed at a very low heating rate (0.5 ºC/min), as shown in **Figure7.7**.

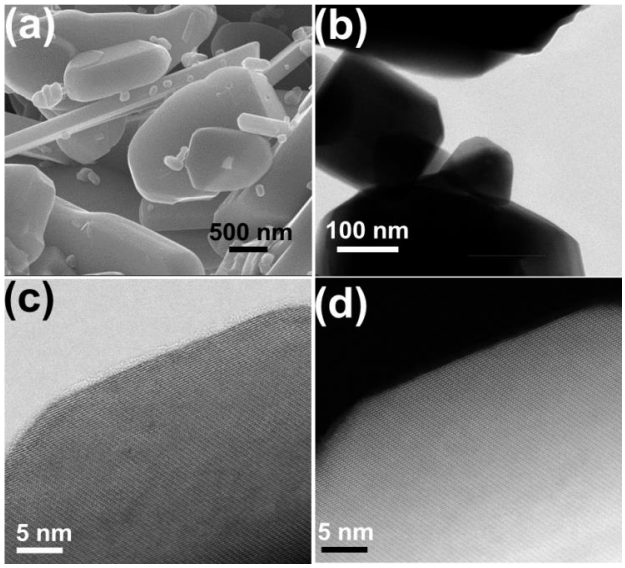

Figure 7.8 (a–d) FESEM and STEM images, showing the morphology variation in $MoTe_2$ powder at a heating rate of 2 ºC/min.

Solid rod-type morphology along with flat hexagonal-type morphologies was observed for the sample with an increased heating rate of 2 ºC/ min (**Figure7.8**).

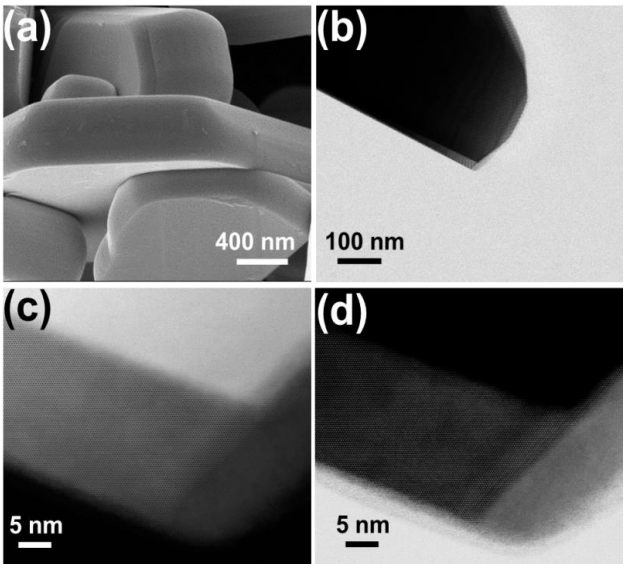

Figure 7.9 (a–d) FESEM and STEM images, showing the morphology variation in $MoTe_2$ powder at a heating rate of 10 ºC/min.

Further, for the sample that was heated at an even higher heating rate (10 ºC/min), only hexagonal-type flat morphologies were observed (**Figure7.9**). This observation confirms the evolution of different kinds of morphologies at different heating temperatures.

7.3.2 Electrochemical performance study of the change of crystallite size and morphology variation of the three sets of samples

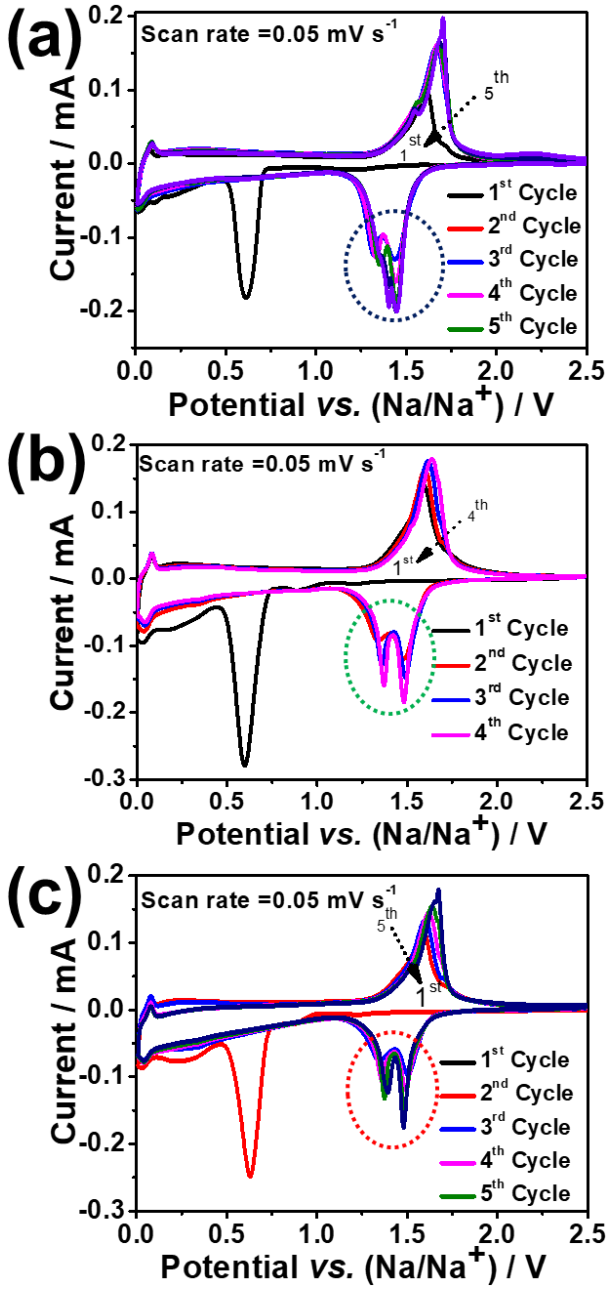

Figure 7.10(a–c) The CV of the $MoTe_2$ electrode at different heating rates (a) at a heating rate of 10 ºC/ min, (b) at a heating rate of 2 ºC/ min, and (c) at a heating rate of 0.5 ºC/ min at 20 ± 2 ºC versus sodium metal in the voltage range of 0.01–2.5 V in a half-cell configuration.

The electrochemical performance of the samples with three different heating rates was investigated to monitor their Na^+ storage properties and the associated mechanism. **Figure 7.10** shows the CV plots of three electrodes for the initial five cycles at 0.05 mV s^{-1}. For all the three electrodes, two broad small peaks between 1.3 to 1.5 V were observed along with a sharp reduction peak at the reduction potential of 0.51 V. The two broad and less intense peaks were identified as the peak of $Na^{+,}$ which were intercalated to the $MoTe_2$ host structure. The sharp peak at 0.51 V corresponds to the formation of the Mo nanocrystal and Na_2Te due to the conversion reaction ($MoTe_2 + 4Na \rightarrow Mo + 2Na_2Te$).[10,15–18]

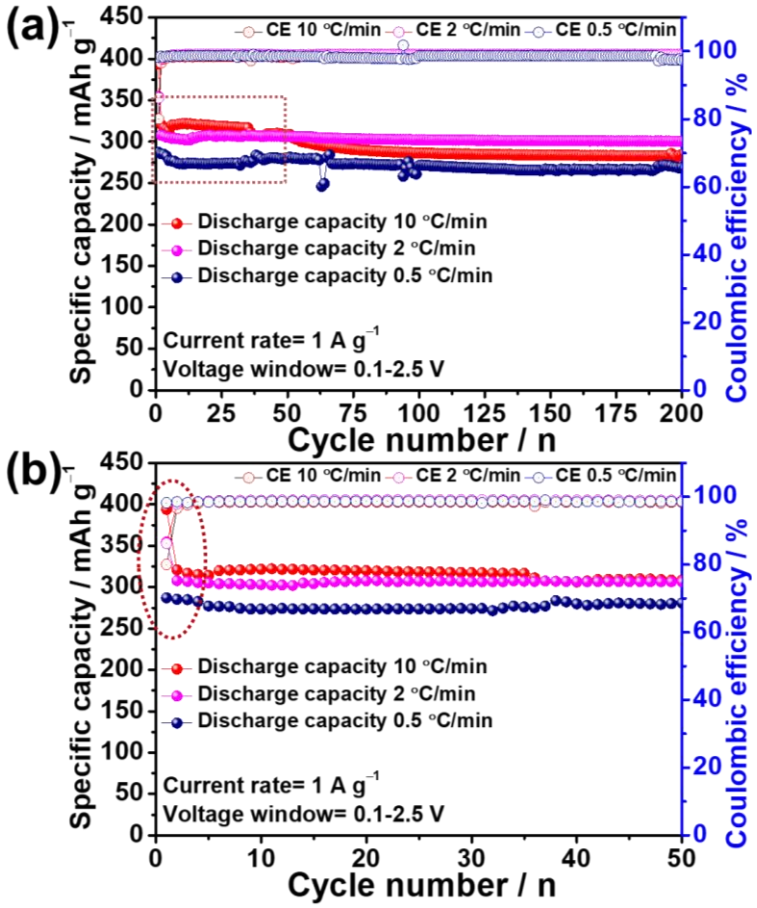

Figure 7.11(a) Comparative study of the charge/discharge cycle stabilities of different heating rates that annealed the $MoTe_2$ electrode at 20 ± 2 ºC in comparison to sodium in the voltage window of 0.1–2.5 V in a half-cell configuration. The inset rectangular denomination shows that the initial 50 cycles result in a magnified view (b). The circle denomination shows the first-cycle irreversible capacity loss; the sample prepared at a low heating rate shows a minimum, irreversible, 1^{st} cycle capacity loss.

The oxidation peaks at 1.51 V correspond to the $MoTe_2$ phase.[10,15,19,20] From the second cycle onwards, the reduction peak shifts and at the same time, a splitting of the peak is observed which corresponds to the peaks at 1.46 and 1.5 V. The highly reversible nature of both the reduction and oxidation peaks confirms the reversible nature of the $MoTe_2$ phase. It was observed that the reduction peak for the sample with high heating rate showed (**Figure 7.10a**) no splitting, whereas, for the low heating rate, the samples showed the splitting feature. The repeatability of the oxidation and the reduction peaks of CV for the samples which were prepared at the heating rate of 2 ºC/ min and 0.5 ºC/ min, respectively, is observed to be better than that of the sample that was prepared at the heating rate of 10 ºC/ min sample. **Figure 7.11** demonstrates the Galvanostatic discharge/charge long-term cycling performance of the $MoTe_2$ electrodes that were prepared at different heating rates against Na/Na^+ in the potential of 0.1 to 2.5Vin a half-cell configuration. It was observed that the sample with a higher heating rate showed higher specific capacity, because the effect of the heating rate helped the formation of thermal gradients, which resulted in the non-uniform sintering between the interior and exterior surfaces of the sample, enhancing both thermal and electrical conductivities including additional porosity.[5–8] The SEM image, as shown in **Figure 7.9**, displays a small amount of porosity, which is a result of the lack of particle rearrangement at the beginning of the annealing.

Table 7.1 Percentage of capacity retention and the decay rate for different cycles of the $MoTe_2$ anode prepared at different heating rates against lithium.

	Discharge capacity			**Capacity retention (%)**		
	Heating rate 10 ºC/min	**Heating rate 2 ºC/min**	**Heating rate 0.5 ºC/min**	**Heating rate 10 ºC/min**	**Heating rate 2 ºC/min**	**Heating rate 0.5 ºC/min**
1st cycle	≈394	**≈355**	≈287			
50th cycle	≈308	**≈306**	≈281	96	**99**	99
100th cycle	≈287	**≈302**	≈271	89	**98**	95
200th cycle	≈284	**≈301**	≈269	88	**97**	94

*Capacity retention when compared with the 2nd cycle discharge capacity

The higher heating rate increases the thermal activation process, which induces the motion and annihilation of any kind of dislocation or defects. This results in the lowering of the threshold strength, which causes the decrease of the overall density. The high heating rate and the synthesis procedure with a low-annealing-temperature lead to a lower crystallite size.

It additionally results in high and compact densification in the growth of the crystal. The sample that was prepared at 2 ℃/ min of heating rate shows both rod- and plate-type of morphology with affordable porosities, as shown in the FESEM (**Figure 7.8**). It has been observed that the irreversible capacity loss in the first cycle of the sample that has a larger crystallite size is low. This may be because the sample with the lower heating rate shows higher crystallinity.[5–7] Our observation shows that not only the crystallite size but also the crystallinity has an impact on the stability of the cycle and its long-term performance. This is possibly the reason that the material that was prepared at 2 ℃/ min of heating rate shows cycle stability, long-term performance, and better capacity retention than the other two samples with heating rate, as shown in **Table 7.1**.

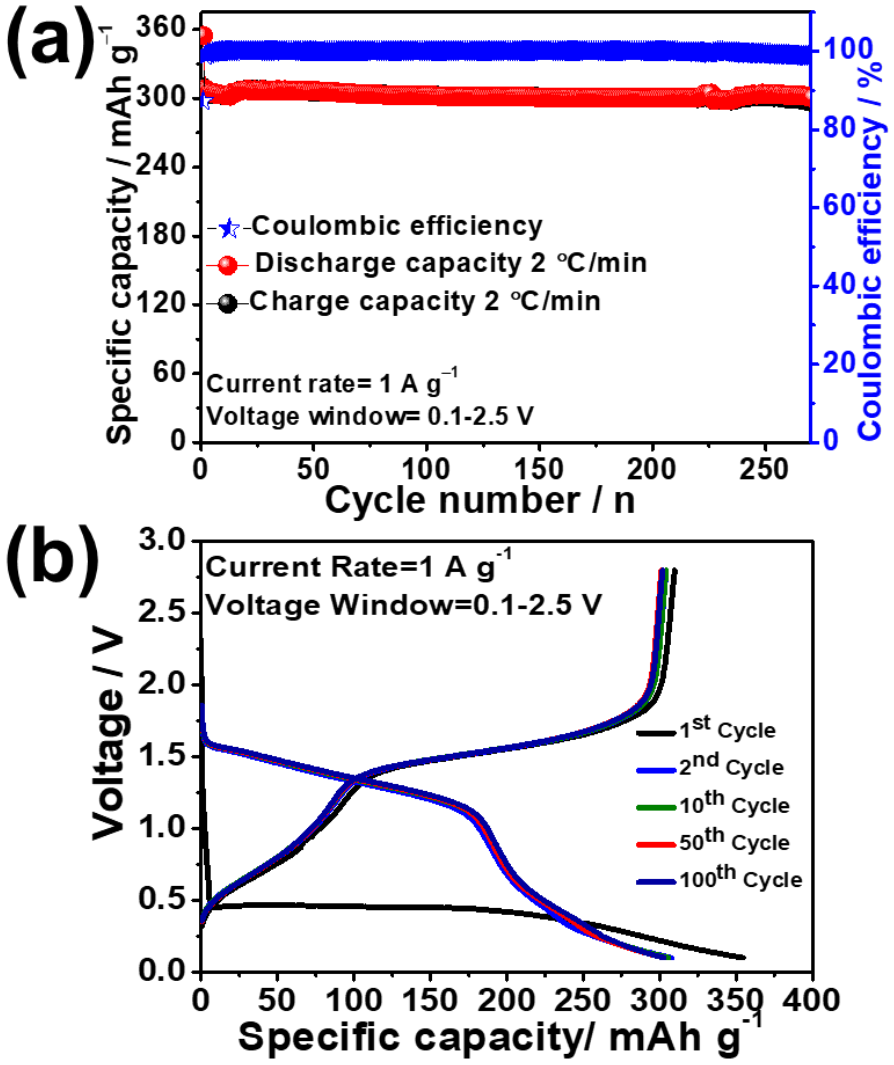

Figure 7.12 (a–b) Cycling performance with Coulombic efficiency and Galvanostatic charge/discharge curves versus specific capacity of $MoTe_2$ electrodes that were prepared at 2°C/ min of heating rate at a current rate of 1 A g^{-1} in the potential window of 0.1–2.5 V at 20 ± 2 ºC in a half-cell configuration.

Figure 7.12 shows the long-term cycling performance along with the galvanostatic charge/discharge profile (**Figure 7.12b**) of $MoTe_2$ electrodes that were prepared at a heating rate of 2°C/ min. The observed result confirmed the suitability of the material for long-term cycling performance, as shown in **Figure 7.12a**. **Figure 7.12a** shows a discharge capacity of 300.94 mAh g^{-1} over 270 cycles, with capacity retention of 97.7 % (when compared with the discharge capacity of the 2nd cycle) at a current rate of 1 A g^{-1}.

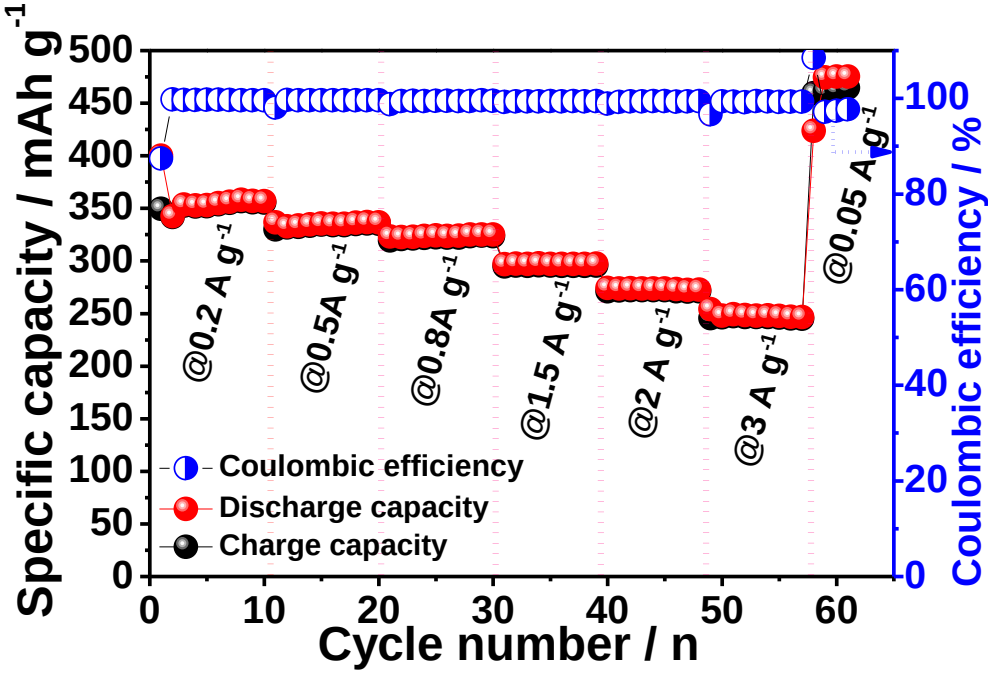

Figure 7.13 Rate performance along with the Coulombic efficiencies of $MoTe_2$ electrodes prepared at a heating rate of 2 °C/min in the potential window 0.1–2.5 Vat 20 ± 2 ºC in a half-cell configuration.

Figure 7.13 displays the rate capability of the $MoTe_2$ electrode that was prepared at a heating rate of 2 °C/min in the potential window 0.1–2.5 V at 20 ± 2 ºC in a half-cell configuration. The $MoTe_2$ electrode showed specific capacities of 353.02, 335.67, 324.18, 297.14, 273.72, and 247.83 mAh g^{-1} at corresponding current densities of 0.2 A g^{-1}, 0.5 A g^{-1}, 0.8 A g^{-1}, 1.5 A g^{-1}, 2 A g^{-1}, and 3 A g^{-1}, respectively, with an outstanding Coulombic efficiency of >99 %. This observation establishes the suitability of the $MoTe_2$ anode to work at various current densities. The $MoTe_2$ electrode further retained a specific capacity of 475.38 mAh g^{-1} at 0.05 A g^{-1}, while switching from higher to lower current, which additionally confirmed the operational capability of the $MoTe_2$ electrode at different current sweep rates. In summary, $MoTe_2$ samples with a small crystallite size and high crystallinity (prepared at a heating rate of

2 °C/min) show the best high-rate ability and long-term cyclability due to the combination of a lower Li^+ diffusion path and a stable crystal structure.

7.3.3 Sodiation mechanism study by in situ XANES and EXAFS analyses, and electrochemical kinetics study of the $MoTe_2$ electrode sample that was annealed at 2 °C/min

Figure 7.14 shows the Mo K-edge normalized XANES spectra of the $MoTe_2$ electrode during the first discharge process. Mo foil was used for the calibration of photon energy. The shifting of binding energy (ΔE), which is determined by the first derivative maxima of the edge, provides information about the variation of the charge state of Mo during the sodiation process. The extent of binding energy shift (ΔE) toward the lower values shows the decrease of the charge state of Mo.[10,13,20,21]

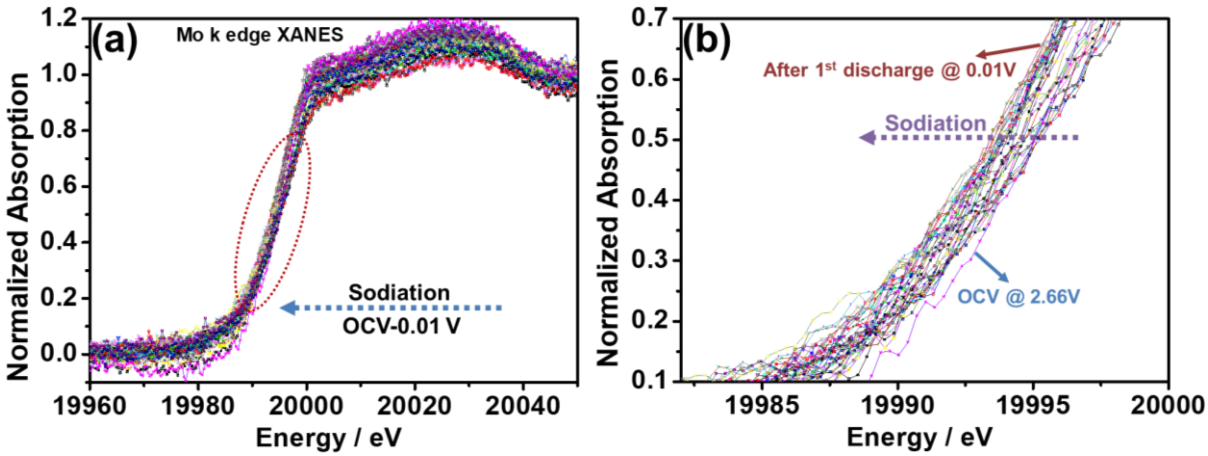

Figure 7.14 In situ XANES spectra of the $MoTe_2$ electrode during the first discharge process.

The value of the binding energy of Mo K-edge XANES spectra, as shown in **Figure 7.14**, confirms that the charge state of Mo at OCV (before cycling) is +4, which refers to the pure phase of the 2H $MoTe_2$. During the first discharge process, that is, during the insertion of Na^+ into the host $MoTe_2$ structure, the absorption energy shifts to a lower value due to the decrease in the binding energy of core electrons. As the concentration of Na^+ increases, the absorption energy (ΔE) slowly shifts to a lower value, which confirms the reduction of the Mo charge state and establishes the metallic form of Mo.[10,12,14,20]

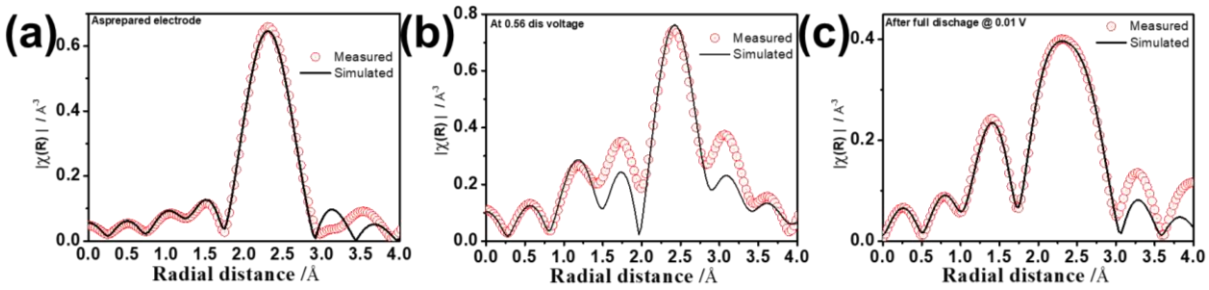

Figure 7.15 Ex situ XAFS spectra of the $MoTe_2$ as-prepared electrode, after 0.56 V discharge voltage and after the 1st discharge process.

Figure 7.15 shows the corresponding fitted Mo FT-EXAFS spectra of as-prepared, and after 0.56V and 0.01 V of full-discharge electrodes in R space. Two peaks at ~2.45 and 3. 51 Å of the FT spectra correspond to the Mo-Mo and Mo-Te bonds, respectively.[12,14] It was observed that the bond length and peak positions in the R space for the electrodes after 0.56 V of discharge (**Figure 7.15b**) voltage and after 0.01 V (full-discharge state, **Figure 7.15c**) during the sodiation process varied by ~0.2 to 0.4 Å, reliant on the nature of the nearest neighbor scatterer. With the increase in sodium concentrations during the first discharge process, the peak that corresponded to the Mo-Te bond started to diminish. The peak that corresponded to the Mo-Te bond finally disappeared after a full discharge. The reducing intensities and the disappearance of the peak that corresponded to the Mo-Te bond refer to the conversion reaction of the $MoTe_2$ during the sodiation process.[12,14] The appearance of the new peak at ~1.15 Å is a result of the nearest Mo-O SS path of the MoO_3 structure.[13,14,22] The peak shifted to 1.4 Å, and it became stronger after the full discharge process, which confirms the strong interaction between Mo and O. This is a result of the Mo-oxide that is formed by the Mo nanoparticles after the first discharge process due to the conversion reaction.[13,22] During the discharge process, the EXAFS spectra of the electrodes further confirm the conversion of the $MoTe_2$ to metallic Mo and Na_2Te during the sodiation process.[10] **Figure 7.16a, b** shows the FESEM images along with the EDS mapping (**Figure 7.16c, h**) of the as-prepared $MoTe_2$ electrode. It has been observed that the as-prepared electrode consists of broken pieces of the bulk $MoTe_2$ morphology, which is a result of the mixing of the $MoTe_2$ powders during the preparation of the slurry. The presence of C, O, and Na is a result of the binder (CMC) and carbon additives.

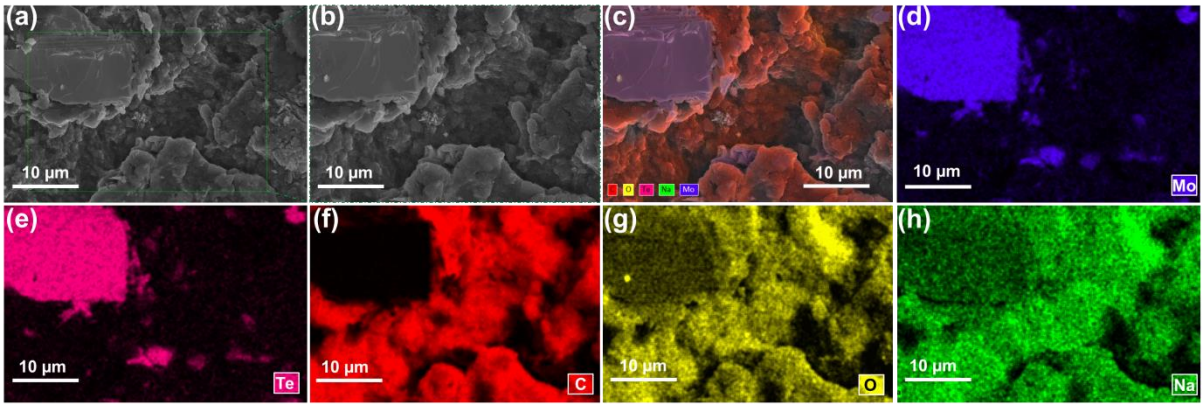

Figure 7.16 FESEM image and EDS mapping of the as-prepared $MoTe_2$ electrode at a heating rate of 2 ºC/ min.

The uniform spread of these elements throughout the electrode surface confirms the uniform mixing of all compositions during electrode fabrication. **Figure 7.17(a–d)** shows the FESEM images of the $MoTe_2$ electrode sample in the as-prepared state, after 1st-discharge full discharged state, after 1st-cycle state (fully charged), after the 5th-cycle state (full charged).

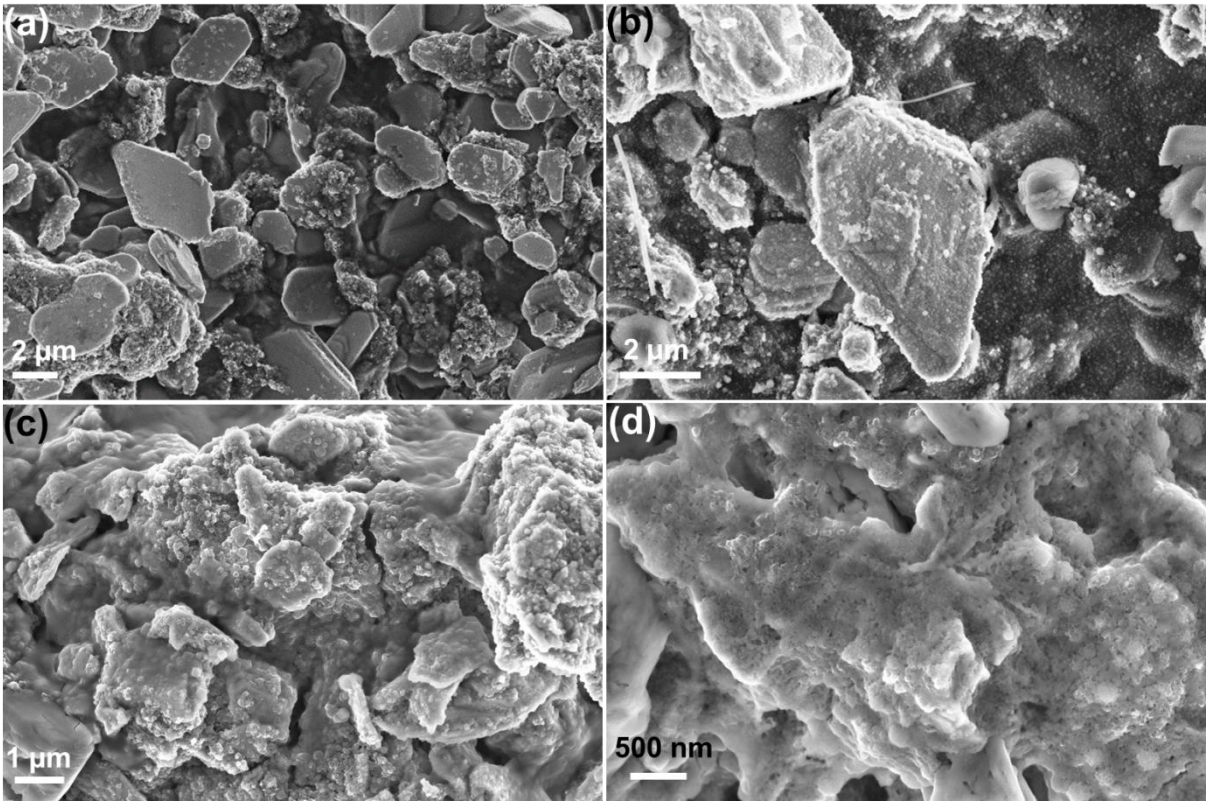

Figure 7.17 FESEM image of (a) the as-prepared electrode, (b) after the 1st-discharge fully discharged state, (c) after the 1st-cycle fully charged state, and (d) after the 10th cycle (fully charged state) of the $MoTe_2$ electrode.

The fully discharged electrode morphology shows the presence of smaller nano-sized particles, which reduced further, as was observed for the electrode after the 5th cycle (**Figure 7.17d**).

7.3.4 Discussion

The effect of the crystallite size and the crystallinity of the bulk 2H $MoTe_2$ phase has been investigated in SIB applications. It has been observed that with the increase of the crystallite size, the electrochemical performance improved for the sample that was prepared at a higher heating rate. With a variation in the heating rate, the densification differs, which affects the thermal and electrical conductivity properties.[5–7] The higher heating rate causes higher thermal gradients, which results in the sintering of the exterior portion before the interior and further enhances the porosity and Te defects that are responsible for the higher electrochemical performances of $MoTe_2$ in SIB applications.[10,19]

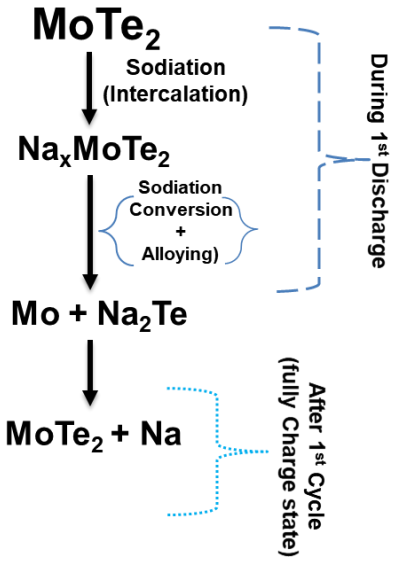

Figure 7.18 Schematic of the Na^+ storage mechanism in the 2H $MoTe_2$.

The experimental observations show that, during Na^+ insertion at the initial concentration, the mechanism follows the intercalation process. With the increase in the concentration of Na^+, the reaction pathway changes to the conversion process. At the end of the discharge process, the followed conversion reaction results in Mo nanoparticles and sodium telluride (Na_2Te).[10] The in situ XANES and ex situ EXAFS observations show that the sodiation/desodiation processes are highly reversible, and the observed features of EXAFS spectra match with the as-prepared $MoTe_2$ electrode. The above-observed mechanism has been illustrated schematically in **Figure. 7.18**.

7.3.5 $MoTe_2$ prepared at the heating rate 2 °C anode versus NVP full-cell study

Figure 7.19 demonstrates the electrochemical performance of the sodium-ion full-cell configuration, which has a combination of $MoTe_2$ as anode and sodium-containing Sodium vanadium phosphate ($Na_3V_2(PO_4)_3$ or NVP) as cathodes.

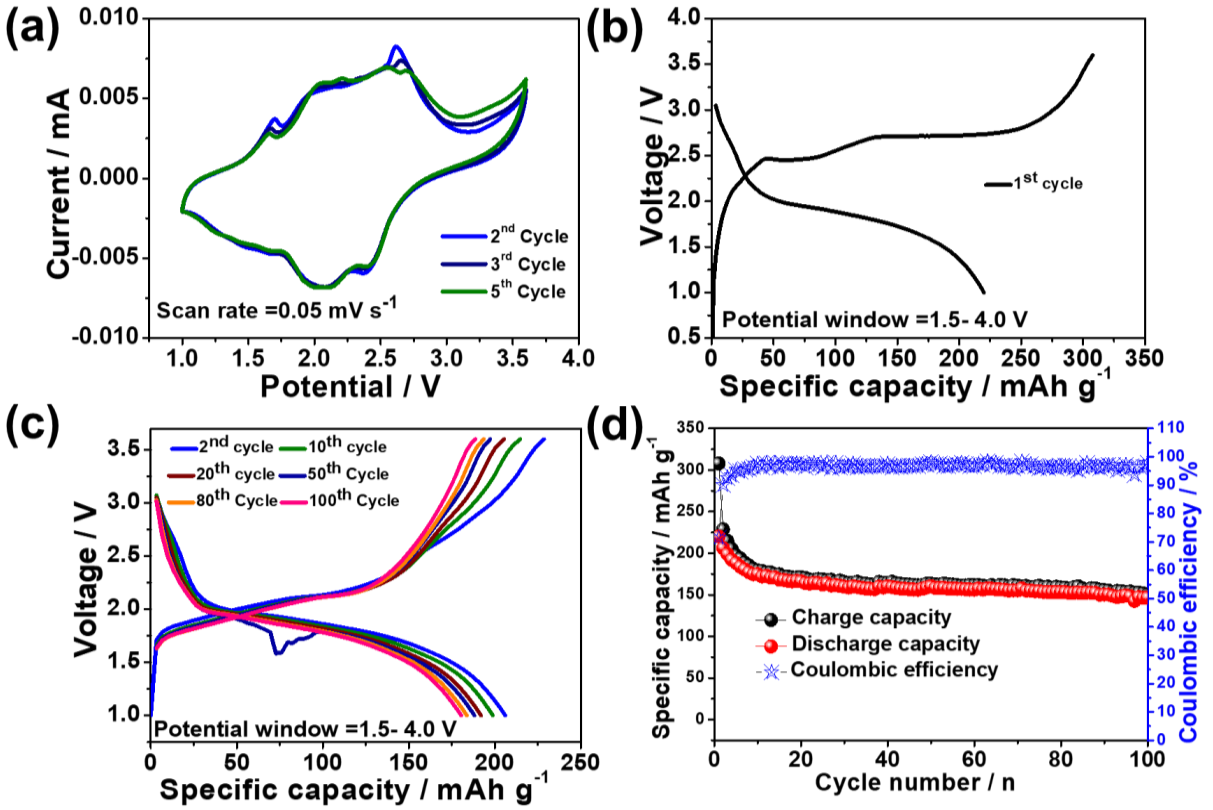

Figure 7.19 (a) CV of the $MoTe_2$//NVP full cell at a sweep rate 0.05 mV s^{-1}. (b) First cycle Galvanostatic charge/discharge curves of the $MoTe_2$//NVP full cell at 0.5 A g^{-1}. (c) Galvanostatic charge/discharge curves of the $MoTe_2$//NVP full cell in the voltage range of 1.0 to 3.6 V for different cycles. (d) Cycling performance of the $MoTe_2$//NVP full cell for 150 cycles at the current rate of 0.5 A g^{-1}.

The sodium-ion full-cell prototype configuration consists of $MoTe_2$ as the anode, NVP as the cathode, borosilicate glass fiber (GF/D, Whatman) as the separator, and 1M of $NaClO_4$ in a mixture of EC and PC (1:1 v/v) with 3 wt % of the additive, fluoroethylene carbonate (FEC), as an electrolyte. The weight ratio of the $MoTe_2$ and the NVP is set at 1:2 for the full-cell fabrication, which was determined by considering the performance of the individual anode and cathode. Further weight balancing is required to optimize the overall improvement of the electrochemical performance of the full cell. The specific capacity of the $MoTe_2$//NVP full cell

has been evaluated based on the active material mass of the anode ($MoTe_2$). The voltage window (1.0–3.5 V) was determined to analyze the individual working potentials of the anode and the cathode. The CV curve at a scan rate of 0.05 mV s^{-1}, as shown in **Figure 7.19a**, illustrates a broad reduction peak of ~2.1 V. This shows that the working potential of the $MoTe_2$//NVP full cell is approximately ~2.1 V. The mechanism of the full-cell has been illustrated by considering the NVP-related full cell as a reference and the reported literature in our previous work.[10] By considering the intercalation mechanism of the $MoTe_2$ and NVP versus Na/Na^+, the overall mechanism of the full-cell is given by equations (1a) and (1b) below.

Anode:

$$MoTe_2 + x Na^+ + x e^- \leftrightarrow Na_x MoTe_2 \quad (1a)$$

Cathode:

$$Na_3V_2^{3+}(PO_4)_3 \leftrightarrow Na_{3-x}V_{2-x}^{3+}V_x^{4+}(PO_4)_3 + x Na^+ + x e^- \quad (1b)$$

The $MoTe_2$//NVP full cell showed an initial charge/discharge specific capacity of ~308 mAh g^{-1} and ~220 mAh g^{-1} at a current density of 0.5 mA g^{-1}. The observed Coulombic efficiency (71.42 %) for the observed initial cycle was a result of the polarization and the irreversible loss of the $MoTe_2$ anode (**Figure7.19b,d**). From the 2nd cycle onward, the charge/discharge capacities of ~228mAh g^{-1} and ~207mAh g^{-1} observed, with an increased Coulombic efficiency of 90 %. Further in long-term cycling, the $MoTe_2$//NVP full cell has shown charge/discharge capacities of~151 mAh g^{-1} and ~147 mAh g^{-1} after 100 cycles (**Figure7.19d**) along with an increase of 98 % in the Coulombic efficiency and an overall capacity retention of 78 % (with reference to the second cycle) over 100 cycles.

The comparative results of the $MoTe_2$//NVP full cell along with our previously reported results and other literature are given in **Table 7.2**. The overall cell voltage of the $MoTe_2$ prepared at the heating rate of 2 ºC/ min anode //NVP full cell observed $MoTe_2$//NVP full cell was 2.1 V with an energy density of 440 Wh kg^{-1}. The current stage of development of full cell required several optimizations to avoid the loss of sodium in the initial cycles. In half cell of MoTe2 anode (sodium foil) is the unlimited source of sodium. In full cell NVP cathode is the source of sodium which cannot be the unlimited source. The loss of sodium in the initial cycles are the loss of capacity after few cycles of the full cell. We believe that due to loss of sodium in the initial cycles, which cannot be compensated by the limited sodium source (NVP cathode). This reflects in the decreased capacity retention (78 % over 100 cycles) in full cell

configuration compared to the half-cell configuration with MoTe2 sample prepared at a heating rate of 2 ℃/min. The experimental results show the potential application of the MoTe2//NVP full cell as a promising candidate in future SIB technology for various energy storage applications.

Table 7.2 A comparison of the conventional SIB full cell, our full-cell configuration, and their performances along with our present full-cell ($MoTe_2$. versus NVP) combination.

Full cell Configuration	Voltage (V)	Current Rate	Specific Capacity (mA h g^{-1})	Energy Density (Wh kg^{-1})	Capacity Retention
H-$Na_2Ti_3O_7$// $Na_{2/3}(Ni_{1/3}Mn_{2/3})O_2$ [23]	2.7	1 C	182 (anode base)	490	(100^{th} cycle)
XXX (FARADION)	3		162	486	
C//($Na_1Fe_{0.5}Mn_{0.5}O_2$ + 10%Na_3P)[24]	3.2		110	352	81% (20^{th} cycle)
TiO_2 //$Na_2V_2O_5$[25]	2.3	1 C	118	271	76% (350^{th} cycle)
Fe_2O_3, NiO//$Na_3V_2(PO_4)_3$[26]	1.8	C/2	100	180	80% (30^{th} cycle)
Fe_3O_4//$Na_2P_2O_7$[27]	2.28	0.1 C	93	203	93.3%(100^{th} cycle)
Hard carbon//$NaNi_{0.5}Ti_{0.5}O_2$[28]	2.75		95	261	72% (100^{th} Cycle)
$Na[Li_{0.05}Mn_{0.50}Ni_{0.30}Cu_{0.10}Mg_{0.05}]O_2$ //hard carbon[29]	2.9	0.1 C	74	215	98% (200^{th} cycle)
Fe_3O_4@FeS//$Na_3V_2(PO_4)_2O_2F$[30]	2.8	500 mA g^{-1}	157	439	92.3% (50^{th} cycle)
$FePO_4$ // $Na_{0.44}MnO_2$[31]	0.7	3 C	70	49	90% (300^{th} cycle)
$Na_2Fe_2(CN)_6$//Cu INPB[32]	3.11	1 C	108	336	76% (100^{th} cycle)
@2 °C/ min heating rate $MoTe_2$// $Na_3V_2(PO_4)_3$	**2**	**500 mA g^{-1}**	**220 (anode base)**	**440**	**78% (100^{th} cycle)**

7.4 The impact of electrolyte additives on the electrochemical performance

Figure 7.20 shows the cycle stability of the $MoTe_2$ anode with and without FEC as an additive in the electrolyte. To investigate this, the electrochemical performance of the $MoTe_2$ anode against sodium metal was evaluated with and without FEC additives in both electrolytes. The electrochemical performance of our $MoTe_2$ electrode, when compared with the electrolyte with the FEC additive material, showed better stability and enhanced electrochemical performance. The electrolyte that was used without FEC showed a degradation phenomenon that was caused by an unstable SEI. The electrolyte with the FEC additive showed better electrochemical performance and better cycle stability due to a stable SEI formed by the electrode surface.[33,34]

The Postmortem investigations of cycled electrodes with FEC additives are shown by the TEM results, as seen in Figure 7.21c; this observation provides a fundamental discussion to understand the degradation caused by the SEI (Figure 7.21a, b). Figure 7.22 shows the Nyquist plots of the $MoTe_2$ electrode at OCV and after cycling (1^{st} to 50^{th} cycle) at fully charged states with and without the FEC additive.

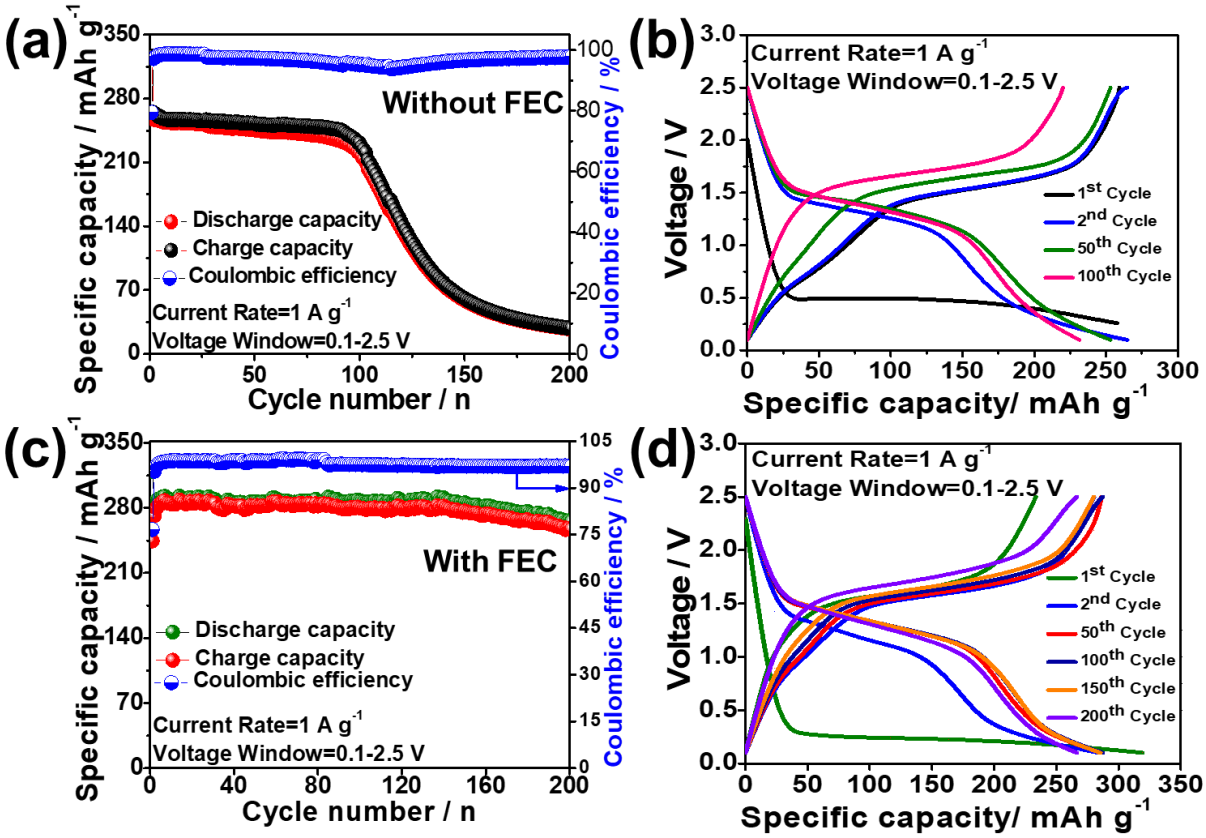

Figure 7.20 Electrochemical performance of $MoTe_2$ electrodes before and after the addition of FEC at 20 ± 2 ºC in a half-cell configuration. (a–b) Cycling performance with Coulombic efficiency and Galvanostatic charge/discharge curves versus specific capacity of $MoTe_2$ electrodes at a current rate of 1 A g^{-1} without addition of FEC additive. (c–d) Cycling performance with Coulombic efficiency and Galvanostatic charge/discharge curves versus specific capacity of $MoTe_2$ electrodes with addition of FEC additive at a current rate of 1 A g^{-1} in the potential window, 0.1–2.5 V.

In the Nyquist plots, the observed diameter of the semicircle of the $MoTe_2$ with FEC is smaller in the high–medium frequency region than that of the $MoTe_2$ without FEC. This observation confirms that the $MoTe_2$ electrode with FEC possesses lower-order contact and charge-transfer resistances.[10,33,34] The observed R_{ct} value decreases continuously and becomes stable after 10

cycles due to the transformation of the $MoTe_2$ into amorphous nanocrystals during the continuous charge/discharge process.[10,20,35–37]

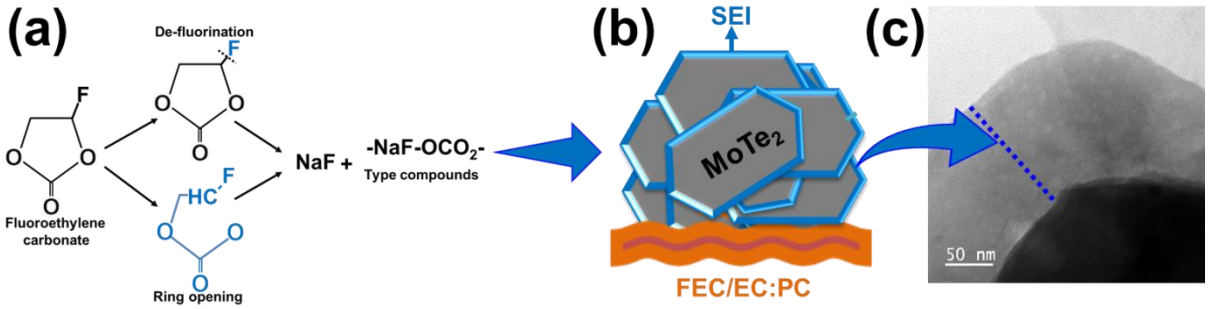

Figure 7.21(a–b) The mechanism of the FEC, to enhance the electrochemical performance of $MoTe_2$ electrode against sodium metal. (c) BFTEM image, showing the SEI layer on the surface of the $MoTe_2$ particle.

The lower R_{ct} values for the $MoTe_2$ with FEC refers to the increasing ionic conductivity, and the constant R_{ct} values after a few cycles refer to the stable SEI layers.[33,34] These results confirm our preliminary tests and suggest that FEC performs better in terms of better reversibility because of an extremely stable SEI.

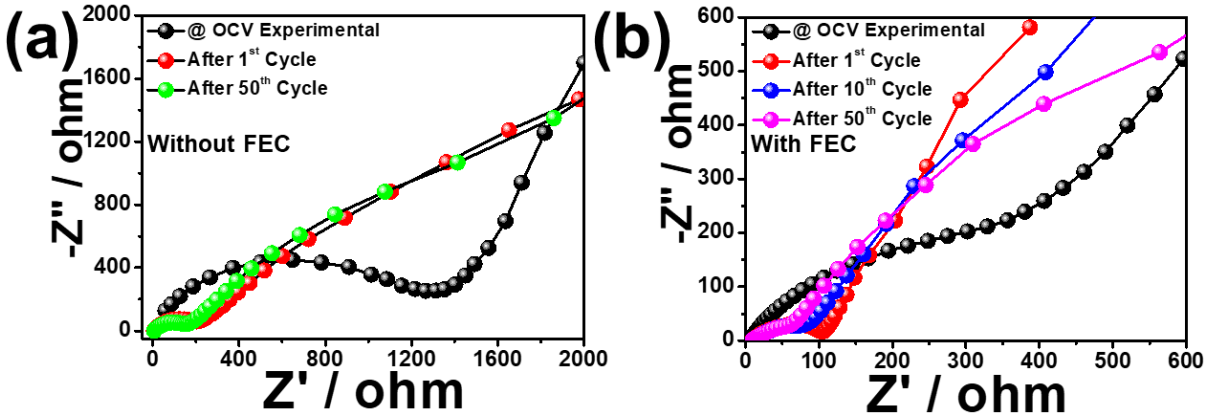

Figure 7.22 EIS spectra of the $MoTe_2$ anode in a half-cell configuration, between 10 mHz to 1 MHz, showing Nyquist impedance plots before the cycle, and after the 1st, 10th, and 50th cycles (a) without FEC additive, (b) with FEC additive at 20 ± 2 °C.

7.5 Conclusions

In summary, the effect of the crystallite size and the morphology of the $MoTe_2$ without carbonaceous materials have been investigated for SIB applications. $MoTe_2$ that was prepared at 2 °C/ min has shown better cycle stability and electrochemical performance, whereas $MoTe_2$ that was prepared at a heating rate of 10°C/ min showed a higher specific capacity for initial cycles. A high heating rate results in higher thermal gradients, which first sinters the external

peripheral and then the internal peripheral. The effect of the variation in the sintered zones of the external and internal regions creates lots of defects and porosity in the sintered samples due to a lack of particle arrangement. As a result, the heating rate and the sintering temperature enable the tuning of the density, crystallinity, porosity, and defects on the material with thermal and electrical conductivity. These factors helped to improve the electrochemical performances of the studied materials. The $MoTe_2$ prepared at the heating rate of 2 ºC/ min anode //NVP full cell has shown an energy density of 440 Wh Kg^{-1} with 98 %Coulombic efficiency after 100 cycles, with an overall capacity retention of 78 % (with reference to the second cycle) over 100 cycles. These studies reveal the effect of crystallite size and additives on the electrochemical performance and the potential of $MoTe_2$ in SIB applications.

7.6 References

(1) Deng, K.; Wan, G.; Deng, P.; Zhang, K.; Ding, S.; Wang, E.; Yan, M.; Huang, H.; Zhang, H.; Xu, Z.; Denlinger, J. Experimental Observation of Topological Fermi Arcs in Type-II Weyl Semimetal $MoTe_2$. *Nat. Phys.* **2016**, 12, 1105–1110.

(2) Shen, Y.; Eltzholtz, J. R.; Iversen, B. Controlling Size, Crystallinity, and Electrochemical Performance of $Li_4Ti_5O_{12}$ Nanocrystals. *Chem. Mater.* **2013**, 25, 5023−5030.

(3) Domi, Y.; Usui, H.; Sugimoto, K.; Sakaguchi, H.; Effect of Silicon Crystallite Size on Its Electrochemical Performance for Lithium-Ion Batteries. *Energy Technol.* **2019**, 7, 1800946.

(4) Lai, J.; Tang, H.; Zhu. X.; and Wang, Y. A Hydrated $NH_4V_3O_8$ Nanobelt Electrode For Superior Aqueous and Quasi-Solid-State Zinc Ion Batteries. *J. Mater. Chem. A* **2019**, 7, 23140–23148.

(5) Zhang, H. H.; Xu, Y. L.; Wang, B.; Zhang, X.; Yang, J. F.; Niihara, K. Effects of Heating Rate on the Microstructure and Mechanical Properties of Rapid Vacuum Sintered Translucent Alumina. *Ceram. Int.* **2015**, 41, 12499.

(6) Gephart, S.; Singh, J.; Kulkarni, A. Field Assisted Sintering of SiC Using Extreme Heating Rates. *J. Mater. Sci.* **2011**, 46, 3659.

(7) Snyder, A.; Bo, Z.; Hodson, S.; Fisher, T.; Stanciu, L. The Effect of Heating Rate and Composition on the Properties of Spark Plasma Sintered Zirconium Diboride Based Composites. *Mater. Sci. Eng.* A **2012**, 538, 98–102.

(8) Singh, L. K.; Bhadauria, A.; Jana, S.; Laha, T. Effect of Sintering Temperature and Heating Rate on Crystallite Size, Densification Behaviour and Mechanical Properties of Al-MWCNT Nanocomposite Consolidated via Spark Plasma Sintering. *Acta Metallurgica Sinica* **2018**, 31, 1019–1030.

(9) Keum, D. H.; Cho, S.; Kim, J. H.; Choe, D. H.; Sung, H. J.; Kan, M.; Kang, H.; Hwang, J. Y.; Kim, S. W.; Yang, H.; Chang, K. J. Bandgap Opening in Few-Layered Monoclinic $MoTe_2$. *Nat. Phys.* **2015**, 11, 482–486.

(10) Panda, M. R.; Ghosh, A.; Kumar, A.; Muthuraj, D.; Sau, S.; Yu, W.; Zhang, Y.; Sinha, A.K.; Weyland, M.; Bao, Q.; Mitra, S. Blocks of Molybdenum Ditelluride: A High Rate Anode for Sodium-Ion Battery and Full Cell Prototype Study. *Nano Energy* **2019**, 64, 103951.

(11) Retuerto, M.; Li, M.; Stephens, P. W.; Sánchez-Benítez, J.; Deng, X.; Kotliar, G.; Croft, M.C.; Ignatov, A.; Walker, D.; Greenblatt, M. Half-Metallicity in Pb_2CoReO_6 Double Perovskite and High Magnetic Ordering Temperature in Pb_2CrReO_6 Perovskite. *Chem. Mater.* **2015**, 27, 4450−4458.

(12) Zhu, Z.; Xi, S.; Miao, L.; Tang, Y.; Zeng, Y.; Xia, H.; Lv, Z.; Zhang, W.; Ge, X.; Zhang, H.; Wei, J.; Cao, S.; Chen, J.; Du, Y.; Chen, X. Unraveling the Formation of Amorphous MoS_2 Nanograins During the Electrochemical Delithiation Process, *Adv. Funct. Mater.* **2019**, 29, 1904843.

(13) Sen, U. K.; Johari, P.; Basu, S.; Nayak, C.; Mitra, S. An Experimental and Computational Study to Understand the Lithium Storage Mechanism in Molybdenum Disulfide. *Nanoscale* **2014**, 6, 10243–10254.

(14) Rehman, Z.; Zhu, W.; Wang, S.; Niu, Y.; Muhammad, Z.; Moses, O. M.; Wu, C.; Habib, M.; Chen, S.; Wu, X.; Sun, Z.; Ajayan, P. M.; Song, L. Selective Selenium-Substituted Metallic $MoTe_2$ toward Ternary Atomic Layers with Tunable Semiconducting Character. *J. Phys. Chem. C* **2019**, 123, 24927−24933.

(15) Cho, J. S.; Ju, H. S.; Lee, J. K.; Kang, Y. C. Carbon/Two-Dimensional $MoTe_2$ Core/Shell-Structured Microspheres as an Anode Material for Na-Ion Batteries. *Nanoscale* **2017**, *9*, 1942–1950.

(16) Liu, Y.; Wang, H.; Cheng, L.; Han, N.; Zhao, F.; Li, P.; Jin, C.; Li, Y. TiS_2 Nanoplates: A High-Rate and Stable Electrode Material for Sodium Ion Batteries. *Nano Energy* **2016**, 20, 168–175.

(17) Yang, W.; Wang, J.; Si, C.; Peng, Z.; Zhang, Z. Tungsten Diselenide Nanoplates as Advanced Lithium/Sodium Ion Electrode Materials with Different Storage Mechanisms. *Nano Res.* **2017**, 10, 2584–2598.

(18) Lv, X.; Wei, W.; Sun, Q.; Huang, B.; Dai, Y. A First-Principles Study of $NbSe_2$ Monolayer as Anode Materials for Rechargeable Lithium-Ion and Sodium-Ion Batteries. *J. Phys. D: Appl. Phys* **2017**, 50, 235501.

(19) Ma, N.; Jiang, X. Y.; Zhang, L.; Wang, X. S.; Cao, Y. L.; Zhang, X. Z. Novel 2D Layered Molybdenum Ditelluride Encapsulated in Few-Layer Graphene as High-Performance Anode for Lithium-Ion Batteries. *Small* **2018**, 14, 1703680.

(20) Panda, M. R.; Gangwar, R.; Muthuraj, D.; Sau, S.; Pandey, D.; Banerjee, A.; Chakrabarti, A.; Sagdeo, A.; Weyland, M.; Majumder, M.; Bao, Q.; Mitra, S. High Performance Lithium-Ion Batteries Using Layered 2H-$MoTe_2$ as Anode. *Small* **2020**, 16, 2002669.

(21) Joseph, D.; Yadav, A. K.; Jha, S. N.; Bhattacharyya, D. Chemical Shift of Mn and Cr K-edges in X-ray Absorption Spectroscopy with Synchrotron radiation. *Bull. Mater. Sci.* **2013**, 36, 1067–1072.

(22) Kisfaludi, G.; Leyrer, J.; Knozinger, H.; Prins, R. EXAFS Study of the Spreading of MoO_3 on the Surface of γ-Al_2O_3. *J. Catal.* **1991**, 130, 192–201.

(23) Fu, S.; Ni, J.; Xu, Y.; Zhang, Q.; Li, L. Hydrogenation Driven Conductive $Na_2Ti_3O_7$ Nanoarrays as Robust Binder-Free Anodes for Sodium-Ion Batteries. *Nano Energy* **2016**, 16, 4544–4551.

(24) Barpanda, P.; Oyama, G.; Nishimura, S. I.; Chung, S. C.; Yamada, A. A 3.8 V Earth Abundant Sodium Battery Electrode. *Nature Commun.* **2014**, 5, 4358.

(25) Oh, S. M.; Pilgun Oh, P.; Kim, S. O.; Manthiram, A.; A High-Performance Sodium-Ion Full Cell with a Layered Oxide Cathode and a Phosphorous-Based Composite Anode *J. Electrochem. Soc.* **2017**, 164 (2) A321–A326.

(26) López, M. C.; Aragón, M. J.; Ortiz, G. F.; Lavela, P.; Alcántara, R. High Performance Full Sodium-Ion Cell Based on a Nanostructured Transition Metal Oxide as Negative Electrode. *Chem. a Eur. J.* **2015**, 2, 4879–14885.

(27) Ming, J.; Ming, H.; Yang, W.; Kwak, W.; Park, J. A Sustainable Iron-Based Sodium Ion Battery of Porous Carbon–Fe_3O_4/$Na_2FeP_2O_7$ with High Performance. *RSC Adv.* **2015**, 5, 8793–8800.

(28) Wang, H.; Xiao, Y.; Sun, C.; Lai, C.; Ai, X. A Type of Sodium-Ion Full-Cell with a Layered $NaNi_{0.5}Ti_{0.5}O_2$ Cathode and a Pre-Sodiated Hard Carbon Anode. *RSC Adv.* **2015**, 5, 06519–106522.

(29) Deng, J.; Luo, W. B.; Lu, X.; Yao, Q.; Wang, Z.; Liu, H. K.; Zhou, H.; Dou, S. X. Sodium-Ion Batteries: High Energy Density Sodium-Ion Battery with Industrially Feasible and Air-Stable O_3-Type Layered Oxide Cathode. *Adv. Energy Mater.* **2018**, 8, 1701610.

(30) Peng, J.; Wang, J.; Yi, H.; Hu, W.; Yu, Y.; Yin, J.; Shen, Y.; Liu, Y.; Luo, J.; Xu, Y.; Wei, P.; Li, Y.; Jin, Y.; Ding, Y.; Miao, L.; Jiang, J.; Han, J.; and Huang, Y. Sodium Ion Batteries: A Dual-Insertion Type Sodium-Ion Full Cell Based on High-Quality Ternary-Metal Prussian Blue Analogs. *Adv. Energy Mater.* **2018**, 8, 1702856.

(31) Wang, Y.; Feng, Z.; Laul, D.; Zhu, W.; Provencher, M. Ultra-Low Cost and Highly Stable Hydrated $FePO_4$ Anodes for Aqueous Sodium-Ion Battery *J. Power Sources* **2018**, 374, 211–216.

(32) Rudolaa, A.; Gajjelaa, S. R.; Balaya, P. High Energy Density In-Situ Sodium Plated Battery with Current Collector Foil as Anode. *Electrochem. commun.* **2018**, 86, 157–160.

(33) Jaumann, T.; Balach, J.; Langklotz, U.; Sauchuk, V.; Fritsch, M.; Michaelis, A.; Teltevskij, V.; Mikhailova, D.; Oswalda, S.; Klose, M.; Stephani, G.; Hauser, R.; Eckert, J.; Giebeler, L. Lifetime vs. Rate Capability: Understanding the Role of FEC and VC in High Energy Li-Ion Batteries with Nano-Silicon Anodes. *Energy Storage Mater.* **2017**, 6, 26–35.

(34) Xu, C.; Lindgren, F.; Philippe, B.; Gorgoi, M.; Björefors, F.; Edström, K.; Gustafsson, T. Improved Performance of the Silicon Anode for Li-Ion Batteries: Understanding the Surface Modification Mechanism of Fluoroethylene Carbonate as an Effective Electrolyte Additive, *Chem. Mater.* **2015**, 27, 2591−2599.

(35) Sarkar, A.; Sarkar, S.; Mitra, S. Exceptionally High Sodium-Ion Battery Cathode Capacity Based on Doped Ammonium Vanadium Oxide and a Full Cell SIB Prototype Study. *J. Mater. Chem. A* **2017**, 5, 24929–24941.

(36) Cho, J. S.; Hong, Y. J.; Kang, Y. C. Design and Synthesis of Bubble-Nanorod-Structured Fe_2O_3–Carbon Nanofibers as Advanced Anode Material for Li-Ion Batteries. *ACS nano* **2015**, 9, 4026–4035.

(37) Xu, Y.; Zhu, Y.; Liu, Y.; Wang, C. Electrochemical Performance of Porous Carbon/Tin Composite Anodes for Sodium-Ion and Lithium-Ion Batteries. *Adv. Energy Mater.* **2013**, 3, 128–133.

CHAPTER 8

General conclusions and future scopes

"This chapter will provide the research outcome of the over thesis and the associated future scopes."

8.1 Conclusions

The aim of this project was to investigate a new class of advanced layered TMDs for LIB and SIB applications. An additional aim was a detailed investigation of the lithium/sodium storage mechanisms to mitigate relevant challenges in the enhancement of the electrochemical performances. By using a facile solid-state reaction route synthesis process, 2H and 1T' phases of molybdenum ditelluride ($MoTe_2$) were synthesized. Various advanced characterization techniques were thoroughly implemented to investigate the structure, morphology, and electronic properties studies of as-synthesized materials. Throughout our investigation, we studied the structural variation that is associated with the charge/discharge process for both 2H and 1T' phases of the $MoTe_2$. The aim of the investigation was to understand the lithium and sodium storage mechanism and strategy to enhance electrochemical performances, and to conduct full-cell studies for both LIBs and SIBs. Synchrotron source-based advanced in situ and ex situ experimental measurements and DFT calculations were carried out to reveal the unique lithium and sodium reaction pathways and storage mechanisms and to understand the electrochemical reaction mechanism better.

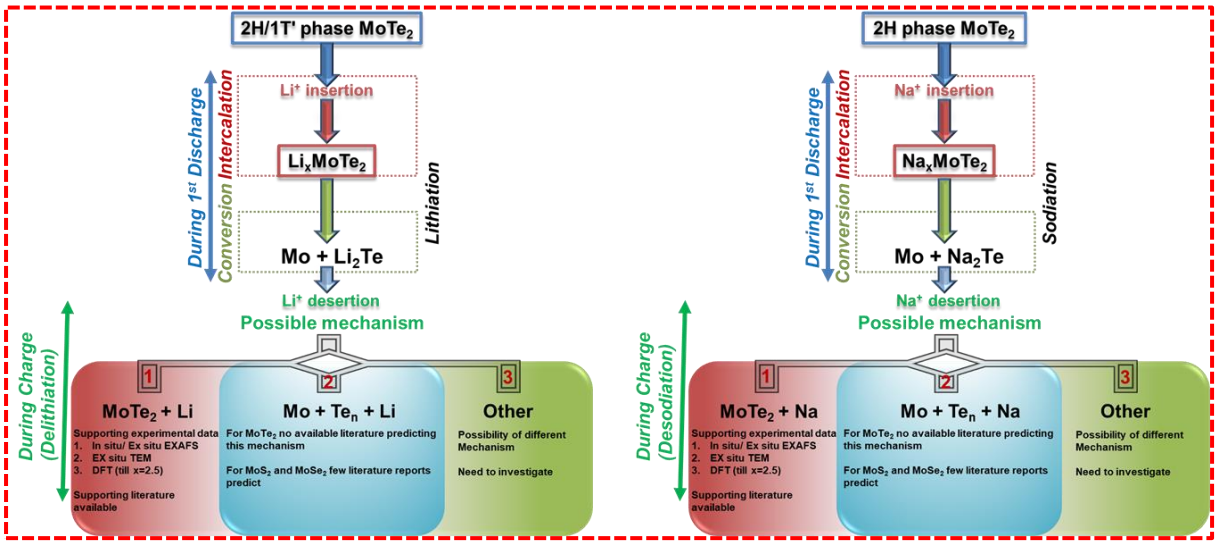

Figure 8.1 Proposed and observed Li^+/Na^+ storage mechanism of the 2H and 1T' phases of the $MoTe_2$ anode.

Ex situ SXRD, HRTEM with SAD, XPS, and XANES studies along with in situ XAS and impedance results for the 2H and 1T' phases of $MoTe_2$ when compared to lithium and sodium showed (after the first discharge process) that the conversion reaction, that is, the formation Li_2Te/Na_2Te + Mo type of structure followed by intercalation reaction (Li_xMoTe_2/Na_xMoTe_2-intercalated structure) was formed for lower concentrations of lithium and sodium. A similar

conversion reaction has been reported in a previous study, in which Li and Na atoms were intercalated in 2H-MoS_2. During the charging process, that is, after the desertion of Li/Na, the 2H and 1T'-$MoTe_2$ phases were reconstituted. Experimental findings confirmed the reversible nature of the 2H and 1T'- phases of the $MoTe_2$ material during the Li^+ and Na^+ insertion/desertion process.

The DFT calculations showed that for $MoTe_2$, when compared to lithium at lower intercalation concentrations ($0 < x \leq 1.5$) of Li atoms in Li_xMoTe_2, the geometrical and electronic properties changed moderately, and a Li_xMoTe_2-intercalated structure was formed. On the other hand, at higher concentrations ($1.5 < x \leq 3.0$), the onset of the conversion reaction occurred, which showed the signature of the formation of Li_2Te + Mo type of structure at an Li concentration of about x = 3.0. Delithiation (removal of Li atoms from Li_xMoTe_2) for the concentration of $x \leq 2$ led to the original bulk structure of the 1T' –$MoTe_2$. However, for x>2, when the system was observed to be distorted significantly, the original $MoTe_2$ structure was not achieved after the delithiation process. Therefore, it could be predicted that the delithiation process is an irreversible process for x>2. However, we wish to mention here that simulating the delithiation process for a higher concentration (for x>2) using an ab initio method is a difficult task. In these cases, static DFT calculations may provide some metastable states or a local minimum. Therefore, for higher concentrations (for x>2), our DFT calculations may not be able to predict the delithiation process accurately.

Table 8.1 A summary of the electrochemical performance of 2H/1T' phase of our $MoTe_2$ anode versus lithium and sodium in half-cell configuration.

Anode Material	Current rate	Discharging Capacity (mAh g^{-1})	Cycling retention
Against lithium			
Pristine 2H $MoTe_2$	1 A g^{-1}	432	260
Pristine 1T' $MoTe_2$	1 A g^{-1}	501	200
Against sodium			
Pristine 2H $MoTe_2$	1 A g^{-1}	290	200
$MoTe_2$ @ 2 °C	1 A g^{-1}	301	270

Figure 8.1 shows the possible Li^+/Na^+ storage mechanism of the 2H and 1T' phase of the $MoTe_2$ anode. Our experimental and theoretical findings (for x>2) along with supporting literature followed mechanism 1 (**Figure 8.1**) during the delithiation process; however, we believe further in situ and dynamic DFT studies are required to support our observation fully. We vigorously deny other possible mechanisms (mechanism 2 and 3, **Figure 8.1**) for Li^+/Na^+ storage of the 2H and 1T' phases of the $MoTe_2$ electrode.

Table 8.2 A summary of the electrochemical performance of our full cell configuration for LIB ($MoTe_2$. versus LCO) and for SIB ($MoTe_2$. versus NVP) combination.

Full cell Configuration	Voltage (V)	Current Rate	Specific Capacity (mAh g^{-1})	Energy Density (Wh kg^{-1})	Capacity Retention
LIB full cell ($MoTe_2$. versus LCO)					
2H $MoTe_2$//LCO	2.10	500 mA g^{-1}	216 (anode base)	454	80% (100^{th} cycles)
1T'- $MoTe_2$//LCO	2.10	100 mA g^{-1}	249 (anode base)	523	96% (100^{th} cycles)
SIB full cell ($MoTe_2$. versus NVP)					
$MoTe_2$// $Na_3V_2(PO_4)_3$	2	500 mA g^{-1}	207 (anode base)	414	88% (150^{th} cycle)
$MoTe_2$ @ 2 ℃ // $Na_3V_2(PO_4)_3$	2	500 mA g^{-1}	220 (anode base)	440	78% (100^{th} cycle)

In summary, Table 8.1 shows the electrochemical performance of the 2H/1T' phase of the $MoTe_2$ anode versus lithium and sodium in both half-cell and full-cell configurations. A detailed comparative study of our observed performances with existing literature is given in each corresponding individual chapter (Table 4.2, Table 6.4, Table 7.1). It was observed that the as-prepared $MoTe_2$ electrodes exhibited an initial lithium-storage-specific capacity of 432 mAh g^{-1} at a current density of 1.0 A g^{-1}. Further, it retained the property of reversible specific capacity of 291 mAh g^{-1} after 250 cycles. The $MoTe_2$ anode and the LCO cathode showed a high energy density of 454 Wh kg^{-1} (at a current density of 0.5 A g^{-1} based on the mass of anode). In the subsequent study, the as-prepared 1T' phase of the $MoTe_2$ showed a specific capacity of 501 mAh g^{-1} at 1.0 A g^{-1}. The half cell showed capacity retention of 91.5 % (with reference to 2^{nd} cycle) and 99 % of Coulombic efficiency over 200 cycles. The 1T' $MoTe_2$//LCO full cell displayed a reversible capacity of 388.4 mAh g^{-1} at 100 mA $g^{-1}$for 100

cycles, which was able to retain 74 % of its initial capacity (with reference to 2nd cycle) with a Coulombic efficiency of ≈96 % at a current density of 0.1 A g^{-1}, based on the mass of the anode.

In the follow-up studies, the layered structured 2H phase of the $MoTe_2$ was used as an anode material in SIB applications. The $MoTe_2$ electrode exhibited an initial specific capacity of 320 mAh g^{-1} at a current density of 1.0 A g^{-1}, and it retained a high specific capacity of 270 mAh g^{-1} after 200 cycles. The sodium-ion full cell that used $MoTe_2$ as the anode and sodium vanadium phosphate $Na_3V_2(PO_4)_3$ (NVP) as the cathode retained 88 % of its initial capacity after 150 cycles at a current density of 0.5 A g^{-1} and an operating voltage of ~2 V, along with a high energy density of 414 Wh kg^{-1}. In the latter portion of this study, the effect of crystallite size, crystallinity, and the reason for the higher first cycle capacity (including the exfoliation of the bulk 2H $MoTe_2$ phase in SIB applications) have been investigated. It was observed that with the increase in crystallite size, the electrochemical performance improved for the sample that was prepared at a higher heating rate. The higher heating rate caused higher thermal gradients, which resulted in the sintering of the exterior portion before the interior, which further enhanced the porosity and Te defects that were responsible for the higher electrochemical performances of $MoTe_2$ in SIB applications. Even though the molecular weight of $MoTe_2$ is (351.14 g/mol) high but its high density of 7.7 g/cm^3 makes it suitable for high volumetric energy storage devices. The fundamental study of this research on the new class of layered TMDs anode materials will open new possibilities to use these 2D layered materials to enhance the electrochemical performance of the LIBs and SIBs in practical applications.

8.2 Future work

The recent thesis work affords a detailed fundamental study of various aspects of the $MoTe_2$ for LIB and SIB applications. In the future, the investigation can be extended according to the following factors.

8.2.1 Exfoliation of the studied bulk as-prepared $MoTe_2$ material

The electrochemical enhancement of the studied bulk as-prepared $MoTe_2$ polycrystalline material needs to investigate through a suitable exfoliation technique, which may provide higher specific capacity and better stability. The possible exfoliation process may include mechanical exfoliation, electrochemical exfoliation, polymer-assisted exfoliation, and ionic

liquid-assisted exfoliation. More emphasis should be placed on low-cost environment-friendly exfoliation techniques by tuning the materials to achieve the best electrochemical performance.

8.2.2 Composite with graphene or doping with any other elements

Suitable doping elements for both Mo and Te sites could help reduce the overall cell voltage and enhance conductivity to enable better electrochemical performance. Developing a composite with graphene or any other carbonaceous substance may enhance the cycle stability, because graphene will provide an excellent conductive path by utilizing the active materials to the maximum extent.

8.2.3 Different preparation techniques of $MoTe_2$

To synthesize the $MoTe_2$ material by other suitable methods such as sol-gel or hydrothermal process and then to observe the change of morphology and synthesis process effects on the electrochemical performance for LIB/SIB applications.

8.2.4 Advanced in situ/operando-based techniques along with detailed DFT study

The electrochemical mechanism could be investigated thoroughly by various advanced in situ/operando-based methods and a detailed DFT study of the 2H and 1T' phases of the $MoTe_2$ for both lithium and sodium insertion/deinsertion processes.

8.2.5 As an additive for metal sulfur batteries

The tunable bandgap and higher electronic conductivity of this class of materials, preferably the semimetallic 1T' phase of $MoTe_2$, can be of benefit if it is used as an additive in order to study the electrochemical performances of metal sulfur batteries.

8.2.6 Electrolyte modifications and engineering of the cell structure

Electrolyte modifications with different low-cost additives may enhance electrochemical performance and the development of new electrolyte compositions and binders, which can enable electrochemical enhancement and reduce the overall cost of both LIBs and SIBs. Ionic liquid-based electrolytes may enable the use of the anode at a broad temperature range for LIB and SIB applications. The optimization of LIB and SIB full-cell parameters and cell-configuration engineering in pouch cells will enable their use in practical applications.

Publications

A.1 List of peer-reviewed journals

1. **Manas Ranjan Panda**, Arnab Ghosh, Ajit Kumar, Divyamahalakshmi Muthuraj, Supriya Sau, Wenzhi Yu, Yupeng Zhang, A. K. Sinha, Matthew Weyland, Qiaoliang Bao, Sagar Mitra, Blocks of Molybdenum Ditelluride: A High Rate Anode for Sodium-Ion Battery and Full Cell Prototype Study, **Nano Energy, 64, 2019, 103951**.
2. **Manas Ranjan Panda**, Rashmi Gangwar, Divyamahalakshmi Muthuraj, Supriya Sau, Dhanshree Pandey, Arup Banerjee, Aparna Chakrabarti, Archna Sagdeo, Matthew Weyland, Mainak Majumder, Qiaoliang Bao and Sagar Mitra, High-Performance Lithium-Ion Batteries Using Layered 2H-$MoTe_2$ as Anode, **Small, 16, 2020, 2002669**.
3. **Manas Ranjan Panda**, Rashmi Gangwar, Divyamahalakshmi Muthuraj, Supriya Sau, Dhanshree Pandey, Arup Banerjee, Aparna Chakrabarti, Qiaoliang Bao, Mainak Majumder and Sagar Mitra et al., An Excellent and Fast Anode for Lithium-Ion Batteries Based on the 1T'–$MoTe_2$ Phase Material, **2021** (**under review**).
4. **Manas Ranjan Panda**, Qiaoliang Bao, Mainak Majumder and Sagar Mitra et al., The Impact of Crystallite Size, Morphology, and Electrolyte Additives on the Electrochemical Performance of Bulk $MoTe_2$ in Rechargeable Sodium-Ion Batteries, **2021 (under review)**.

A.2 List of conference proceedings

1. **Manas Ranjan Panda**, Anish Raj, Qiaoliang Bao and Sagar Mitra, $MoTe_2$, A Novel Anode Material for Sodium Ion Battery, **AIP Conf. Proc., 1942, 2018, 140078**.
2. **Manas Ranjan Panda**, Anish Raj, Qiaoliang Bao, Sagar Mitra, "Electrochemical Investigation of $MoTe_2$/rGO Composite Materials for Sodium-Ion Battery Application, **AIP Conf. Proc., 1961, 2018, 030033**.
3. **Manas Ranjan Panda**, Anish Raj, M. N Singh, Archana Sagdeo, A. K Sinha, Qiaoliang Bao, Sagar Mitra, Structural and Electrochemical Mechanism Study of Layered $MoTe_2$ Anode Material for Sodium-Ion Battery, **AIP Conf. Proc., 2115, 2019, 030615**.
4. **Manas Ranjan Panda**, Qiaoliang Bao, Mainak Majumder, Sagar Mitra, Efficient Sodium Storage Property of Layered $MoTe_2$: A High Rate Anode for Sodium-Ion Battery, **Engineers Australia, 201, 2020**.

A.3 List of databases

1. **Manas Ranjan Panda**, Anish Raj, Qiaoliang Bao, Sagar Mitra, Molybdenum Ditelluride ($MoTe_2$) as a reference pattern added to inorganic **ICDD pattern assigned PDF no 00-070-0155**.

A.4 List of patents

1. **Manas Ranjan Panda**, Supriya Sau, Sagar Mitra, Spectroelectrochemical Cell Holding Set-up for In-Situ/Operando Synchrotron-Based Measurements, **2019, Indian Patent Application number 201921023104**.
2. **Manas Ranjan Panda**, Anish Raj, Sagar Mitra, Rechargeable Sodium-Ion Batteries Based on Layered Electrode Materials and Method of Fabricating the Same, **2018, Indian patent, Application number 201821032876**.
3. **Manas Ranjan Panda**, A. Raj, S Mitra, D. P Dutta, Electrochemical Cell, Method for Synthesis of Bio-Derived Carbon and Preparation of Electrode from Bio-Derived Carbon. **2018, Indian patent, Application number 201841036449**.

A.5 List of awards recipients

1. **Tata Chemicals Best Journal Paper award** by the IITB-Monash Research Academy for the year 2019–2020 (**The Oskar Award Organized by IITB-Monash Research Academy**).
2. **Thermo fisher Scientific Best Collaborations award** by the IITB-Monash Research Academy on 11 August 2019 (**The Oskar Award organized by IITB-Monash Research Academy**).
3. **Best Poster Award**, The 62nd DAE Solid State Physics Symposium 2017 (**DAESSPS-2017**), December 26–30, 2017, BARC, DAE Convention Centre Anushaktinagar, Mumbai, India.

A.6 List of National/ International conference presentations

1. **Manas Ranjan Panda**, Supriya Sau, Qiaoliang Bao, Mainak Majumder and Sagar Mitra, Layered 2H-$MoTe_2$: A Novel Anode Material for Lithium-Ion Battery, International Virtual Conference on Advanced Nanomaterials and Applications (**VCAN 2020**) Vellore Institute of Technology, Vellore, Tamil Nadu, India. (Oral Presentation)

2. **Manas Ranjan Panda**, Qiaoliang Bao, Mainak Majumder, Sagar Mitra, Efficient Sodium Storage Property of Layered $MoTe_2$: A High Rate Anode for Sodium-Ion Battery, International Conference on Nanostructured Materials (**NANO 2020**), Clayton VIC 3800, Australia. (Oral Presentation)
3. **Manas Ranjan Panda**, Supriya Sau, Qiaoliang Bao and Sagar Mitra, $MoTe_2$ as a Potential Anode Material for Lithium-Ion Battery Applications, 7th International Conference on Advances in Energy Research 2019 (**ICAER-2019**), December 10–12, 2019, IIT Bombay, Mumbai, India. (Poster Presentation)
4. **Manas Ranjan Panda**, Qiaoliang Bao, Sagar Mitra, Molybdenum Ditelluride: A High Rate Anode for Sodium-Ion Battery, 9th Annual Chemical Engineering Postgraduate Association Conference (**CEPA-2019**) October 31, 2019, Monash University, Wellington Rd, Clayton VIC 3800, Australia. (Oral Presentation)
5. **Manas Ranjan Panda**, Anish Raj, M. N Singh, Archana Sagdeo, A. K Sinha, Qiaoliang Bao, Sagar Mitra, Structural and Electrochemical Mechanism Study of Layered $MoTe_2$ Anode Material for Sodium-Ion Battery, The 63rd DAE Solid-State Physics Symposium (**DAE-SSPS 2018**), December 18-22, 2018, Guru Jambheshwar University of Science and Technology (GJUS&T), Hisar, Haryana, India. (Poster Presentation)
6. **Manas Ranjan Panda**, Anish Raj K, Arnab Ghosh, Ajit Kumar, Qiaoliang Bao and Sagar Mitra, Electrochemical Study of Novel $MoTe_2$ Anode Based Lithium-Ion Full Cell, 2018 MRS Fall Meeting & Exhibit (**MRS-2018**), November 25–30, 2018, Boston, Massachusetts, USA (Oral Presentation)
7. **Manas Ranjan Panda**, Anish Raj K, Ananta Sarkar, Qiaoliang Bao and Sagar Mitra, Electrochemical Investigation of $MoTe_2$/rGO Composite Materials for Sodium-Ion Battery Application, International Conference on Nano-materials for Energy Conversion and Storage Applications (**NECSA-2018**) January 29–31, 2018, Pandit Deendayal Petroleum University, Gandhinagar, Gujarat, India. (Poster Presentation)
8. **Manas Ranjan Panda**, Anish K Raj, Qiaoliang Bao, Sagar Mitra, $MoTe_2$, A Novel Anode Material for Sodium-ion Battery, The 62nd DAE Solid State Physics Symposium 2017 (**DAESSPS-2017**), December 26–30, 2017, BARC, DAE Convention Centre Anushaktinagar, Mumbai, India. (Best Poster Award)
9. **Manas Ranjan Panda**, Anish Raj K, Ananta Sarakar, Arnab Ghosh, Ajit Kumar, Qiaoliang Bao and Sagar Mitra, $MoTe_2$ as a Potential Anode Material for Lithium-Ion

Battery Applications, 6th International Conference on Advances in Energy Research 2017 (**ICAER-2017**), December 12–14, 2017, IIT Bombay, Mumbai, India. (Oral Presentation)

10. **Manas Ranjan Panda**, Anish K Raj, Qiaoliang Bao, Sagar Mitra, $MoTe_2$ as a Potential Anode Material for Sodium-Ion Battery Applications, 1st World Conference on Solid Electrolytes for Advanced Applications: Garnets and Competitors September 06-09, 2017, Department of Physics, Pondicherry University, India. (Poster Presentation)
11. **Manas Ranjan Panda**, Anil Kumar Sinha, Qiaoliang Bao and Sagar Mitra, Electrochemical Mechanism Study of Layered $MoTe_2$ Anode Material for Sodium-Ion Battery The 7th Interdisciplinary Symposium on Materials Chemistry (**ISMC–2018**) December 4–8, 2018, Bhabha Atomic Research Centre (BARC), Trombay, Mumbai, India. (Poster Presentation)

A.7 List of other contributions

List of Patents

1. Ajit Kumar, Arnab Ghosh, **Manas Ranjan Panda**, Sagar Mitra, Electrochemical Cell Including Optical Window Made of Transparent Adhesive Tape and Method for Manufacturing thereof. 2018, Indian patent, **Application number 201821048139**.

List of Peer-Reviewed Journals

1. **Manas Ranjan Panda[1]**, Anish Raj[1], Dimple P Dutta and Sagar Mitra, Bio-Derived Mesoporous Disordered Carbon: An Excellent Anode in Sodium-Ion Battery and Full-Cell Lab Prototype, **Carbon, 2019 143, 402−412**.
2. Akhilesh Kumar Patel, **Manas Ranjan Panda**, Ekta Rani, Harishchandra Singh, S. ShanmukharaoSamatham, Abharana Nagendra, Sambhu Nath Jha, Dibyendu Bhattacharyya, Krishnawarrier G. Suresh, and Sagar Mitra, Unique Structure-Induced Magnetic and Electrochemical Activity in Nanostructured Transition Metal Tellurates $Co_{1-x}Ni_xTeO_4$ (x = 0, 0.5, and 1), **ACS Appl. Energy Mater. 2020, 3, 9436−9448**.
3. Md Adil, Ananta Sarkar, Amlan Roy, **Manas Ranjan Panda**, Abharana Nagendra, Sagar Mitra, Practical Aqueous Calcium-Ion Battery Full-Cells for Future Stationery Storage, **ACS Appl. Mater. Interfaces, 2020, 12, 11489–11503**.
4. S. Singh, A. Raj K, **Manas Ranjan Panda**, Raja Sen, Priya Johari, Anil Kumar Sinha, Sher Singh Meena, Sagar Mitra, Study of Higher Discharge Capacity, Phase Transition, and Relative Structural Stability in Li_2FeSiO_4 Cathode upon Lithium Extraction using

an Experimental and Theoretical Approach and Full Cell Prototype Study, **ACS Appl. Energy Mater., 2019, 2, 6584–6598**.

5. Arnab Ghosh, Ajit Kumar, Amlan Roy, Manas Ranjan Panda, Mega Kar, Douglas R MacFarlane, Sagar Mitra, Three-Dimensionally Reinforced Freestanding Cathode for High-Energy Room Temperature Sodium-Sulfur Batteries, **ACS Appl. Mater. Interfaces, 2019, 11, 14101−14109**.
6. Ajit Kumar, Arnab Ghosh, Amlan Roy, **Manas Ranjan Panda**, Maria Forsyth, Douglas R MacFarlane, Sagar Mitra, High-Energy Density Room Temperature Sodium-Sulfur Battery Enabled by Sodium Polysulfide Catholyte and Carbon Cloth Current Collector Decorated with MnO_2 Nanoarrays, **Energy Storage Mater., 2019, 20, 196–202**.

List of Conference Proceedings

1. Ananta Sarkar, Md Mofasser Mallick, **Manas Ranjan Panda**, Satish Vitta, Sagar Mitra, Free Standing Cu_2Te, New Anode Material for Sodium-Ion Battery, **AIP Conf. Proc., 2018, 1961, 030032.**

Acknowledgment

I am grateful to the Almighty for blessing me with this opportunity to explore my knowledge in this field. I am thankful to God for strengthening me to carry out this work during my PhD journey.

Undertaking this PhD has been a truly life-changing experience for me, and it would not have been possible without the support and guidance that I received from many people.

Firstly, I would like to express my sincere gratitude and respect to my supervisors Prof. Sagar Mitra, Prof. Mainak Majumder, and Prof. Qiaoliang Bao, for their continuous support of my PhD research, their patience, motivation, and sharing of their immense knowledge. I have benefited immensely from their guidance at all times in my research and during the writing of this thesis. I could not have imagined having better advisors and mentors for my PhD study.

I would like to extend my deepest gratitude to Prof. Sagar Mitra for his constant support and encouragement. The freedom and the affirmation he extended to me in all aspects of my work will always be the highlight of the memories of my study here. His guidance has enabled me to become an independent researcher.

I spent a remarkable one and a half years of learning with Prof. Qiaoliang Bao and Prof. Mainak Majumder at Monash University, which has given a unique depth and breadth to my thinking. I will always be grateful to them for their encouragement.

The interactions, encouragement, freedom, and support from Prof. Mainak Majumder motivated me to carry out my work to the final stages of my thesis.

Besides my advisors, I would like to thank Prof. C. Subramaniam and Prof. Douglas R. MacFarlane for their insightful comments and encouragement, which encouraged me to widen my research from various perspectives.

I am absolutely grateful to Prof. Murali Sastry, the CEO of IITB-Monash Research Academy, for his constant support and encouragement to carry out this work. I would additionally like to thank Dr. Kyatanahalli Nagabhushana, the COO of the Academy, for his support. My special thanks to Ms. Sheba Sanjay for the tremendous efforts she has taken to review the language of this thesis and my research publications, rendering them reader-friendly through global conventions of English syntax. I thank every member of the staff in the Academy for their friendly and timely support.

I thank Prof. Aparna Chakrabarty, Prof. Arup Banerjee, Rashmi Gangwar, and Dhanshree Pandey of RRCAT, Indore for the DFT analysis of my samples. All the DFT studies have been performed by them and have been included in this thesis with their permission.

I sincerely thank Prof. K. G. Suresh for providing me access to his laboratories and research facilities. I am thankful to Prof. Matthew Weyland and Dr. Tim Williams for contributing to the STEM and TEM experiments and analyses. I am ever thankful to Prof. A.K. Sinha, Prof. Archna Sagdeo, Prof. Sambhu Nath Jha, and Prof. Dibyendu Bhattacharyya of RRCAT, Indore, for helping me with the Synchrotron facilities of my samples. I thank Abharana Nagendra, Anuj Upadhyay, Abhaya, and M. N Singh for their assistance in SXRD and XANES measurements.

I thank SAIF, IIT Bombay, for their support in FEGTEM; NCPRE, for providing FESEM; and IRCC, for their assistance in the XPS study. I thank RRCAT, Indore, for providing SXRD, XANES, and EXAFS experimental facilities. I acknowledge the use of the facilities at the Monash Centre for Electron Microscopy (MCEM) and the support from the PD beamline at the Australian Synchrotron, which is part of Australian Nuclear Science and Technology Organisation (ANSTO).

I extend a big thank you to my lab mates at ECEL in IITB, especially to Mr. Ajit Kumar, Mr. Arnab Ghosh, Mrs. Divyamahalakshmi, Mr. Ananta Sarkar, Mr. Supriya Sau, Mr. Amlan Roy, Mr. Md. Adil, Mr. Tuhin Subhra Sahu, Mr. Govind Mishra, Mr. Manoj Gautam, Ms. Abhinanda Sengupta, Ms. Harshita Lohani, Ms. Pratima Yadav, Ms. Bhawana, Mr. Pradeep Kumar, Mr. Murali Krishna, Dr. Arpita Ghosh, and others for their support and encouragement. I especially thank Mr. Anish Raj and Mr. Ajit Kumar for their support during the initial stages of my PhD. I also thank Mr. Ajay, lab assistant at ECEL, for his help during the experiments.

I extend my thanks also to my lab mates at NSEL in Monash University, especially, Mr. Areeb Shehzad, Ms. Sally El Meragawi, Mr. KaziImdadul Hassan, Mr. Md. Joynul Abedin, Ms. Gargi Mukhopadhyay, Mr. Petar Jovanovic, Mr. Ehsan Ghasemiestahbanati, Ms. Yingyi Huang, Ms. Wanqing Chen, Mr. Declan McNamara, Dr. Mahdokht Shaibani, Dr. Meysam Sharifzadeh, Dr. Dilusha Cooray, Dr. Tanesh Gamot, and others for their support and encouragement.

I would like to thank Mr. Ranjeet Singh for all his support throughout my stay in IITB and Monash. I thank my friends Mr. Anil Pal, Ms. Sujata Kumari, Ms. Alaka Panda, and Ms. Lipsa Panigrahi for their support and encouragement.

Finally, there are no words to express my gratitude to my father (Mr. Akshaya Kumar Panda), mother (Ms. Manjulata Panda), sister (Ms. Gayatree Panda), my friends, and relatives. They have made silent sacrifices for the sake of my PhD study and have always been encouraging and supportive throughout my PhD.

Thank you all!
Manas Ranjan Panda